

Development of selective analytical methods for the characterization of complex crude oil mixtures

Dissertation

zur Erlangung des akademischen Grades eines

Doktors der Naturwissenschaften

– Dr. rer. nat. –

vorgelegt von

Xuxiao Wang

aus

Dengfeng, China P. R.

Fakultät für Chemie

der

Universität Duisburg-Essen

2016

Die vorliegende Arbeit wurde im Zeitraum von November 2011 bis Mai 2016 im Arbeitskreis von Prof. Dr. Wolfgang Schrader am Max-Planck Institut für Kohlenforschung im Mülheim an der Ruhr durchgeführt.

Tag der Disputation: 22.09.2016

Gutachter: Prof. Dr. Wolfgang Schrader

Prof. Dr. Carsten Schmuck

Vorsitzender: Prof. Dr. Stefan Rumann

DuEPublico

Duisburg-Essen Publications online

UNIVERSITÄT
DUISBURG
ESSEN

Offen im Denken

ub | universitäts-
bibliothek

Diese Dissertation wird über DuEPublico, dem Dokumenten- und Publikationsserver der Universität Duisburg-Essen, zur Verfügung gestellt und liegt auch als Print-Version vor.

DOI: 10.17185/duepublico/42269

URN: urn:nbn:de:hbz:464-20200317-074500-4



Dieses Werk kann unter einer Creative Commons Namensnennung - Nicht kommerziell - Keine Bearbeitungen 4.0 Lizenz (CC BY-NC-ND 4.0) genutzt werden.

Für meine geliebte Familien

“The more I study science, the more I believe in God.”

Albert Einstein

Erklärung

Hiermit versichere ich, dass ich die vorliegende Arbeit mit dem Titel

„Development of Selective Analytical Methods for the characterization of complex crude oil mixtures“

selbst verfasst und keine außer den angegebenen Hilfsmitteln und Quellen benutzt habe, und dass die Arbeit in dieser oder ähnlicher Form noch bei keiner anderen Universität eingereicht wurde.

Mülheim an der Ruhr, im April 2016

Xuxiao Wang

Abstract

The demand for affordable and large-scale energy throughout the world drives people to focus on the fossil-based materials continuously; meanwhile, the depletion of light sweet crude oils has led to an increase in refining the unconventional and heavier petroleum feedstocks. However, the unwanted presence of heteroatoms (sulfur, nitrogen and oxygen)-containing compounds in heavier crude oils causes poisoning of refining catalysts and harms the environment after combustion. A better understanding of crude oil composition is the beginning to develop new methods to lower the heteroatoms content of fuels efficiently. High Resolution Mass Spectrometry (HRMS), such as Fourier Transforms Ion Cyclotron Resonance Mass Spectrometry (FT-ICR MS) and High-field Orbitrap (HF Orbitrap) FTMS, has emerged as a powerful and valuable tool for detailed analysis of supercomplex crude oil mixtures at a molecular level. Even though the extraordinary complexity of crude oil and the inherent space charge effects in the ICR-cell as well as the ionization discrimination make it impossible to fully characterize crude oils. Selective analysis of crude oil is significant to gain a better understanding of the material. Electrospray Ionization Mass Spectrometry (ESI-MS) has proven efficient for the analysis of polar compounds in petroleum. This study is focusing on developing different derivatization techniques in combination with ESI-MS to characterize selectively the complex crude oil mixtures. In turn, the mechanistic studies of reactions promote a deeper exposition and better employment of the electrochemical character of ESI-MS. Theoretical calculations based on Quantum Mechanics (QM) as well as Proton Nuclear Magnetic Resonance (^1H NMR) facilitate the illustration of reaction mechanism. The combination of analytical chemistry together with organic chemistry, electrochemistry and theoretical chemistry offers an efficient way to gain better understanding of complex crude oil mixtures.

Kurzfassung

Der weltweit große Bedarf an bezahlbarer Energie führt dazu, dass fossile Materialien weiterhin im Fokus stehen; gleichzeitig führt die Erschöpfung von Quellen leichter, süßer Öle zu einer erhöhten Prozessierung schwerer, unkonventioneller Öle. Der unerwünscht hohe Gehalt an heteroatomhaltigen (Schwefel, Stickstoff und Sauerstoff) Komponenten in schweren Ölen führt jedoch zu einer Vergiftung der bei der Raffinerie eingesetzten Katalysatoren und zu einer nach der Verbrennung erhöhten Umweltbelastung. Ausgangspunkt für die Entwicklung neuer Verfahren, um den Heteroatomgehalt von Treibstoffen zu senken, ist ein besseres Verständnis der Erdölzusammensetzung. Die hochauflösende Massenspektrometrie (HRMS), wie Fourier-Transform Ionenzyklotron-Resonanz Massenspektrometrie (FT-ICR MS) oder Hochfeld Orbitrap (HF Orbitrap) FTMS, hat sich als schlagkräftige Methode zur Analyse hochkomplexer Erdöle auf molekularer Ebene entwickelt. Nichtsdestotrotz verhindern die hohe Komplexität der Probe, Space-Charge-Effekte in der ICR-Zelle oder Diskriminierungseffekte bei der Ionisation eine allumfassende Analyse von Erdölen. Selektive Analyse einzelner Komponenten ist wichtig, um ein besseres Verständnis von der Zusammensetzung zu erhalten. Die Elektrospray-Ionisations-Massenspektrometrie (ESI-MS) ist eine effektive Methode zur Charakterisierung polarer Komponenten in Erdöl. Diese Arbeit behandelt die Entwicklung verschiedener Derivatisierungsmethoden, die mit Hilfe von ESI-MS eingesetzt werden können, um Erdölbestandteile selektiv zu untersuchen. Mechanistische Studien der Reaktionswege erlauben darüber hinaus ein tieferes Verständnis des elektrochemischen Charakters der Elektrospray Quelle. Theoretische, auf Quantenmechanik (QM) basierende, Berechnungen sowie Protonen-Magnetresonanz-Spektrometrie (^1H NMR) erlauben einen Blick auf die Reaktionsmechanismen. Die Kombination analytischer Chemie und organischer Chemie mit Elektrochemie und

theoretischer Chemie erlaubt eine effektive Möglichkeit, ein besseres Verständnis komplexer Erdölmischungen zu erlangen.

Contents

<i>Erklärung</i>	5
<i>Abstract</i>	6
<i>Kurzfassung</i>	7
Chapter 1 Introduction	11
1.1 Crude oil	11
1.2 Analytical chemistry of crude oil	15
1.3 Ionization in mass spectrometry	41
1.4 Data interpretation	50
1.5 Scope of this study	54
Chapter 2 Selective Analysis of Sulfur-Containing Species in a Heavy Crude Oil by Deuterium Labeling Reactions and Ultrahigh Resolution Mass Spectrometry*	58
2.1 Abstracts	59
2.2 Introduction	60
2.3 Experimental section	62
2.4 Results and Discussion	64
2.5 Conclusion	73
Chapter 3 Adding a Chemical Dimension as Tool for Selective Analysis of a Heavy Crude Oil by Fourier Transform Ion Cyclotron Resonance Mass Spectrometry (FT-ICR MS)*	75
3.1 Abstracts	76
3.2 Introduction	77
3.3 Experimental section	79
3.4 Results and Discussion	82
3.5 Conclusion	91
Appendix 3	93
Chapter 4 Experimental and Theoretical Evaluation of Electrochemically-induced Electron Transfer Reaction in Electrospray Mass Spectrometry*	98
4.1 Abstracts	99
4.2 Introduction	100
4.3 Experimental section	100
4.4 Results and Discussion	100
4.5 Conclusion	110
Appendix 4	112
Chapter 5 Electrochemically-induced Selective Analysis of Sulfur-Containing in Heavy Crude Oils on the Millisecond Time Scale by Electrospray Ionization Mass Spectrometry*	168

Contents	10
5.1 Abstracts	169
5.2 Introduction	170
5.3 Experimental section	171
5.4 Results and Discussion	172
5.5 Conclusion	181
Appendix 5	183
<i>Chapter 6 Electrospray Fourier Transform Ion Cyclotron Resonance Mass Spectrometry (ESI FT-ICR MS): Reactivity of Poly Aromatic Hydrocarbon and Poly Aromatic Heterocycles in Heavy Crude Oils towards Benzyl Halides*</i>	203
6.1 Abstracts	204
6.2 Introduction	204
6.3 Experimental section	206
6.4 Results and Discussion	208
6.5 Conclusion	219
<i>Chapter 7 Summary</i>	221
<i>References</i>	226
<i>Appendix</i>	234
List of Figures	234
List of Schemes	240
List of Tables	241
List of Abbreviations	242
List of Publications	244
Curriculum Vitae	246
<i>Acknowledgements</i>	247

Chapter 1 Introduction

1.1 Crude oil

1.1.1 Crude oil composition

Crude oil is a complex mixture of hydrocarbons and other organic compounds that contain nitrogen, oxygen and sulfur atoms as well as trace amounts of metals such as iron, nickel, copper and vanadium [1, 2]. The composition of crude oil varies widely depending where and how it was formed. Generally, there are four main types of hydrocarbon compounds found in crude oil, and they are alkanes (paraffins), naphthenes, aromatics and asphaltics. The relative abundance of each kind of molecules varies widely from oil to oil, for example, the percent range for alkanes in crude oils spans from 15% to 60%, and for aromatics from 3% to 30% as shown in Table 1.1 [3].

Table 1.1: Hydrocarbon composition of crude oil

Hydrocarbon	Percent Average (%)	Percent Range (%)
Alkanes	30	15 to 60
Naphthenes	49	30 to 60
Aromatics	15	3 to 30
Asphaltics	6	Remainder

Although the relative abundance of different organic molecules widely vary, the elemental composition of petroleum varies over fairly narrow range as shown in Table 1.2 [3], for example, the percent range of carbon spans only from 83% to 85%, and for hydrogen from 10% to 14%. It is worth noting that the percent range of heteroatom elemental composition in crude oils varies wider than the percent ranges of carbon and hydrogen, for example, it spans

from 0.1% to 2% for nitrogen, and from 0.05% to 6% for sulfur depending on oil sources.

Table 1.2: Elemental composition of crude oil

Hydrocarbon	Percent Range (%)
Carbon	83 to 85
Hydrogen	10 to 14
Nitrogen	0.1 to 2
Oxygen	0.05 to 1.5
Sulfur	0.05 to 6
Metals	< 0.1

1.1.2 Crude oil properties



Figure 1.1: Heavy crude oil liquid.

The composition of crude oil determines the physical and chemical properties. In petroleum field, “heavy” and “viscous” are commonly used to describe heavy oils or unconventional oils. Heavy oils derive from the biodegradation of crude oil under anoxic conditions *in situ* in reservoirs. They

contain higher concentrations of heteroatoms and metals, tend to be more viscous and heavy than conventional oils, therefore they do not flow as easily as conventional “light” oils as shown in Figure 1.1 [4].

In general, the heavier or more viscous the crude oil is, the lower is its economic value, and main reasons can be covered as follows:[5]

- I. Making their extraction process more difficult;
- II. Causing fouling and deposits in storage;
- III. Causing catalyst poisoning in upgrading process;
- IV. Causing environmental harm during combustion in the form of nitrogen oxides (NO_x) and sulfur oxides (SO_x), respectively.

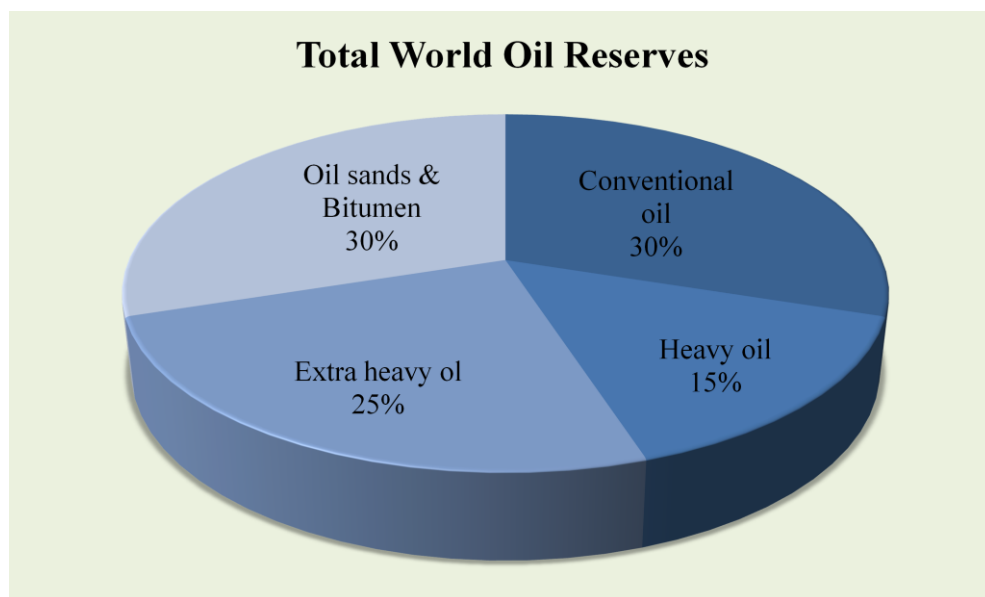


Figure 1.2: Distribution of world oil reserves.

Up to 70% of the world oil reserves of 9 to 13 trillion bbl (Unit of volume for crude oil and petroleum products. One barrel equals 42 US gallons or 35 UK gallons) as shown in Figure 1.2 [6] are made up by the unconventional oil resources including heavy oil, extra heavy oil and bitumen [6]. As the decline of the conventional oil reserves and the increase of the oil demand across the world, the oil industry focus is shifting towards the investment and exploitation

of the unconventional oil sources due to its abundant reserve, and its lower price comparing to other new energy sources.

Thus, understanding and knowing of chemical properties of petroleum make more sense to solve the above problems, especially by heavy crude oils.

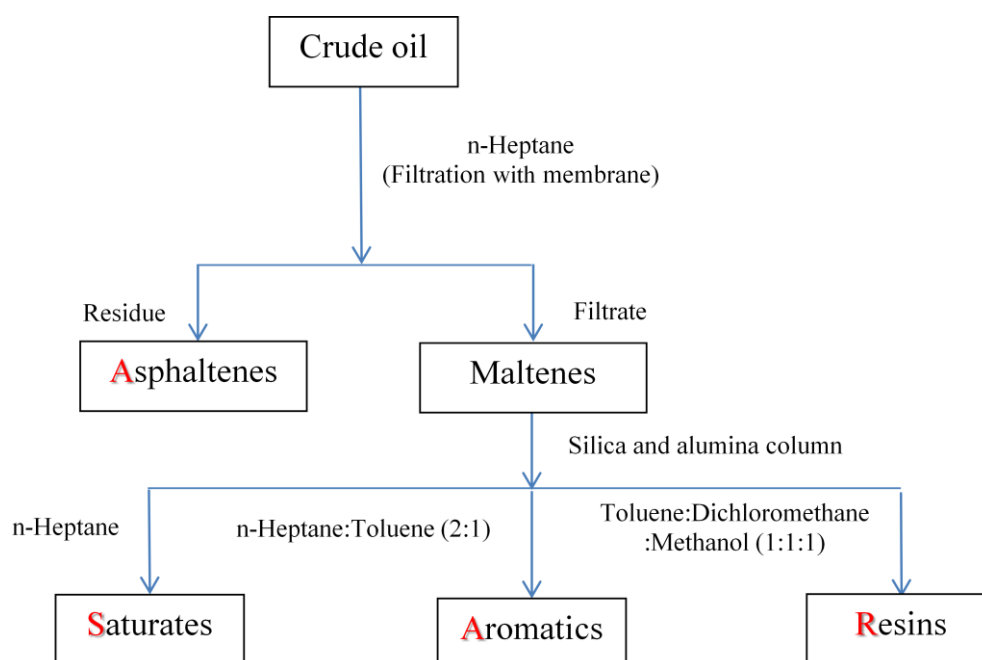


Figure 1.3: Schematic illustration of SARA analysis.

Crude oil is a highly heterogeneous mixture found in nature [7], and simplification is an important way to uncover the chemical composition and to further understand the chemical properties of crude oils. In petrochemistry, **Saturate Aromatic Resin and Asphaltene (SARA)** as depicted in Figure 1.3 [8] is a commonly used fractionation method that divides crude oil components according to their solubility and polarity [9, 10]. Saturates consist of nonpolar molecules including linear, branched and cyclic saturated hydrocarbons called paraffins. Aromatics are slightly more polarizable and contain one or more aromatic rings. Resins consist of more polar NSO-containing species than aromatics, and need to be eluted out from the column through more polar solvents. Asphaltenes are the most aromatic and NSO atom-rich fractions, and

they are insoluble in heptane, therefore asphaltenes are first filtered out in SARA-separation.

Typically, the light or conventional oils contain a higher content of the saturated and aromatic hydrocarbons with a smaller proportion of resins and asphaltenes, while heavy oils contain a higher amount of more polar resins and asphaltens and a lower proportion of saturated and aromatics. The heaviness (density and viscosity) of heavy oil is due to the higher ratio of aromatics and naphthene compounds and higher amounts of NSO (nitrogen, sulfur, oxygen and heavy metals).

1.2 Analytical chemistry of crude oil

Each crude oil has a unique mix of different molecules, different composition of each crude oil determines the different physical and chemical properties, and different property of crude oil determines the different reactivity, which makes the characterization and analysis of crude oil significant. However, crude oil is a “super-complex” mixture [8] and its complexity challenges the analytical techniques [10]. Various techniques,[11] such as nuclear magnetic resonance (NMR),[12, 13] X-ray diffraction (XRD) [14], have been used to examine the structure of crude oil components. These techniques are efficient to determine the molecular structures of compounds of a mixture with certain number of molecules; however, they are very difficult to study the molecular structures of the myriad of individual distinct compounds present in crude oil. Ultrahigh resolution mass spectrometry (HRMS)[15] is the most sensitive scale, and it has flourished as the most powerful tool to obtain the composition of such super complex mixtures. By now, from the mass analyzer point of view, there are many types of mass spectrometers, but magnetic sectors and quadrupoles, which just select one single mass to charge ratio at a time, are unrealistic to characterize complex mixtures such as crude oils, so they are excluded in this section. Ion traps (IT), Time-of-flight (TOF), Fourier Transform

Ion Cyclotron Resonance (FT-ICR) and Orbitrap, which are capable of addressing the entire mass range, therefore they are most likely used in complex mixtures analysis. However, mass spectrometers based ion traps alone are not competent to the task of characterization of crude oils due to their quite limited mass accuracy of ion traps; mass spectrometers based on TOF suffer from the limited resolving power, and thus, IT and TOF are not employed in this work. Fourier Transform Ion Cyclotron Resonance Mass Spectrometry (FT-ICR MS) [16-18] and the newly emerging technique of High-field (HF) Orbitrap FTMS are two main types of mass spectrometers employed in petroleum analysis due to their ultrahigh mass resolution, high mass accuracy and high dynamic mass range, and they will be discussed in this section in details.

1.2.1 Fourier Transform Ion Cyclotron Resonance Mass Spectrometry (FT-ICR MS)

One of the most interesting applications of motion of charged particles in electric and magnetic fields is the cyclotron. It was invented by E.O. Lawrence and M. S. Livingston in 1934 to accelerate the charged particles.

1.2.1.1 Physical principle of FT-ICR

1.2.1.1.1 Lorenz Force

In a static magnetic field \mathbf{B} , an ion moving with a velocity \mathbf{v} experiences a force \mathbf{F} called Lorenz force, and according to the Newton's second law, the force can be given by Eq. (1.1) [16]

$$\mathbf{F} = m \, dv/dt = q \, \mathbf{v} \times \mathbf{B} \quad (1.1)$$

where \mathbf{F} is the force vector, q is the charge, \mathbf{v} is the velocity vector and \mathbf{B} is the magnetic flux density vector. The direction of the force \mathbf{F} is determined by the vector cross product of $\mathbf{v} \times \mathbf{B}$ and always perpendicular to the velocity \mathbf{v} of the particles, so the magnetic force does not work on the particles, which means the kinetic energy of the particle stays unaffected.[19] The magnitude is determined by $q|\mathbf{v}||\mathbf{B}|\sin\theta$ and remains constant; θ is the angle between \mathbf{v} and \mathbf{B} . When θ is equal to 90° , that is, the ion is perpendicular to the magnetic field, the particle will move in a circular orbit as shown in Figure 1.4 [20].

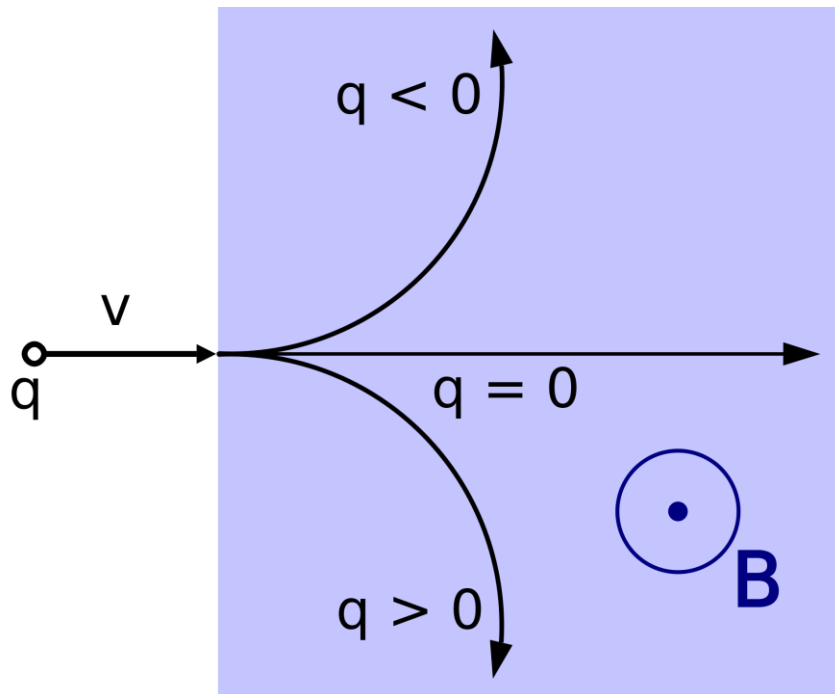


Figure 1.4: Trajectory of a particle with a positive ($q>0$) or negative ($q<0$) charge under the influence of a spatially uniform magnetic field \mathbf{B} , which is pointing perpendicularly out of the screen. Charged particles experience the Lorentz force ($\mathbf{F} = q \mathbf{v} \times \mathbf{B}$).

The ion angular acceleration in a plane is given by $dv/dt = v^2/r$, substituting it to Eq. (1.1), Eq. (1.2) is derived as:

$$m v^2/r = q \mathbf{v} \times \mathbf{B} \quad (1.2)$$

whereas, angular velocity, ω (in rad/s), is defined as $\omega = v/r$, so we substitute the ω and simplify it, Eq. (1.3) is obtained

$$\omega_c = q \mathbf{B}/m \quad (1.3a)$$

or

$$v_c = \omega_c/2\pi = q \mathbf{B}/2\pi m = \mathbf{B}/2\pi(m/q) \quad (1.3b)$$

in which, v_c in Hz; \mathbf{B} in tesla; m in u; q in multiples of elementary charge.

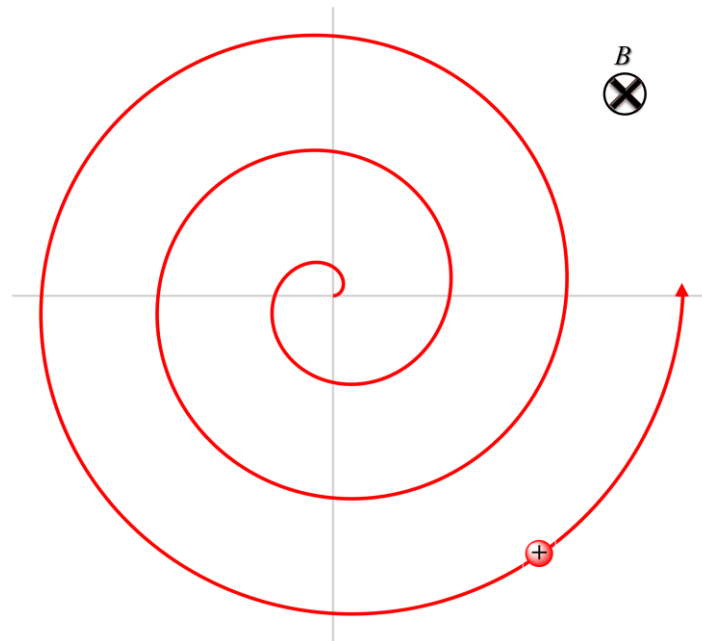


Figure 1.5: Sketch of ion cyclotron motion in a spatially uniform magnetic field \mathbf{B} with direction perpendicularly pointing inwards the screen. A positive ion has a spiral-shape ion cyclotron motion.

The motion is called “ion cyclotron motion” (see Figure 1.5), and the Eq. (1.3b) is called “ion cyclotron equation”, and so v_c is called “ion cyclotron frequency”. From Eq. (1.3b), we see that all ions with a given mass-to-charge

ratio, m/q , have the same ICR frequency, *independent of their velocity*, which makes **ICR** useful and meaningful for **mass spectrometry**. [16]

The ICR frequency of an ion is inversely proportional to m/q and directly proportional to the strength of the applied magnetic field. When ions of two different m/q ratios are excited on resonance with the same excitation voltage in the same amount of time, the ion with the lower m/q ratio will have a higher cyclotron frequency; oppositely, the ion with the higher m/q ratio will have a lower cyclotron frequency.

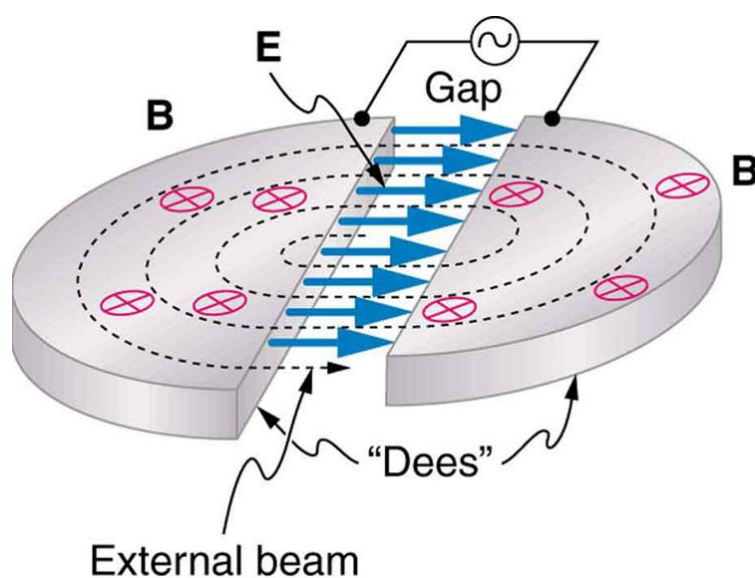


Figure 1.6: Cyclotron.

FT-ICR MS is built based on the cyclotron, and cyclotron as depicted in Figure 1.6 [21] uses a magnetic field to cause particles to move in circular orbits. As the particles pass between the plates of the two metallic plates called "Dees" that are connected to an alternating electric source (radio-frequency voltage), the voltage across the gap is oscillated to accelerate them to a high velocity in a higher radius orbit until to exit the system. To maintain the spiral movement, the frequency of the applied field has to be the same as ICR frequency of the ion, and this condition is called the resonance condition. The same physical principle is applied to FT-ICR MS.

1.2.1.1.2 Ion trapping

Before ion excitation and detection, ions first need to be trapped in the ICR cell and restrained to move along the axis of the magnetic field. A low potential of an order of 1 V is applied to the trapping plates as shown in Figure 1.7.

1.2.1.1.3 Ion excitation

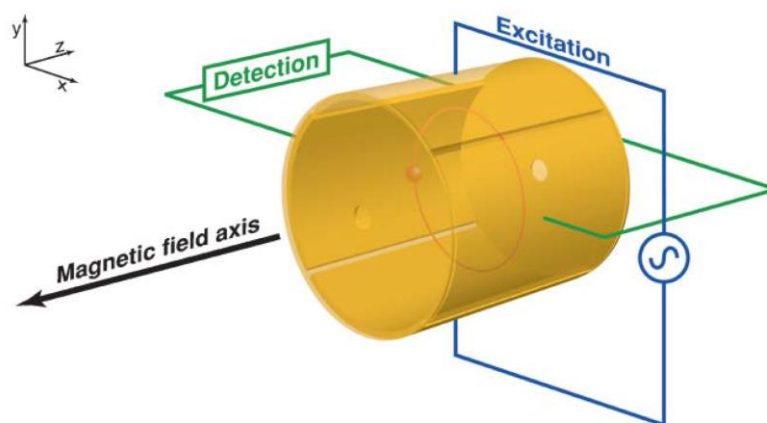


Figure 1.7: Schematic representation of a cylindrical FT-ICR analyzer cell. The magnetic field axis is coaxial with the trapping axis (z-axis), and the trapping electrodes not shown are located at each end of the cell. A charged particle is orbiting in the ICR cell.

When the ions enter the FT-ICR cell, ion cyclotron motion in a static magnetic field will not generate any signal if placed between a pair of detection electrodes, because the orbit radii of ions are too small to be detectable. In order to collect a signal, ions of a given m/q need to be excited through usage of a radio frequency (RF) potential applied to the two excitation plates as depicted in Figure 1.7 [22]. When the frequency of the applied oscillating electric field is the same as the cyclotron frequency of the ions, the ions absorb energy and are accelerated to higher orbit of radius. Finally, all ions with different m/q will be excited to orbits of the same radii (detectable radii), although their ICR frequencies are different [16, 23].

1.2.1.1.4 Ion detection

When the rf current is turned off, the ion packets with a given m/q will induce an image current that is detected by a pair of electrodes called detection plates in the analyzer cell [16]. The two plates are connected to ground through a resistor. When the ion packets (e.g. positive ions) approach the detection plate, a stream of electrons attracted from the ground will travel through the external circuit and accumulate on the detection plate causing a temporary current. As the ions continue to rotate and approach the other detection plate, the electrons then accumulate on the other detection electrode. As the electrons chase the ions back and forth, the resistor in the external circuit measures the ac voltage, which is an indirect measure of the ions circling inside the cell. The stream of electrons in the external circuit represents the image current, and the amplitude of this current is proportional to the number of ions in the ICR analyzer cell, while its frequency is equal to the ICR frequency of the ions. As the ion packets lose energy and spiral back down to their original orbits, the alternating current induced in the external circuit gradually subsides, and the image current data are captured as a function of time and it is from here that the raw data (known as a transient, time-domain data, or a free induction decay of FID) is obtained. The raw data represent the detection at the same time of all ions with their different ICR frequencies. The ions are detected without colliding with the electrodes, and this non-destructive detection is unique to FT-ICR and improves sensitivity compared to other destructive detection methods.[19, 24]

1.2.1.1.5 Fourier Transform (FT) of ICR transients

Fourier Transformation of ICR transients were first developed by M. B. Comisarow and A. G. Marshall in 1973 [25], and the data processing of FT-ICR MS is shown in Figure 1.8 [22]. The time-domain ICR signals go through a mathematical procedure known as Fourier Transform (FT) [26], and then the

frequency-domain ICR signals will be obtained, and a spectrum will be produced where the signal intensity is plotted as a function of the ICR frequency of the ions based on calibration. Recall the “ion cyclotron equation” in which ν_c is related to mass-to-charge ratio and a mass spectrum is finally created where the signal intensity is plotted as a function of m/z .

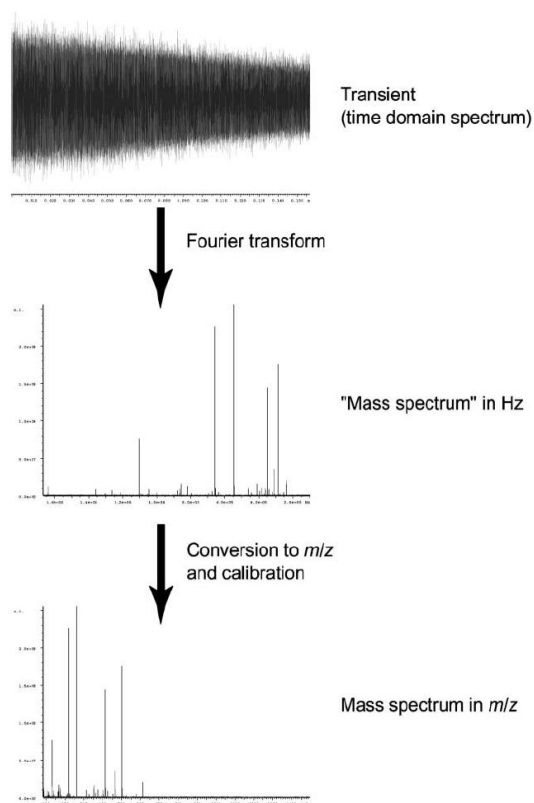


Figure 1.8: An overview of FT-ICR MS raw data processing.

1.2.1.2 Ultrahigh resolution of FT-ICR

Mass resolving power is the measure of the ability to distinguish two peaks of slightly different m/z . FT-ICR MS is capable of powerful mixture analysis due to its ultrahigh mass resolving power (distinguish peaks separated by as little as 1.1 mDa) as well as its high dynamic mass range [7].

We do the first derivative of the “ion cyclotron equation” with respect to m , we get Eq. (1.4) expressed by:

$$d\omega_c/dm = -q \mathbf{B}/m^2 = -\omega_c/m \quad (1.4)$$

Organizing the Eq. (1.4) we obtain the relation given by Eq. (1.5)

$$\omega_c/d\omega_c = -m/dm \quad (1.5)$$

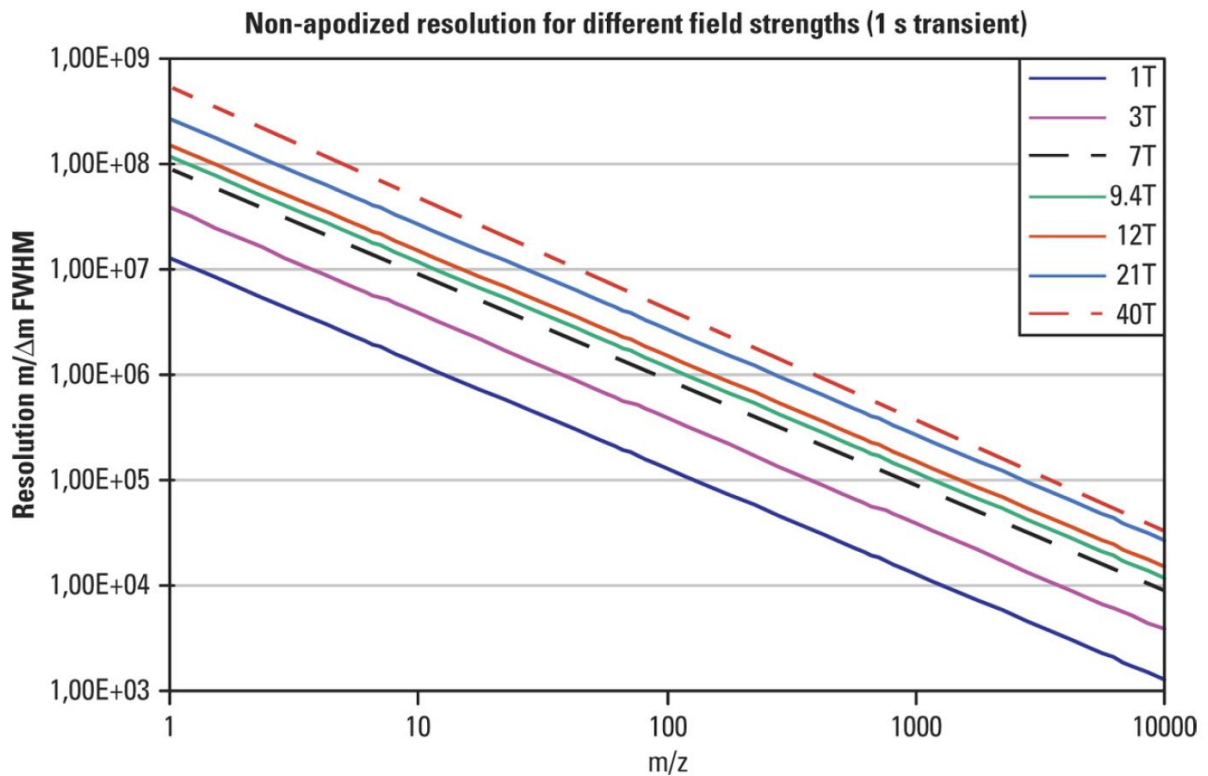


Figure 1.9: Influence of magnetic field strength on resolution. A comparison of the non-apodized resolution (full width at half maximum, FWHM) achievable for a range of masses for 1 s transient employing magnetic field strengths of 1 to 40 T is presented. Both axes are logarithmic.

The resolution is defined as the full width of a spectral peak height in all types of FT spectroscopy as follows: $\Delta\omega_{50\%}$ for frequency-domain or $\Delta m_{50\%}$ for mass-domain FT-ICR spectra. The resolving power is therefore defined as $\omega/\Delta\omega_{50\%}$ and $m/\Delta m_{50\%}$ based on Eq. (1.5), from which, we know that the frequency resolving power and mass resolving power in ICR MS are actually

same. Substituting Eq. (1.3) into Eq. (1.5), we obtained a mass resolution given by Eq. (1.6):

$$m/\Delta m_{50\%} = -q B/m\Delta\omega_{50\%} \quad (1.6)$$

Eq. (1.6) shows that FT-ICR MS resolving power is inversely related to m/z , which means that the higher mass resolving power will be obtained at the lower m/z . Eq. (1.6) also indicates that FT-ICR MS resolving power directly varies with the magnetic field strength, which means that FT-ICR MS achieves the highest mass resolution possible by operating at the maximum magnetic field strength throughout the mass range, and this can also be seen in Figure 1.9 [27], where the resolution achievable within 1 s transient for magnetic field strengths of 1 to 40 T versus mass is compared, and the resolving power will increase linearly with increasing magnetic field.

The relation between mass resolving power and acquisition period at low-pressure is expressed by Eq. (1.7) [16]:

$$m/\Delta m_{50\%} = 1.274 \times 10^7 q B T_{acq'n}/m\Delta\omega_{50\%} \quad (1.7)$$

where $T_{acq'n}$ is time-domain ICR signal acquisition period.

Eq. (1.7) demonstrates that mass resolution is directly proportional to acquisition period, and that means mass resolution can be remarkably high if the time-domain acquisition period is long enough. This can also be seen in Figure 1.10 [27], where the resolution achievable with magnets of 7 and 21 T for duration of transient of 1 s (solid lines) is compared with the resolution obtained with 5 s transients (dash lines). The resolving power increases linearly with increasing acquisition time duration.

ICR frequencies can be measured with high precision, which leads to ultrahigh mass resolving power. In this work, a 7T FT-ICR MS (Actively

Shielded) is employed. It achieves a resolution of >750000 at m/z 400 at slower scan repetition rates under broadband mode, and enables unambiguous compound characterization even for complex mixtures as crude oils.

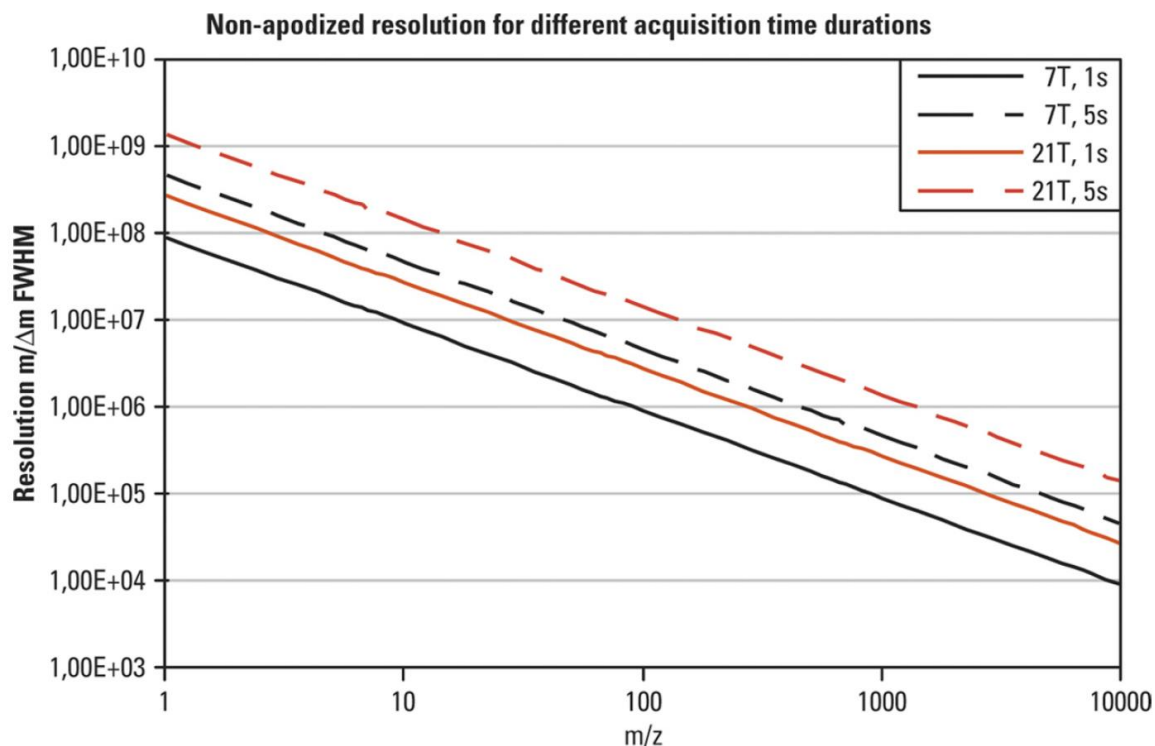


Figure 1.10: Influence of transient duration on resolution. A comparison of the non-apodized resolution (full width at half maximum, FWHM) achievable for a range of masses with magnetic field strengths of 7 and 21 T and for durations of transients of 1 and 5 s is represented. Both axes are logarithmic.

1.2.1.3 High accuracy of FT-ICR

Mass accuracy and resolution is now a dominant tool for structural characterization and elemental composition determination in various applications fields. Mass accuracy is the ratio of the m/z measurement error to the true m/z , and is usually measured in ppm represented by Eq. (1.8),

$$E_{ppm} = (\text{exact mass} - \text{accurate mass}) * 10^6 / \text{exact mass} \quad (1.8)$$

where exact mass is the calculated mass based on adding up the masses of each atom in the molecule; accurate mass is the experimentally measured mass value; E_{ppm} is the mass error in parts per million (ppm).

Mass accuracy is the ability to measure or calibrate the instrument response against a known entity, its measurement (ppm) indicates the deviation of the instrument response from a known monoisotopic calculated mass [28]. A comprehensive method of evaluating instrument mass accuracy measurement capability is by calculating the root-mean-square (RMS) error given by Eq. (1.9):

$$\text{RMS} = \sqrt{\sum (E_{ppm})^2 / n} \quad (1.9)$$

where E_{ppm} is the ppm error, and n is the number of masses.

It is worth noting that the RMS error allows some measurements to fall outside the ppm error “window of interest”. An instrument calibration, normally operating conditions, sufficient intensity, free from interferences and good reference ensure good mass accuracy measurement.

Increasing the trapping voltage of ICR cell helps preventing ions with exorbitant translational energy from escaping axially from the ICR trap, but it causes trapping too many ions inside ICR cell. Too much ions in ICR cell cause Coulomb repulsions between ions, and the Coulomb repulsions can then shift and broaden FT-ICR mass spectral peaks by pushing like-charge ions apart into regions of a different applied external electric or magnetic field, which finally causes ICR frequency shifting and mass accuracy decreasing [16].

In view of the above problem, the hybrid Linear ion Trap FT-ICR Mass Spectrometer (LTQ-FT-ICR MS), which is also employed in this work, enables employment of Automatic Gain Control (AGC) in 2-D linear Ion trap to regulate number of ions that are forwarded to ICR cell to reduce space charging

effects in the ICR cell, and achieve a mass accuracy of better than 2 ppm with external calibration [29].

Ultrahigh mass resolution and high mass accuracy of FT-ICR MS allows for unambiguous assignment of molecular formulas for tens of thousands of chemically distinct components, and FT-ICR MS is thus a valuable and powerful tool for characterization of compositionally complex mixtures, such as crude oils [1, 2, 7, 8, 16-18, 23, 30-43].

1.2.2 High-field Orbitrap FTMS

1.2.2.1 Physical principle of Orbitrap FTMS

1.2.2.1.1 The Kingdon trap

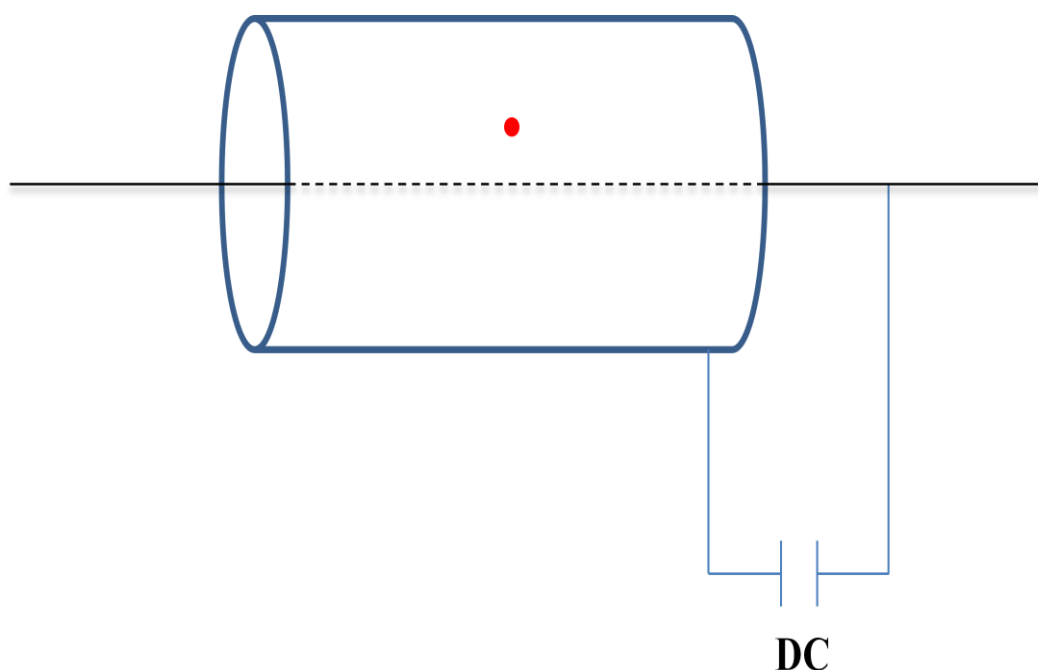


Figure 1.11: Sketch of the cylindrical Kingdon trap. A direct current (DC) voltage is applied between a rectilinear wire and a surrounding cylinder. As a result, a charged particle represented in red is dynamically trapped in the free space between the inner and outer electrodes.

The Orbitrap mass analyzer is based on an electrostatic ion traps called Kingdon trap [44]. The Kingdon trap invented in 1923 consists of two coaxial electrodes, a thin wire central electrode (cathode for positive ion) and a cylindrical outer electrode (anode for positive ion) as shown in Figure 1.11 [44]. Ideally, if the electrodes are assumed to be infinitely long with a DC voltage applied to the central electrode and outer electrode grounded, it creates a hypothetical “radial logarithmic” potential (Φ) between the two electrodes of the form given by Eq. (1.10):

$$\Phi = A \ln r + B \quad (1.10)$$

where r is the radial coordinate, and A and B are constants at a particular value of applied voltage [45].

When a positive ion was created by discharging inside the trap and processed the appropriate kinetic energy and direction of motion (a sufficient initial velocity perpendicular to the central electrode), this ideal “radial logarithmic” field would allow the ion to orbit around the central wire. In reality, in order to confine the ions in the axial direction, two endcaps are introduced and a DC potential was applied to endcaps with the same polarity as the positive ion (negative DC voltage when trapping negative ions), so the ions both stably rotate around the wire and oscillate along the central electrode of the Kingdon trap, nevertheless, the endcaps distorts the hypothetical field created by the infinite electrodes.

1.2.2.1.2 The Knight-style Kingdon trap

Although the Kingdon trap provided an approach to trap and store ions for a certain time in an electrostatic field, it did not provide an effective way to differentiate between the m/z values of the trapped ions. In 1981, Knight modified the geometry of the outer electrode to give a harmonic axial potential

(an axial quadrupole potential), and this modified ion trap was called the “ideal Kingdon trap” or “Knight-style Kingdon trap” [46], and the pure quadrupolar potential is given by Eq. (1.11)

$$\Phi = A (z^2 - r^2 / 2) \quad (1.11)$$

In addition to the “radial logarithmic potential” in Eq. (1.10), the cylindrically symmetric potential for the modified Kingdon trap is represented approximately by Eq. (1.12):

$$\Phi = A (z^2 - r^2 / 2 + B \cdot \ln r) \quad (1.12)$$

where z and r are cylindrical coordinates, and A and B are constants related to the electrode geometry and applied voltages. The z^2 portion of the potential (the axial quadrupolar potential) causes ions within the trap to undergo harmonic oscillation in the z -direction (axial motion), and the frequency of ion motion in the z -axis is m/z dependent, while the logarithmic portion of the potential between the central and outer electrodes causes the ions to orbit the central electrode (rotation motion).

As shown Figure 1.12 [46], the outer electrode was split at the middle ($z = 0$), allowing ions to be injected into the trap from “an external source”. Knight’s trap was used to monitor ions by measuring the time-dependent ion current due to continuous axial loss, or by pulsing the central electrode positive and collecting the radially ejected ions on the collector plate at the equator ($z = 0$). The application of an RF waveform between the split outer electrodes allows observing the resonances in both the axial and radial ion signals. However, the simplified electrode shape made of linear mesh segments instead of smooth, solid electrodes distorts the quadrupolar nature of the axial potential and leads to a considerably weaker, broadened resonances, and so limits the ability to

discriminate between similar m/z values. However, Knight did not focus on image current detection and mass analysis. Despite the shortcoming of the Knight trap, the notion of m/z dependent harmonic motion along the axial direction was fundamental to the innovation of the Orbitrap.

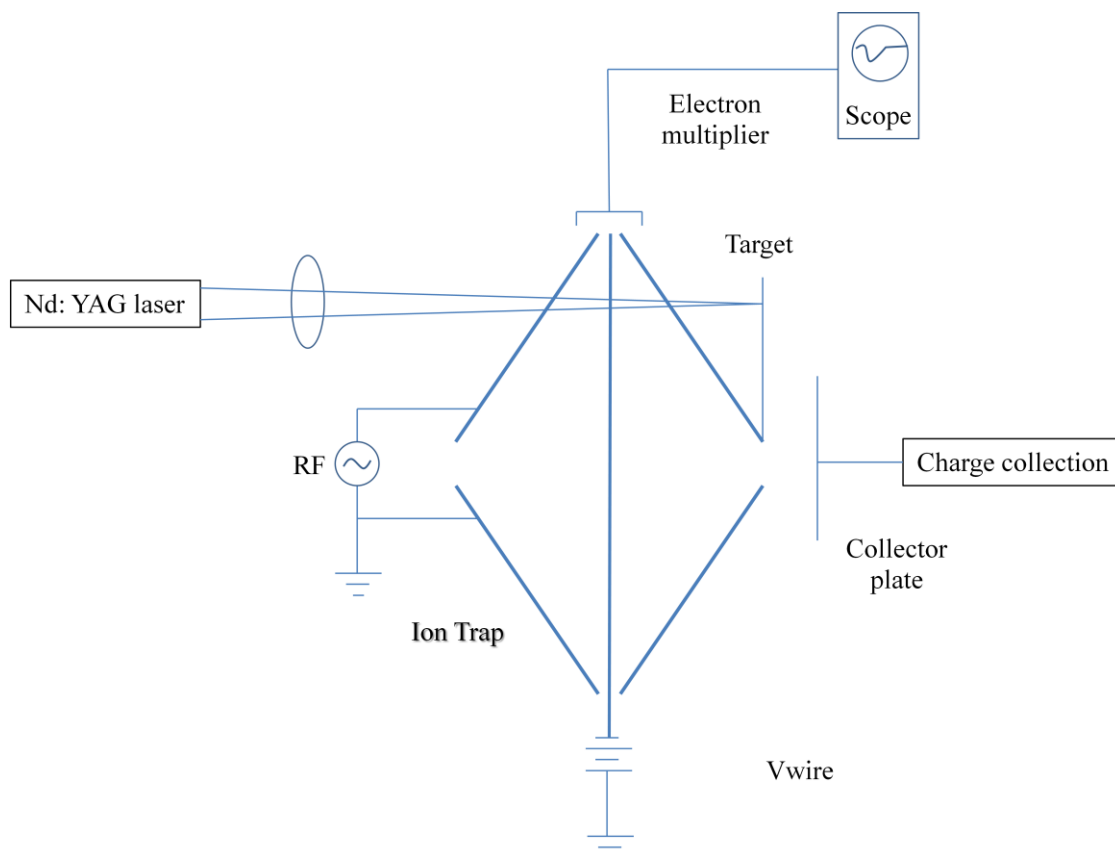


Figure 1.12: Sketch of the Knight-style Kingdon trap. The modified geometry of the outer electrode creates a quadrupolar potential superimposed upon the radial logarithmic potential of the trap. Ions are produced by pulsed laser ablation of solid targets.

In order to achieve a purely harmonic potential in the z -direction, SIMION calculations [47] suggested that the central electrode and the trapping volume should have a “spindle-like” geometry, which was adapted by Makarov to shape the electrodes to match the equipotential lines described by Eq. (1.11). A novel mass analyzer is thus invented on the basis of harmonic ion oscillations along the z -axis of the electrostatic trap.

1.2.2.1.3 The Orbitrap mass analyzer

As shown in Figure 1.13 [48], the Orbitrap mass analyzer is a modified “Knight-style” Kingdon trap. It consists of a spindle-like central electrode and a barrel-like outer electrode. A DC voltage is applied between the two axially symmetric electrodes, resulting in a “quadro-logarithmic field”, which can be considered as the sum of a quadrupole field of the ion trap and a logarithmic field of a cylindrical capacitor.

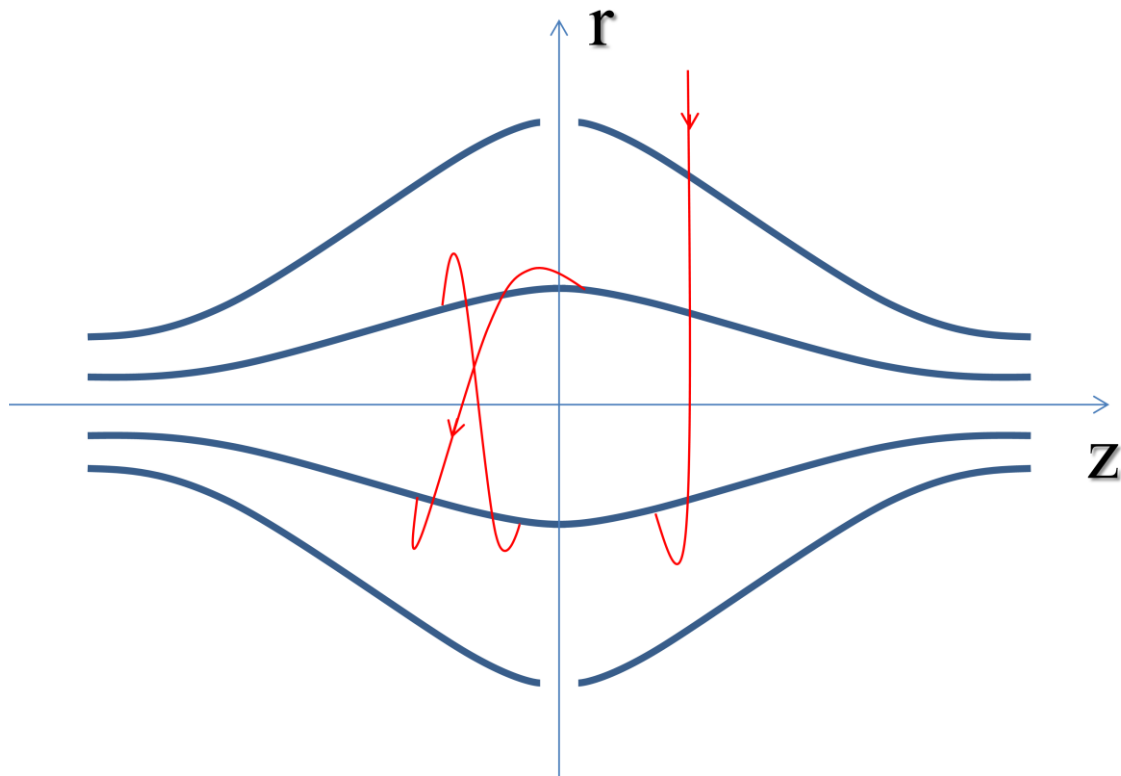


Figure 1.13: Sketch of the Orbitrap mass analyzer from side view. Ions are injected into the Orbitrap at the point displaced from its equator with a velocity (red arrow) perpendicular to the z -axis, and then they begin coherent axial oscillations without any further excitation.

In cylindrical coordinates (r, φ, z) , the ideal “quadro-logarithmic” electrostatic potential $U(r, z)$ distribution can be expressed as Eq. (1.13):

$$U(r, z) = k/2 [z^2 - r^2/2] + k/2 R_m^2 \ln[r/R_m] + C \quad (1.13)$$

where k is the field strength constant or the axial restoring force, $R_m > 0$ is the characteristic radius, and C is a potential constant.

Axial Motion. When ions of the same m/z are introduced to the trapping field under tight temporal/spatial windows, the motion of them along the z -axis in the quadro-logarithmic field ($k \cdot q > 0$) is a harmonic oscillator near the plane $z = 0$ and its solution can be described as Eq. (1.14):

$$z(t) = A_z \cos(\omega t + \theta) \quad (1.14)$$

where t is the time, and A_z and θ are the amplitude and the initial phase of the oscillation along the z -axis respectively, and the frequency of motion in the z -axis, ω (in rad/sec), is given by Eq. (1.15):

$$\omega = \sqrt{(k q / m)} \quad (1.15)$$

where m and q are the mass and charge of the ion, respectively. As is clear from Eq. (1.15), the frequency of these harmonic oscillations depends only on mass-to-charge ratio m/z and field curvature k .

Rotational motion. The ion motion in the polar plane (r, ϕ) consists of radial (r) motion and angular (ϕ) motion, and generally the r, ϕ -motion is a complex elliptical rotation around the z -axis which is completely decoupled from the ion axial oscillations. When the initial kinetic energy is appropriately matched to the radial component of the electric field, the ellipse is close to a circle of radius R , and the frequency of ion radial oscillation ω_r is given by Eq. (1.16)

$$\omega_r = \sqrt{\omega [(R_m/R)^2 - 2]} \quad (1.16)$$

and the ion rotational frequency ω_ϕ is described as Eq. (1.17):

$$\omega_{\phi} = \sqrt{\omega} (1/2 [(R_m/R)^2 - 1]) \quad (1.17)$$

As is shown in Eq. (1.17), the ion rotational motion becomes unstable when at $R > R_m$, and is stable at lower rotational radii ($R < R_m$). The ion kinetic energy K_{ϕ} associated with this rotational motion is independent on mass and is given by Eq. (1.18):

$$K_{\phi} = q^k/4 (R_m^2 - R^2) \quad (1.18)$$

The frequencies of the r , ϕ -motion depends very strongly on the initial positions and kinetic energies, since the initial conditions can't be perfectly controlled, so ions dipphase in approximately 50-100 oscillations in this polar plane, orders of magnitude faster than in the axial direction [45], and for this reason, the r , ϕ -motion is not used for mass analysis, but it is still important because the ions must be trapped in the radial plane, and SIMION simulations also illustrated that the stable motion in the polar plane is essential and makes for larger trapping capacity [47].

Due to properties of quadro-logarithmic potential, the electrostatic field strength E_z along the z -axis directs the ions toward the equator of the trap with the force proportional to the distance from the equator ($E_z = 0$ at $Z = 0$), and ions oscillate naturally along the z -axis. The coherency of ion axial motion combined with the randomization of the r , ϕ -motion results in packets of ions that resemble rings. These rings oscillate back and forth along the z -axis, with each ring having its own specific axial frequency that is determined by the m/z value of its respective ion population as shown in Eq. (1.15).

Ion injection. Injecting ions into the Orbitrap and ensuring evolution of ions in stable trajectories is a quite complicated task. Firstly, as mentioned above, the ions' kinetic energy must be well matched to the voltage on the center electrode.

If the kinetic energy is too low, the centrifugal forces created by kinetic energy is less than the centripetal force created by the electric field, and the ions will collide with the center electrode; conversely, if the kinetic energy is too high, ions will collide with the outer electrode. Secondly, ion packets should be introduced in a relatively narrow spatial ($< \text{few mm}$) and temporal window ($< 1 \mu\text{s}$) so that ions of any given m/z will oscillate along the z -axis in narrow bands, and provide optimal signal-to-noise for the image current detection. It is worth noting that although ions of the same m/z will oscillate with the same frequency along the central electrode, they will not oscillate coherently with each other if they enter the trap at different times, and ions could even essentially cancel each other's image current out in an extreme case.

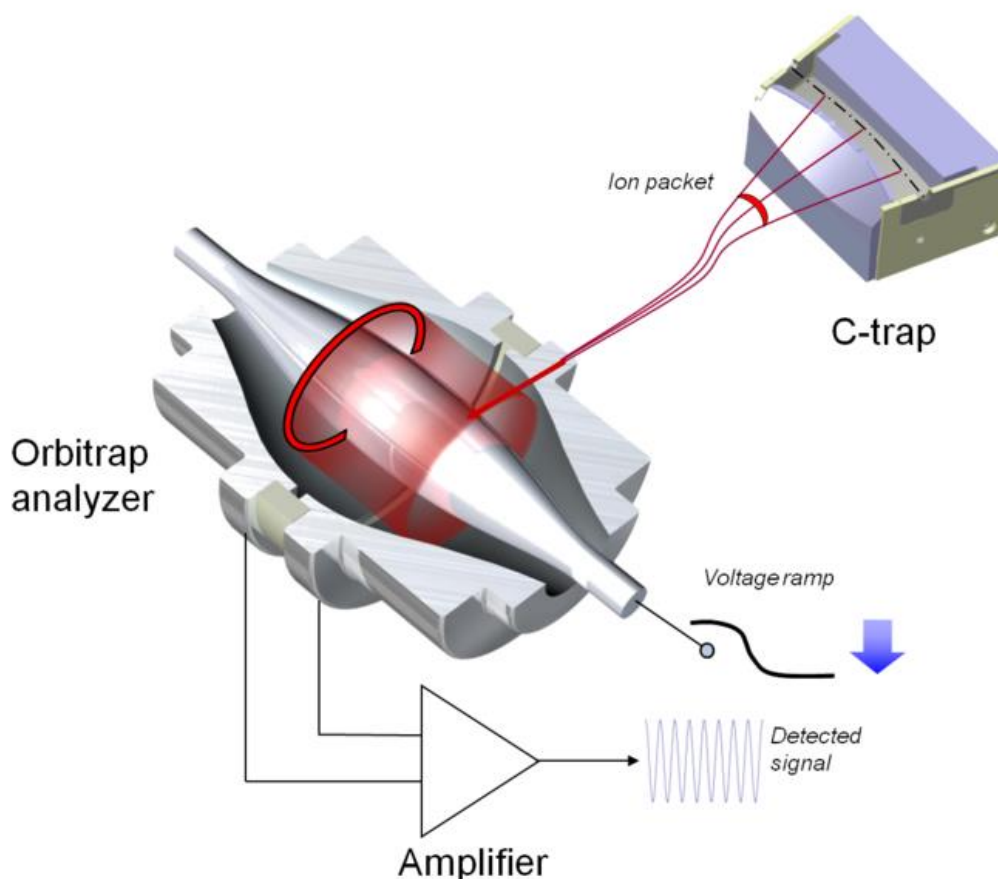


Figure 1.14: Cross-section of the C-trap and Orbitrap analyzer (ion optics and differential pumping not shown) is represented. Ion packet enters the analyzer during the voltage ramp and form rings that induce current detected by the amplifier.

There are three injection methods in the development of the Orbitrap [45, 48-50], but C-trap is the best and is embedded in commercial Orbitrap MS since 2006 [50, 51]. As shown in Figure 1.14 [52], the C-trap is a bent quadrupole and comprises four curved electrodes of rectangular cross section. The rods are arranged evenly around a central bent axis. The rod on the “inside” portion of the bend contains a slit through which ions are ejected. The trap is typically filled with ~ 1 mTorr of nitrogen gas, and when ions enter the C-trap along axis, they lose energy by colliding with gas and get trapped there, and then rf on the rods is quickly removed (in ~ 1 -2 μ s) as depicted in Figure 1.14. Once the RF amplitude has dropped, a DC field is immediately applied to the rods with the electrode furthest from the Orbitrap most positive and the slotted electrode closest to the Orbitrap least positive for positive ions. As a result, ions are forced to exit the C-trap through the slotted electrode. They are subsequently accelerated/focused through the lens system into the Orbitrap. Since the ions had very low kinetic energy within the C-trap, they have a narrow distribution of kinetic energies upon entering the Orbitrap. The rapid changes in RF and DC potentials mean that the ions will enter the Orbitrap in a narrow temporal window, so the ions get to the entrance to the Orbitrap as very short packet [50].

Electrodynamic squeezing and ion trapping. As ions enter the Orbitrap with the trajectories tangential to the central axis, voltage on the central electrode is ramped down quickly (tens of μ s) to a more negative voltage for positive ions, by which, it forces ions to squeeze towards the center electrode, and causes the radial and axial components of ion motion to contract and thus avoid the collision of ions with the outer electrode. When the voltage ramp stops, ions get trapped inside this volume between the center and outer electrodes. The use of a rapid DC ramp to allow effective ion injection/trapping is called “electrodynamic squeezing”. As ions get captured and squeezed closer and closer to the central electrode, then the voltage on the central electrode is stabilized and ions are on the stable trajectory between electrodes. This original

packet of ions with same mass-to-charge ratio will spread very quickly into a ring as depicted in Figure 1.14. This ring rotates around the central electrode and bounce back and forth down the center axis with periodic motion, the frequency of this motion is detected. It is very important that ions are distributed into the ring, because one part of the ring is shielded from the other by the central electrode, because this results in very high space charge capacity of the trap, and also pulsed injection is later used for so called enhanced Fourier Transform (eFT) for signal processing.

Ion detection and Fourier Transform. As every packet of ions contains thousands of thousands of different ions, they all spread around circle forming rings. As the rings oscillate back and forth along the axial direction, they induce image currents simultaneously which is differentially amplified from each half of the outer electrode and then undergoes analog-to-digital conversion to produce a time-domain transient (sinusoidal signal), and then the time-domain signals are converted to their frequency-domain signal by using inverse Fourier-Transform, and then according to Eq. (1.15), the frequency spectrum is converted into a mass spectrum using a two-point calibration [51].

Finally, the external pulsed ion source, the electrodynamic squeezing, the orbital trapping and the image current detection are all essential for high performance of mass analysis.

1.2.2.2 Ultrahigh resolution of high-field Orbitrap FTMS

The most commonly used method to measure the resolving power (or resolution) in MS, e.g. Quadrapole MS, FT-ICR MS, Orbitrap MS and TOF MS, follows the Full Width at Half Maximum (FWHM) definition, which uses the width of a peak at 50% of its height as a measure for $\Delta\omega$ or Δm . As mentioned in FT-ICR section, the frequency and mass resolving power are defined as $\omega/\Delta\omega_{50\%}$ or $m/\Delta m_{50\%}$. In Orbitrap MS, the frequency resolving power is twice

higher than the mass resolving power due to the square root in Eq. (1.15) [48], and so the mass resolving power (or resolution) can be given by Eq. (1.19):

$$m/\Delta m_{50\%} = \omega/2\Delta\omega_{50\%} = (1/2\Delta\omega_{50\%}) \sqrt{k} \ q/m \quad (1.19)$$

As is clear from Eq. (1.19), the best m/z resolution is obtained at low m/z charge ratios and then decreases with the square root of the ion's m/z value, which is more slowly than FT-ICR, because the frequency of FT-ICR is directly proportional to m/z . Nevertheless, it is worth noting that FT-ICR instruments can acquire longer transients than the Orbitrap's. A longer transient analysis means a lower $\Delta\omega$ value, and lower $\Delta\omega$ value allows for finer discrimination between frequencies and therefore higher resolving power [50].

Any process that causes imperfections in the ions' axial motions will cause ions of the same m/z to lose their coherence with each other in the z -axis, and the loss in coherence between the ions of the same m/z shortens the transient length, and eventually affects the resolution. Numerous processes that cause imperfections in z -axis motion can be covered as:

- Imperfections in the trap electrodes (injection slot and split of the halves outer electrodes) produces non-ideal quadro-logarithmic field causing anharmonicities in the axial direction.
- Instability of the DC voltage applied to the spindle electrode.
- Space-charge repulsions between ions
- Collisions with background gas molecules

It is worth noting that the collision with background gas is more pronounced in the Orbitrap than in FT-ICR analyzers with increasing mass, because the ion energy is independent of m/z in the former, while decreases as $(m/z)^{-1}$ in FT-ICR, and so the ultrahigh vacuum is critical in the Orbitrap for high resolution performance of compounds with high m/z value.



Figure 1.15: Cut-outs of a standard (top) and a high-field (bottom) Orbitrap analyzer.

More accurate manufacturing and highly stable modern electronics offset the imperfections in the trap electrodes and the instability of the applied DC voltage. AGC in the linear ion trap on the front minimizes the third by carefully controlling the number of ions in the trap. Ultrahigh vacuum system is employed to offset the last effects.

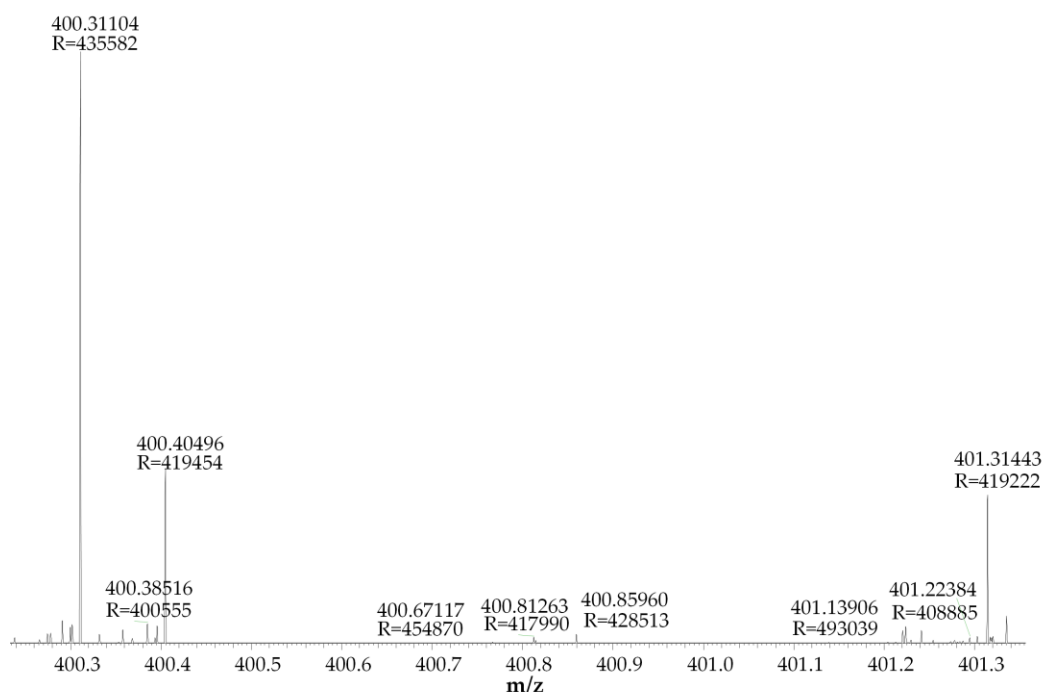


Figure 1.16: Experimental values of resolving power at 400 m/z for a deuterated heavy crude oil sample. Resolving power obtained using 1.5 s detection time and external mass calibration under full scan mode.

For the Orbitrap Elite which is used in this work, the compact high-field Orbitrap analyzer (the outer electrode is scaled down by a factor of 1.5 and center electrode by a factor of 1.2) is employed to increase the electric field strength as shown in Figure 1.15 [52], which allows almost double the acquisition rate ($1.8 \times \text{AcqRate}$), and therefore $1.8 \times \text{Res}$; the enhanced Fourier Transform (eFT) signal processing method described in details in [27] allows converting spectra in such a way that they correspond to zero initial phase for all m/z values (so-called absorption spectra) and exhibit narrower peaks based on the excitation-by-injection mechanism of Orbitrap analyzer, and this new data processing method achieves up to 2-fold increase of resolving power for the same transient. As a result, a resolving power of 480,000 at m/z 400 is achieved as shown in Figure 1.16, and when 3 s transient is employed, the Orbitrap Elite is capable of resolving power in excess of 1,000,000 for $m/z < 300$ -400, which allowing for the detection of baseline-resolved 1.1 mDa splits p to $m/z \sim 480$ [53, 54]. Advanced signal processing development such as filter diagonalization method-based MS, may further provide increased resolving power for a given transient length [55].

1.2.2.3 High accuracy of high-field Orbitrap FTMS

Mass accuracy is dependent on mass spectrometer's ability to resolve adjacent m/z peaks, so the factors that distort ion trajectories and mass resolution in the Orbitrap will also affect mass accuracy for external calibration. Internal calibration is affected by factors that change the frequency spectra to mass-to-charge ratio spectra in a non-proportional way, such as space-charge effects, variations in initial injection positions as a function of m/z , very weak r, z -cross-terms in the potential [50, 56]. Solutions to the problems are the same as described in resolution section. Modern Orbitrap instruments have mass accuracies in the range of ~ 1 -5 ppm RMS for a longer time. Figure 1.17 demonstrates a mass error distribution for a deuterated heavy crude oil sample

with external mass calibration where a mass accuracy of below ~ 1 ppm RMS is obtained for a mass range from 100-1200.

The electrodynamic squeezing and the additional shielding provided by the thicker central electrode increase space-charge capacity and thus increase the mass range of trapped ions (m/z 50 - 2,000, m/z 200 - 4,000). Dynamic range is more than five orders of magnitude within a single scan offering specified mass accuracy [51].

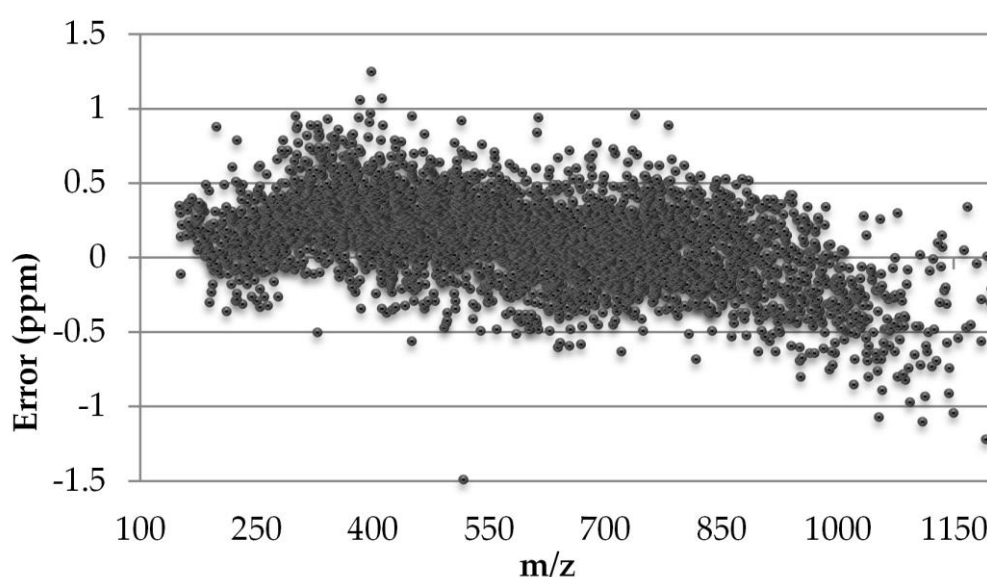


Figure 1.17: Experimental mass accuracy vs m/z with external mass calibration under full scan mode for a deuterated heavy crude oil sample.

Another important feature about this instrument is the very high transmission of ions from the external ion source or ion accumulation device to the final signal in broadband mode. Currently, it is 30 to 50%, which is 1 order or even two orders of magnitude higher than the transmission in all other accurate mass analyzers.

The high performance of mass analysis, such as, ultrahigh mass resolution, high mass accuracy and high mass range makes the high-field Orbitrap FTMS adequate enough for mass analysis of extremely complex samples [38, 43, 54,

57], and it also has the advantage of modest power requirements, size, and cost in comparison to FT-ICR MS [28].

1.3 Ionization in mass spectrometry

In mass spectrometry (MS), ionization refers to the production of gas phase ions, and it occurs in the ion source of a mass spectrometer. There are bunches of ion sources available, and each has particular applications. Hard ionization method, e.g. electron ionization (EI) causes a high degree of fragmentation, so it is good for structural elucidation and facilitates identification of unknown compounds by comparison to mass spectral libraries. Soft ionization refers to those processes that impart little energy onto the molecules and produce little or no fragmentation. Crude oil, however, is such a supercomplex mixture that contains hundreds of thousands of compounds in a single shot [8], so soft ionization is the best choice for crude oil characterization, because the fragmentation would complicate the spectra even more.

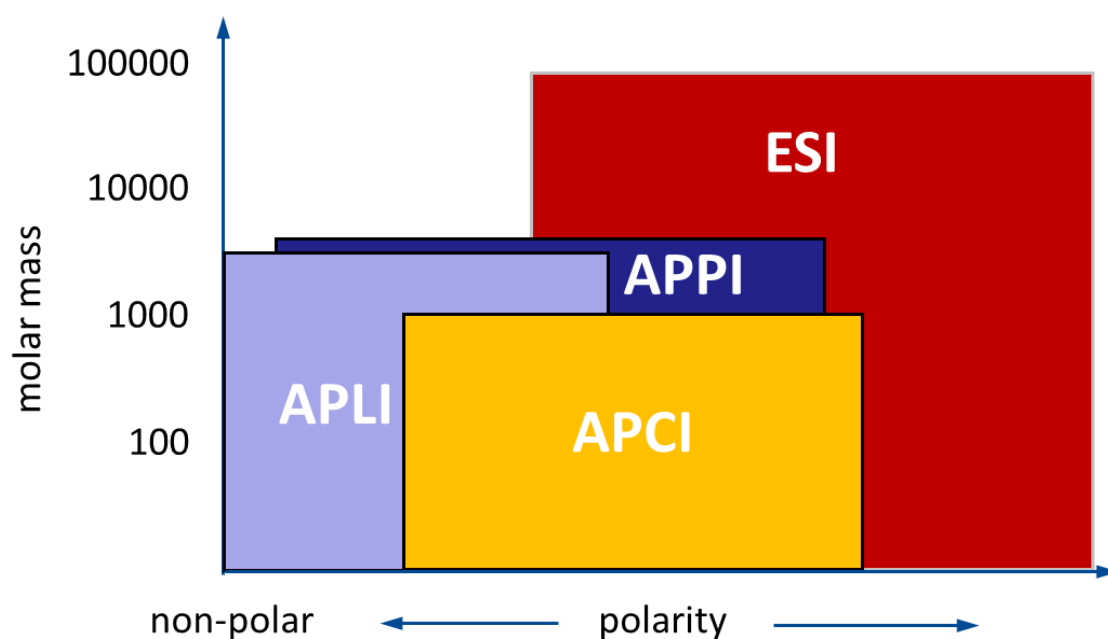


Figure 1.18: API ionization methods and applicable compounds.

Among the soft ionization methods, Atmospheric Pressure Ionization (API) has been well broadly employed, and it includes Atmospheric Pressure Photoionization (APPI), Atmospheric Pressure Chemical Ionization (APCI), Atmospheric Pressure Laser Ionization (APLI) and Electrospray ionization (ESI) as depicted in Figure 1.18. APPI is an ionization method in which samples are ionized using ultraviolet radiation ($h\nu = 10 \text{ eV}$ or 10.6 eV), and it achieves broadest ionization of compounds with low to moderate polarity. APCI is an ionization method in which the analytical sample is subjected to a corona discharge, and it is suitable for moderately polar substances. APLI is an ionization technique in which samples are ionized by laser light at 248 nm (KrF^*) in a resonance-enhanced multiphoton ionization (REMPI) process [8, 41, 58, 59], and it is a selective and sensitive ionization method for aromatic and polyaromatic compounds with low polarity as shown in Figure 1.18. ESI, introduced to MS by Yamashita and Fenn in 1984, is an ionization technique used to produce ions using an electrospray in which a high voltage is applied to a liquid to create an aerosol, and it is a very selective ionization method for polar compounds [60].

A great advantage of ESI-MS in comparison with other methods is that ionic solutions used for the transfer of ions to the gas phase are the same solutions used in conventional wet chemistry, and it is unlimited in mass. In this work, ESI is the only ionization method employed for complex heavy crude oil analysis due to the connection with the chemical reactions, and so ESI will be discussed in details in this section.

1.3.1 The electrospray process

In general, there are three major steps of how ions are first generated in the solution phase and then converted to gas phase ions in the ESI process before analysis:

- Excess charge is generated in the Taylor cone and charged droplets are generated at the ESI capillary tip;
- The charged droplets shrink through solvent evaporation and repeated uneven fission to form very small, highly charged offspring droplets capable of producing gas-phase ions;
- The gas-phase ions are formed from these very small highly charged droplets by the **actual** mechanism.

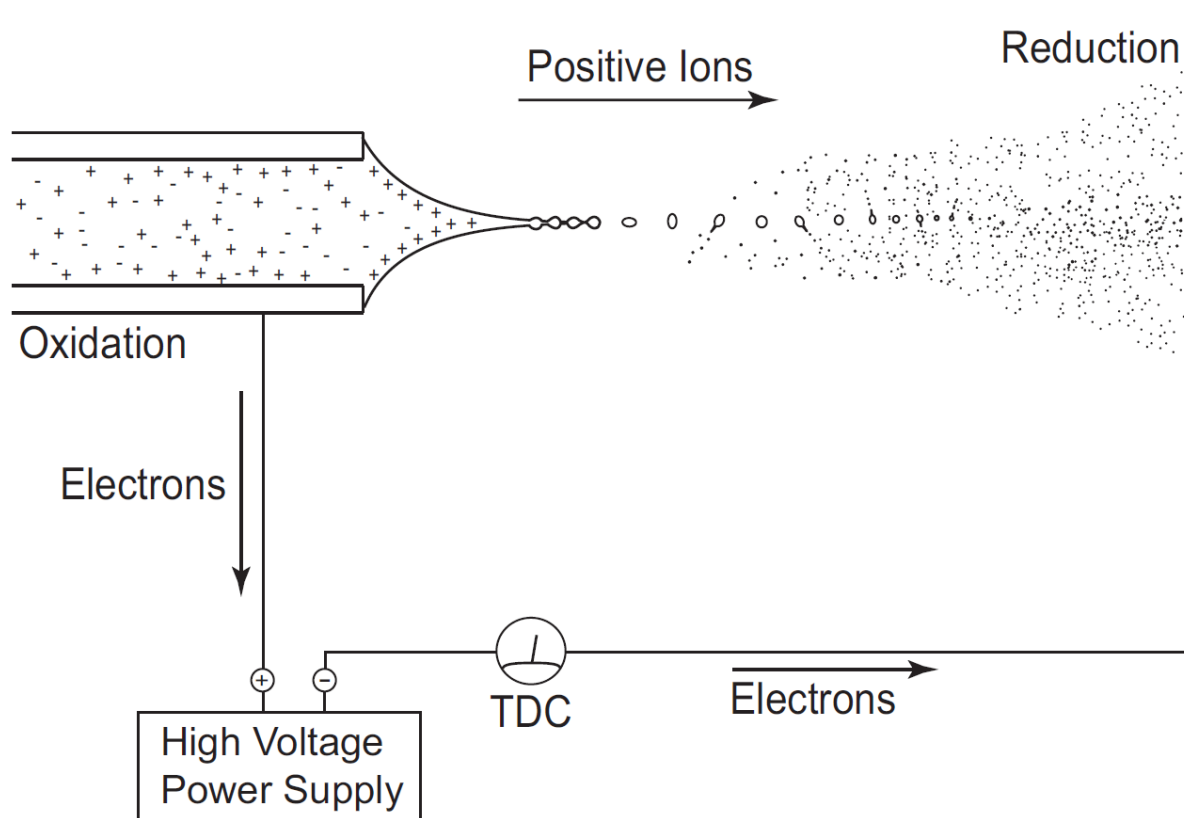


Figure 1.19: Schematic diagram of major processes in the atmospheric pressure region of an ESI ion source in the positive ion mode. The penetration of the imposed electric field into the liquid leads to an enrichment near the meniscus of positive ions in solution, which causes a destabilization of the meniscus and formation of a cone and a jet charged by an excess of positive ions. Solvent evaporation of the droplets brings the charges closer together. The increasing Coulombic repulsion destabilizes the droplets, which results in emitting jets of charged offspring droplets. The evaporation of offspring droplets leads to emission of the

second generation of offspring droplets, and so forth, until the free gas-phase ions form at some point. Charge balance is achieved in the ESI device by electrochemical oxidation at the positive electrode and reduction at the negative electrode. TDC represents the total droplets current.

In electrospray as shown in Figure 1.19 [61], the bulk electrolytic solution of analyte is continuously flowing into a high voltage ($\sim 2\text{-}5$ kV) capillary tip at a flow rate of $\sim 1\text{-}10$ $\mu\text{L}/\text{min}$. The electric field gradient by the applied voltage causes the charge separation at the surface of the liquid, and then the liquid protrudes from the capillary tip to form a “Taylor cone”. When the Taylor cone reaches the Rayleigh limit [62], the Coulombic repulsion between the positive ions overcomes the surface tension of the solution, and the primary droplets (parent droplets) are emitted from the tip of the Taylor cone. Due to the charge separation caused by the voltage gradient, these droplets have excess charge that exists on the surface of the droplet while the solvated paired ions or neutrals are present in the inner part of the droplet (inner phase). The concentration of the excess charge is determined by the flow rate and applied voltage, and the production rate of excess charge is equal to the maximum rate of production of vapor-phased ions. Continuous solvent evaporation at constant charge leads to droplet shrinkage and uneven fission to form offspring droplets from the surface phase of parent droplets with significantly higher charge-to-mass ratio [63] on the offspring droplets. The repeated solvent evaporation and uneven droplets fission lead to ultimate gas-phase ions. *The gas-phase ions would undergo gas-phase reactions in the atmospheric-pressure sampling regions of the mass spectrometer.* Finally, the ultimate gas-phase ions in the sampling region will be sampled and guided through an orifice, into the differentially pumped regions of the mass spectrometer to be processed. The neutral will be blocked by an interface metal plate or curtain gas.

Any components that interfere with any of the above process might affect the ionization efficiency of an analyte, such as the chemical nature of the

analyte, the volatility of the solvent [64], the surface activity of the droplet [65, 66], the flow rate of solution [67], the concentrations of other ionizable species [66] and the competition of gas-phase ion transfer reaction between analytes and other ionized ions [68].

1.3.2 The electrospray ionization mechanism

After the discovery of an ESI ion source capable of generating large molecular ion beams, two main models were proposed to describe the gas-phase ion generation from charged liquid droplets in a mathematical way, and the two models are the Ion Evaporation Model (IEM) [69, 70] and the Charge Residue Model (CRM) [71, 72].

1.3.2.1 Ion evaporation model (IEM)

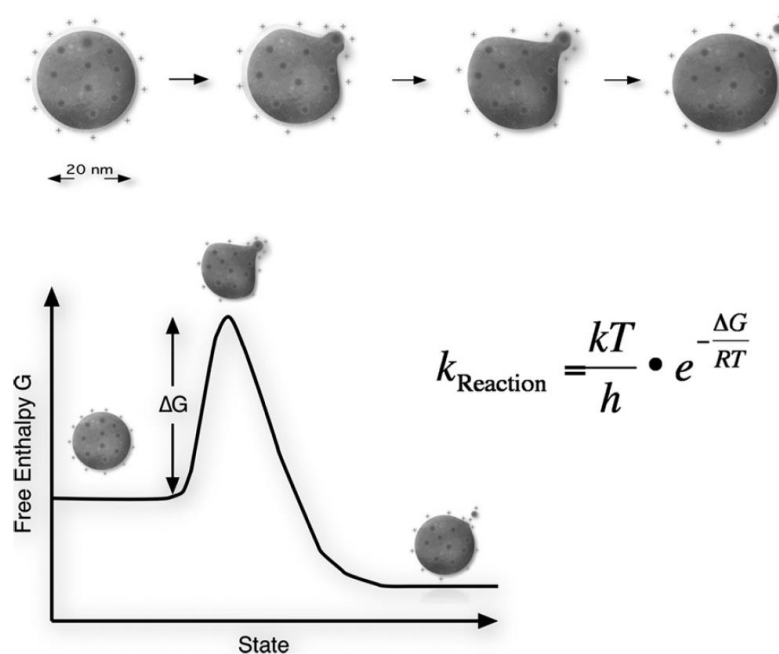


Figure 1.20: The ion evaporation model (IEM). An individual ion leaves the charged droplet in a solvated state, because the reaction free enthalpy that needs to be overcome when the ion escapes from the droplet, ΔG , is lowest not for the naked ion, but for the solvated ions.

The Ion Evaporation Model (IEM) [69, 70] was first introduced by Iribarne and Thomson. The IEM states that, as solvent evaporates from the parent droplet, the surface charge density increases until the field strength at their surface is sufficiently large that charged yet solvated analytes to readily escape, namely “evaporate”, once fission occurs at 80-100% of the Rayleigh limit [61, 62]. It is worth noting that: 1) ion evaporation is expected to occur when the droplet reaches a size of about 20 nm in diameter as depicted in Figure 1.20 [73]; 2) the chemical properties of the ion affects the reaction rate kinetic a lot; 3) The ion evaporation rate constant k_{Reaction} depends exponentially on the ΔG , and ΔG is a function of the physicochemical properties of the ion itself even though the ion is solvated in a small shell.

IEM can also well explain the generation of large ions from electrosprayed droplets [74], which is superior to CRM in the early study work.

1.3.2.2 Charge residue model (CRM)

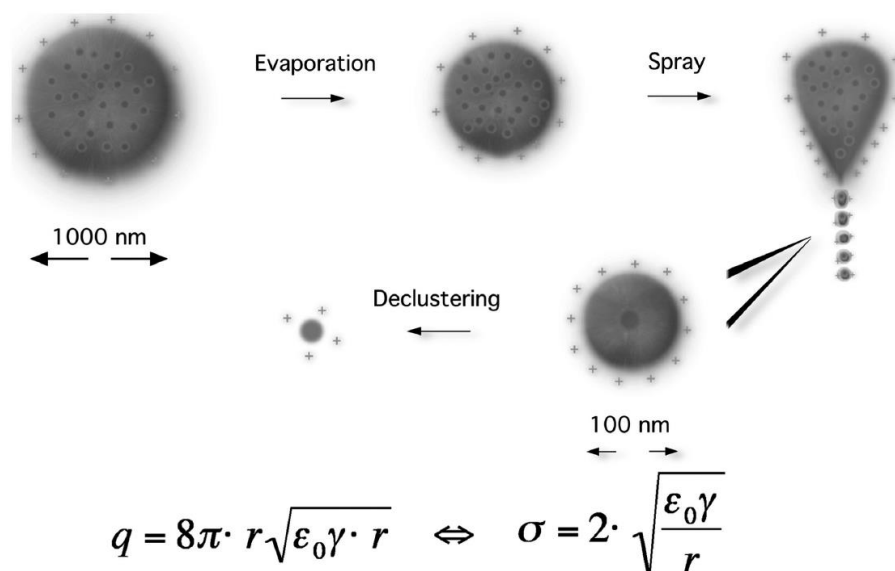


Figure 1.21: The charged residue model (CRM). It assumes that the ESI droplets are generated by containing one ion that is released after solvent evaporation. A calculation shows that for a concentration of 1 pmol/ μl , a droplet with a diameter of 200 nm contains on average less than one analyte molecule.

The charge residue model (CRM) proposed by Dole [71, 72] is strongly independent of the ion, and it assumes a sequence of Rayleigh instabilities driven by successive solvent evaporation and droplet fissions due to Coulombic repulsions of charges at the surface of the droplet (Figure 1.21 [73]). The CRM process results in ultimate droplets, each of them contains only one molecule of solute. This molecule becomes a free gas-phase ion by retaining some of its droplet's charge after its last solvent molecule evaporation. Non-covalent complexes are expected to survive the process because they are cooled by solvent evaporation, and do not have to overcome an energy barrier with subsequent acceleration in an electric field. The available charge to the molecule depends on the Rayleigh stability limit because the final droplet comes from a spraying process caused by a Taylor Cone as depicted [73]. The CRM is unlimited in mass of analyte.

No matter IEM or CRM, they both try to approach to the reality. Experimental data can be interpreted within the framework of a specific model.

1.3.3 Electrochemical nature of an ESI ion source

An ESI ion source can be viewed as a *special* type of electrolytic cell [75, 76], and the working electrode is the metal ESI capillary, the counter electrode is the atmospheric sampling aperture plate and the series of lens elements and detector of mass spectrometer, and the specialty lies in that the ion transport does not occur through the uninterrupted solution like normal electrolysis, and part of the ion transport occurs through the gas phase. In the ESI process, the generation of ions in solution-phase, the generation of charged ESI droplets, and the generation of gas-phase ions result in a quasi-continuous steady-state current in the electric circuit. To sustain the loss of an excess of charges of one polarity in the charged ESI droplets and maintain the quasi-continuous steady-state current, heterogeneous electron-transfer reactions (an electrochemical reaction) must occur at the working electrode and the counter electrode in the circuit. As

illustrated in Figure 1.19, in ESI(+) mode, oxidation reactions dominate at the working electrode and reduction reactions dominate at the counter electrode. Depending on the electrochemical conditions, the solvents, additives, the metal capillary materials and analytes are suspected to undergo the oxidation. Van Berkel and co-workers, have studied a series of the electrochemical processes to ESI-MS [77]. From the electrolytic perspective [78], three major electrochemical principles—the interfacial working electrode potential, the faradaic current at the working electrode, and mass transport to the working electrode might help understanding of the inherent electrochemistry of the ESI ion source [79].

1.3.3.1 The interfacial potential of the working electrode

The interfacial potential inside the ESI capillary determines which reactions may happen and the rate at which they take place. It is not a fixed value during an ESI-MS experiment, but adjusts to a given level, which depends on a bunch of variables which include the redox potential and the concentrations of all species in the system, the current density at the working electrode, the electrode material and geometry, and any parameters that affect the flux of reactive species to the electrode surface. Computational simulations by Van Berkel's group [80] has been done to estimate the interfacial potential inside the ESI capillary, and found that the interfacial potential is highest at the spray tip of the capillary, and decreases towards the inside of the capillary, thus the interfacial potential has a non-uniform spatial distribution along the capillary.

1.3.3.2 The faradaic current at the working electrode

The faradaic current (I) determines the extent of the possible redox reactions that occur at the working electrode. It is provided by electron-transfer reaction there and represents the total number of the excess charges leaving the capillary.

A significant part of the faradaic current was generated as far as 1 cm into the capillary [78]. According to Faraday's 1st law of electrolysis, the mole concentration of excess charge in the ESI droplets [Q] can be calculated by Eq. (1.20):

$$[Q] = I / (F v) = \sum_j n_j c_j \quad (1.20)$$

in which, I is the current in the circuit, F is the Faraday constant (9.648×10^4 C/mol), v is the flow rate, j is the number of different electrochemical reactions that occur, n_j is the molar equivalent of electrons involved in the production of 1 mol of electrochemical product in reaction j , and c_j is the concentration of product j . Eq. (1.20) shows that c_j will be minimized at high v , low I , and large n_j , and it will compete with other electrochemical reactions that occur simultaneously. So the set of the parameters effects the solution composition.

1.3.3.3 The mass transport to the working electrode

The heterogeneous electron transfer reactions cannot take place unless a reactive species is transported to the electrode surface. The mass transport is very poor with the tubular electrode at very low flow rate v , and so increasing concentrations to a certain value might be a solution. Due to the spatial distribution of the efficient total current and interfacial potential along the capillary tube, the electrochemical reactions are restricted to a small range, and so the reaction time is also limited based on the usual flow rate used in ESI-MS experiment. The design of the capillary might be a direction for more application.

The potential, current and mass transport as well as the solvent system can be well controlled to promote ionization and detect specific analytes. It is worth noting that gas-phase reaction of ESI-MS might alter ions in solution.

1.3.4 Gas-phase reaction

ESI is an atmospheric pressure ionization method, and so the ESI-MS response can be affected by gas-phase reaction that occurs after the analytes have been released from the solution, so the gas-phase effects are the last and important stage of ESI. When the protonated molecules enter into the gas phase, it can transfer the proton to those neutral species with higher *gas-phase basicity*, the neutrals or solvents evaporated from the droplets become charged species, and the new formed charged species via gas-phase reaction are observed on mass spectra. Gas-phase basicity is defined as the negative change in enthalpy for the hypothetical protonation reaction, and can be expressed in terms of gas phase proton affinity (PA). It is worth noting that solution-phase basicity does not necessarily relate to the gas-phase proton affinity. Species with high gas phase PA may be weak basic in solution [81].

1.4 Data interpretation

Ultrahigh resolution and high mass accuracy of the high-field FT-ICR MS and the high-field Orbitrap FTMS enables molecular formula assignment of the detected species of complex mixtures. Ultrahigh resolution mass spectrometry has revealed that petroleum crude oil is a highly heterogeneous mixture that contains PAXHs ($C_cH_hO_oS_s$) as well as metal species (V, Ni and Fe.). Due to the presence of an enormous number of isomers, it is unrealistic to analyze individual compounds in such supercomplex mixtures [8], thus, only statistical information will be gained for class the compounds, data interpretation pathway and visualization tools will be explained in this following sections.

1.4.1 Elemental composition assignment from accurate mass data

Mass defect is defined as the difference between the mass of a composite particle and the sum of the masses of its parts, and it can be given by Eq. (1.21):

$$\Delta m = Zm_{\text{H}} + (A-Z) m_{\text{n}} - M \quad (1.21)$$

where, Δm is the mass defect (AMU), Z is the atomic number (number of protons), m_{H} is the mass of H-1 atom (1.0078 AMU), A is the atomic mass number (number of nucleons), m_{n} is the mass of a neutron (1.0087 AMU) and M is the mass of the atom.

The obtained mass data are imported to Composer (Sierra Analytics, Modesto, CA). Kendrick plots are calculated according to the procedure described by Kendrick [82] where the IUPAC mass can be converted to the Kendrick mass scale by Eq. (1.22):

$$\text{Kendrick mass} = \text{IUPAC mass} \times (14.00000/14.01565) \quad (1.22)$$

the Kendrick mass scale is converted to the mass of CH_2 from 14.01565 to 14.00000, thus, compounds that contain the same heteroatoms (same class) and same number of rings plus double bonds (same type, Double Bond Equivalent DBE) but with different numbers of CH_2 units will be sorted in the homologous series at the horizontal line of the Kendrick plot and have an identical Kendrick mass defect (KMD) represented by Eq. (1.23):

$$\text{Kendrick mass defect (KMD)} = \text{Kendrick nominal mass (KNM)} - \text{Kendrick exact mass} \quad (1.23)$$

the Kendrick nominal mass is obtained by rounding the Kendrick exact mass to the nearest integer. Any change in class or type will change KMD, and then vertically shifts each corresponding homologous series in the Kendrick plot. The

masses are sorted into different homologous series by their nominal mass and KMDs, and according to their unique combination of nominal mass and Kendrick mass defect, molecular compositions of different homologues are ultimately assigned. For simplicity and better correlation to the chemical structures, DBEs (double bond equivalent) replace the KMDs in Kendrick plots [41], and DBE is the sum of the number of rings (R) and double bonds (DB) present in a molecule, and DBE can be calculated by Eq. (1.24):

$$\text{Double Bond Equivalent (DBE)} = c - h/2 + n/2 + 1 \quad (1.24)$$

where, c is the number of carbon atoms, h is the number of hydrogen atoms, and n is the number of nitrogen atoms. A change in DBE value indicates a change in the number of rings or double bonds and further reflects the change in the degree of the unsaturation or aromaticity.

1.4.2 Compositional sorting: heteroatom class, DBE and carbon number

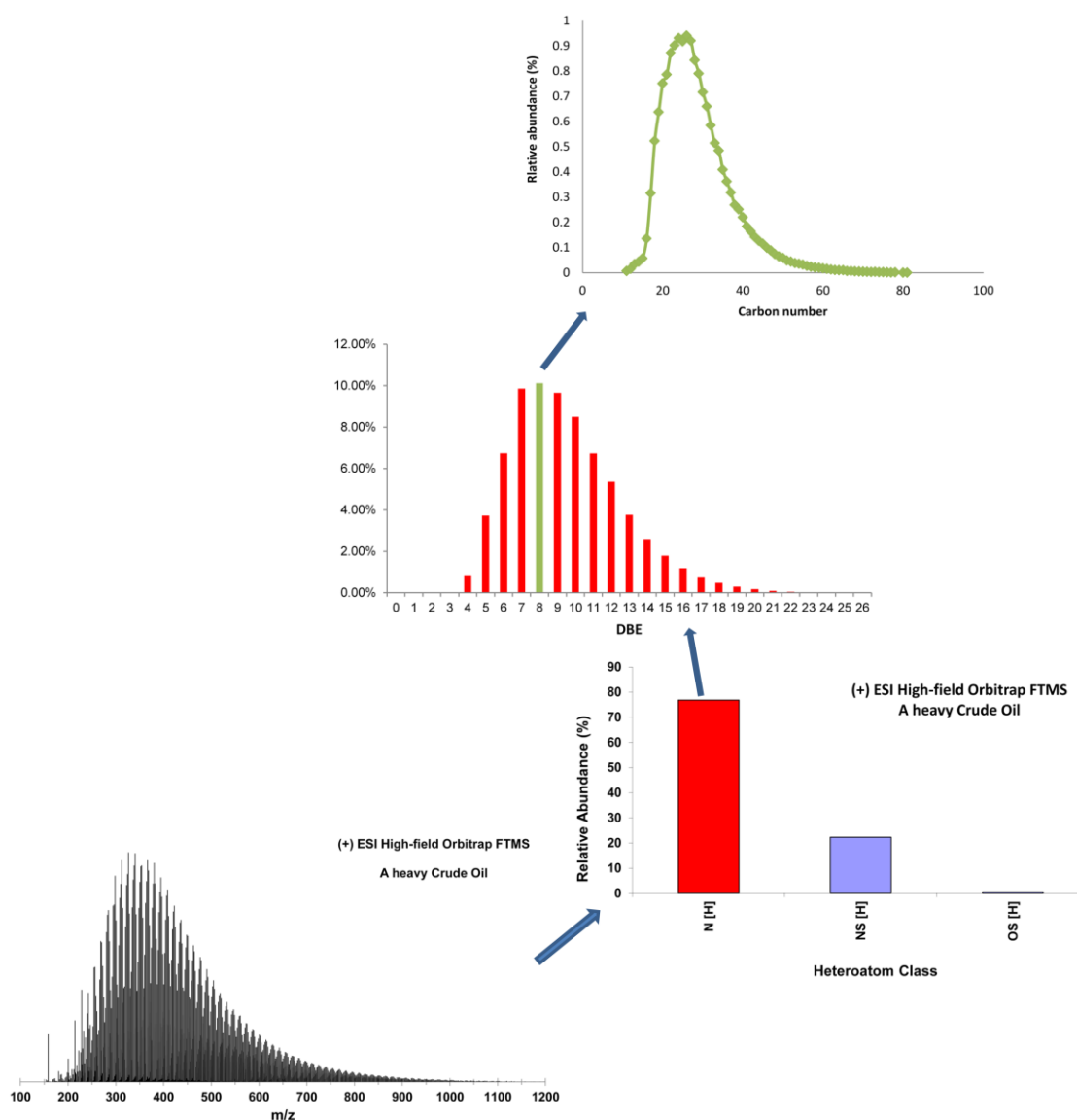


Figure 1.22: Compositional sorting process based on their elemental compositions. Above the mass spectra (bottom) is heteroatom class distribution, and above the class plots is the DBE distribution for N_1 class. Carbon number (a degree of alkylation) is placed on the top for N_1 species with DBE = 8.

Having obtained from thousands of accurate masses and then to thousands of elemental composition, the data can be visualized needs to be visualized in a reasonable way. Overall representation includes mass spectra, class distribution, etc. as depicted in Figure 1.22.

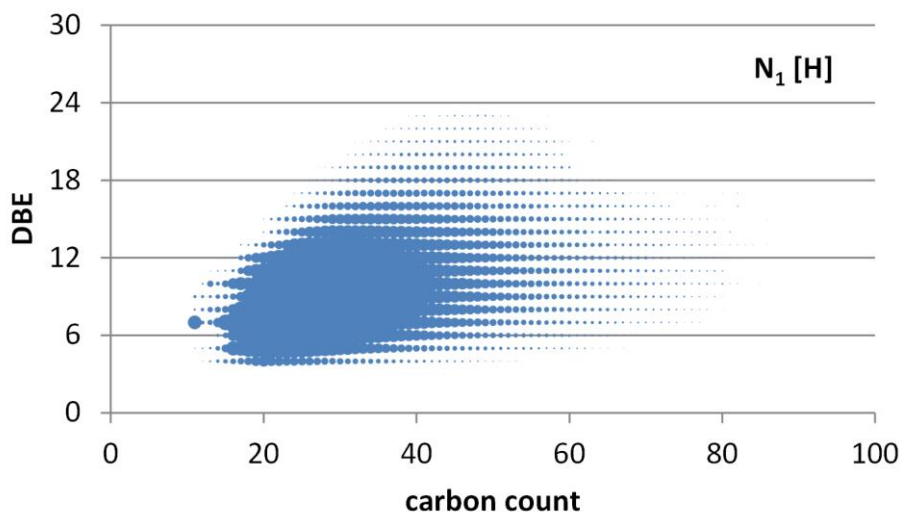


Figure 1.23: DBE vs. carbon number plots for the N_1 [H] class from a protonated heavy crude oil, obtained by (+) ESI high-field Orbitrap FTMS.

For a given heteroatom class (e.g. N_1), data can be displayed via Kendrick plots, DBE plots, etc. as shown in Figure 1.23. The plot of DBE vs. carbon number distribution (Kendrick plot) is most useful for a given heteroatom class among the various graphs. From Kendrick plots we can clearly see the aromaticity of a given class and then further presume the first structure information. Plots of DBE vs. Carbon number distribution are especially useful in analysis of hydro-treatment process due to the change of the aromaticity in it [33].

1.5 Scope of this study

This study is focusing on developing chemical methods for selective analysis of compounds with the same functionality or with the same classes that present in heavy crude oils.

Crude oil is considered as the most complex natural mixture of chemical components known [8], with reports estimating more than 1 million different compounds. Different ionization methods show different spectra as each method

ionizes different compounds present in a crude oil [8]. Physical simplifications (e.g. chromatographic separation and extraction) [36, 40, 42] reduces the complexity and increases the data depth towards specific species in crude oils, which might be due to reduced suppression effects or also be the result of an increased concentration in the fractions. Thus, from the analytical point of view, a selective analysis of such a complex mixture as a crude oil is not possible.

The goal of this project is to find **chemical reactions (derivatization reactions)** that offer selective differentiation and gain a deeper composition information and even structural information.

Chapter 1 gives an introduction of crude oil, mass analyzers (ICR and Orbitrap), electrospray ionization method and data interpretation. ESI coupled with ultrahigh resolution mass spectrometry, e.g. FT-ICR MS, and high-field Orbitrap FTMS, has emerged as an efficient technique for the *selective* speciation of polar compounds in complex mixtures, like crude oils [8, 18]. In order to make an analyte amenable to analysis by ESI-MS, the analyte must already exist as ions in the solution phase, or bear acidic (or basic) functional groups that are readily chargeable via Brønsted acid/base chemistry, Lewis acid/base chemistry, or be chargeable through chemical or electrochemical reactions [83-85], or be chargeable via gas-phase reactions. The **derivatization in combination with ESI-MS** approach, which uses a specific reaction based on a functional group to create an ionic or solution ionizable derivative of the target analytes, provides a highly selective approach to analysis of a specific species in complex mixtures [38, 40].

Chapter 2 presents alkylation reactions (methylation and ethylation) of a heavy crude oils in the present of alkylating reagents and AgBF_4 at room temperature. Deuterium technique is introduced in this work to differentiate the tagged sulfur species from the original crude oil.

Chapter 3 reports the extension of the reaction described in Chapter 2. By varying the reaction condition (the more ratio between the crude oil, alkylating reagents and AgBF_4), a wide range of compounds from basic nitrogen-containing species, and neutral sulfur- and CH- containing species, and even acidic species in crude oil is accessible to ESI-MS.

Chapter 4 represents a mechanism study of sulfur-containing compounds with ethyl triflate. This reaction is taking advantage of the inherent electrochemistry of an ESI ion source. A silica electrospray capillary setup is used to investigate the mechanism. Both oxidations in the solution-phase in the spray capillary and secondary gas-phase reactions play roles for the final mass spectra obtained. Theoretical calculation based on QM captures the key information (short-lived intermediates) that escapes from our technique scope and facilitates the mechanism study.

Chapter 5 reports the application of the method developed in Chapter 4 to a real heavy crude oil. For a comparison, not only ethyl triflate but also ethyl iodide is used to evaluate the method. As a result, rapid selective analysis towards sulfur-containing species on a millisecond scale is achieved with ethyl triflate under ESI(+). Ethyl iodide accesses both sulfur- and nitrogen-containing species. A series of theoretical calculations have been done for mechanism study with the sulfur-containing standard (dibenzothiophene) and nitrogen-containing standard (acridine) involved.

Chapter 6 represents benzylation reactions to heavy crude oils. Different benzyl halides emphasize different class compounds: benzyl chloride for polycyclic aromatic nitrogen heterocycles (PANHs); benzyl iodide for polycyclic aromatic sulfur heterocycles (PASHs); benzyl bromide for both

PANHs and PASHs. When AgBF_4 is involved, PASHs as well as polycyclic aromatic hydrocarbons (PAHs) are detectable under ESI(+) for both benzyl halide and benzyl bromide; benzyl iodide accesses both PASHs and PANHs but weakens PAHs.

Chapter 7 summarizes this work.

Chapter 2 Selective Analysis of Sulfur-Containing Species in a Heavy Crude Oil by Deuterium Labeling Reactions and Ultrahigh Resolution Mass Spectrometry*

**Redrafted from “Wang, X.; Schrader, W., Selective Analysis of Sulfur-Containing Species in a Heavy Crude Oil by Deuterium Labeling Reactions and Ultrahigh Resolution Mass Spectrometry. Int J Mol Sci 2015, 16 (12), 30133-43.”*

2.1 Abstracts

A heavy crude oil has been treated with deuterated alkylating reagents (CD_3I and $\text{C}_2\text{D}_5\text{I}$) and directly analyzed without any prior fractionation and chromatographic separation by high-field Orbitrap Fourier Transform Mass Spectrometry (FFTMS) and Fourier Transform Ion Cyclotron Resonance Mass Spectrometry (FT-ICR MS) using electrospray ionization (ESI). The reaction of a polycyclic aromatic sulfur heterocycles (PASHs) dibenzothiophene (DBT), in the presence of silver tetrafluoroborate (AgBF_4) with ethyl iodide ($\text{C}_2\text{H}_5\text{I}$) in anhydrous dichloroethane (DCE) was optimized as a sample reaction to study heavy crude oil mixtures, and the reaction yield was monitored and determined by proton nuclear magnetic resonance spectroscopy ($^1\text{H-NMR}$). The obtained conditions were then applied to a mixture of standard aromatic CH-, N-, O- and S-containing compounds and then a heavy crude oil, and only sulfur-containing compounds were selectively alkylated. The deuterium labelled alkylating reagents, iodomethane- d_3 (CD_3I) and iodoethane- d_5 ($\text{C}_2\text{D}_5\text{I}$), were employed to the alkylation of heavy crude oil to clearly differentiate the tagged sulfur species from the original crude oil.

2.2 Introduction

The demand for affordable and reliable energy leads to a continuous focus on fossil-based materials, and nowadays the trend is shifting to heavier petroleum resources. One of the huge disadvantage of heavy crude oils as energy supply is that they contain rich heteroatoms, such as sulfur, nitrogen and oxygen. The sulfur content is detrimental to refining processes and harmful to the environment after combustion, and thus must be removed. Various stringent legislations and regulations have been implemented to limit the sulfur content of fuels [8]. A better understanding of heavy crude oil composition is necessary for that aim.

Heavy petroleum is a supercomplex [8] mixture of hydrocarbons containing various amounts of heteroatoms (N, O and S), and it challenges and meanwhile promotes the development of analytical techniques [18]. Mass spectrometry has been established as the most powerful and promising method to characterize such complex mixtures [86, 87]. FT-ICR MS provides sufficient mass resolving power and mass accuracy to identify each of the thousands of different molecules and their elemental compositions from the most complex mixtures [16]. Recently, a new commercially available type of the high-field Orbitrap FTMS, the Orbitrap Elite [50, 53, 88], has been evaluated and employed successfully to analyze the petroleum samples with a resolving power of up to 900 000 at m/z 400 [54, 89].

Electrospray ionization (ESI) [60] coupled with ultrahigh resolution mass spectrometry [31, 54, 57] is an excellent method employed to ionize polar species in crude oil. It efficiently ionizes the acidic or basic molecular species in petroleum by deprotonation or protonation to form $[M-H]^-$ or $[M+H]^+$ ions [31, 60, 90] and even highly condensed polyaromatic compounds can be ionized by ESI as radical cations [43].

However, PASHs are not basic enough to be efficiently ionized by ESI. Thus, some achievements have been made to enhance ionizing efficiency of

nonpolar sulfur species in ESI process. Muller et al. [40] developed a derivatization method by forming the polar sulfonium salts in solution prior to ESI, but the selectivity toward sulfur aromatics is achieved by relying on chromatographic separations. Purcell et al. [91] derivatized a vacuum bottom bitumen residue by this derivatization procedure, and observed not only sulfur compounds but also detected nitrogen and other heteroatom containing classes at high abundance by positive ESI FT-ICR MS.

Metal complexation methods, such as Pd²⁺ ESI-MS [92] and especially Ag⁺ ESI-MS [93], have also been developed for the detection of sulfur-containing compounds in petroleum by the formation of positive metal-complexes [94]. However, the relatively flexible coordination sphere of the metal ions allows them to coordinate with a variety of ligands even the solvents with the coordination numbers from 2 to 6, which on some level, increases the complexity of crude oil analysis [93, 95, 96].

Here, on the basis of previous research, we combine the silver coordination chemistry and nucleophilic chemistry of heteroatoms compounds with ESI-MS, and introduce the deuterium labelling technique to develop a method that allows determination of sulfur-containing species in a whole crude oil with high selectivity, and avoiding the complexity from the transition metal complexation. When using the derivatization procedure with methyl iodide in a crude oil sample, where the elements C, H, O, N, S and a few metals are usually present, it is difficult to separate the derivatized from the non-derivatized compounds. The difference cannot really be established because the derivatizing group contains the same elements as the compounds present in a crude oil sample and only the increase in signal intensity of sulfur compounds can be an indication of the reaction. Here, the usage of a deuterated reactant for the derivatization is introduced which allows to clearly distinguish the reacted from potentially unreacted compounds and allows an unambiguous characterization.

2.3 Experimental section

2.3.1 Alkylation

DBT, DCE, AgBF_4 , anthracene (ANTH), dibenzofuran (DBF), acetic acid (AcOH) and dichloromethane (DCM) were purchased from Sigma-Aldrich (high purity, St. Louis, MO). $\text{C}_2\text{H}_5\text{I}$, acridine (ACR), CD_3I and $\text{C}_2\text{D}_5\text{I}$ were purchased from Sigma-Aldrich (high purity, Steinheim, Germany). A heavy crude oil of North American origin was used.

10 mg of DBT were dissolved in 1 mL anhydrous DCE. During mixing, a solution of 2 molar eq. AgBF_4 (21.13 mg) in 0.5 mL DCE was added. After 2 min, 8 molar eq. (28 μL) of $\text{C}_2\text{H}_5\text{I}$ was then added and yellow silver iodide precipitated immediately. After 4 h, the solid was removed by centrifugation and washed with 0.5 mL of DCE. A final concentration of 500 $\mu\text{g/mL}$ of the ethylated DBT was obtained through dilution with DCM; the procedure above was successively applied to a mixture of standard compounds: 6.5 mg of ANTH, 2.75 mg of DBT, 0.25 mg of ACR, 0.5 mg of DBF. The same procedure was further employed to 10 mg of the heavy crude oil by replacing $\text{C}_2\text{H}_5\text{I}$ with CD_3I and $\text{C}_2\text{D}_5\text{I}$. For a comparison, a heavy crude oil sample with a final concentration of 500 $\mu\text{g/mL}$ in DCE containing 0.2% AcOH was used for ESI analysis.

2.3.2 Nuclear magnetic resonance spectroscopy

^1H NMR spectra were recorded on a Bruker Advance 300 NMR spectrometer. The chemical shifts and the coupling constants were obtained through analysis of the spectra using Bruker TopSpin NMR-Software version 2.1. The chemical shifts of ^1H NMR spectra is reported as in units of parts per million (ppm). The ^1H NMR spectrum is referenced through the solvent lock (^2H) signal according to IUPAC recommended secondary referencing method

and the manufacturer's protocols based on impurity of CHCl_3 in CDCl_3 . Multiplicities were given as: s (singlet); br s (broad singlet); d (doublet); t (triplet); q (quartet); m (multiplets), etc. The number of proton (n) for a given resonance is indicated by nH. The ethylated DBT was evaporated to dryness under reduced pressure to remove DCE and the excess of $\text{C}_2\text{H}_5\text{I}$. The dry ethylated DBT was then dissolved in 0.5 mL of CDCl_3 was used for ^1H NMR analysis.

2.3.3 ESI Orbitrap FTMS analysis

Mass analysis were performed on a hybrid mass spectrometer combining the dual linear ion trap with a novel high field Orbitrap mass analyzer (LTQ Orbitrap Elite FTMS, Thermo Scientific, Bremen, Germany)[54]. Up to 500 spectra were collected in positive mode using the ESI source (Thermo Fisher, Bremen, Germany). A standard data acquisition and instrument control system was employed (Thermo Scientific). Acquisition mass range was $150 < m/z < 1200$ and the target value (AGC value) was set between $1\text{E}5$ and $1\text{E}6$; typical ESI conditions were as follows: flow rate $5 \mu\text{L}/\text{min}$; spray voltage 3.0 kV ; a sheath gas flow of 5 (arbitrary unit), an auxiliary gas flow of 2 (arbitrary unit). MS data were recorded with a resolving power of 480 000 at m/z 400 using a 1.5 s transient and up to 900 000 at m/z 400 using transient signals of 3 s for comparison. These parameters allow separating all important mass splits throughout the detected scan range. The instrument was calibrated with the Thermo Scientific Pierce LTQ Velos ESI positive ion calibration solution. In addition, external calibration was performed using a mixture of the Agilent electrospray calibration with the masses 300.04812, 622.02896, 922.00980, thus the whole mass range was covered in the samples. The mass accuracy below 1 ppm and the resolving power up to 480 000 at m/z 400 allows to analyze the crude oil by the high-field Orbitrap.

2.3.4 ESI FT-ICR MS analysis

Corresponding mass analysis was performed on a 7 T linear quadrupole ion-trap (LTQ) FT-ICR MS (Thermo Fisher, Bremen, Germany). The same ESI source was employed. Mass acquisition, ESI condition, AGC control and mass calibration follow the same setting implemented on ESI Orbitrap FTMS.

2.3.5 Data analysis

The obtained mass data were imported into Composer software V1.06 (Sierra Analytics, Modesto, CA). The following chemical constraints were applied: number of H 1000, $0 < D < 3$ for reaction with CD_3I and $0 < D < 5$ for reaction with C_2D_5I , $0 < C < 100$, $0 < S < 3$, $0 < O < 3$, $0 < N < 3$, and $0 < \text{double bond equivalent (DBE)} < 40$, with a maximum mass error of 1.5 ppm. The calculated molecular formulas were sorted into their heteroatom class ($N_nO_oS_s$) according to their denoted Kendrick mass defects, double bond equivalence ($\text{DBE} = \text{number of rings plus double bonds involving carbon}$) distribution, and carbon number distribution [97].

2.4 Results and Discussion

Ultrahigh-resolution MS has an unparalleled advantage for crude oil analysis, but as of yet, not all compositions present in heavier petroleum can be completely and accurately analyzed by any single available analytical method. Thus, simplification methods [17, 98] and methods for selective analysis need to be developed to gain a deeper insight into crude oil composition. It has been shown that Ag^+ ions kinetically coordinate preferentially to sulfur atoms instead of oxygen or nitrogen atoms to form metal-ligand bonds.[94, 99] This Ag^+ selectivity towards sulfur species can now be used for selective reactions with derivatization agents to tag sulfur heterocycles in crude oil. To achieve this goal,

the reaction has been investigated in detail in three steps: 1) The reaction was carried out using a standard sulfur-containing compound. Here, dibenzothiophene (DBT) was chosen as a probe to optimize the reaction condition and monitored by proton nuclear magnetic resonance (^1H NMR) and ultrahigh resolution MS; 2) In the second stage the obtained conditions were applied for a simple mixture of standard aromatic CH-, N-, O- and S-containing compounds to investigate the selectivity; 3) Finally, the conditions were applied to a heavy crude oil.

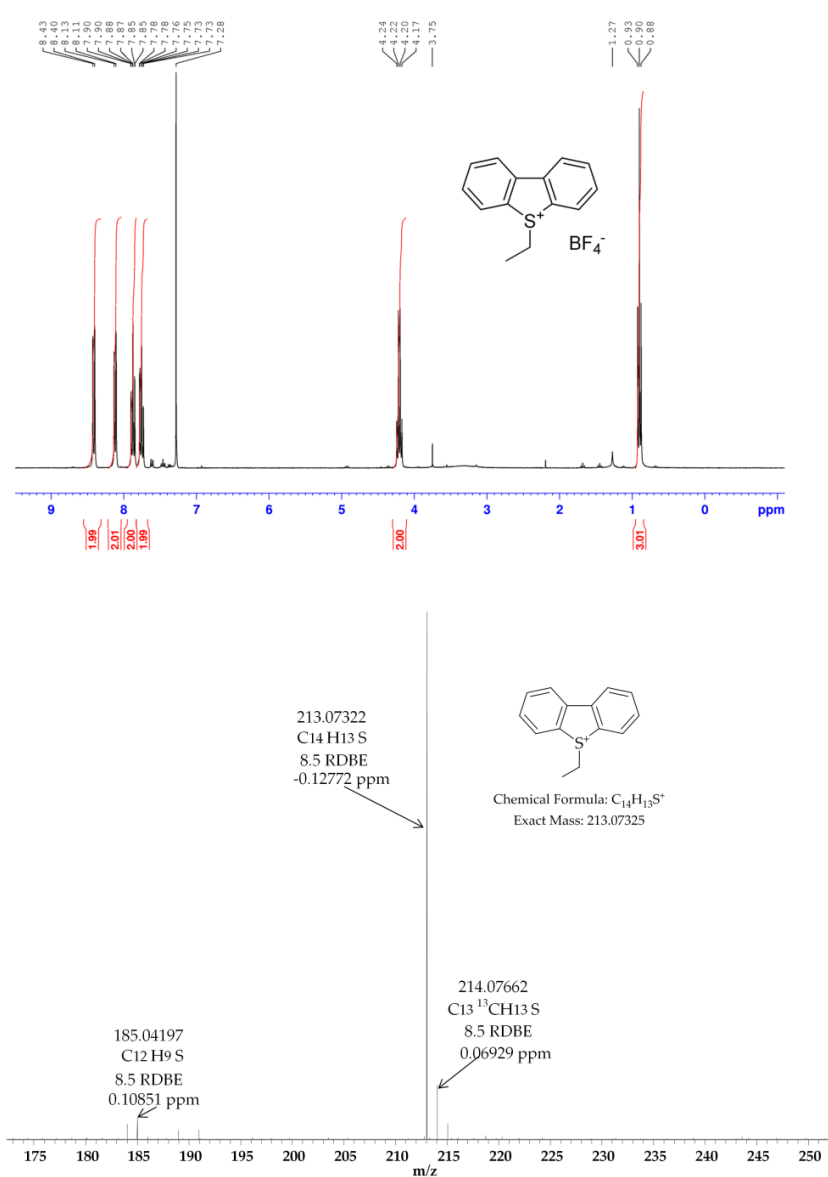
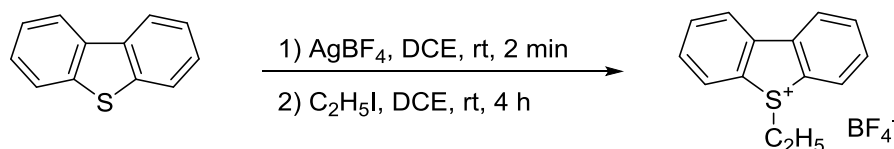


Figure 2.1: ^1H NMR spectra (top) and HRMS (ESI FT-ICR MS) spectra (bottom) of 5-ethyldibenzo[*b,d*]thiophenium tetrafluoroborate.

It is worth noting that the feeding sequence plays an important role on the selectivity towards sulfur. Here, a certain amount of AgBF_4 was added into the mixture of standards or crude oil, by which Ag^+ is first allowed to selectively coordinate with sulfur atoms to form complex Ag^+ adducts over a short time,[34] then the alkylating reagent was added dropwise to the system and the S-C covalent bond was formed by the strong driving force of the precipitation of silver iodide (AgI). This derivatization procedure allows detection of sulfur compounds with very high selectivity, and meanwhile avoids the extra complications arising from silver complexation [96, 100] and silver natural isotopes (51.84% ^{107}Ag and 48.16% ^{109}Ag) [94]. The implementation of multi-chemical methods combined with the ultrahigh resolution mass spectrometry (FT-ICR MS and Orbitrap FTMS) with electrospray ionization offers an efficient and feasible approach to detect the sulfur-containing species directly from the heavy petroleum without any time-consuming fractionation and separation.

2.4.1 Ethylation of dibenzothiophene (DBT)

The standard derivatization reaction that was previously introduced [40] was carried out under the following condition: containing 10^{-2} and 4×10^{-3} mmol sulfur and 1 mmol of CH_3I , were dissolved in 3 mL of dry DCE. A solution of 1 mmol AgBF_4 in 2 mL of DCE was then added. While the initial reaction that was reported by Muller et al. was only implemented for the derivatization with CH_3I ; here an additional derivatization agent, $\text{C}_2\text{H}_5\text{I}$, was studied as ethylating agent. In addition, the reaction was carried out using both reagents in the deuterated form to directly study the reaction product and distinguish derivatized from non-derivatized compounds in the crude oil sample that was not chromatographically simplified.



Scheme 2.1: Ethylation of DBT.

The molar ratio of DBT, CH_3I (or $\text{C}_2\text{H}_5\text{I}$) and AgBF_4 remains 1:2:2, and the yield of crude product determined by ^1H NMR was 70% for CH_3I and 87% for $\text{C}_2\text{H}_5\text{I}$. Similar experimental results were obtained by Acheson et al. [101], so $\text{C}_2\text{H}_5\text{I}$ was chosen for the continuous studies. In regard to selectivity, the reaction needed to be altered. Instead of adding equal molar ratio of CH_3I and AgBF_4 (1 mmol) that are 250 times the concentration of sulfur, as mentioned by Muller et al., the reaction condition depicted in Scheme 2.1 were optimized to produce a high yield of sulfonium salt.

When the molar ratio of DBT, AgBF_4 and $\text{C}_2\text{H}_5\text{I}$ remains 1:2:8, i.e. the amount of AgBF_4 is only 2 times more than DBT, the yield determined by ^1H NMR increases significantly (99%), as shown in Figure 2.1 (top).

The ^1H NMR spectrum of the above salt is simple because of the molecular symmetry (see Figure 2.1 top). The 4 groups of protons with the integral ratio 2:2:2:2 in the downfield belong to the aromatic rings; the 2 groups of protons with the integral ratio 2:3 in the upfield are attributed to the ethyl group. With the appropriate splitting according to the relevant environments of each proton, the structure of 5-ethyldibenzo[*b,d*]thiophenium tetrafluoroborate was ambiguously determined. ^1H NMR (300 MHz, CDCl_3): δ 8.41 (d, $J = 7.6$ Hz, 2H, $2 \times Ph$), 8.12 (d, $J = 7.1$ Hz, 2H, $2 \times Ph$), 7.87 (t, $J = 7.6$ Hz, 2H, $2 \times Ph$), 7.76 (t, $J = 7.9$ Hz, 2H, $2 \times Ph$), 4.21 (q, $J = 7.1$ Hz, 2H, $2 \times \text{CH}_2\text{CH}_3$), 0.90 (t, $J = 7.1$ Hz, 3H, $3 \times \text{CH}_2\text{CH}_3$).

The ethylated DBT salt, 5-ethyldibenzo[*b,d*]thiophenium tetrafluoroborate was obtained as colorless needles. It was determined by the positive HRMS (ESI FT-ICR MS) in Figure 2.1 (bottom) at m/z 213.07322 (calcd 213.07325) for $\text{C}_{14}\text{H}_{13}\text{S}^+$. A tiny peak of $[\text{M}+\text{H}]$ was also observed at m/z 185.04197, and

explanation might be given by the loss of the ethyl group under ESI condition. It was shown, that when using a heated nebulizer the derivatization group can be removed during the ionization process [8].

2.4.2 Ethylation of a mixture of standards (ANTH, DBT, ACR and DBF)

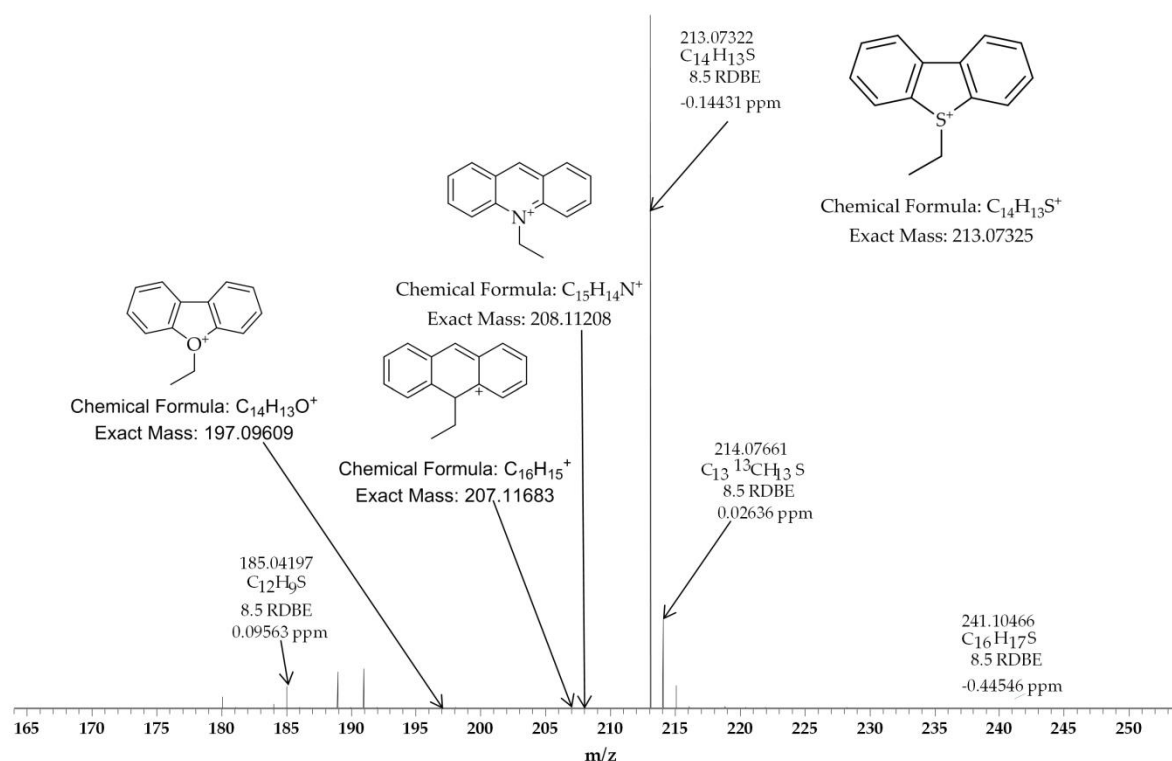


Figure 2.2: ESI FT-ICR MS spectrum of a mixture of the ethylated standards (ANTH, DBT, ACR and DBF).

Based on the results of the reaction of a pure standard sulfur compound, the conditions were applied to a mixture of standards (anthracene (ANTH), dibenzothiophene (DBT), acrinine (ACR) and dibenzofuran (DBF)). The HR ESI-MS spectrum of the ethylated mixture of standards was obtained as shown in Figure 2.2. No corresponding signals of derivatized ANTH, ACR and DBF were observed (calcd. m/z values at 207.11683, 208.11208 and 197.09609), and only DBT was selectively ethylated among this standards mixture. Besides the peaks from DBT, a very minor signal $[M + H]^+$ from underivatized ACR at

m/z 180.08084 was detected. Additionally, a minor trace of the disubstituted product of DBT was observed as well. From the results obtained above, we can see, even in the presence of other polyromantic heterocyclic compounds, the nucleophilic substitution of sulfur aromatic compound works with high selectivity towards sulfur species due to activation by the silver ions.

2.4.3 Methylation and ethylation of a heavy crude oil

Deuterated alkylating reagents (CD_3I and C_2D_5I) were utilized to alkylate the whole heavy crude oil instead of the standard reagents to distinguish the compounds present in a crude oil that contain CHNSO elements from the derivatized ones. An adjustment for CD_3I had to be made to a molar ratio of crude oil, $AgBF_4$ and CD_3I of 1:2:10.

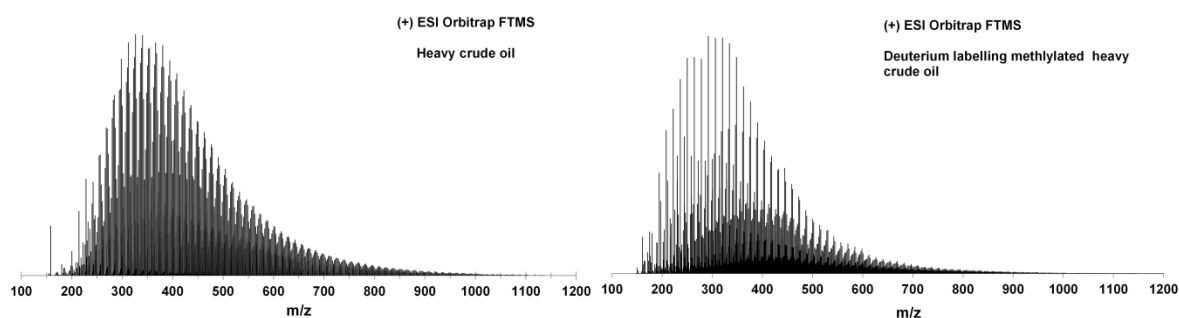


Figure 2.3: ESI(+) Orbitrap FTMS mass spectrum of heavy crude oil (left) and deuterium labelling methylated heavy crude oil (right).

Positive ESI Orbitrap FTMS analysis was performed for the untreated and methylated heavy crude oil. For a better signal-to-noise ratio, up to 500 scans in the mass range of m/z 150-1200 were accumulated, and a difference of the mass spectra before and after methylation can be seen in Figure 2.3. It is worth noting that the dramatic change of heteroatom class distribution before and after deuterium labelled methylation in Figure 2.4 is immense. Before the

derivatization reaction, the more polar compounds are detected as expected. Here, the majority of signals that were assigned belong to the $N_1[H]$ class, with additional signals from the $N_1S_1[H]$ and in very minor amounts from the $O_1S_1[H]$ class. Note that the protonated molecules that were detected are distinguished by $[H]$. Radical ions would be described without $[H]$.

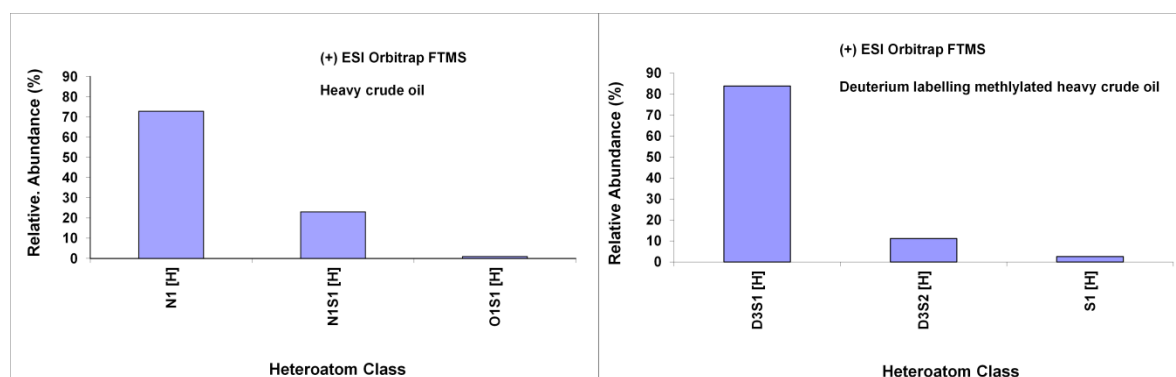


Figure 2.4: Class distribution for heavy crude oil from direct analysis (left) and after deuterium labelling methylated heavy crude oil (right).

After methylation, the compound classes that were assigned changed drastically. Now, instead of the polar compounds that are usually ionized by ESI, the nonpolar S_1 and S_2 classes which are usually not ionized by ESI are detected at high abundance. The deuterated version of the derivatization agent now also makes it possible to readily distinguish that the sulfur species detected are arising from the derivatization reaction and not only from the crude oil. After the reaction the sulfur species are present as S-methyl (d_3) sulfonium salts. A small amount of S_1 compounds (2.6%) are assumed to result from the loss of the alkyl radical which is removed during spraying in the heated nebulizer as mentioned above.

The details of the results are shown in Figure 2.5. The $N_1[H]$ class in the non-derivatized sample generated from protonation has a DBE range between 4 and 24 with a carbon number distribution from 11 to 86. The $N_1S_1[H]$ class meanwhile has a DBE range of 5-25 and carbon number of 10-83. The

deuterated $S_1[H]$ class spans a range of DBE (2-25) and carbon number (9-84), where the compounds with DBE value of 2 are assumed to be the aliphatic sulfides containing a ring or a double bond. The deuterated $S_2[H]$ class has a DBE range of 3-25 and carbon number (8-73).

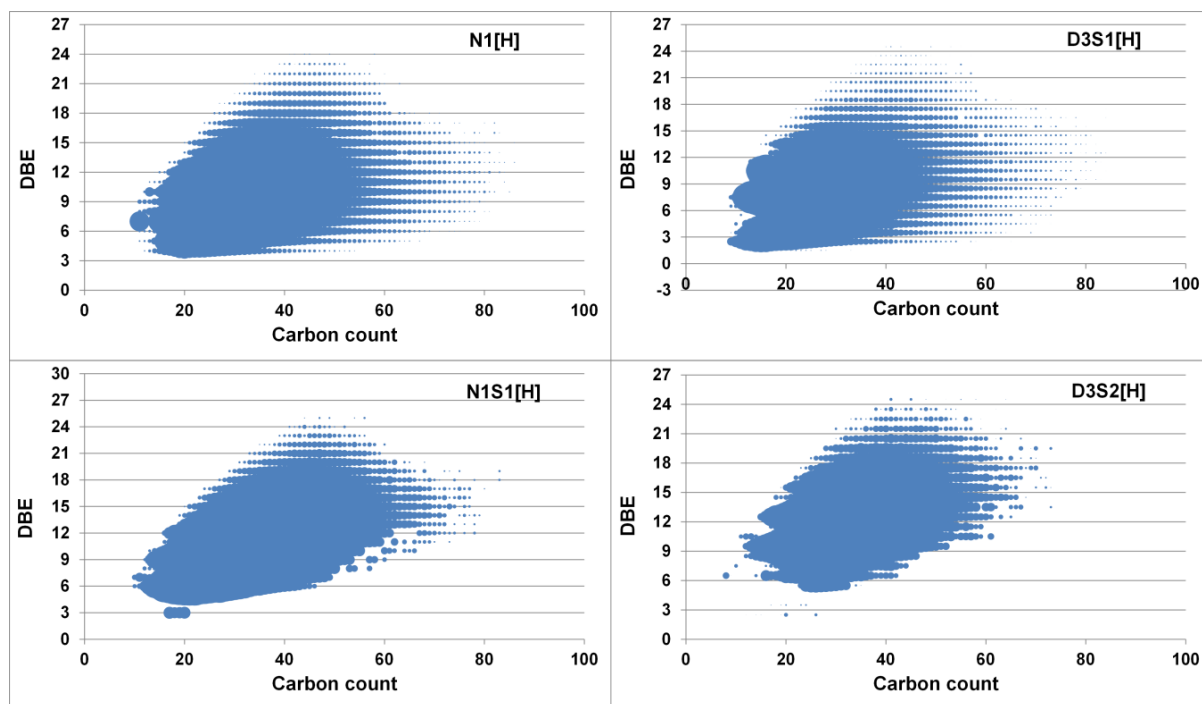


Figure 2.5: DBE versus carbon number plots for the $N_1[H]$ and $N_1S_1[H]$ classes from the protonated heavy crude oil (left) and for the $D_3S_1[H]$ and $D_3S_2[H]$ classes from the deuterated methylated heavy crude oil (right). Note that the [H] indicates a protonated molecule.

Additional ESI(+) FT-ICR MS analyses were performed on the deuterated ethylated heavy crude oil, as shown in Figure 2.6. Here, the results of the ethylation reaction are consistent with those from the methylation reaction. The nonpolar sulfur-containing compounds (S_1 , S_2 and S_1O_1 species) can be selectively detected by ESI (+) and differentiated by the C_2D_5 -group from the original crude oil. In comparison with the methylation procedure, a small difference in S_1O_1 class (2.5%) distribution appears which could result from different reactivities of the alkylating reagents. Still in both cases the S_1 class is the dominant class in both alkylation reactions, followed by the S_2 class.

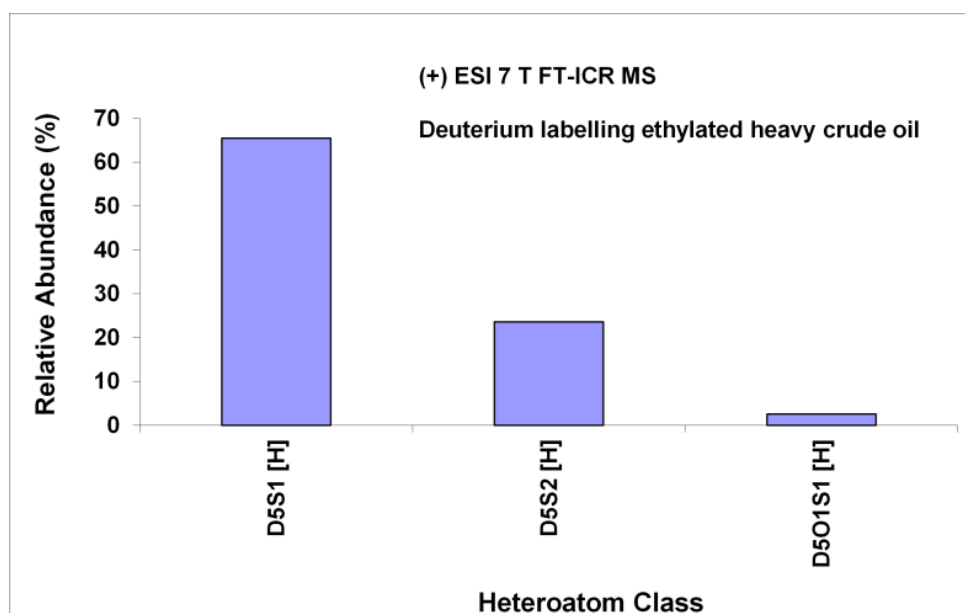


Figure 2.6: Heteroatom class distribution for deuterium labelling ethylated heavy crude oil.

When comparing the methylation reactions, the deuterated S_1 class in the ethylation extends a slightly narrower DBE range of 4-24, and the S_2 class has a slightly wider DBE range from 1 to 25 as demonstrated in Figure 2.7. The slight difference of the DBE range for S_1 and S_2 classes in methylation and ethylation might lie in the slight disparity of heteroatom class distribution of the two cases.

When considering the results from this study, the most interesting point is that sulfur containing compounds in a very complex crude oil mixture can be selectively analyzed by ESI-MS after derivatization. While in theory, the pyridine nitrogen is a better nucleophile than the thiophene sulfur to react in an S_N2 reaction with alkylating reagents in the polar aprotic solvent (DCE), things change when Ag^+ ions are involved in the reaction with crude oil. Here, the coordination chemistry of the silver ions plays an important role to kinetically favor the sulfur atoms and form weak silver-ligand bonds. When we then add the alkyl iodide to the above system, the relatively weak metal-ligand bond will be broken and a much stronger S-C covalent bond will be formed accompanied by the strong thermodynamic drive of releasing solid silver iodide (AgI) from the solution. The generated AgI could also further react with nitrogen compounds, to form insoluble coordination compounds of larger size that can

subsequently be removed from the system [102]. An important factor for the better selectivity toward sulfur compounds in crude oil is therefore, the right amount of AgBF_4 .

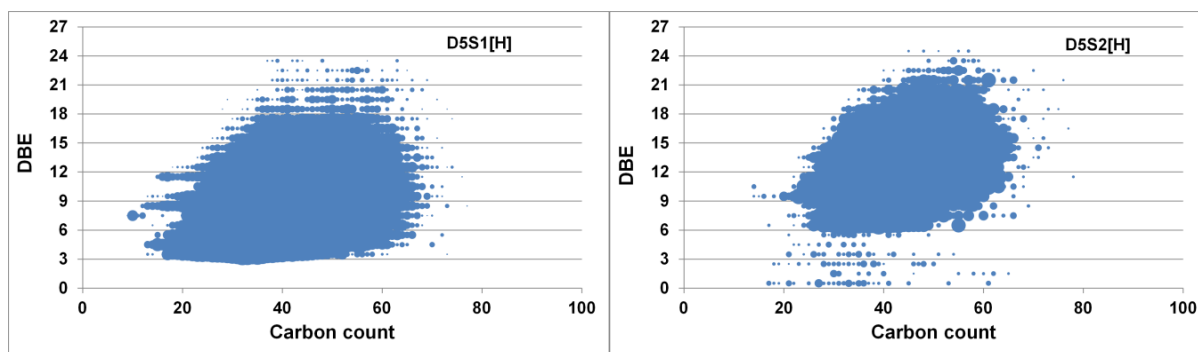


Figure 2.7: DBE versus carbon number plots for the D_5S_1 and D_5S_2 classes from the deuterated ethylated heavy crude oil.

2.5 Conclusion

Ultrahigh-resolution FT-ICR MS is an undoubtedly powerful analytical method for the analysis of incredibly complex petroleum samples. Nowadays, the high-field Orbitrap FTMS with a resolving power of up to 900 000 at m/z 400 is becoming an attractive alternative to FT-ICR MS for petroleum analysis as shown in this work and others[54, 89]. Different chemical methods, such as protonation and alkylation, have certain selectivity toward some classes of compounds in crude oil, and although MS has an unmatched advantage for the analysis of petroleum-type samples, it is still not able to fully characterize such tremendously complex mixtures. The combination of various selective methods [103], such as chemical derivatization, chromatographic methods, etc. might make a comprehensive characterization of a crude oil possible. Herein, by combining the coordination chemistry and organic chemistry together with the ultrahigh resolution mass spectrometry (FT-ICR MS and high-field Orbitrap FTMS) coupled with positive ESI, we demonstrate a highly selective method toward sulfur-containing compounds analysis in a whole heavy crude oil without

any fractionation and chromatographic separation. Deuterium labeling is utilized to introduce specific information of isotopically labelled atoms which are not present at high abundance in crude oil and allow unambiguous differentiation of the nonpolar sulfur species formed from CD_3 or C_2D_5 from the original crude oil in positive ESI. Using the labeling procedure also allows to fully assigning all reacted components within the very complex crude oil mixture thus allowing to fully characterizing the reaction.

Acknowledgements

The authors thank Dr. David Stranz (Sierra Analytics, Modesto, CA) for assistance during data interpretation. The authors gratefully acknowledge Royal Dutch Shell Amsterdam, The Netherlands, and Houston, TX, USA for the generously financial support and gift of samples. The authors also thank Jeffrey Garber (MPI) for additional proofreading of the manuscript.

**Chapter 3 Adding a Chemical Dimension as Tool for
Selective Analysis of a Heavy Crude Oil by
Fourier Transform Ion Cyclotron Resonance
Mass Spectrometry (FT-ICR MS)***

**Redrafted from “Wang, X.; Schrader, W., Chemically Controlled Selective Analysis of A Heavy Crude Oil by Fourier Transform Ion Cyclotron Resonance Mass Spectrometry (FT-ICR MS), will be submitted to Anal. Chem.”*

3.1 Abstracts

Ultrahigh-resolution Fourier transform ion cyclotron resonance mass spectrometry (FT-ICR MS) has been a powerful tool to characterize supercomplex mixtures such as crude oil. However, due to the complexity mass spectrometry alone is only able to provide data about the elemental compositions of compounds that are ionized by the individual ionization method. This is a very unselective process that is depending on different parameters such as volatility, polarity among others. A selective analysis is not possible. To achieve a selective analysis of different classes present in a heavy crude oil here a chemical reaction is used, that is carried out at different reaction conditions. These different reaction conditions in combination with electrospray ionization allow to accentuate different classes present in the complex mixture therefore introducing a selective step into the analytical scheme. Studies using standard compounds allow insight into the different reaction mechanisms.

3.2 Introduction

The rapid growth of energy demand drives the focus to more unconventional resources. Renewable supplies are still not available in the desired amounts, so the demand is satisfied mostly by fossil fuels.[8, 86] While sweet and light materials are diminishing the still available heavy crude oils need to be upgraded into usable energy sources. These heavy resources are complex heterogeneous mixture of hydrocarbon molecules containing various amounts of heteroatoms (N, S and O) and trace amounts of metal (Fe, Ni and V).[91] Although only less than 10% $N_nO_oS_s$ -containing compounds are present in petroleum, they are the most problematic with respect to pollution and corrosion of environment, inhibition of catalysts, deposits of production and processing.[33] In order to make better use of the petroleum resources and increase economic values, molecular-level understanding of supercomplex crude oil mixtures is highly desirable.[8]

Ultrahigh-resolution Fourier Transform Ion Cyclotron Resonance Mass Spectrometry (FT-ICR MS) which provides sufficient mass resolving power and mass accuracy, and allows unambiguously assigning tens of thousands of ions to their elemental compositions in crude oils has developed into the method of choice for such analyses.[10, 104-107]

Different ionization methods have been applied for a thorough analysis but it has been shown, that the complexity of the sample does not allow fully analyzing a whole crude oil with one method alone.[8, 108-110] To the contrary, different ionization methods allow detecting different compound classes.[108] In addition, ion suppression is occurring.[111] Therefore, it has been shown that the simplification of the complexity using a SARA fractionation scheme allows increasing the data depth and gain more information than when analyzing the whole crude oil sample.[42, 112] In addition, the direct coupling of separation methods where the complexity in individual spectra is decreased has also been

helpful for the overall analysis of a crude oil.[37, 89, 113, 114] Electrospray (ESI)[60] is a widely used ionization method applied for polar compounds in all kinds of matrices and especially efficient in generating $[M + H]^+$ or $[M - H]^-$ ions at atmospheric pressure via protonation or deprotonation. It can ionize the most acidic and basic components in petroleum complex mixtures and provide complete characterization without fragmentation.[115] This method in combination with FT-ICR MS has emerged as a powerful technique for the characterization of polar species in petroleum crude oils.[87] However, most species in crude oils (such as sulfur, oxygen heterocycles and hydrocarbons) are not basic or acidic enough to be efficiently ionized, which inherently limits the classes and types of compounds ionized by ESI. Given these limitations, Muller et al.[40] used a methylation procedure to derivatize polycyclic aromatic sulfur compounds (PASHs) to sulfonium salts which are polar enough to be visible in ESI; however the selectivity is based on the premise of the necessary chromatographic separation. Other methods have been applied to produce stable intermediates to improve ionization efficiency for electrospray ionization of non- to low polar compounds such as using Pd^{2+} ESI-MS or Ag^+ ESI-MS for speciation of sulfur-containing compounds in petroleum by the formation of the positive metal-complexes. The relatively flexible coordination sphere of the silver ion increases the complexity of crude oil analysis.[92, 94]

These results have shown that a chemical derivatization technique has one major advantage when comparing it to instrumental analysis alone: the chemical reaction can introduce selectivity to the analytical scheme in such complex mixtures. Thus, it is necessary to develop reactions that can promote the selective and differentiated analysis of compounds within a complex mixture across a wide pK_a or pK_b range in combination with a chosen ionization method.

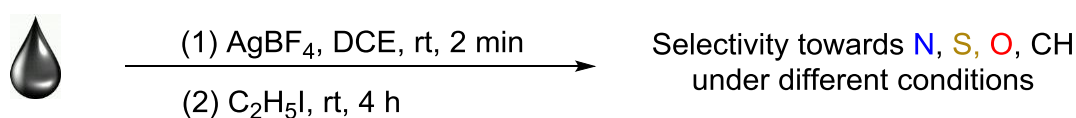
Here, a chemical method was developed to selectively analyze different compound classes present in a complex crude oil mixture. The optimization of

the reaction was done with individual compounds. The optimized conditions were then applied to a heavy crude oil.

This procedure in combination with electrospray ionization and ultrahigh resolution mass spectrometric detection allows a selective analysis of the different classes in a heavy crude oil where suppression and discrimination effects are reduced due to the selectivity of the chemical reaction.

3.3 Experimental section

3.3.1 Alkylation



Scheme 3.1: Ethylation of crude oil under different reaction conditions.

10 mg of dibenzo[*b,d*]thiophene (DBT) (5.43×10^{-2} mmol) were dissolved in 1 mL of anhydrous 1,2-dichloroethane (DCE). During mixing, a solution of 21.13 mg of silver tetrafluoroborate (AgBF_4) (10.86×10^{-2} mmol, 2 molar eq.) in 0.5 mL DCE was added. After 2 min, 28 μL (43.44×10^{-2} mmol, 2 molar eq.) of ethyl iodide $\text{C}_2\text{H}_5\text{I}$ was then added and yellow silver iodide precipitated immediately. After 4 h, the solid was removed by centrifugation and washed with 0.5 mL of DCE. A final concentration of 500 $\mu\text{g}/\text{mL}$ of the ethylated sample was obtained through dichloromethane (DCM) diluting for ESI measurement. With the standardization in mind, 10 mg of a heavy crude oil was used instead of DBT. As shown in Table 3.1, different amounts of AgBF_4 and $\text{C}_2\text{H}_5\text{I}$ were used respectively, and eight heavy crude oil samples obtained were named with a sequence number from B1 to B8. The eight samples were prepared

at a concentration of 500 $\mu\text{g/mL}$ in DCM. The color of the reaction solution varies depending on the reaction condition (Figure A3.1 in the Appendix 3).

3.3.2 ESI FT-ICR MS analysis

Mass analysis was performed on a 7 T LTQ FT-ICR MS (Thermo Fisher, Bremen, Germany). The spectra were collected in positive mode using an ESI source (Thermo Fisher, Bremen, Germany).

The measurements were carried out with a transfer capillary temperature of 275 $^{\circ}\text{C}$, a skimmer voltage of 30 V, and a tube lens voltage of 110 V. Data were acquired in a mass range from 150 - 1200; the target value (AGC value) were set between 1E5 and 1E6; typical ESI conditions were as follows: flow rate flow rate 5 $\mu\text{L/min}$; spray voltage, 4.0 kV; a sheath gas flow of 5 (arbitrary unit); an auxiliary gas flow of 2 (arbitrary unit). The Instrument was calibrated with the Thermo Scientific Pierce LTQ Velos ESI positive ion calibration solution. In addition, external calibration was performed using a mixture of the Agilent electrospray calibration with the masses 300.04812, 622.02896, 922.00980, thus the whole mass range was covered in the samples.

3.3.3 Data acquisition analysis

Data were collected and processed with the LTQ FT Ultra 2.5.5 (Thermo Fisher, Bremen, Germany) data acquisition system, and then was imported into the composer software (Sierra Analytics, Modesto, CA). The following chemical constraints were applied: number of H unlimited, $0 < C < 200$, $0 < S < 3$, $0 < O < 5$, $0 < N < 3$, and $0 < \text{double bond equivalent (DBE)} < 40$, with a mass accuracy better than 1 ppm. The calculated molecular formulas were sorted into their heteroatom class ($\text{N}_n\text{O}_o\text{S}_s$) according to their denoted Kendrick mass defects, double bond equivalence ($\text{DBE} = \text{number of rings plus double bonds}$

involving carbon) distribution, and carbon number distribution.[82] The assignments of the most abundant ions were confirmed by corresponding ^{13}C peak. The obtained mass lists were transferred into Excel for data evaluation and preparation of the figures shown.

Table 3.1: The heteroatom class distribution of the 4 most abundant classes with different mole ratios of AgBF_4 : $\text{C}_2\text{H}_5\text{I}$: heavy crude oil

Serial No.	Mole ratio	The 4 most abundant Classes
B1	1: 0 mmol: 0 mmol	$\text{N}_1, \text{N}_1\text{S}_1, \text{S}_1, \text{N}_1\text{O}_1\text{S}_1$
B2	1: 0.11 mmol: 0.44 mmol	$\text{S}_1, \text{S}_2, \text{O}_2\text{S}_1, \text{S}_3$
B3	1: 0.5 mmol: 0.5 mmol	$\text{O}_1, \text{CH}, \text{S}_1, \text{O}_2$
B4	1: 1 mmol: 1 mmol	$\text{O}_1, \text{CH}, \text{O}_2, \text{S}_1$
B5	1: 2 mmol: 2 mmol	$\text{CH}, \text{O}_1, \text{O}_2, \text{S}_2$
B6	1: 3 mmol: 3 mmol	$\text{CH}, \text{O}_1, \text{O}_2, \text{O}_3$
B7	1: 3.5 mmol: 3.5 mmol	$\text{CH}, \text{O}_1, \text{O}_2, \text{O}_3$
B8	1: 4 mmol: 4 mmol	$\text{O}_1, \text{CH}, \text{O}_2, \text{O}_3$

3.3.4 Nuclear magnetic resonance spectroscopy

^1H NMR was performed on Bruker Advance 300 NMR spectrometer. Chemical shifts of ^1H NMR spectra and the coupling constants were obtained through analysis of the spectra using MestReNova NMR-Software version 10.0.2-15465. Chemical shifts of ^1H NMR spectra is reported as in units of parts per million (ppm) and relative to the signal of CHCl_3 in chloroform-*d* ($\delta = 7.26$, singlet). Multiplicities were given as: s (singlet); br s (broad singlet); d (doublet); t (triplet); q (quartet); ddd (doublet of doublet of doublets); td (triplet of doublets); m (multiplets), etc. The number of proton (n) for a given resonance is indicated by nH. The ethylated standards were evaporated to dryness under reduced pressure to remove DCE and the excess $\text{C}_2\text{H}_5\text{I}$ respectively. The NMR sample was prepared by dissolving it in 0.5 mL of CDCl_3 for ^1H NMR analysis.

3.4 Results and Discussion

3.4.1 Positive ESI FT-ICR spectra

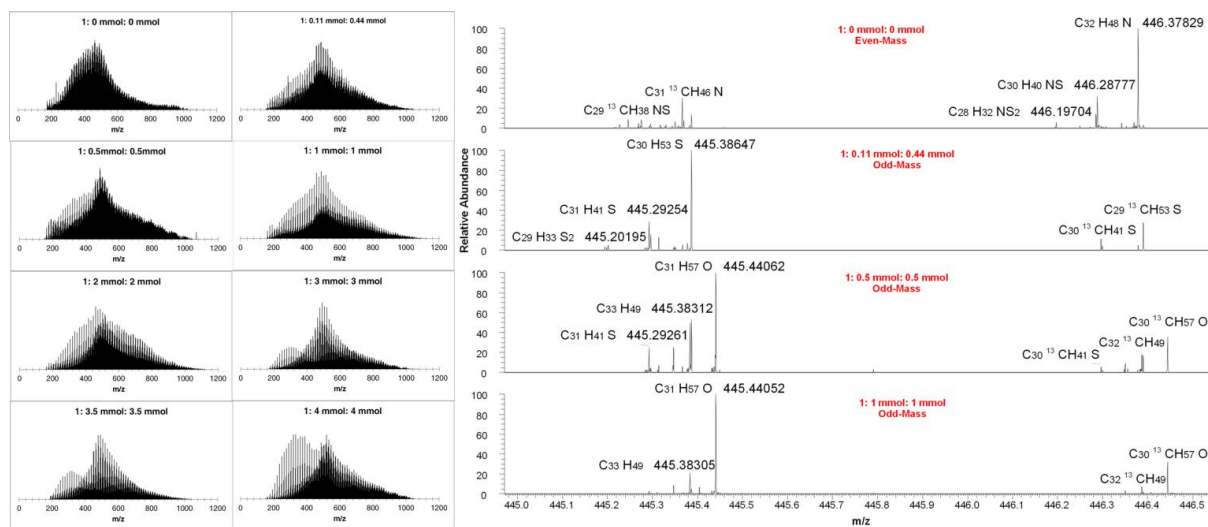


Figure 3.1: 7 T FT-ICR mass spectra obtained from eight samples based on Table 3.1 in (+) ESI ionization mode for the mass range 150-1200 Da (left column) and the corresponding enlarged section of the first four samples in a range between m/z 445.0-446.5 (right column) with the assigned molecular formulas.

An overview of the results obtained from the eight different samples is shown in Figure 3.1 (left column). The spectra show the results in a range between m/z 150-1200. Additionally, a 1.5 Da mass windows from the first four samples (B1-B4) is compared to further exhibit the information on elemental compositions changes as shown in Figure 3.1 (right column). The results obtained directly from the crude oil sample without ethylation show that basic nitrogen species with even-mass distribution are present. After applying the chemical reaction in various ratios, less basic species, neutral species and even acidic species (sulfur, oxygen and hydrocarbon) of odd mass numbers were observed.

3.4.2 Selectivity of heteroatom classes

Selectivity can be investigated further from the heteroatom class distributions of the eight samples based on the reaction conditions used in Table 3.1 (Figure 3.2).

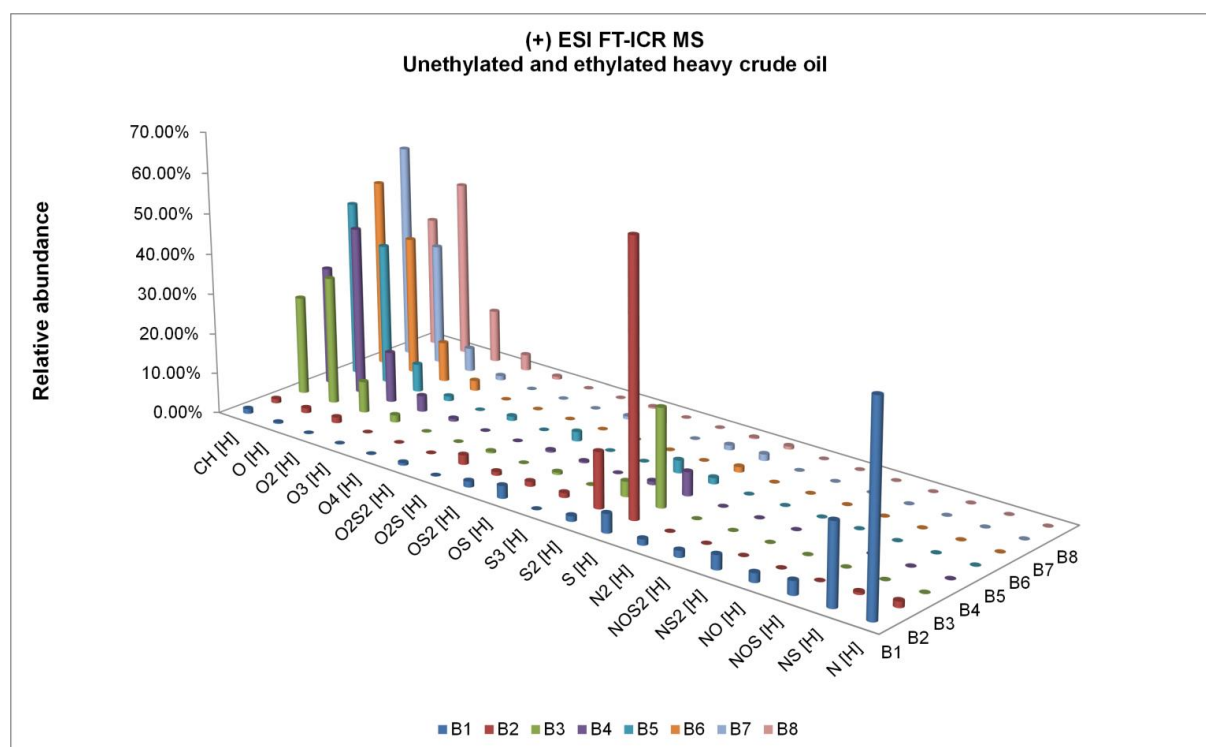


Figure 3.2: Comparison of heteroatom class distributions obtained from the above eight samples based on Table 3.1. Note that relative and not absolute abundances are shown; the summary of all abundances from one method is 100%.

As the mole ratio increases, the heteroatom class distribution shifted, starting from the basic species (e.g., nitrogen-containing species) to the more neutral species (e.g., hydrocarbons) and finally arriving at the more acidic species (e.g., oxygen-containing compounds). In the B1 sample, N₁ class is dominant, followed by N₁S₁, S₁, N₁S₂, N₁O₁S₁, O₁S₁, N₁O₁ classes. When AgBF₄ and C₂H₅I were introduced to crude oil to do the ethylation with a mole ratio of crude: AgBF₄:C₂H₅I of 1:2:8 as shown in B2 sample, the S₁ class replaced decisively the N₁ class to be absolutely dominant, followed by S₂, O₂S and S₃ classes. The

relative abundance of S_1 class in B2 reaction was at least 14 times higher than in case of the B1 reaction; in contrast, N_1 class has a 33-fold decrease. Other nitrogen-containing species decreased sharply or disappeared. Instead, O_1 and O_2 classes appeared with a very low relative abundance. CH class in B2 case kept similar at around 1.1 % as in B1 case.

When the reaction conditions were changed according to the reaction B3, O_1 class was present as the most significant class with a 26-fold increase of relative abundance comparing to B2 sample, followed by CH class, which increased by a factor of 22, and then O_2 class which increase 5-fold. In the B3 reaction O_3 class appears. From reaction B3 on, nitrogen-containing species fully disappeared. The relative abundance of S_1 and S_2 classes in B4 case decrease another 3 and 4 times respectively comparing to B3 case. From B5 to B8, the sulfur-containing species have become rather humble, but CH and oxygen-containing species play the major roles. CH class was the dominant class in B5, B6 and B7 reactions, and the relative abundance of CH class in B7 case reached the highest point among the eight observed reaction conditions. O_1 class becomes the dominant class first in B3 and B4, and then fell into the second place in B5, B6 and B7, but rose up to the dominant place in reaction B8 again. The relative abundance between CH and O_1 class did not vary considerably from B3 to B8 reactions. In the B8 sample, the relative abundance of O_1 class reached the maximum among the eight samples, similar to O_2 and O_3 classes. It was worth noting that O_4 class was detected by ESI(+) FT-ICR MS in B4 and B8 sample, in which O_1 class was the dominant class. In general, the basic nitrogen containing species were selectively detectable in B1 samples, and in the B2 reaction and afterwards the less basic sulfur-containing species took the place to be selectively ionized. The conditions of the B3 reaction seems to be somewhere in the middle between the reactions B2 and B4 where in B3 S_1 , O_1 and CH class were present at a comparable relative abundance, the neutral (e.g., hydrocarbons) and even acidic species (e.g., O_1 , O_2 and O_3 class) played the main roles to be visible in ESI(+)

spectra from the B4 to B8 reactions. In particular, the data reveal that not all components are present in the spectra of one reaction, and each reaction condition emphasizes a certain subset of the whole complex sample and allows a deeper insight of crude oil.

3.4.3 Double bond equivalents (DBE)

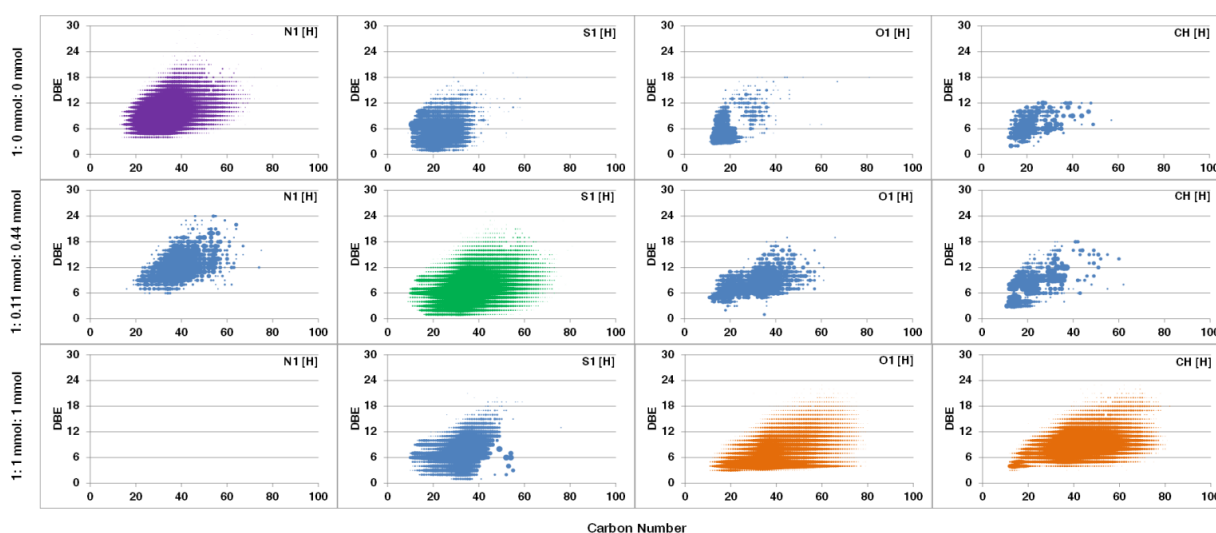


Figure 3.3: Comparison of Kendrick plots of the N_1 , S_1 , O_1 and CH classes obtained from B1 (top), B2 (middle) and B4 (bottom) samples using ESI(+) 7 T FT-ICR MS.

Since there are thousands of different compounds present within a crude oil sample it is difficult to visualize the different combinations of classes and individual compounds. Here, Kendrick plots[82] further facilitate the visualization of the unsaturation of a single chemical class from a certain reaction condition. Some components in crude oils are selectively discriminated during the reaction condition. In order to simply and clearly demonstrate the difference, herein three samples (B1, B2 and B4) were taken to exhibit the selectivity of the reactions. Figure 3.3 clearly illustrates the changes within the different N_1 , S_1 , O_1 and CH classes present in B1, B2 and B4 samples based on positive ion ESI (for N_1S_1 , S_2 , O_2 and O_3 species see Figure A3.2 in the Appendix 3).

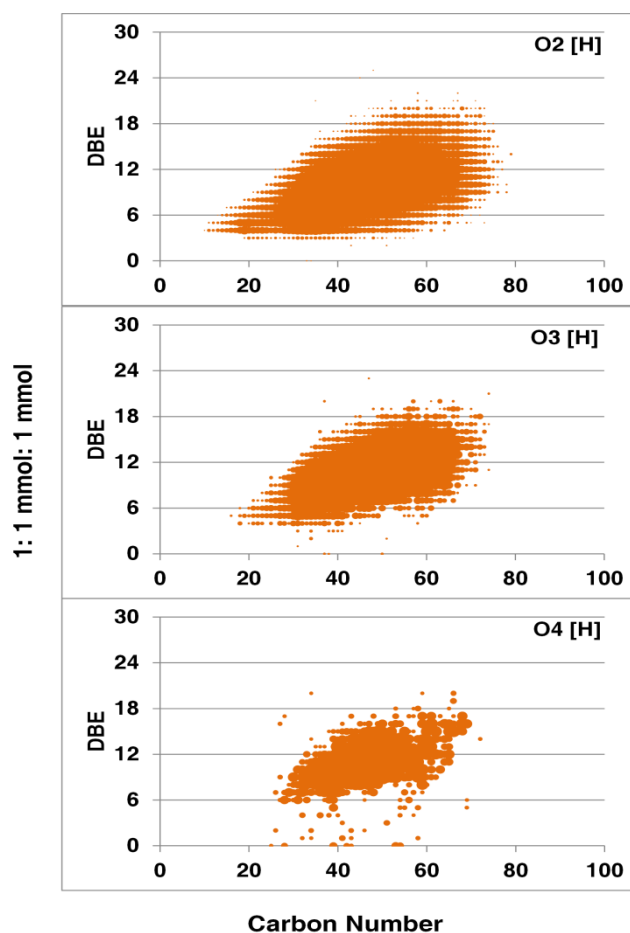


Figure 3.4: Plots of DBE vs. carbon number distribution for O₂, O₃ and O₄ from B4 sample.

The DBE vs. carbon number distribution for a given chemical class varies significantly among the three samples. For N₁ class, B1 reaction condition shows a wider range of DBE (4-29) and carbon numbers (13-75); B2 shows a lower range in the DBE vs. carbon number distribution, while in B4 sample the N₁ class fully disappears. In the data of the B2 reaction especially the sulfur-containing species are emphasized as marked in green, e.g. for S₁ class, the mole ratio of 1:0.11 mmol:0.44 mmol allows analysis of a broader regional distribution of DBE (3-24) vs. carbon number (9-81) with high ion abundance comparing to B1 and B4. As for O₁ and CH class, as the mole ratio of AgBF₄:C₂H₅I: crude oil increase, the scope of Kendrick plots change from small discontinuous to larger continuous and the detectable ion abundance for these two classes also increase. When interpreting the data from B4 reaction, O₁ class

has a DBE vs. carbon number distribution with DBE ranging from 3 to 24 and carbon number from 11 to 80 as colored in orange, and CH class DBE (3-23) and carbon number (12-80) as coded in orange.

It is worth noting that as the mole ratio of crude oil: AgBF₄: C₂H₅I increases, more oxygen-containing species were accessed (O₁, O₂ and O₃). The higher the mole ratio is, the further the tendency goes to the acidic species. Figure 3.4 exhibits the DBE vs. carbon number distribution of O₂ and O₃ classes from B4 sample. To the best of our knowledge, it is the first time that under ESI(+) that the acidic species were detectable in high abundance. Both O₂ and O₃ classes cover a wider range of DBE and carbon number respectively, DBE value for O₂ class 3-24, and O₃ class 0-23. O₄ class was detected in lower intensities in B4 sample with DBE range from 0-20.

The mechanisms behind the selectivity are different for each class:

- N-containing species: protonation;
- S-containing species: nucleophilic substitution;
- CH-class and O-containing species: first electrophilic aromatic substitution (EAS), and then protonation.

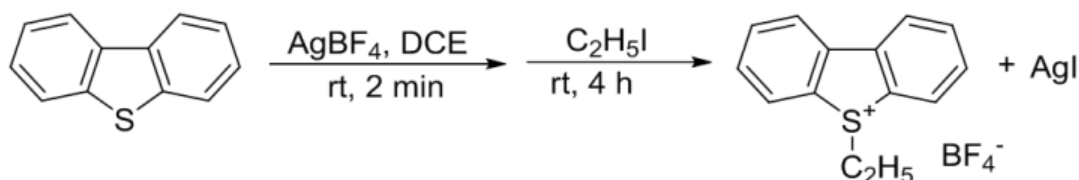
3.4.4 Protonation for nitrogen-containing species

The combination of the ultrahigh mass resolution and mass accuracy of FT-ICR MS combined with electrospray ionization is the most efficient method to ionize polar species in complex mixtures.[33] Positive ESI accesses the most basic components of crude oils by the generation of quasi-molecular ions [M + H]⁺ (e.g., pyridines pK_b 8.8)[31] through protonation, such as the selective analysis towards nitrogen-containing species as seen in B1 reaction. Species which are insufficiently basic, such as thiophenes and furans, neutral

hydrocarbons and similar compounds are not detectable under conventional ESI(+) conditions. There is only one exception to the rule as it has been shown that polyaromatic hydrocarbons can be detected as radical ions under certain conditions by ESI-MS.[43]

3.4.5 Nucleophilic substitution for sulfur-containing species

Sulfur containing compounds can easily react in an alkylating reaction.[40] The sulfur atom in thiophenes is a nucleophilic functional group and the reactivity towards alkylation has been shown for crude oil before.[8, 40] Herein we modified the previously used reaction conditions[40] by replacing methylation with ethylation (see Figure A3.3 in the Appendix 3) and changing reaction conditions (e.g., the mole ration and adding order of AgBF_4 and $\text{C}_2\text{H}_5\text{I}$, as seen in experimental section above) as shown in Scheme 3.2. In this case, Ag^+ kinetically preferentially coordinated with sulfur atoms to the relatively weak metal-ligand bond[34, 99] and the strong S-C covalent bond was formed by the strong driving force from the precipitating action of silver iodide (AgI). The thiophenium salts were released and dissolved in DCE. Basic nitrogen-species coordinated with Ag^+ and even AgI [102] to form the bulk insoluble complex in DCE and was excluded from the system (for more details see Figure A3.4 in the Appendix 3). The thiophenium salts were therefore, preformed ionic compounds that could be easily detected by positive ESI (for ^1H NMR data and HRMS data see Figure A3.5 – A3.6 in the Appendix 3).



Scheme 3.2: Ethylation of a sulfur-containing compound.

For sulfur-containing species, the nucleophilic substitution on S atom is energetically favorable reaction comparing to the electrophilic aromatic substitution on aromatic rings. The mole ratio is the key to the selectivity towards sulfur-containing compounds, which allows that the thermodynamics control the reaction in whole crude oil, and allows the nucleophilic substitution to occur first on sulfur atom.

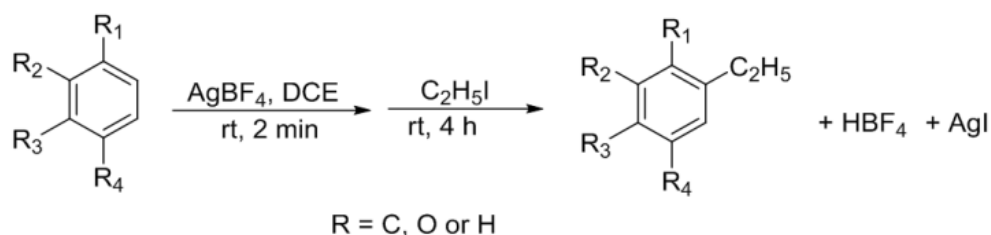
3.4.6 Electrophilic aromatic substitution (EAS) and protonation for Hydrocarbons and Oxygen-containing species

As illustrated in Figure 3.2, both neutral hydrocarbons and even acidic oxygen-containing species (O_1 , O_2 , O_3 and O_4 classes) were detectable in ESI(+) and played the roles, which went beyond the conventional detection dimension of positive electrospray mass spectrometry. Formic acid (pK_a 3.77) and acetic acid (pK_a 4.76) are conventional positive electrospray reagents that provide protons for ionization, but they are not acidic enough to protonate most species weaker than pyridines. Therefore, those weakly basic, neutral and even acidic species can not directly be ionized by ESI(+). But when an electrophilic aromatic substitution (Friedel-Crafts alkylation) occurs on the main functional group-aromatic ring, H^+ is released from the aromatic ring and the strong acid HBF_4 is produced from the EAS reaction (pH value increased to pH 0.4, for more details see Figure A3.7 in the Appendix 3). The strong acid then protonates the oxygen heterocycles and hydrocarbon species and makes them detectable in ESI(+).

The driving force still comes from the precipitating action of silver iodide (AgI). HBF_4 is acidic enough that it is capable of protonating hydrocarbons and even acidic oxygen-containing species (O_1 , O_2 , O_3 and O_4 classes). O_1 may include furan/phenol-type compounds; [116] if former, nucleophilic substitution might occur on oxygen atom, and produce polar O-ethyl dibenzofuranium

salts,[117] which is similar like the reaction on sulfur atom. If the latter EAS might occur on the aromatic rings and the product HBF_4 enabled O_1 class to being ionized in ESI(+). O_2 class is most likely carboxylic acids, and O_3 class may be the compounds containing a carboxylic acid group and a phenol group or a hydroxyl group, O_4 class can include two carboxylic acid groups.[116] The aromatic rings are π electrons rich, and carboxylate oxygen atom, phenol oxygen atom or hydroxyl oxygen atom have the lone pair electrons, and such electrons (π electrons or lone pair electrons) can catch a free proton from the dissociation of strong acid like HBF_4 , and the corresponding species detectable in ESI(+) FT-ICR MS. In the EAS mechanism, the active site is the carbon atom not the heteroatoms, which explained why hydrocarbons and oxygen-containing species were always observed together, especially CH and O_1 class showed up with a comparable relative abundance, not like the selectivity towards nitrogen atom and sulfur atom. As for the absence of nitrogen, complex effect between Ag^+ and pyridine-type nitrogen is significant.

In theory, pyridine-types are good nucleophiles, but meanwhile they are also excellent ligands for most metal ions (e.g., silver ions), and they can form large and stable complexes that are insoluble in DCE (see Figure A3.4 in the Appendix 3).[102] For the sharp decline of sulfur-containing compounds, the complex is one of the reasons, but the main reason is based on the weight percentage content in a heavy crude oil of every elements. The sulfur content in this heavy crude oil is 5.60%, nitrogen 0.14%, oxygen 2.08%, carbon 81.68% and hydrogen 9.98%. As the mole ratio of AgBF_4 and $\text{C}_2\text{H}_5\text{I}$ increases, the more active ethyl cation are produced in the system, the less selectivity towards sulfur occurs. Since the hydrocarbon content of the crude is more than 90 wt% now the reaction of the whole sample shifts to the reaction at the carbon atom on the aromatic ring (EAS).



Scheme 3.3: Electrophilic Aromatic Substitution (EAS).

All things considered, it is possible to provide a selective analytical scheme for very complex samples such as a heavy crude oil when introducing an organic chemical dimension as well as a coordination chemical dimension to the analytical scheme. A focus on the different functional groups from the perspective of organic chemistry by selecting appropriate conditions for the reactions, a wide range of species are becoming selectively accessible by ESI (+) mass spectrometric detection.

3.5 Conclusion

A methodology of chemically controlled selective analysis of a heavy crude oil by positive ESI FT-ICR MS is introduced. The present study extends the range of chemical classes present in one heavy crude oil and allows selectively detecting a wide range of compounds from basic, less basic, neutral and even acidic species with a wide DBE values to be analyzed by positive ESI. Usually negative ESI is able to access the acidic fraction of crude oil by deprotonation, but has the problem of unstable signals comparing to ESI (+).[118] Positive APPI has enabled the detailed speciation of a broader range of polar and nonpolar compound classes, but with no selectivity towards molecular classes. Here, however the use of ESI (+) widens the compound range and makes a selective analysis of heterocyclic classes within the crude oil possible. This method will not replace a detailed analysis using different ionization methods, but aids the characterization and analysis of a supercomplex crude oil in details,

because the greatest challenge for the analysis of heavy crude oils is the high complexity. The target selective analysis is very helpful, because it can gain more information of individual classes and may even lead to structural information. Controlling the reaction condition is like controlling the selective switch to certain species, and makes them visible under positive ESI, because each condition stresses certain heteroatom compounds. The combination of chemical method with positive ESI FT-ICR MS enables the selective analysis of a whole heavy crude oil with a wide compound classes and double bond equivalents without any prior fractionation and chromatographic separation, and offers some analytical help for such challenging analytical problems.

Acknowledgements

The authors thank Dr. David Stranz (Sierra Analytics, Modesto, CA) for assistance during data interpretation.

Appendix 3

This section contains additional information about the experimental section and Appendix Figures that mentioned in the main text, for details see below.

Experimental section

Sample and chemicals. A heavy crude oil was used for these studies with the following bulk properties: carbon 81.68%, hydrogen 9.98%, nitrogen 0.14%, sulfur 5.60%, and oxygen 2.08%. Dibenzothiophene (DBT), silver tetrafluoroborate (AgBF_4), dichloroethane (DCE) and dichloromethane (DCM) were purchased from Sigma-Aldrich (high purity, St. Louis, MO). Iodoethane ($\text{C}_2\text{H}_5\text{I}$) was purchased from Sigma-Aldrich (high purity, Steinheim, Germany).

Alkylation of crude oil. With the standardization in mind, 10 mg of heavy crude oil was used instead of DBT. According to Table 3.1, different amounts of AgBF_4 and $\text{C}_2\text{H}_5\text{I}$ were used, and the eight heavy crude oil samples obtained were named with a sequence number from B1 to B8. The eight samples were prepared at a concentration of 500 $\mu\text{g}/\text{mL}$ in DCM.

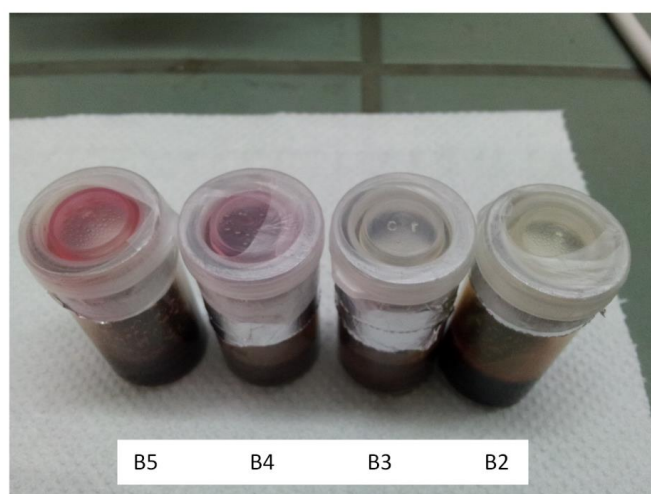


Figure A3.1: Comparison of color change of untreated reaction solutions from B2, B4, B5 and B6 samples. Original crude oil solution in anhydrous DCE is yellow brown, but after reaction the color is changed because the molecular structures are changed.

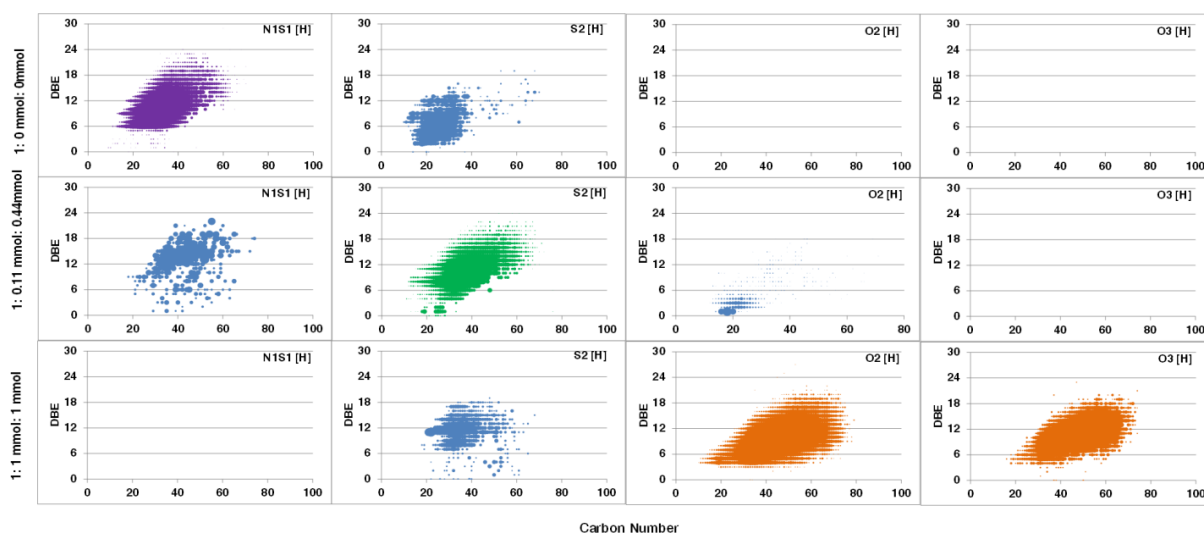


Figure A3.2: Comparison of Kendrick plots of the N₁S₁, S₂, O₂ and O₃ classes obtained from B1 (top), B2 (middle) and B4 (bottom) samples using ESI (+)FT-ICR MS.

Figure A3.2 clearly illustrates the different discrimination of the different classes in each reaction sample with N₁S₁, S₂, O₂ and O₃ are classes being present in B1, B2 and B4 samples based on positive ion ESI. The results here are consistent with those in Figure 3.3. B1 favors nitrogen-containing species and accesses a wider range of DBE and carbon number distribution of N₁S₁ class coded in purple comparing to other case. B2 emphasizes sulfur-containing species marked in green comparing other case. As the mole ratio of AgBF₄: C₂H₅I: Bitumen increasing, more oxygen-containing species are detectable, such as O₂ especially O₃ classes colored in orange with a broader regional distribution of DBE vs. carbon number.

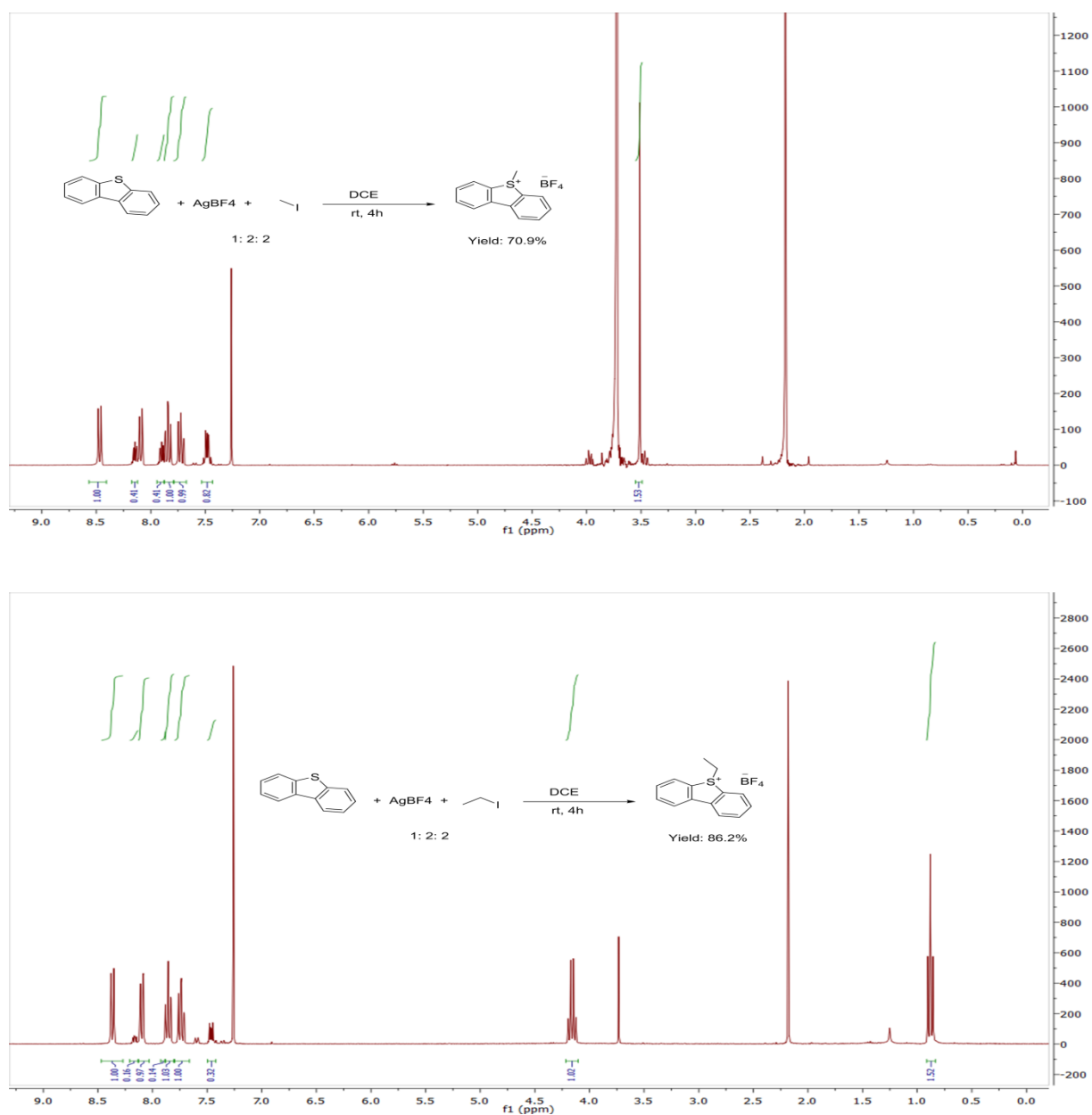


Figure A3.3: Comparison of ¹H NMR spectra from methylation and ethylation of dibenzothiophene (DBT) under the same reaction condition (the mole ratio of DBT: AgBF₄: C₂H₅I (or CH₃I) as 1: 2: 2).

Ethylation yield of DBT is higher than methylation yield, similar results also is observed by Acheson et al. [101], so ethylation replaces methylation for the study.

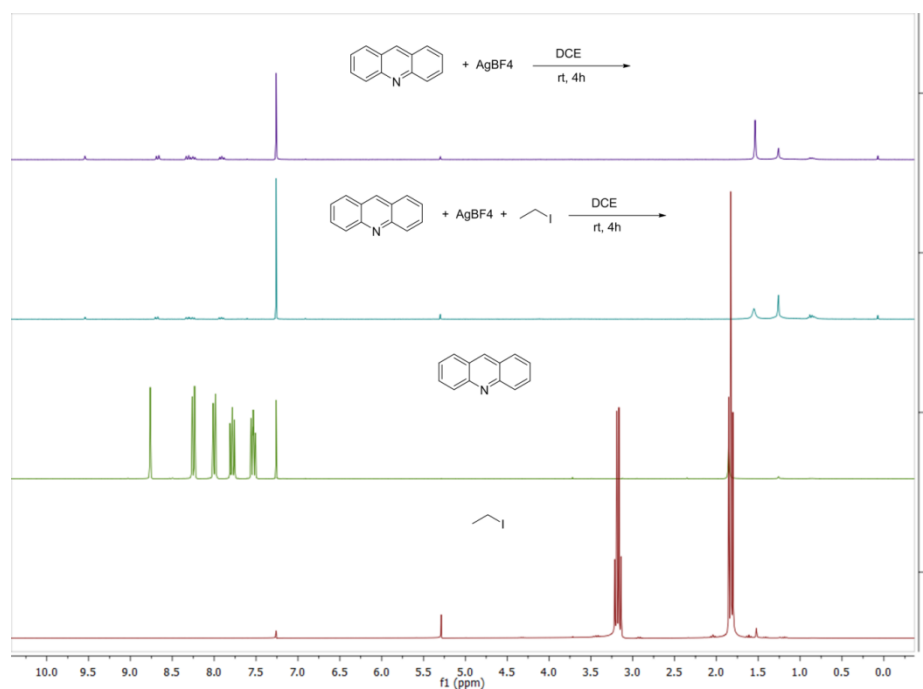


Figure A3.4: A comparison of ^1H NMR spectra of Acridine under different reaction conditions. The significant complex effect between Ag^+ and basic nitrogen can be illustrated by the ^1H NMR spectra of Acridine under different reaction conditions. In the presence of Ag^+ , larger insoluble complex in DCE are generated and exit from the reaction solution.

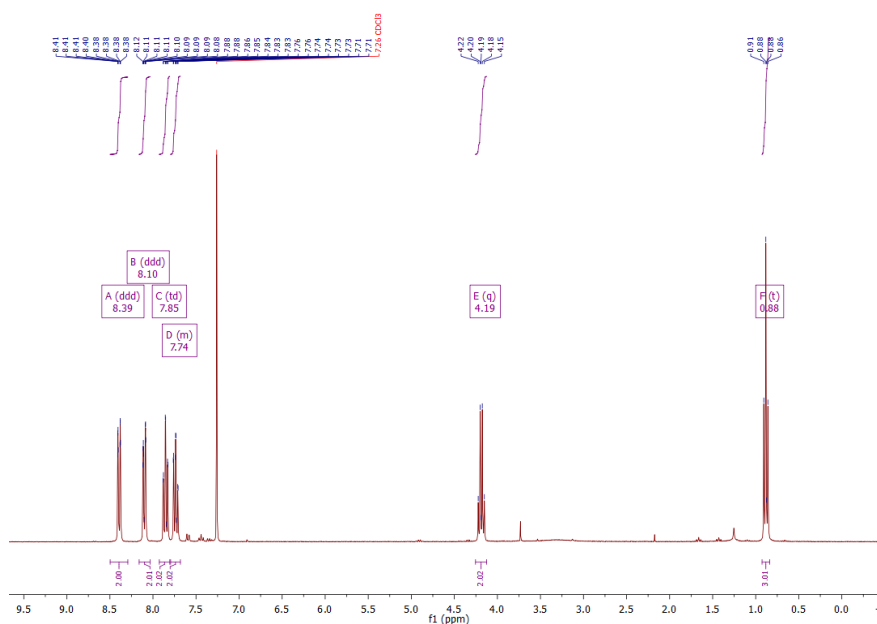


Figure A3.5: ^1H NMR data of 5-ethyldibenzo[*b,d*]thiophenium tetrafluoroborate. **5-ethyldibenzo[*b,d*]thiophenium tetrafluoroborate (colourless needles, 99%).** ^1H NMR (300 MHz, CDCl_3): δ 8.39 (ddd, $J = 8.0, 1.1, 0.6$ Hz, 2H, $2 \times Ph$), 8.10 (ddd, $J = 7.8, 1.3, 0.6$

Hz, 2H, 2 × *Ph*), 7.85 (td, $J = 7.7, 1.1$ Hz, 2H, 2 × *Ph*), 7.79 – 7.68 (m, 2H, 2 × *Ph*), 4.19 (q, $J = 7.1$ Hz, 2H, 2 × CH_2CH_3), 0.88 (t, $J = 7.1$ Hz, 3H, 3 × CH_2CH_3).

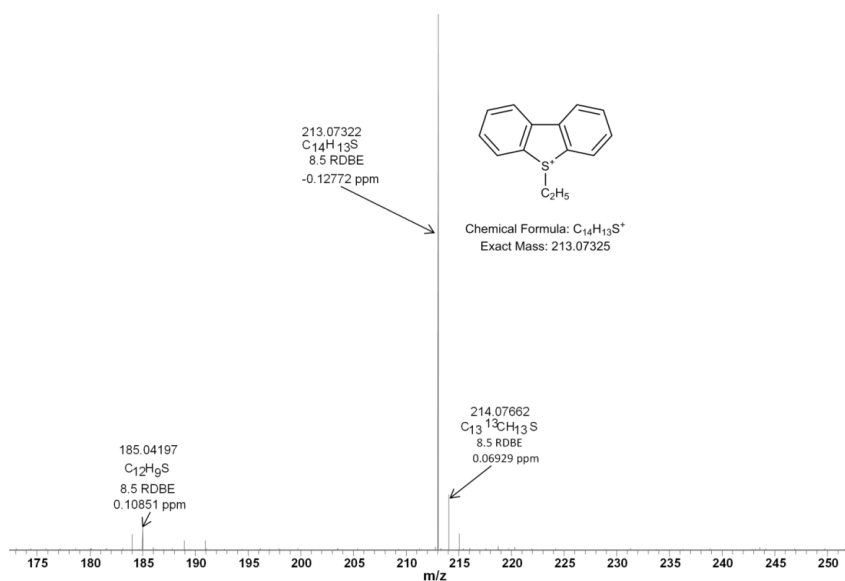


Figure A3.6: HRMS (ESI FT-ICR MS) data of 5-ethyldibenzo[*b*, *d*]thiophenium tetrafluoroborate. Found: m/z 213.07322. Calcd for $\text{C}_{14}\text{H}_{13}\text{S}^+$: m/z 213.07325.

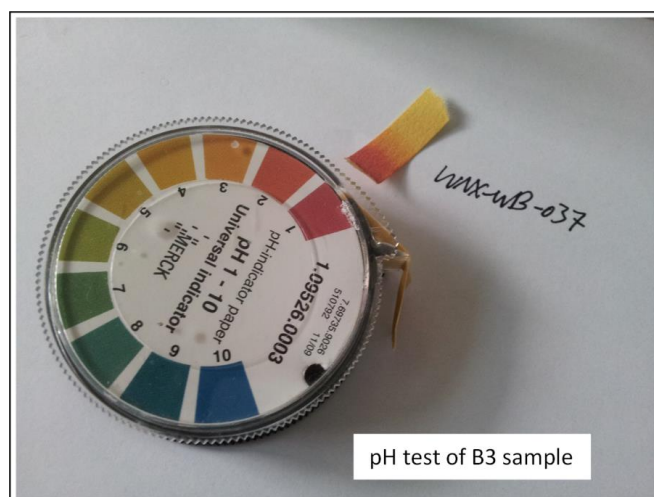


Figure A3.7: The pH test of B4 sample. B4 is diluted by 2 mL of anhydrous 1,2-DCE after reaction before pH test. HBF_4 ($\text{HF} + \text{BF}_3$) system is actually a superacid system, which was observed in the pH test. Also a white fume in moist air was observed when opening the reaction bottle cap.

Chapter 4 Experimental and Theoretical Evaluation of Electrochemically-induced Electron Transfer Reaction in Electrospray Mass Spectrometry*

**Redrafted from “Wang, X.; Wu, X.; Thiel, W.; Schrader, W., Electrochemically-induced Electron Transfer Reaction of Thiophene-Type Compounds with Ethyl Triflate in Electrospray Mass Spectrometry, will be submitted to Angew Chem Int Edit.”*

4.1 Abstracts

It is described that electrospray capillary can serve as a controlled current electrolytic cell. Ethyl trifluoromethanesulfonate is being electrochemically activated in solution phase to form an active intermediate that enables secondary reactions with thiophenic sulfur compounds in gas phase. Electrons from thiophenic sulfur compounds play triple roles including nucleophile, base and reductant. Water molecule in air is assumed to participate the production of protonated peak. The corresponding peaks are observed in ultrahigh resolution mass spectrometry (HRMS). A combination of mass spectrometric experiments and quantum chemical calculations unravels the mechanistic details of electrochemical process in positive electrospray.

4.2 Introduction

Electrospray Mass Spectrometry (ESI-MS) has been shown to be an excellent ionization method for a large number of different analytical and chemical problems. Especially in life science applications ranging from proteomics and metabolomics applications further to energy related problems.[8, 74, 119] This method is helpful in studying mechanisms of catalytic reactions as it is a sensitive and soft ionization method that allows studying reactive intermediates in low concentrations with structural information when using MS/MS methods.[120-129]

Nonetheless, ESI-MS also has been reported to suffer from side reactions that can occur during the ionization process.[61] The operation condition of producing highly charged droplets and desolvating them with heated gas flow in the neighborhood of heated metallic surfaces can cause unknown reactivities towards the analytes.[130] Although, ESI is known to ionize “only” polar compounds,[60] it also has been shown to be able to produce radical cations of non-polar hydrocarbons of high aromaticity.[43, 85] Here, the dualism of electrospray plays a role where the nebulizer which is set to a high voltage potential acts as an electrochemical cell.[43, 75]

4.3 Experimental section

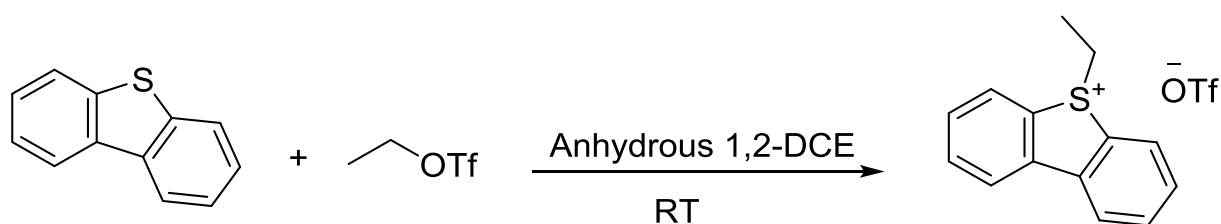
For experimental details, please see Appendix 4.

4.4 Results and Discussion

We have studied derivatization reactions in combination with ultrahigh resolution ESI-MS to understand reactivities of thiophenic sulfur compounds that are present in crude oil.[8, 40] Those compounds are not polar enough to be analyzed by ESI-MS alone. A derivatization reaction such as the methylation of

aromatic sulfur compounds with iodomethane in the presence of silver tetrafluoroborate forms sulfonium salts that are easily analyzed by ESI-MS.[40] Utilizing different reaction conditions allows to even change the class distribution and use a chemical reaction as a tool for the selective analysis of polyaromatic heterocycles in complex mixtures

A reaction of dibenzo[*b,d*]thiophene with ethyl trifluoromethanesulfonate shown in Scheme 4.1 was studied to see if this would be a reaction that can selectively tag thiophenic sulfur compounds and be used as a tool for selective analysis of crude oil. Unfortunately, when studying the reaction in glassware (named as “off-ESI” reaction, the reaction in electrospray ion source named as “in-ESI”), ¹H-NMR spectra of the reaction came up negative (see entry 2 in Table A4.1; Figures A4.3 – A4.4 in the Appendix 4). This reaction is not happening in “off-ESI” fashion.



Scheme 4.1: Reaction of dibenzo[*b,d*]thiophene (DBT) and ethyl trifluoromethanesulfonate (C₂H₅OTf) in anhydrous 1,2-dichloroethane (1,2-DCE) at room temperature.

Theoretical calculation[131-135] for this “off-ESI” reaction then confirmed that this is a thermodynamically and kinetically unfavorable reaction ($\Delta_r G^\circ = 9.19$ and $\Delta_a G^\circ = 29.35$), suggesting that it does not occur in a spontaneous manner at room temperature (see Figures A4.9 – A4.10; entry 2 in Table A4.2 in the Appendix 4). Other thiophenic sulfur compounds, Benzothiophene (BT), benzonaphthothiophene (BNT), and 4,6-dimethyldibenzothiophene (4,6-DMDBT) are also investigated in this study by ¹H NMR analysis and theoretical

calculation, and none of them may occur in “off-ESI” fashion (see Figures A4.1 – A4.2 and A4.5 – A4.9; Tables A4.1 – A4.2 in the Appendix 4).

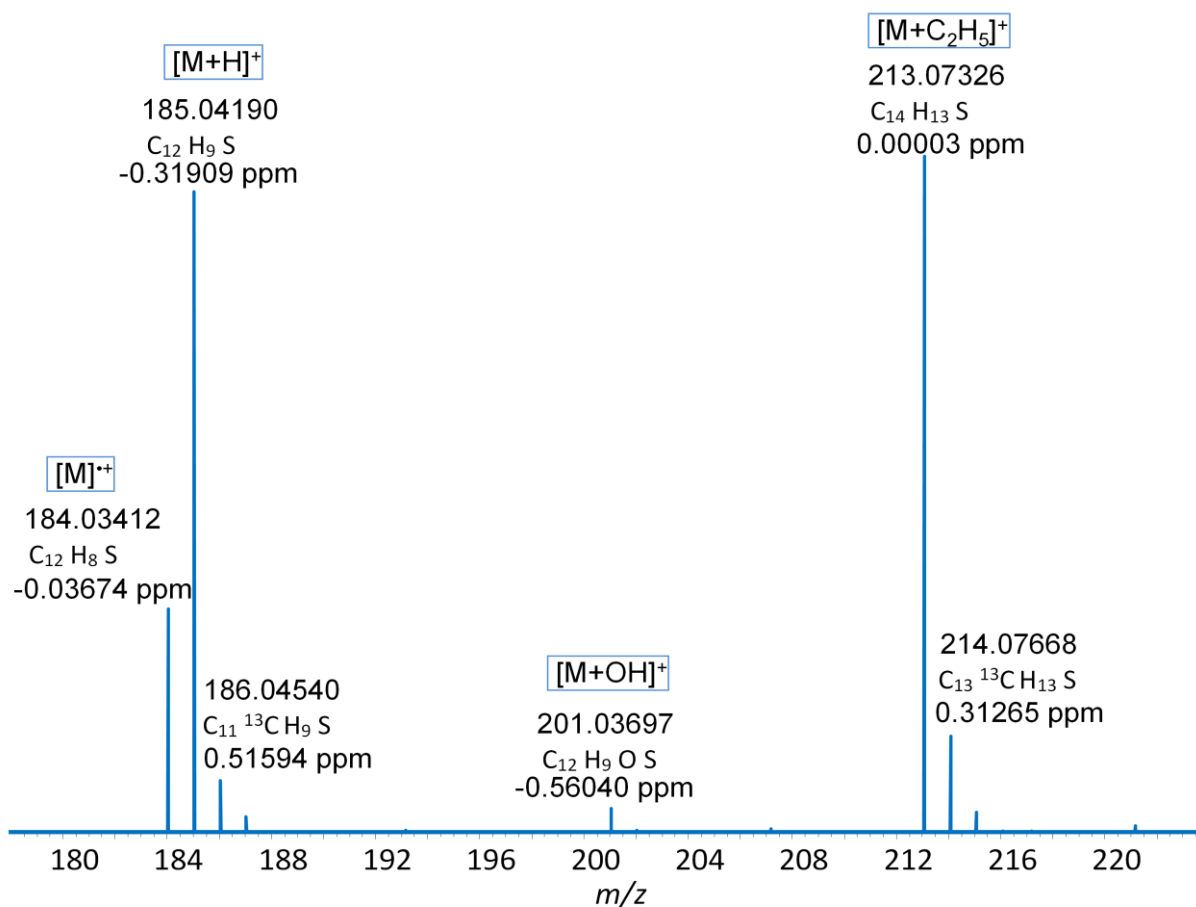


Figure 4.1: Electrospray(+) mass spectrum of the reaction mixture of DBT and C₂H₅OTf in anhydrous 1,2-DCE on 7 T FT-ICR MS using standard ESI spray capillary set-up as shown in Figure 4.3b. M represents DBT.

When studying the reaction by ESI-MS though, things became more interesting. Here, an alkylation of DBT with an ethyl group from the C₂H₅OTf can be observed at *m/z* 213.07326 as shown in Figure 4.1. Besides the ethylated signal to DBT [M+C₂H₅]⁺, the radical cation to DBT [M]^{•+} at *m/z* 184.03412, protonated signal to DBT [M+H]⁺ at *m/z* 185.04190 and a tiny hydroxylated signal to DBT [M+OH]⁺ at *m/z* 201.03697 could also be observed. We have to ask: how can the results from two different analytical methods (¹H NMR and ESI-MS) be so different and how can such a difference occur?

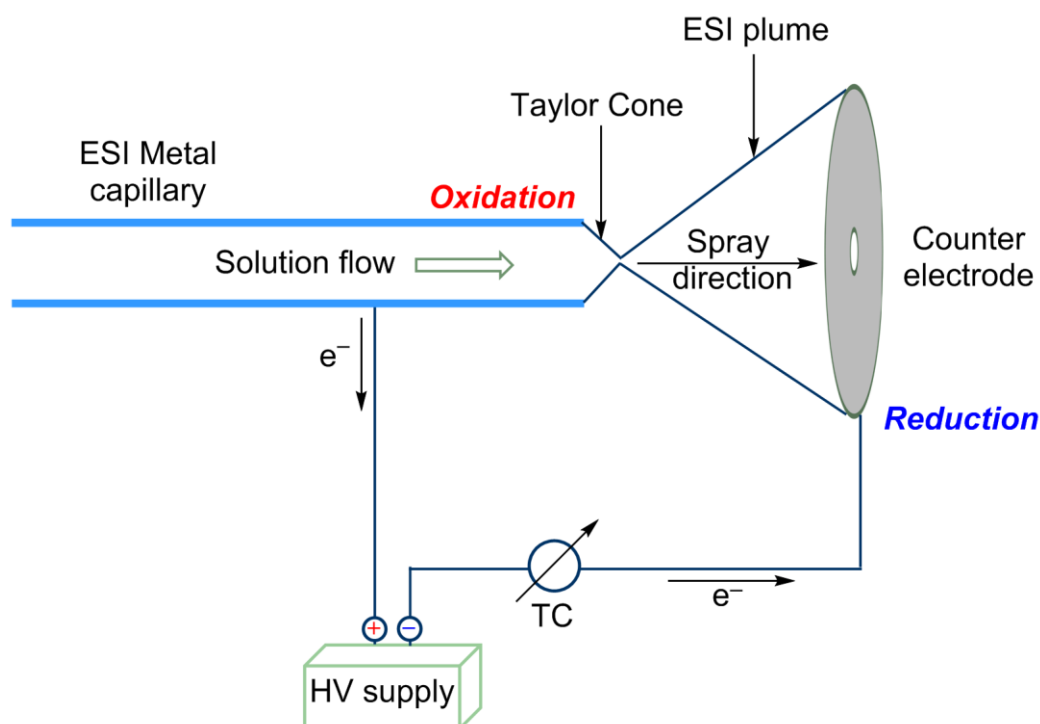


Figure 4.2: Sketch of electro spray ionization system at the positive ion mode. ESI metal capillary is connected to a High Voltage (HV) supply. The electrons are produced via the oxidation inside the ESI metal capillary. A circuit that consists of the ESI spray capillary, the HV supply and the counter electrode is established when electrons move to the counter electrode through the metal wire continuously. TC represents the total current in the circuit.

The NMR results are obtained from the reaction solution in the same manner as the reaction is carried out, so here no interference to the reaction is done. The ESI-MS results are obtained from spraying the reaction solution into the mass spectrometer. Although, ESI-MS is known that some modifications can occur they are mostly involving cluster formation and gas-phase chemistry.[61, 64, 81] Here, a chemical reaction was activated during the spray and ionization process that is not active in solution alone. In ESI there are two different areas where reactions can occur as shown in Figure 4.2. One is the spray capillary where the metallic spray capillary can act as electrolysis cell, and the other is in the gas phase where gas phase chemistry near the counter electrode can play a major role during the ionization process. The reactivity on polyaromatic heterocycles suggested an electrochemical activation of the reaction which we therefore

investigated in detail using four different thiophenic sulfur compounds, BT, DBT, BNT, and 4,6-DMDBT (for details see Figures A4.35 – A4.38 in the Appendix 4). Here, results from DBT are being shown.

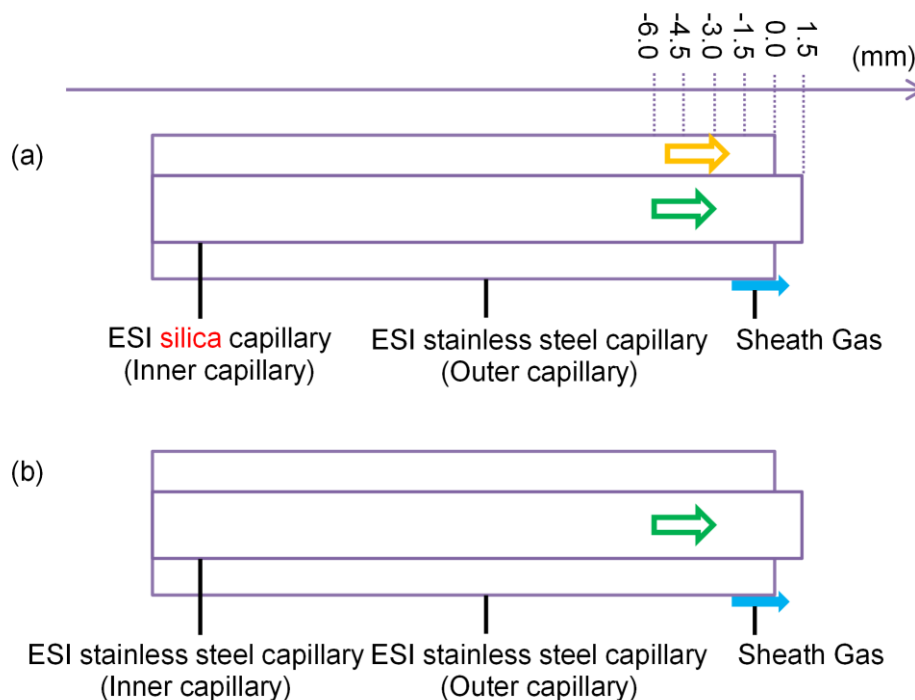


Figure 4.3: (a) Fused silica electro spray capillary setup. In a 1-D space, the origin is defined at the edge of the outer capillary with the positive direction pointing to the right. The fused silica capillary position relative to the outer capillary can be understood as a location in the 1-D space. Green arrow represents that the solution flow is injected through the inner fused silica capillary. Yellow arrow represents that the solution flow is injected through the outer metallic capillary. The inner solution flow is isolated by the fused silica capillary from the outer solution flow. (b) Standard electro spray capillary setup. The solution is usually injected only through the inner metallic capillary.

If the ESI spray capillary acts as an electrode the reaction should be suppressed when using an isolating fused silica capillary. Therefore, a set-up was implemented that uses a dual layer spray assembly with a fused silica spray capillary inside of a metallic capillary as shown in Figure 4.3a (for details see Figure A4.11 in the Appendix 4). The inner fused silica capillary was positioned

at different positions in relation to the outer metallic capillary and therefore allowing different time intervals of interaction between the reaction solution and the metal electrode. The results of this set-up show that the reaction is also inactive when the fused silica capillary is placed 1.5 mm outside of the metallic capillary. Here, the reaction solution has no contact with the metallic capillary and the reaction is not activated. Moving the inner fused silica capillary further inside leads to an increase of the intensity of the reaction products due to the fact that with more metallic surface available and therefore longer reaction times the reaction could be initiated. Figure 4.4 shows the difference of the major signals detected for the most important ions at different fused silica capillary position relative to the outer metallic capillary. The corresponding ESI-MS experiments are summarized in Table A4.3 in the Appendix 4, the corresponding mass spectra are documented in Figures A4.13 – A4.17 in the Appendix 4, and a comparison of these obtained mass spectra is depicted in Figure A4.18 in the Appendix 4.

Increasing the spray voltage, the intensity of the major signals of $[M+C_2H_5]^+$, $[M+H]^+$ and $[M]^{2+}$ also increases (For details see the Appendix 4 Figure A4.19). These results clearly show that the reaction is an “in-ESI” reaction and occurring with assistance of the electrospray sprayer which is acting as an electrolytic cell to initiate the reaction. Now, the question remains what is the mechanism of the reaction. There are two different possibilities, with one that the DBT is being activated electrochemically and second, the C_2H_5OTf is being activated.[136] This has been investigated in details both devising different ESI-MS experiments (summarized in Table A4.4 in the Appendix 4) as well as using theoretical calculations to understand the chemistry about it.

A fused silica ESI capillary setup with capillary locating 1.5 mm outside of the metallic capillary is taken for the mechanism investigation as shown in Figure 4.3a. When the C_2H_5OTf in DCE solution is injected through the inner silica capillary as green arrow shows, as expected, no derived peaks from

C_2H_5OTf and DCE are observed due to no contact with the metallic capillary. Injecting the C_2H_5OTf solution through the outer metallic capillary as yellow arrow represents, similar results are obtained as it is injected through the inner silica capillary, but the reason could be different. This might be because that the radical cations of C_2H_5OTf and DCE are short-lived species and can't be detected on the time scale of FT-ICR MS; or the active open-shell radical cation species have reacted with other nucleophilic species and vanished before MS detection. The corresponding mass spectra for these two ESI-MS experiments are shown in Figure A4.21 – A4.22 in the Appendix 4.

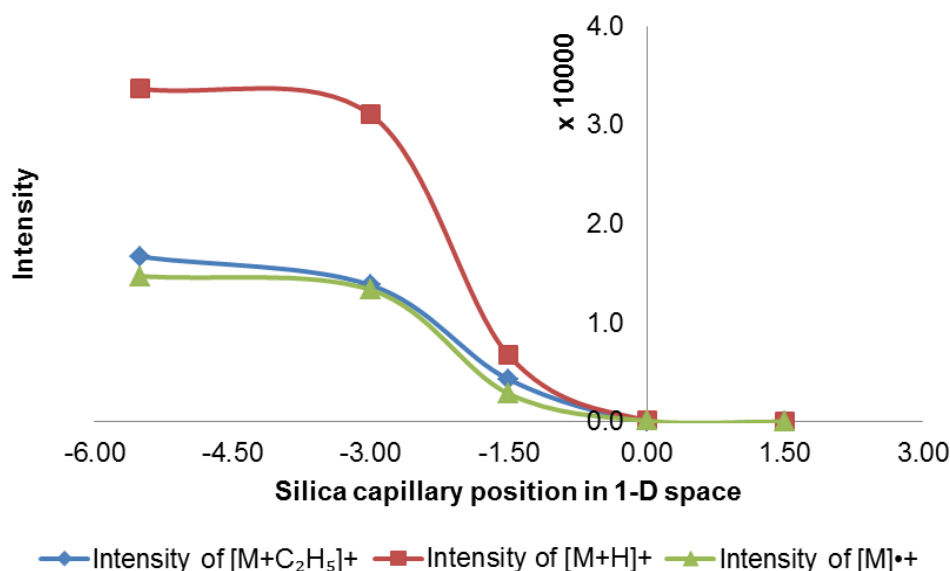


Figure 4.4: Evaluation of the influence of electrochemistry on the intensity of characteristic peaks of $[M+C_2H_5]^+$, $[M+H]^+$ and $[M]^{\bullet+}$ through silica position in 1-D space.

When the DBT in DCE solution is injected through the inner silica capillary as green arrow shows, as expected, no derived peaks from DBT and DCE are observed due to no contact with the metal capillary. Injecting the DBT solution through the outer metallic capillary as yellow arrow represents, $[M]^{\bullet+}$ derived from DBT is observed at m/z 184.03412 due to contact with the metal material that is connecting to a high voltage supply as shown in Figure 4.2. This might be

because the radical cation to DBT $[M]^{•+}$ is stable enough and can be detected on the time scale of FT-ICR MS (For details see Figures A4.23 – A4.24 in the Appendix 4).

When the DBT in DCE solution is injected through the inner fused silica capillary and meanwhile the solvent DCE is injected through the outer metallic capillary as yellow arrow shows, no characteristic peaks from DBT are observed (See Figure A4.25 in the Appendix 4). Nevertheless, interesting things appear when the DBT in DCE solution is injected through the inner silica capillary and meanwhile the C_2H_5OTf in DCE solution is injected through the metallic capillary. The characteristic peaks derived from DBT, $[M+C_2H_5]^+$, $[M+H]^+$ and $[M]^{•+}$, are observed in this case (See Figure A4.26 in the Appendix 4). Repeating this experiment by positioning the silica capillary to 0.0 mm relative to the outer metallic capillary, similar results are obtained with the increasing intensity of $[M+C_2H_5]^+$, $[M+H]^+$ and $[M]^{•+}$ of DBT (See Figure A4.27 in the Appendix 4). The intensity trend of $[M+C_2H_5]^+$, $[M+H]^+$ and $[M]^{•+}$ of DBT from these two ESI-MS experiments (Figures A4.26 – A4.27) has been depicted in Figure A4.28 in the Appendix 4. This clearly shows that the activation of C_2H_5OTf is the key to initiate a series of reactions including ethylation, protonation, charge-transfer reaction, etc.

Based on the above ESI-MS experiments, a possible mechanism is proposed as follows: C_2H_5OTf is first oxidized in solution by loss of one electron to the anode to produce its corresponding radical cation with a low-lying LUMO; DBT then reacts with $[C_2H_5OTf]^{•+}$ to produce the corresponding $[M+C_2H_5]^+$ via nucleophilic substitution and $[M]^{•+}$ via charge-transfer reaction in gas phase.

Theoretical calculations have been done at the PBE0-GD3/6-311+G(d,p) level for the proposed mechanism, and have been represented in Figure 4.5. Here, it is worth noting that the radical cation of C_2H_5OTf as shaded in purple in Figure 4.5 is a local minimum point on the potential energy profile indicating that it is a chemical intermediate, even though it has not been observed under

ESI-MS experiments. The changes in standard Gibbs free energy $\Delta_r G^\circ$ are negative for the nucleophilic substitution and charge-transfer reaction between $[\text{C}_2\text{H}_5\text{OTf}]^{*+}$ and DBT, which indicates that the two reactions are highly exergonic and occur spontaneously. Theoretical calculations about the mechanism study are documented in Figures A4.30 – A4.32; Table A4.5 in the Appendix 4.

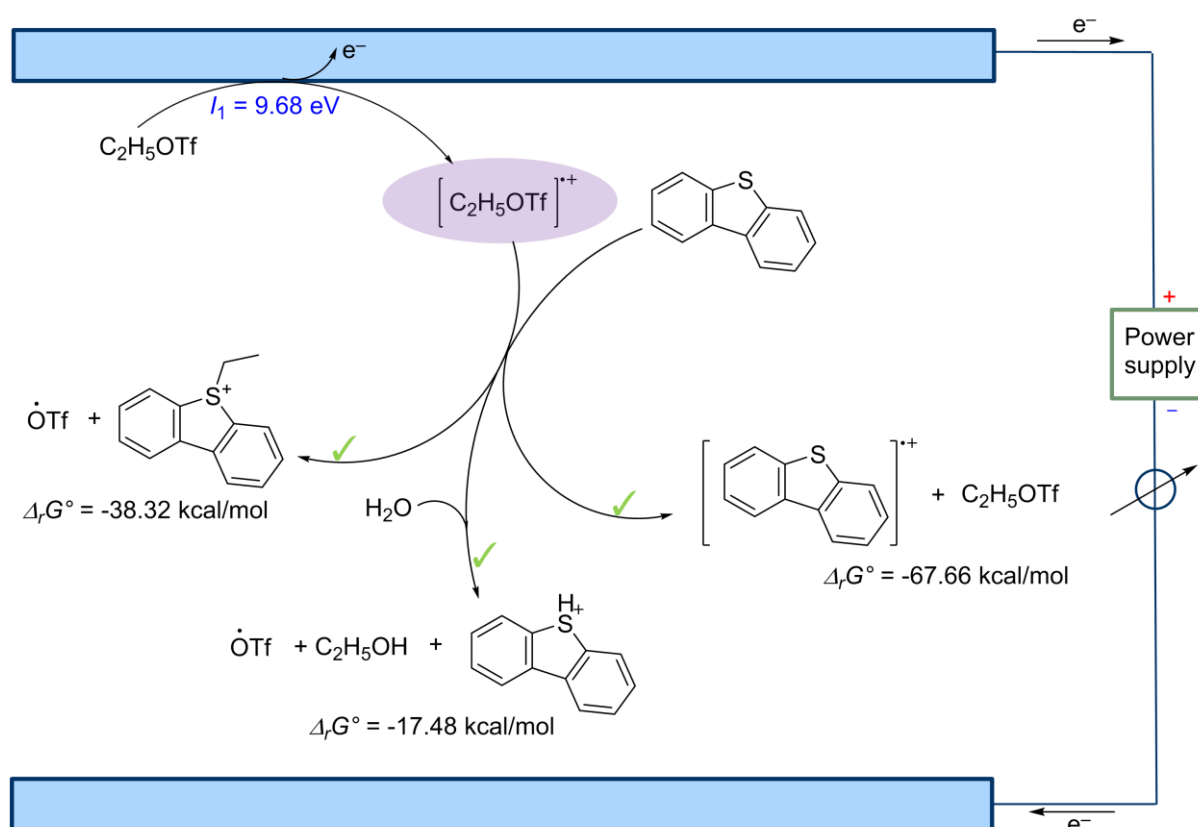


Figure 4.5: Proposed mechanism.

ESI is an atmospheric pressure ionization method, and gas-phase reaction occurs in the sampling regions of the mass spectrometer (near the counter electrode).[61] H_2O in the air is thus hypothesized to be involved in the production of the protonated peak to DBT $[\text{M}+\text{H}]^+$ via $[\text{C}_2\text{H}_5\text{OTf}]^{*+}$ in the gas phase. An evidence for this hypotheses is the observation of the hydroxylated signal to DBT $[\text{M}+\text{OH}]^+$ at m/z 201.03697. In order to validate our hypotheses, a

series of ESI-MS experiments are carried out using the standard ESI capillary set-up as shown in Figure 4.3b by changing the sweep gas flow rate. As the sweep gas flow rate increases, the relative abundance of $[M+H]^+$ and $[M+OH]^+$ decreases, while the relative abundance of $[M]^{++}$ increases. Figure 4.6 shows the comparison of mass spectra obtained from ESI-MS experiments with different sweep gas flow rates. The relative abundance trend of the $[M]^{++}$, $[M+H]^+$ and $[M+OH]^+$ versus the sweep gas flow rate is documented in Figure A4.29 in the Appendix 4.

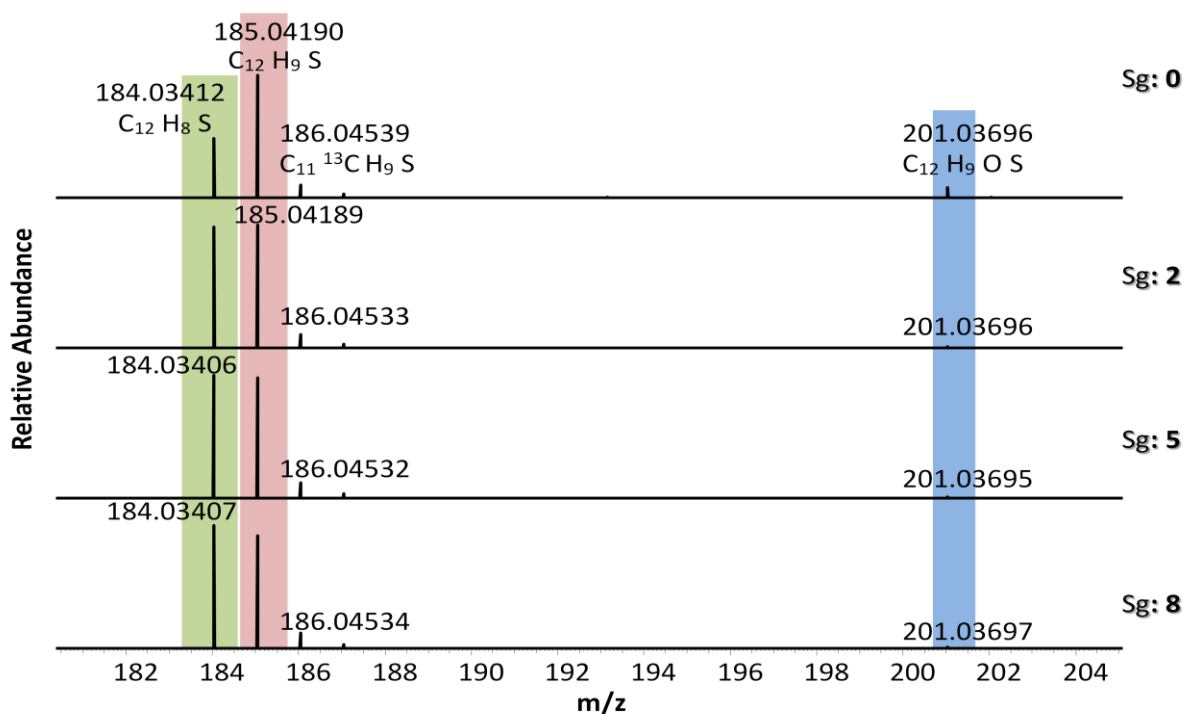


Figure 4.6: Comparison of mass spectra obtained from the ESI-MS experiments with different sweep gas flow rates. Sg represents sweep gas. As the sweep gas flow rate increases, the relative abundance of $[M]^{++}$ to DBT increases, but the relative abundance of $[M+OH]^+$ and $[M+H]^+$ decreases.

Due to the complicated hydrogen bondings, it can be very difficult to determine the true conformation of water molecule(s) [137, 138]. We propose a single water molecule is involved to produce the $[M+H]^+$ peak to DBT, e.g.

H₂O, as a prototype and the change of the standard Gibbs free energy in Figure 4.5 is predicted to be -17.48 kcal/mol (for details see Figure A4.33 in the Appendix 4). Therefore, the detected [M+H]⁺ in the ESI-MS experiment might be produced via the channel with water molecules involved.

The other possible pathway with DBT activated first has also been theoretically evaluated at the same level of theory. The first ionization energies for both DBT and C₂H₅OTf in DCE are respectively 6.27 eV and 9.68 eV, and it might seem "reasonable" if DBT is first being activated. However, further calculation for the channel where collision occurs between DBT radical cation and C₂H₅OTf give positive $\Delta_r G^\circ$ values (see ch-2 Figure A4.31; Table A4.5 in the Appendix 4) suggesting that this is highly endothermic (see Figure A4.34 in the Appendix 4). Hence, the pathway with DBT activated first is discarded.

DBT can of course be directly oxidized in solution by losing one electron to the anode to produce the DBT radical cation [M]^{•+} (see Figure A4.24 in the Appendix 4). However, C₂H₅OTf is 10 times concentrated than DBT in DCE suggesting that C₂H₅OTf has 10 times more chance to be transferred to the solution-metal surface than DBT does (see Figure A4.20 in the Appendix 4). What's more, the charge-transfer reaction between DBT and [C₂H₅OTf]^{•+} is highly exergonic with $\Delta_r G^\circ = -67.66$ kcal/mol as shown in Figure 4.5 suggesting that the charge-transfer channel should be a main channel for the generation of DBT radical cation.

4.5 Conclusion

In conclusion, a kind of reaction between the thiophenic sulfur compounds and ethyl trifluoromethanesulfonate has been investigated. This reaction is triggered by the inherent electrochemistry of electrospray ion source under positive mode in solution phase, followed by a series of electron transfer reactions in gas phase to produce the mass spectra observed. ESI-MS

experiments using silica ESI capillary setup as well as theoretical calculations suggest that the activation of ethyl trifluoromethanesulfonate is the key, and H₂O is assumed to participate in the formation of the protonated molecules. Herein, ESI-MS serves as not only an analytical tool, but also an electrolytic cell where interesting reactions might occur. Further extensions for the use of ESI-MS from the aspect of electrochemistry are currently underway in our laboratories.

Acknowledgements

The authors gratefully acknowledge Royal Dutch Shell Amsterdam, The Netherlands, and Houston, TX, USA for the generously financial support.

Appendix 4

This section contains information about the experimental section and Appendix Figures and tables that mentioned in the main text.

NOTE: For better explanation and understanding in this study, “**Off-ESI**” reaction represents the reaction in glassware. “**In-ESI**” reaction represents the reaction in ESI ion source.

General considerations

Chemicals and Solvents. All chemicals and anhydrous dichloroethane (DCE) were purchased from Sigma-Aldrich Co. and used without further purification. Dichloromethane (DCM) was purchased from Sigma-Aldrich Co. and was dried before used. The sulfur-containing standards employed in this study including: benzo[b]thiophene (BT); dibenzo[b,d]thiophene (DBT); benzo[b]naphtho[2,1-d]thiophene (BNT); 4,6-dimethyldibenzo[b,d]thiophene (4, 6-DM DBT). All “off-ESI” reactions were carried out in dried glassware under argon protection with magnetic stirring.

Nuclear Magnetic Resonance Spectroscopy. Proton ^1H NMR spectra was performed and recorded on Bruker AV-300 NMR spectrometer using CDCl_3 as solvent. Chemical shifts were recorded as parts per million (δ , ppm) and were referenced through the solvent lock (^2H) signal with the residual solvent resonance as the internal standard (CHCl_3 : δ 7.26) for ^1H NMR. Data were reported as follows: chemical shift, multiplicity (s: singlet, br s: broad singlet, d: doublet, t: triplet, q: quartet, dd: doublet of doublets, dt: doublet of triplets, ddd:

doublet of doublets of doublets; m: multiplet), coupling constants (J in Hz) and integration. The number of proton (n) for a given resonance is indicated by nH .

UltraHigh Resolution Mass Spectrometry. Mass spectra were acquired using a 7 T linear quadrupole ion-trap (LTQ) Fourier Transform Ion Cyclotron Resonance Mass Spectrometer (FT-ICR MS, Thermo Fisher, Bremen, Germany) equipped with a Thermo Fisher electrospray ion source. ESI conditions were as follows: flow rate 3 $\mu\text{L}/\text{min}$; spray voltage, 3.5 kV; a sheath gas flow of 5 (arbitrary unit); an auxiliary gas flow of 2 (arbitrary unit); a sweep gas flow of 0 (arbitrary unit). The Instrument was calibrated with the Thermo Scientific Pierce LTQ Velos ESI positive ion calibration solution.

Computational Details. All gas-phase calculations were carried out by using the hybrid PBE0 functional[131] plus the Grimme-type D3 correction for dispersion interaction[132] and Pople's triple- ζ basis set with polarization and diffuse functions, i.e. PBE0-GD3/6-311+G(d,p). This computational protocol had been benchmarked and recommended for general chemical application.[133] The reactions in the 1, 2-dichloroethane solution (DCE) were studied by means of the self-consistent reaction field method of the integral equation formalism model.[134] All optimized structures of the energy minimum and transition state were confirmed by subsequent frequency analyses. Intrinsic reaction coordinate calculations, moreover, were also performed for the transition states, so that they can be validated further along the reaction coordinate and the starting geometries for searching the reactant and product complexes could be determined as well. The Gaussian 09 program was used for all calculations.[135]

General procedure for “off-ESI” reaction

To a stirred solution of DBT (10 mg, 0.05 mmol) in dichloroethane (1 mL), ethyl trifluoromethanesulfonate (65 μ L, 0.50 mmol) was added at room temperature, and the reaction solution was stirred at 25 RT for 24 hours. Solvent was removed under reduced pressure and the crude residue was ready for ^1H NMR without any purification. The same procedures employed for reactions that involve other sulfur-containing compounds.

General procedure for “in-ESI” reaction

Sample preparation: DBT, $\text{C}_2\text{H}_5\text{OTf}$ and TBA BF_4 were dissolved respectively in anhydrous DCE at a concentration of 2.43 mM (DBT), 22.36 mM ($\text{C}_2\text{H}_5\text{OTf}$) and 39.2 μM (TBA BF_4) for the ESI experiments. Here, TBA BF_4 was taken as a reference.

Where does it happen?

*¹H NMR spectroscopy for “off-ESI” reaction***Table A4.1:** Evaluation of sulfur-containing standards in the S_N2 reaction^a

entry	A	B	C	Yield, % ^b
1				0
2				0
3				0
4				0

^aA (0.05 mmol) and B (0.50 mmol) in DCE (1 mL) at 25°C. ^bDetermined by ¹H NMR analysis of the crude reaction mixture.

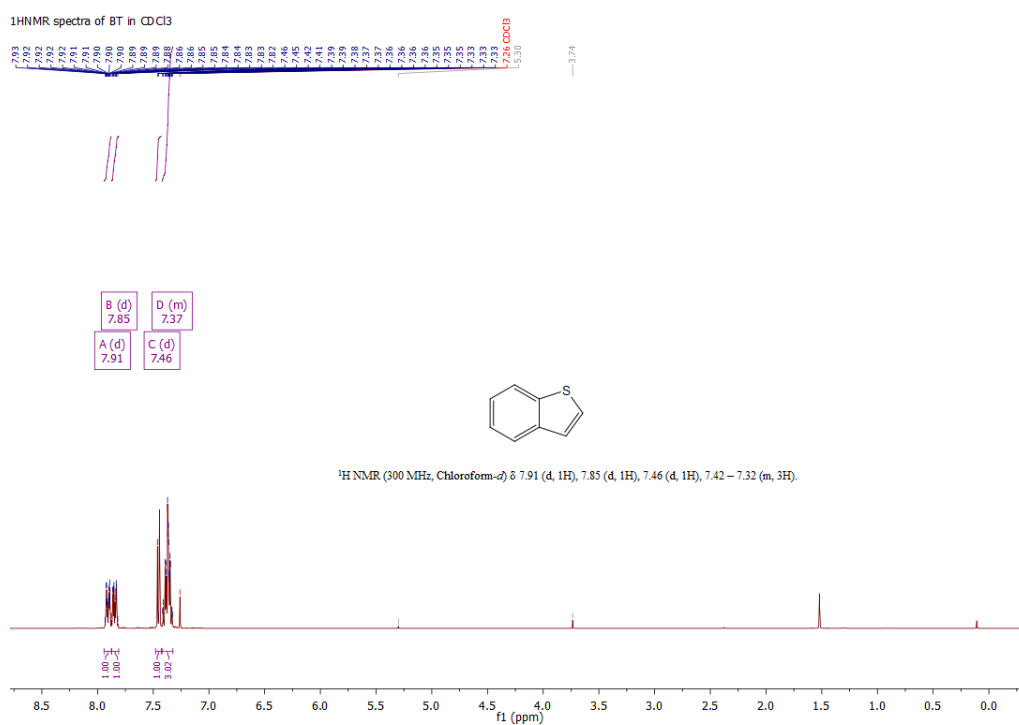


Figure A4.1: ¹H NMR spectra of BT in CDCl₃. [139]

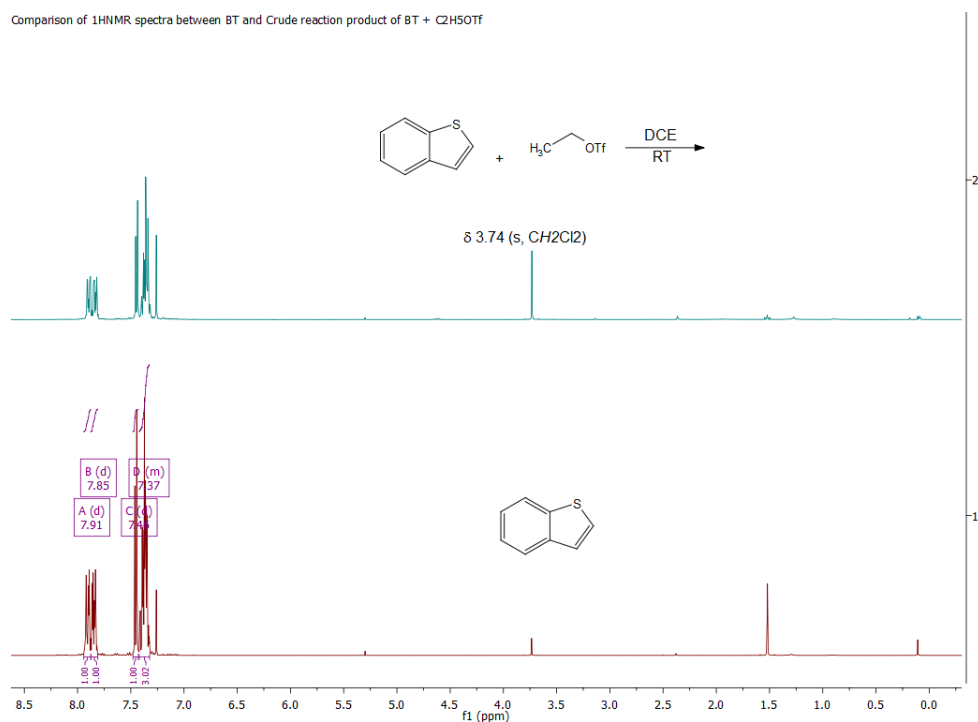


Figure A4.2: Comparison of ¹H NMR spectra obtained from BT standard and the crude reaction mixture of BT with C₂H₅OTf in 1 mL DCE at room temperature. From the comparison of ¹H NMR spectra above, we know that no reaction occurs between BT and C₂H₅OTf in DCE at 25 °C in glass flask.

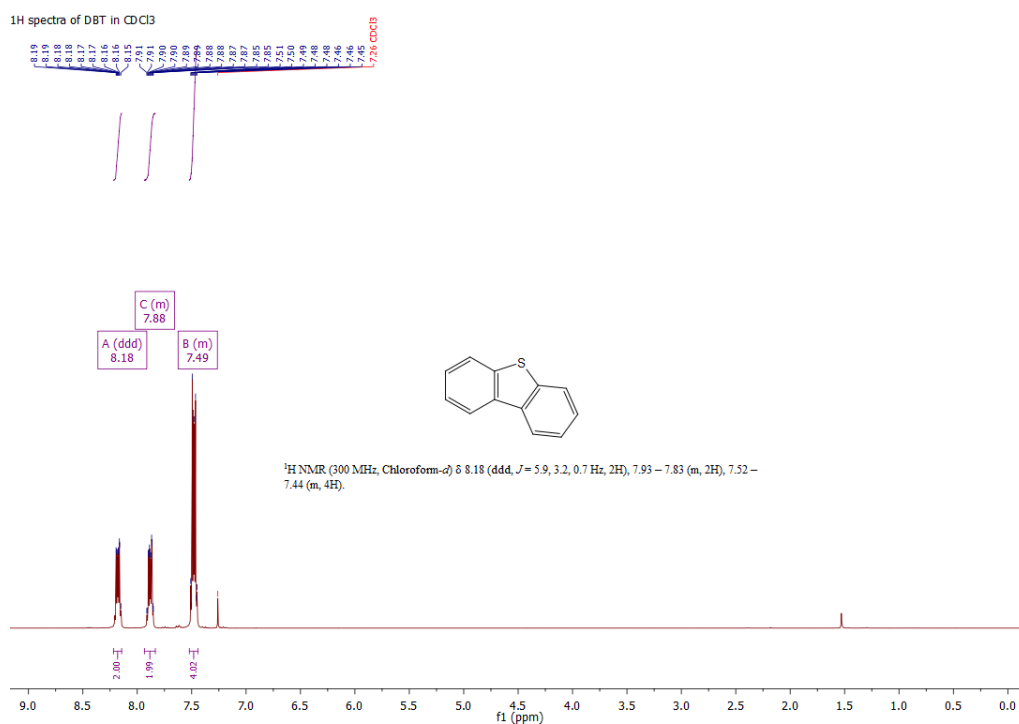


Figure A4.3: ¹H NMR spectra of DBT in CDCl₃. [140]

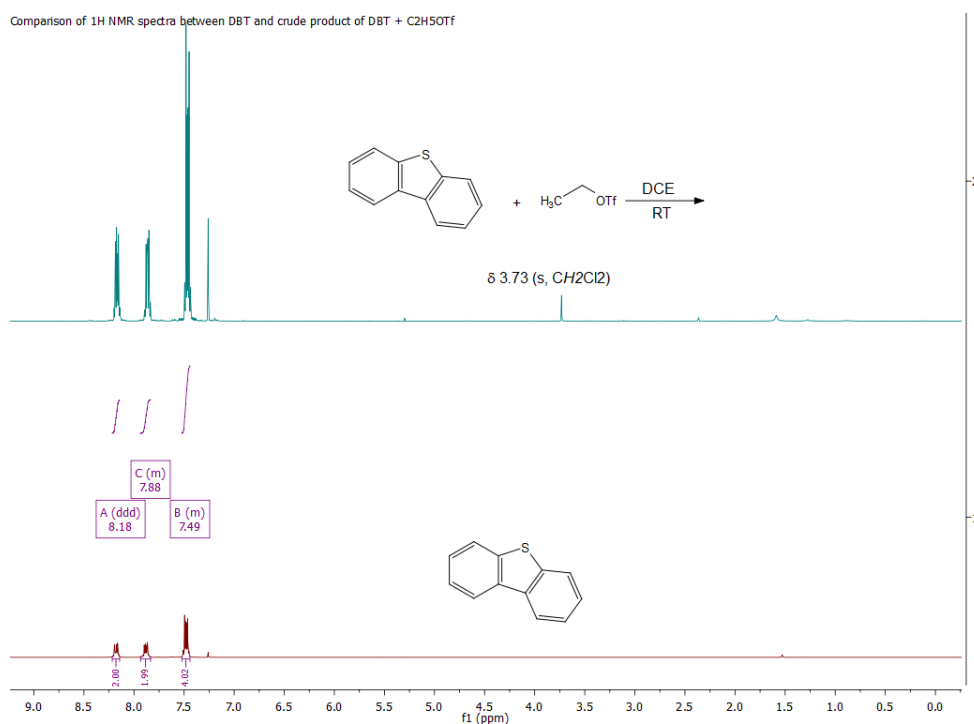


Figure A4.4: Comparison of ¹H NMR spectra obtained from DBT standard and the crude reaction mixture of DBT with C₂H₅OTf in 1 mL DCE at room temperature. From the comparison of ¹H NMR spectra above, we know that no reaction occurs between DBT and C₂H₅OTf in DCE at 25 °C in glass flask.

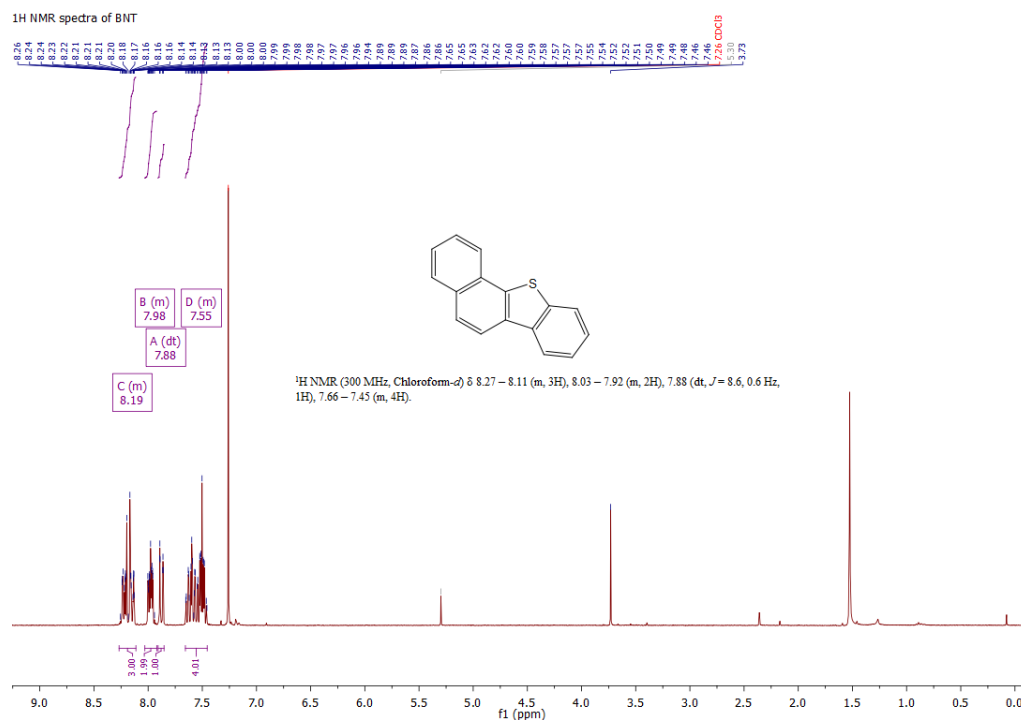


Figure A4.5: $^1\text{H NMR}$ spectra of BNT in CDCl_3 . [141]

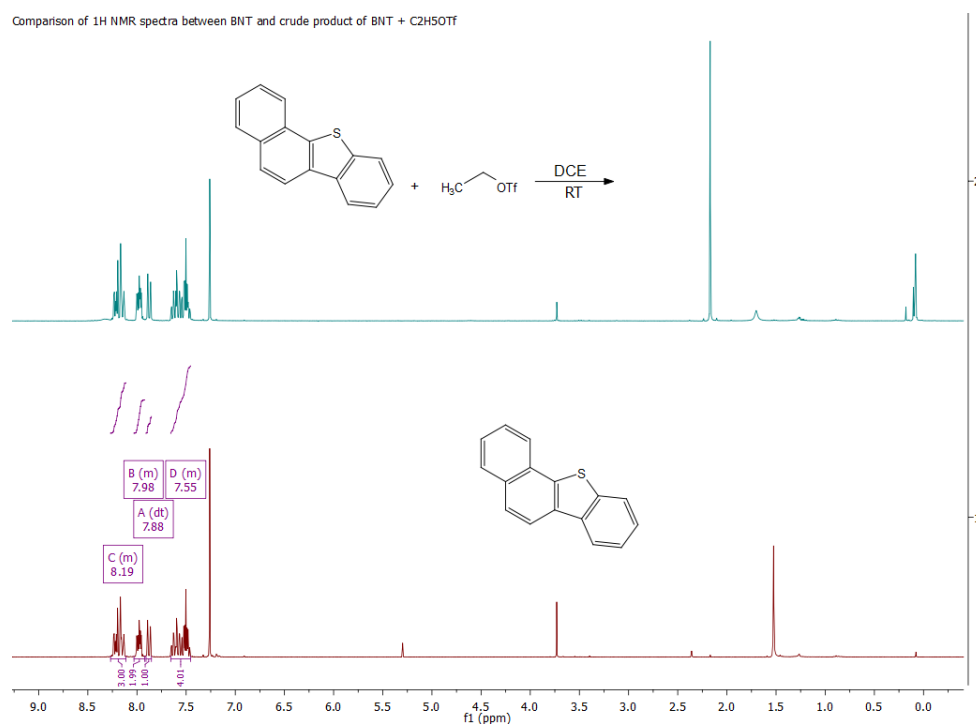


Figure A4.6: Comparison of $^1\text{H NMR}$ spectra obtained from BNT standard and the crude reaction mixture of BNT with $\text{C}_2\text{H}_5\text{OTf}$ in 1 mL DCE at room temperature. From the comparison of $^1\text{H NMR}$ spectra above, we know that no reaction occurs between BNT and $\text{C}_2\text{H}_5\text{OTf}$ in DCE at 25 °C in glass flask.

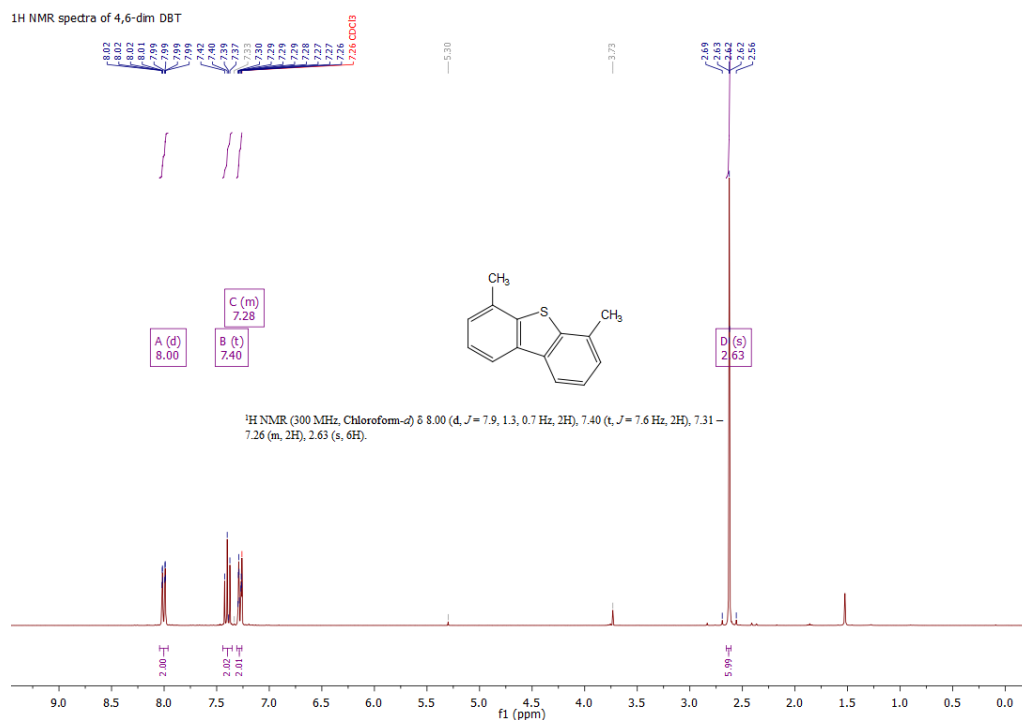


Figure A4.7: ¹H NMR spectra of 4, 6-dimethyl DBT in CDCl₃. [142]

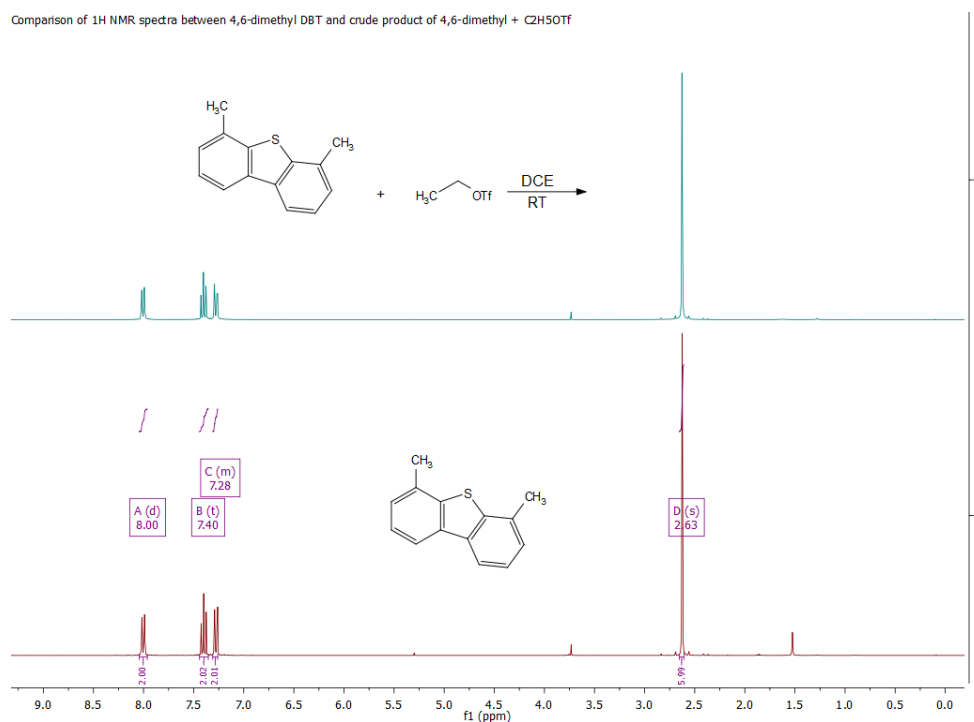


Figure A4.8: Comparison of ¹H NMR spectra obtained from 4, 6-dimethyl DBT standard and the crude reaction mixture of 4, 6-dimethyl DBT with C₂H₅OTf in 1 mL DCE at room temperature. From the comparison of ¹H NMR spectra above, we know that no reaction occurs between 4, 6-dimethyl DBT and C₂H₅OTf in DCE at 25 °C in glass flask.

Theoretical calculation for “off-ESI” reaction

The four solvent reactions in DCE at room temperature are depicted in Figure A4.9. The changes of the standard Gibbs free energy for reactions and activations are listed in Table A4.2. It is obvious that all reactions are endergonic, e.g. $\Delta_r G^\circ$ is positive, and the activation barriers are also rather high, e.g. $\Delta_a G^\circ > 28$ kcal/mol. The Gibbs free energy profile together with the relevant molecular structures for the second reaction is shown in Figure A4.9. Because $\Delta_r G^\circ$ for all steps but the last one are positive, it can be expected that none of them may occur in a spontaneous manner.

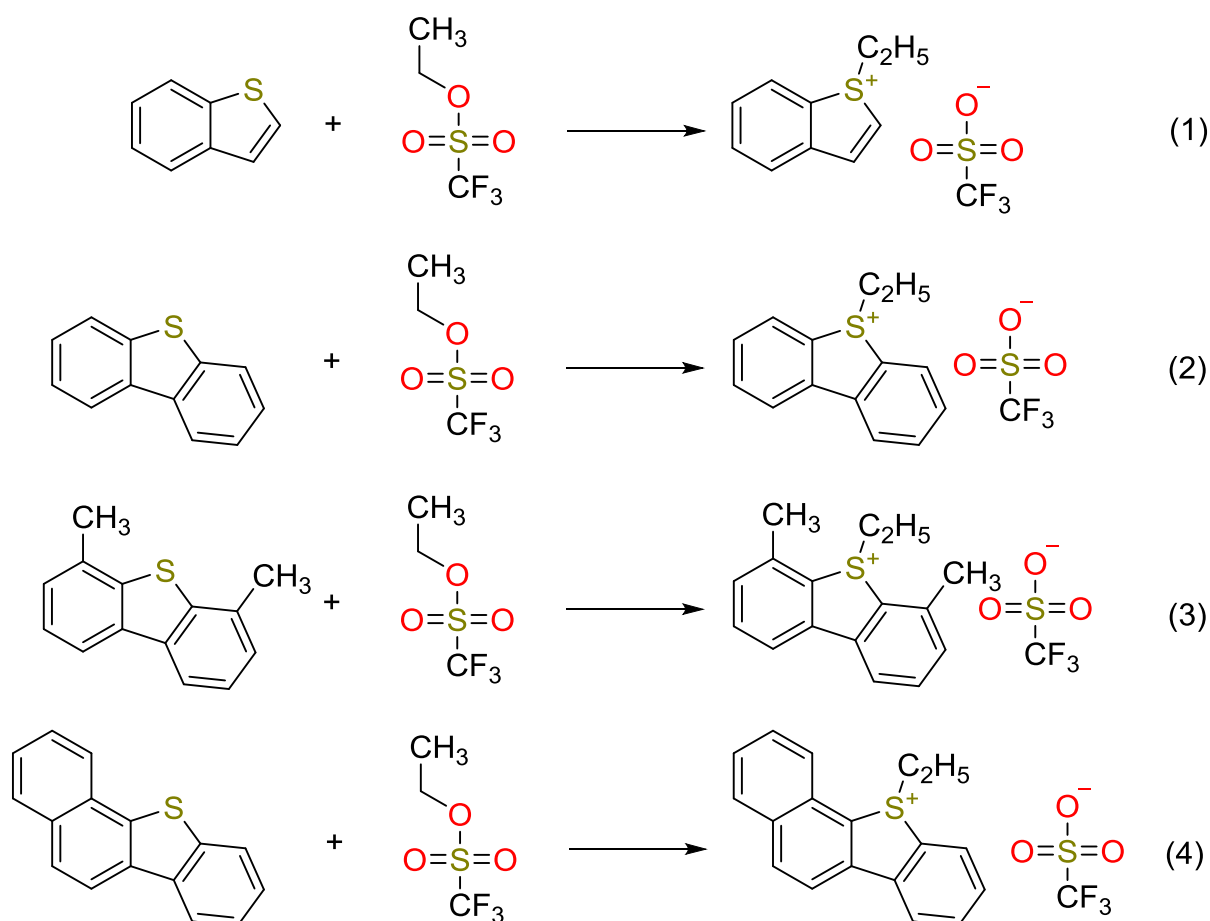


Figure A4.9: The reactions in 1,2-dichloroethane at 298.15 K.

Table A4.2: The changes of the standard Gibbs free energy (in kcal/mol) for the solution reactions ($\Delta_r G^\circ$) and activation ($\Delta_a G^\circ$) with respect to the separated reactants

reaction	$\Delta_r G^\circ$	$\Delta_a G^\circ$
(1)	12.73	31.38
(2)	9.19	29.35
(3)	10.07	28.39
(4)	11.14	29.68

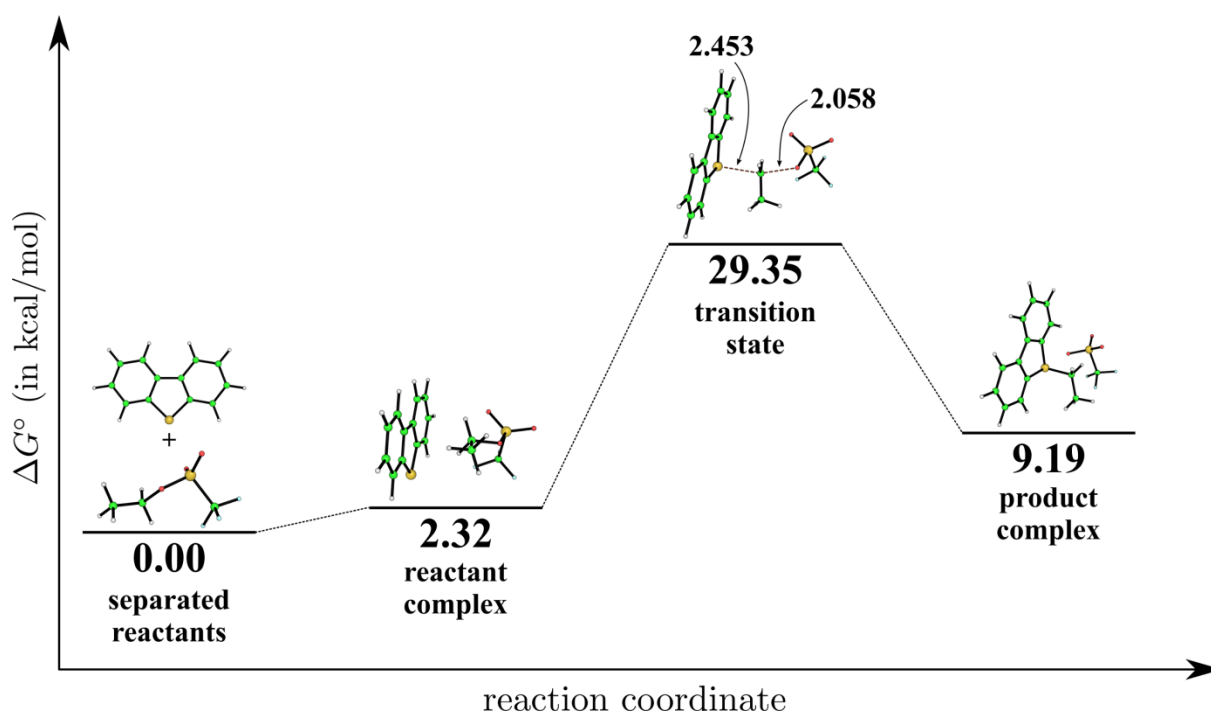


Figure A4.10: The Gibbs free energy surface for the reaction of dibenzothiophene and ethyl trifluoromethanesulfonate in the 1, 2-dichloroethane solution. The key atomic distances (in Å) for the transition state are indicated by dash lines.

The optimized molecular structures for the solution reactions

```
# benzothiophene
15
Ch 0 Mul 1 (E,H,G) -706.23640830 -706.114438 -706.152896
C 0.009536 -0.856439 0.000000
C 0.000000 0.555216 0.000000
C 1.181608 1.296522 0.000000
C 2.384409 0.611541 0.000000
C 2.414649 -0.791097 0.000000
C 1.243105 -1.524218 0.000000
C -1.317859 -1.400673 0.000000
C -2.274499 -0.443162 0.000000
H 1.159659 2.380720 0.000000
```

H	3.315212	1.168543	0.000000	
H	3.370733	-1.303607	0.000000	
H	1.268311	-2.609138	0.000000	
H	-1.533270	-2.461984	0.000000	
H	-3.347229	-0.577377	0.000000	
S	-1.629944	1.169794	0.000000	
# dibenzothiophene				
21				
Ch 0	Mul 1 (E,H,G)	-859.74656744	-859.574475	-859.618520
C	0.000000	2.624423	0.960966	
C	0.000000	1.251311	0.728990	
C	0.000000	0.723848	-0.575502	
C	0.000000	1.604262	-1.661526	
C	0.000000	2.970415	-1.436553	
C	0.000000	3.477039	-0.132149	
C	0.000000	-0.723848	-0.575502	
C	0.000000	-1.251311	0.728990	
S	0.000000	0.000000	1.955912	
C	0.000000	-2.624423	0.960966	
C	0.000000	-3.477039	-0.132149	
C	0.000000	-2.970415	-1.436553	
C	0.000000	-1.604262	-1.661526	
H	0.000000	1.216604	-2.674984	
H	0.000000	3.654896	-2.277782	
H	0.000000	4.549726	0.028788	
H	0.000000	3.018044	1.971324	
H	0.000000	-3.018044	1.971324	
H	0.000000	-4.549726	0.028788	
H	0.000000	-3.654896	-2.277782	
H	0.000000	-1.216604	-2.674984	
# dimethyldibenzothiophene				
27				
Ch 0	Mul 1 (E,H,G)	-938.31033424	-938.079862	-938.132168
C	-0.000005	-1.801695	2.965390	
C	-0.000007	-0.496094	3.467198	
C	-0.000006	0.611783	2.627115	
C	-0.000005	0.354753	1.251982	
C	-0.000004	-0.947622	0.723891	
C	-0.000004	-2.035576	1.601657	
H	-0.000006	-2.637841	3.656410	
H	-0.000013	-0.336873	4.541282	
H	-0.000004	-3.049577	1.216010	
C	-0.000005	0.354753	-1.251982	
C	-0.000006	0.611783	-2.627115	
C	-0.000007	-0.496094	-3.467198	
C	-0.000005	-1.801695	-2.965390	
C	-0.000004	-2.035576	-1.601657	
C	-0.000004	-0.947622	-0.723891	
H	-0.000013	-0.336873	-4.541282	
H	-0.000006	-2.637841	-3.656410	
H	-0.000004	-3.049577	-1.216010	
S	0.000002	1.583529	0.000000	
C	0.000017	2.014316	3.151386	
H	0.881208	2.564007	2.802791	
H	-0.880928	2.564177	2.802443	
H	-0.000195	2.028692	4.242342	
C	0.000017	2.014316	-3.151386	
H	-0.880928	2.564177	-2.802443	
H	0.881208	2.564007	-2.802791	
H	-0.000195	2.028692	-4.242342	
# naphthobenzothiophene				
27				
Ch 0	Mul 1 (E,H,G)	-1013.24909213	-1013.027325	-1013.078225
C	2.373787	0.972204	0.000000	
C	1.027496	1.441258	0.000000	
C	0.000000	0.462362	0.000000	
C	0.275998	-0.901072	0.000000	
C	1.622306	-1.339844	0.000000	
C	2.637111	-0.426206	0.000000	
H	3.670665	-0.757129	0.000000	
H	1.840977	-2.402329	0.000000	
C	-2.086887	-0.910700	0.000000	
C	-0.924375	-1.704342	0.000000	
C	-1.056782	-3.097127	0.000000	
C	-2.319534	-3.663841	0.000000	
C	-3.464174	-2.857791	0.000000	
C	-3.359624	-1.475647	0.000000	
C	0.782094	2.832320	0.000000	
C	1.823967	3.726631	0.000000	
C	3.155919	3.268008	0.000000	
C	3.421461	1.920795	0.000000	
H	3.971154	3.983549	0.000000	
H	4.446599	1.563010	0.000000	
H	-0.241628	3.193849	0.000000	

```
H      1.621541      4.792267      0.000000
H     -0.173997     -3.727937     0.000000
H     -2.424743     -4.743271     0.000000
H     -4.446422     -3.317849     0.000000
H     -4.246479     -0.851758     0.000000
S     -1.716890      0.799096     0.000000
# ethyl triflate
15
Ch 0 Mul 1 (E,H,G) -1040.05127505 -1039.943800 -1039.993396
C      2.112199     -0.439225     0.436996
C      3.418410     -0.578466     -0.291485
O      1.180865      0.200435     -0.504052
S     -0.162628      0.850346     0.023006
C     -1.293628     -0.626974     -0.028105
F     -2.498731     -0.252979     0.359597
O     -0.612758      1.755355     -0.999109
O     -0.050429      1.241278     1.406702
F     -1.345739     -1.103999     -1.256731
F     -0.832759     -1.559651     0.792246
H      1.687677     -1.404521     0.717225
H      2.192070      0.196519     1.319218
H      3.303309     -1.191623     -1.187294
H      3.810424      0.399887     -0.575328
H      4.140325     -1.064705     0.369316
# transition state for benzothiophene and ethyl triflate
30
Ch 0 Mul 1 (E,H,G) -1746.25392873 -1746.025208 -1746.096282
C     -2.954503      2.066014     -0.148724
C     -2.070858      1.879920     -1.147250
S     -1.975267      0.205630     -1.655214
C     -3.196060     -0.261757     -0.486976
C     -3.619932      0.852431     0.260355
C     -4.582575      0.668143     1.255961
C     -5.089830     -0.601778     1.481078
C     -4.657713     -1.694172     0.723051
C     -3.706581     -1.536797     -0.276352
C     -0.049558     -0.301355     -0.246682
C     -0.072882     -1.781108     -0.318605
H     -4.924299      1.514666     1.841409
H     -5.836176     -0.751455     2.253323
H     -5.073385     -2.677759     0.910801
H     -3.384910     -2.380247     -0.876408
H      0.532317      0.291032     -0.939420
H     -0.586692      0.227188     0.528956
H      0.139475     -2.139738     -1.325832
H      0.709908     -2.155927     0.346132
H     -1.020759     -2.184539     0.041469
S      2.726208      0.716333     0.625415
O      1.549017     -0.090930     1.083475
O      3.511993      1.250370     1.725803
O      2.406638      1.614913     -0.480838
C      3.795499     -0.583845     -0.146674
F      4.129077     -1.507240     0.747742
F      3.133966     -1.178122     -1.141220
F      4.903773     -0.043803     -0.639095
H     -3.146343      3.032092     0.301340
H     -1.436761      2.606768     -1.634444
# transition state for dibenzothiophene and ethyl triflate
36
Ch 0 Mul 1 (E,H,G) -1899.76745014 -1899.488488 -1899.565149
C     -3.135366      2.375309     0.789438
C     -2.840107      1.184915     0.124498
C     -1.880406      1.207148     -0.899364
C     -1.204619      2.363402     -1.263024
C     -1.512610      3.534549     -0.583117
C     -2.471656      3.539186     0.431740
S     -1.614155     -0.394731     -1.588012
C     -2.826156     -1.098891     -0.523001
C     -3.387367     -0.143970     0.340301
C     -4.353501     -0.558182     1.256987
C     -4.731818     -1.892274     1.295575
C     -4.162644     -2.824187     0.425841
C     -3.202337     -2.435482     -0.499753
C      0.351423     -0.783258     -0.173668
C      0.455757     -2.257487     -0.291466
H     -4.805207      0.158608     1.934067
H     -5.482113     -2.215169     2.008609
H     -4.474108     -3.861841     0.466297
H     -2.768112     -3.153392     -1.185948
H     -0.458835      2.356690     -2.049358
H     -0.999060      4.452520     -0.845491
H     -2.697479      4.464666     0.949561
H     -3.874522      2.387793     1.582939
H      0.854752     -0.118114     -0.861326
```

H	-0.238073	-0.330079	0.611181
H	0.730619	-2.563189	-1.300988
H	1.238627	-2.594571	0.392700
H	-0.470867	-2.746171	0.016077
S	2.977739	0.505930	0.710045
O	1.915156	-0.469465	-1.126388
O	3.712503	1.054083	1.837681
O	2.530212	1.430183	-0.327687
C	4.178139	-0.602840	-0.161959
F	4.644913	-1.529975	0.666026
F	3.568137	-1.212192	-1.179823
F	5.198469	0.099613	-0.639099
# transition state for dimethyldibenzothiophene and ethyl triflate			
42			
Ch 0	Mul 1 (E,H,G)	-1978.33460071	-1977.997171 -1978.080320
C	-3.422927	2.425471	0.706260
C	-2.916429	1.247350	0.158128
C	-1.752565	1.310759	-0.623197
C	-1.069892	2.497673	-0.892773
C	-1.608072	3.651575	-0.325636
C	-2.759839	3.617591	0.461237
S	-1.260292	-0.284098	-1.195274
C	-2.648614	-1.039611	-0.421471
C	-3.434887	-0.105961	0.270608
C	-4.566954	-0.553539	0.950707
C	-4.873949	-1.904717	0.926804
C	-4.072363	-2.812435	0.232709
C	-2.935315	-2.404878	-0.461389
C	0.532857	-0.542492	0.519693
C	-0.318001	-0.787702	1.702968
H	-5.196149	0.146368	1.489074
H	-5.751705	-2.264945	1.452066
H	-4.337886	-3.864754	0.226497
H	-1.114509	4.600415	-0.510041
H	-3.143213	4.541034	0.881294
H	-4.321414	2.407356	1.313092
H	0.912976	-1.352141	-0.084149
H	0.786638	0.466211	0.227449
H	-0.825294	-1.751345	1.655077
H	0.332266	-0.786259	2.582305
H	-1.046417	0.014925	1.839385
S	3.441011	0.296779	0.872999
O	2.375635	-0.583690	1.458546
O	4.546610	0.529570	1.786537
O	2.897483	1.448143	0.156020
C	4.131282	-0.776463	-0.469526
F	4.659359	-1.882573	0.038826
F	3.156458	-1.120738	-1.314163
F	5.067388	-0.125119	-1.147821
C	0.168113	2.530265	-1.736566
H	0.387297	3.548752	-2.060519
H	1.042082	2.165757	-1.185503
H	0.055494	1.907146	-2.629388
C	-2.065455	-3.370797	-1.205184
H	-1.884988	-3.031833	-2.230258
H	-1.088836	-3.480178	-0.721299
H	-2.526443	-4.358250	-1.249336
# transition state for naphthobenzothiophene and ethyl triflate			
42			
Ch 0	Mul 1 (E,H,G)	-2053.26947744	-2052.940967 -2053.024321
C	-1.642412	3.629541	0.641212
C	-1.742590	2.359381	0.071231
C	-0.853622	2.013202	-0.958440
C	0.130741	2.876167	-1.418022
C	0.213242	4.132356	-0.831632
C	-0.667760	4.504498	0.186229
S	-1.108347	0.359192	-1.507272
C	-2.449335	0.151122	-0.385721
C	-2.659135	1.281293	0.391412
C	-3.686197	1.269998	1.362508
C	-4.454570	0.150578	1.521838
C	0.687421	-0.463832	-0.063302
C	0.352083	-1.906138	-0.009989
H	-3.857732	2.146919	1.976497
H	-5.240811	0.133546	2.269546
H	0.814624	2.583737	-2.206147
H	0.972460	4.828187	-1.170100
H	-0.585546	5.490710	0.629225
H	-2.317644	3.926724	1.436025
H	1.352508	-0.059067	-0.813643
H	0.290158	0.225264	0.668867
H	0.477485	-2.386791	-0.980278
H	1.040477	-2.380571	0.694439
H	-0.658724	-2.067485	0.367940

```
S      3.615029      0.070535      0.691017
O      2.325057     -0.489936      1.212371
O      4.530861      0.460512      1.750198
O      3.428783      0.994590     -0.424101
C      4.381165     -1.424190     -0.089674
F      4.566809     -2.380779      0.812465
F      3.575738     -1.893961     -1.044442
F      5.551097     -1.117212     -0.636685
C      -4.259101     -1.007899      0.723065
C      -5.062359     -2.160049      0.881731
H      -5.837898     -2.152420      1.641053
C      -3.236586     -1.019126     -0.272244
C      -3.068124     -2.168335     -1.078349
H      -2.304014     -2.177106     -1.849455
C      -3.868871     -3.267730     -0.897580
H      -3.731889     -4.143042     -1.522943
C      -4.871509     -3.266594      0.092989
H      -5.495655     -4.143431      0.225687
# product complex for benzothiophene and ethyl triflate
30
Ch 0 Mul 1 (E,H,G) -1746.28649866  -1746.055607  -1746.126006
C      -2.587493      2.124631     -0.195263
C      -1.275573      1.880052     -0.112431
S      -0.934249      0.139485     -0.129676
C      -2.668079     -0.246179     -0.204982
C      -3.420896      0.935021     -0.246937
C      -4.805795      0.846428     -0.340754
C      -5.398035     -0.410921     -0.387874
C      -4.627290     -1.571173     -0.359138
C      -3.237644     -1.503508     -0.280225
C      -0.543422     -0.191985      1.645053
C      -0.342359     -1.668282      1.891224
H      -5.407797      1.747144     -0.380573
H      -6.476976     -0.489965     -0.458559
H      -5.108806     -2.540823     -0.410165
H      -2.636132     -2.404288     -0.286876
H      0.377402       0.369637      1.801852
H      -1.368773      0.240662      2.211797
H      0.467635     -2.067033      1.278989
H      -0.059369     -1.790684      2.939582
H      -1.252435     -2.247348      1.723046
S      2.824478      0.699602      0.362200
O      2.686298      0.058722      1.674246
O      4.028140      1.503139      0.165828
O      1.580258      1.320804     -0.132226
C      3.043377     -0.733392     -0.790858
F      4.133410     -1.429262     -0.480720
F      1.989530     -1.556291     -0.714915
F      3.150494     -0.318397     -2.050267
H      -2.995145      3.127953     -0.226021
H      -0.422482      2.539434     -0.069998
# product complex for dibenzothiophene and ethyl triflate
36
Ch 0 Mul 1 (E,H,G) -1899.80177261  -1899.520546  -1899.597273
C      -3.408054      2.452863      0.257281
C      -2.811287      1.219707      0.013708
C      -1.428425      1.184381     -0.200780
C      -0.625573      2.309027     -0.189745
C      -1.245217      3.529321      0.063362
C      -2.619078      3.596764      0.284508
S      -0.854893     -0.482357     -0.480524
C      -2.516307     -1.113394     -0.345516
C      -3.436382     -0.095304     -0.072747
C      -4.780241     -0.433899      0.052163
C      -5.163969     -1.761131     -0.098836
C      -4.229536     -2.753361     -0.387758
C      -2.881636     -2.435662     -0.526805
C      -0.159710     -0.903194      1.174816
C      0.121121     -2.383333      1.289002
H      -5.520993      0.330180      0.258724
H      -6.210679     -2.026397     -0.001465
H      -4.550927     -3.780258     -0.516717
H      -2.152499     -3.197236     -0.774958
H      0.435902      2.229836     -0.381790
H      -0.647736      4.433336      0.081299
H      -3.082896      4.558002      0.475599
H      -4.477435      2.520003      0.422318
H      0.751119     -0.303040      1.219556
H      -0.889537     -0.543027      1.901313
H      0.799545     -2.727116      0.506570
H      0.610716     -2.553757      2.251004
H      -0.792690     -2.979895      1.270610
S      2.982242      0.741485     -0.073903
O      2.629102      0.893607      1.343891
```

```

O      3.924662      1.724454      -0.603065
O      1.823143      0.456475      -0.941010
C      3.922709      -0.853748      -0.117479
F      5.015093      -0.778967      0.638860
F      3.165617      -1.853929      0.343224
F      4.290931      -1.151238      -1.361064
# product complex for dimethyldibenzothiophene and ethyl triflate
42
Ch 0 Mul 1 (E,H,G) -1978.36463112 -1978.025068 -1978.109513
C      -3.171061      2.675873      0.549639
C      -2.764688      1.421612      0.111449
C      -1.511135      1.304144      -0.500929
C      -0.634612      2.360905      -0.715449
C      -1.079399      3.603361      -0.252986
C      -2.315972      3.756054      0.365427
S      -1.199007      -0.374241      -1.000245
C      -2.770718      -0.914473      -0.367687
C      -3.483435      0.153829      0.188370
C      -4.742617      -0.098758      0.720169
C      -5.236266      -1.397035      0.683379
C      -4.500011      -2.436111      0.122113
C      -3.233497      -2.223037      -0.428022
C      0.020921      -0.966606      0.244135
C      -0.399687      -0.782754      1.677089
H      -5.328778      0.702842      1.154206
H      -6.217280      -1.605707      1.095449
H      -4.914106      -3.438599      0.102580
H      -0.437602      4.467171      -0.389881
H      -2.620520      4.740141      0.704068
H      -4.136573      2.809288      1.023454
H      0.194708      -2.007035      -0.035225
H      0.915432      -0.393140      0.004051
H      -1.282943      -1.372662      1.929280
H      0.441203      -1.116611      2.288958
H      -0.586310      0.268039      1.907775
S      3.507360      -0.244840      1.066842
O      2.882762      -1.533682      1.386302
O      4.781705      0.023352      1.732166
O      2.571660      0.890702      1.029358
C      3.967936      -0.434174      -0.718576
F      4.812041      -1.447551      -0.895479
F      2.876174      -0.671992      -1.459726
F      4.539983      0.675930      -1.182115
C      0.704512      2.191735      -1.359552
H      1.052089      3.138728      -1.774572
H      1.441593      1.852493      -0.623400
H      0.675571      1.456897      -2.169944
C      -2.423839      -3.338674      -1.010907
H      -1.890144      -3.023167      -1.912356
H      -1.680669      -3.695040      -0.290023
H      -3.060709      -4.184149      -1.272699
# product complex for naphthobenzothiophene and ethyl triflate
42
Ch 0 Mul 1 (E,H,G) -2053.30375543 -2052.972842 -2053.053862
C      -2.451317      3.649044      -0.262615
C      -1.976233      2.343683      -0.182325
C      -0.590955      2.143498      -0.175607
C      0.332906      3.168809      -0.234458
C      -0.168911      4.466191      -0.308300
C      -1.542223      4.699367      -0.322881
S      -0.196113      0.412393      -0.028320
C      -1.922767      -0.022736      -0.061237
C      -2.730693      1.097471      -0.123453
C      -4.130639      0.930840      -0.153367
C      -4.656118      -0.333716      -0.133961
C      0.191206      0.349903      1.781054
C      0.262020      -1.059699      2.313590
H      -4.780383      1.797269      -0.193871
H      -5.732458      -0.470593      -0.148226
H      1.394853      2.956880      -0.226809
H      0.522111      5.299568      -0.360736
H      -1.910318      5.717336      -0.385017
H      -3.517379      3.844994      -0.278410
H      1.160455      0.847738      1.823741
H      -0.581924      0.956122      2.255561
H      1.031284      -1.639411      1.803390
H      0.547687      -0.992396      3.366476
H      -0.699064      -1.573190      2.257750
S      3.589856      0.150997      0.286451
O      3.365307      -0.335953      1.650620
O      4.958530      0.547833      -0.035611
O      2.549196      1.077591      -0.198906
C      3.306673      -1.357712      -0.754095
F      4.213281      -2.293005      -0.489117

```

```
F      2.094377      -1.877062      -0.504490
F      3.366420      -1.063794      -2.049308
C     -3.832937      -1.488571      -0.121812
C     -4.383722      -2.790688      -0.146075
H     -5.463425      -2.899244      -0.147085
C     -2.411454      -1.345223      -0.109369
C     -1.597588      -2.500946      -0.163464
H     -0.517364      -2.401985      -0.194638
C     -2.169253      -3.746591      -0.197395
H     -1.537120      -4.626247      -0.245209
C     -3.571759      -3.895150      -0.177589
H     -4.005228      -4.888746      -0.199440
# reactant complex for dibenzothiophene and ethyl triflate
36
Ch 0 Mul 1 (E,H,G) -1899.81091232 -1899.529336 -1899.608224
C      1.322554      1.983443      -1.773548
C      1.704281      1.333603      -0.596114
C      1.123209      1.731484      0.621541
C      0.176818      2.751074      0.679846
C     -0.185970      3.379409      -0.500868
C      0.383946      2.998988      -1.720663
S      1.711454      0.793300      1.981565
C      2.742022     -0.154088      0.926441
C      2.638523      0.241278      -0.420623
C      3.389434     -0.438036      -1.384966
C      4.217867     -1.479113      -1.000453
C      4.310490     -1.856336      0.344218
C      3.574893     -1.198997      1.318697
C     -0.152197     -1.580999      -0.487550
C      0.590133     -2.880296      -0.373552
H      3.319544     -0.150695      -2.428878
H      4.799678     -2.008154      -1.747159
H      4.963047     -2.674033      0.630357
H      3.644520     -1.494405      2.359557
H     -0.270004      3.042974      1.623427
H     -0.925355      4.172499      -0.476413
H      0.081748      3.500922      -2.633087
H      1.757346      1.687855      -2.722618
H      0.054455     -0.913767      0.349322
H      0.050197     -1.061837      -1.424249
H      0.352804     -3.384846      0.565124
H      0.349437     -3.541985      -1.207823
H      1.662355     -2.668582      -0.390873
S     -2.659158     -0.801861      -0.792919
O     -1.586673     -1.914041      -0.453505
O     -3.867374     -1.488252      -1.164174
O     -2.092327      0.249671      -1.600289
C     -2.952933     -0.084766      0.901264
F     -3.535316     -0.986383      1.668390
F     -1.798620      0.275908      1.441445
F     -3.733168      0.974045      0.782020
```

MS experiments for “off-ESI” reaction

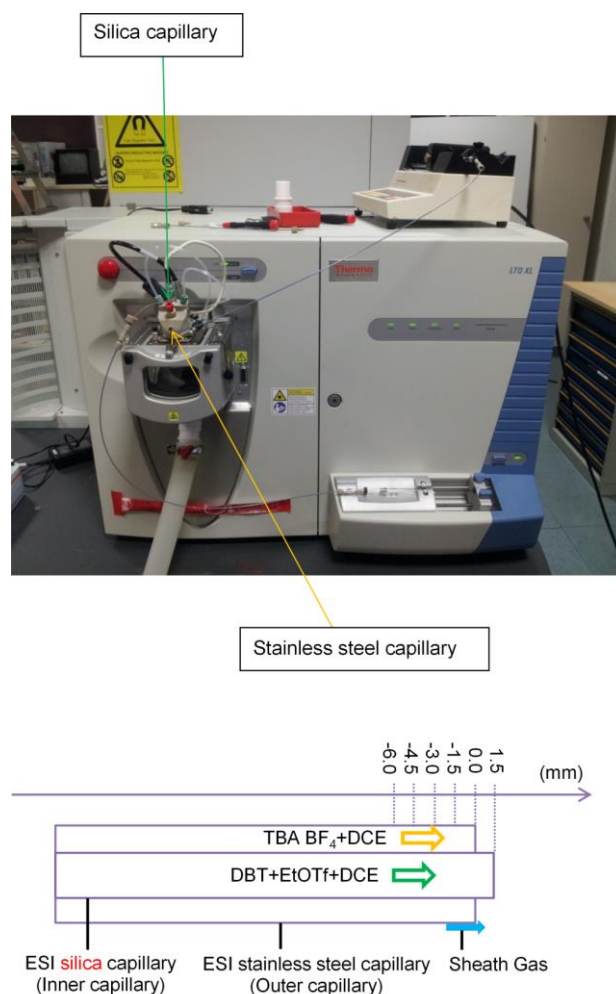


Figure A4.11: Silica electro spray capillary setup on 7 T FT-ICR MS.

Silica capillary position: In a 1-D space, the origin is defined at the edge of the outer capillary with the positive direction pointing to the right, and it is considered as positive value when silica capillary is outside of stainless steel, vice versa.

Solution flows: the reaction solution is injected through the inner silica capillary as the green arrow shows. To ensure that our ESI setup works well, TBA BF₄ is taken as a reference and dissolved in DCE, and the obtained ionic TBA BF₄ solution is injected through the outer stainless capillary as the yellow arrow shows in **Figure A4.11**. The inner solution and outer solution is isolated by the silica capillary.

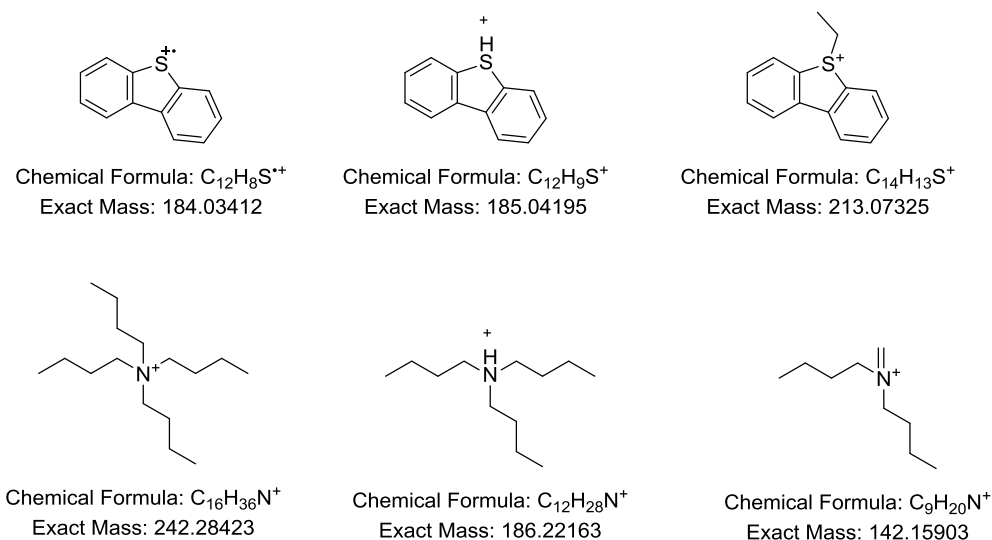


Figure A4.12: Characteristic peaks from DBT and reference peaks from TAB BF₄ obtained on ESI(+) 7 T FT-ICR MS.

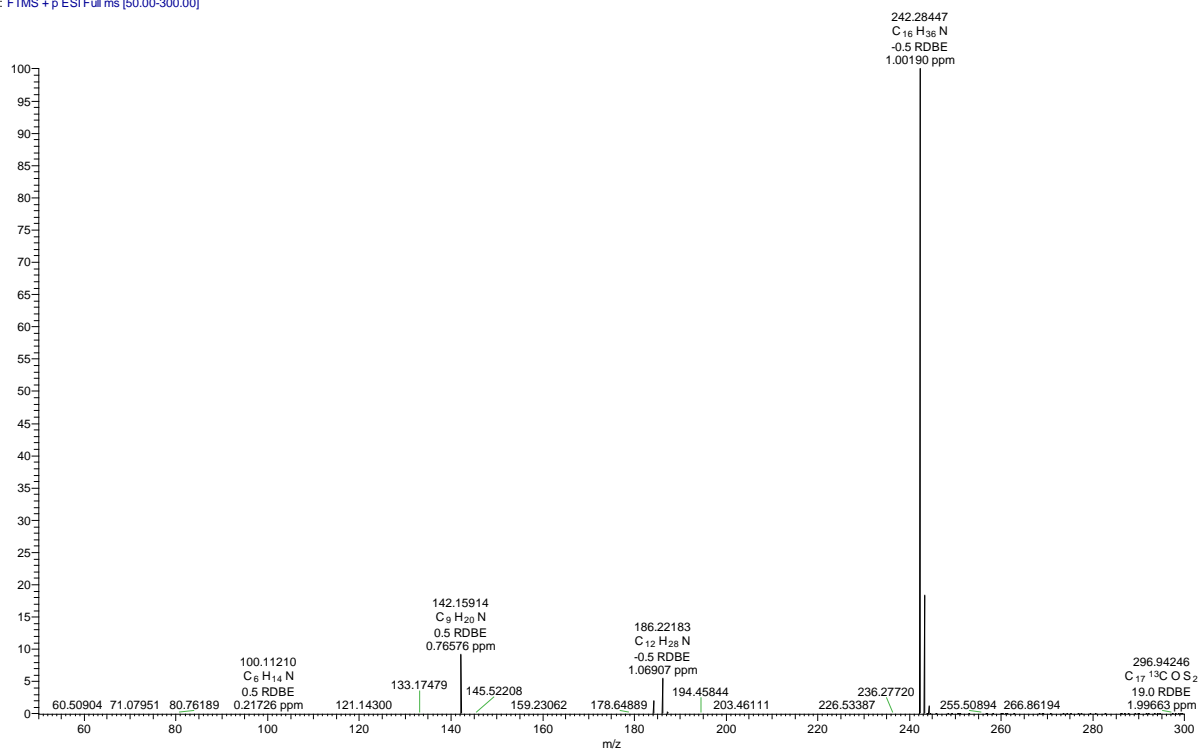
Sample preparation: DBT, C₂H₅OTf and TBA BF₄ were respectively dissolved in anhydrous DCE at a concentration of 2.43 mM (DBT), 22.36 mM (C₂H₅OTf) and 39.2 μM (TBA BF₄) for the ESI experiments.

Table A4.3: Evaluation of the influence of silica capillary position on characteristic peaks derived from DBT

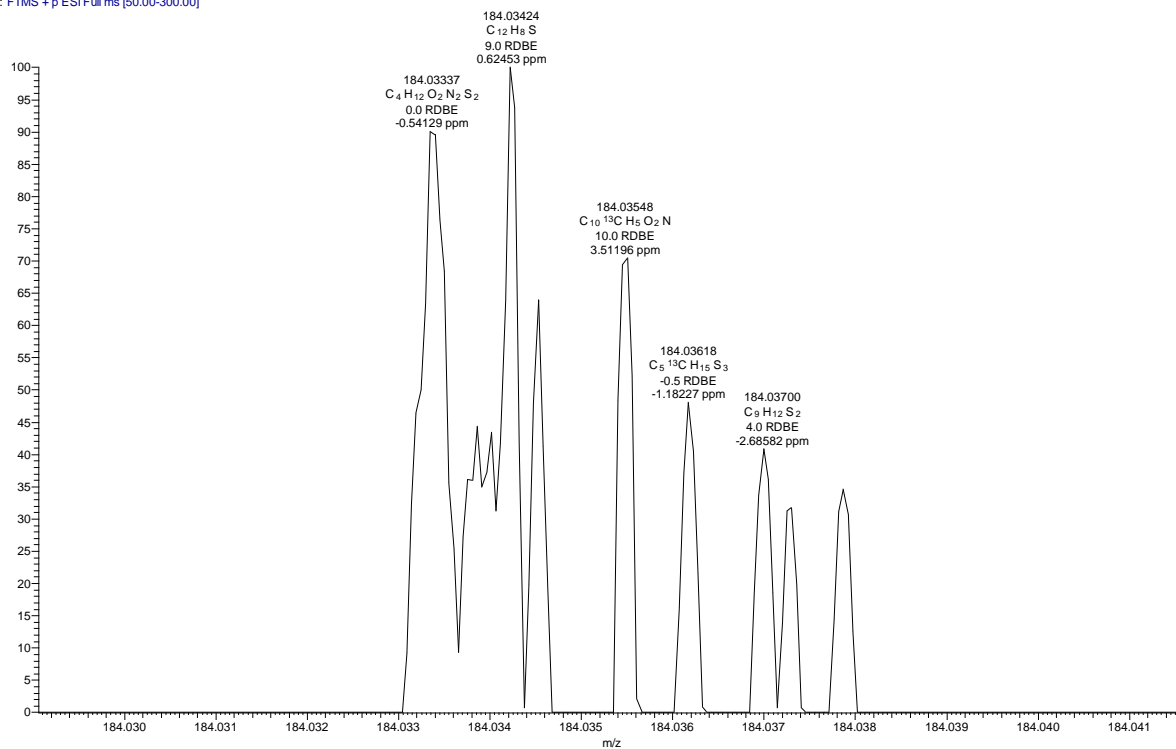
	Silica capillary position	[M] ⁺ , a	[M+H] ⁺ , a	[M+C ₂ H ₅] ⁺ , a
Figure A4.13	1.5	×	×	×
Figure A4.14	0.0	√	√	√
Figure A4.15	-1.5	√	√	√
Figure A4.16	-3.0	√	√	√
Figure A4.17	-5.5	√	√	√

^aM represents DBT

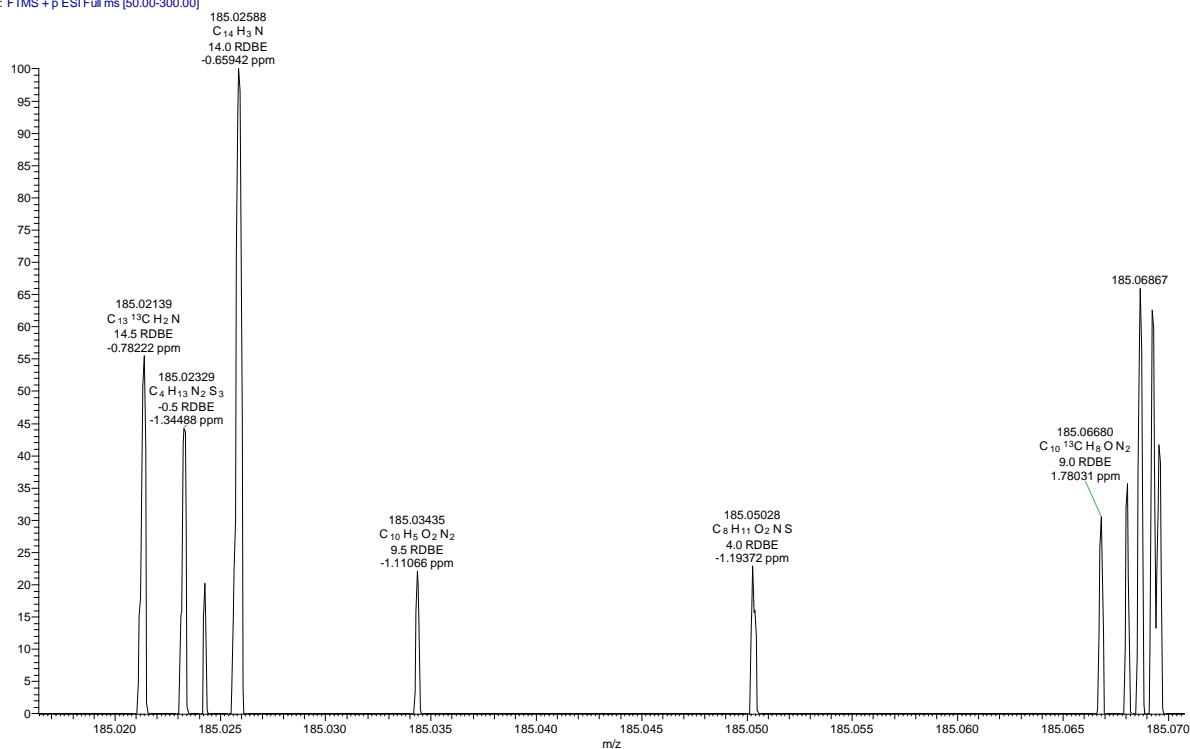
WNX-WB-105_1-1(3 kV) #1-113 RT: 0.04-6.57 AV: 113 NL: 2.89E5
T: FTMS + p ESI Full ms [50.00-300.00]



WNX-WB-105_1-1(3 kV) #1-113 RT: 0.04-6.57 AV: 113 NL: 3.00E-1
T: FTMS + p ESI Full ms [50.00-300.00]



WNX-WB-105_1-1(3 kV) #1-113 RT: 0.04-6.57 AV: 113 NL: 6.19E-1
T: FTMS + p ESI Full ms [50.00-300.00]



WNX-WB-105_1-1(3 kV) #1-113 RT: 0.04-6.57 AV: 113 NL: 3.74E-1
T: FTMS + p ESI Full ms [50.00-300.00]

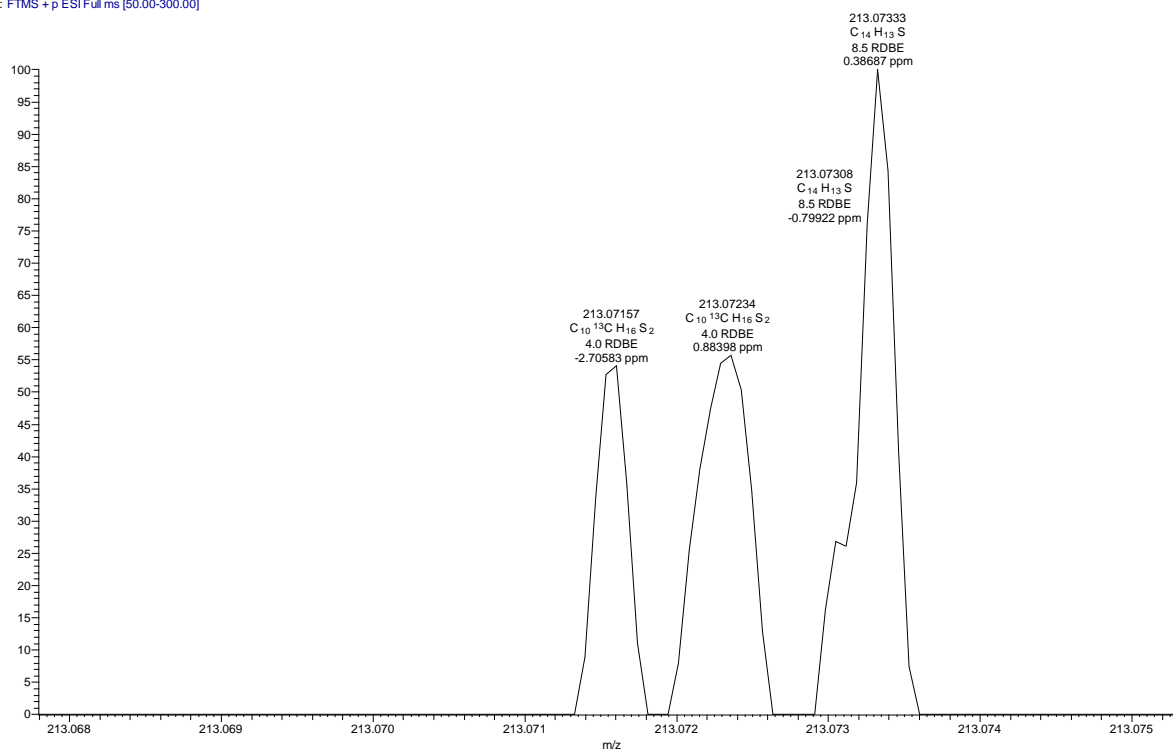
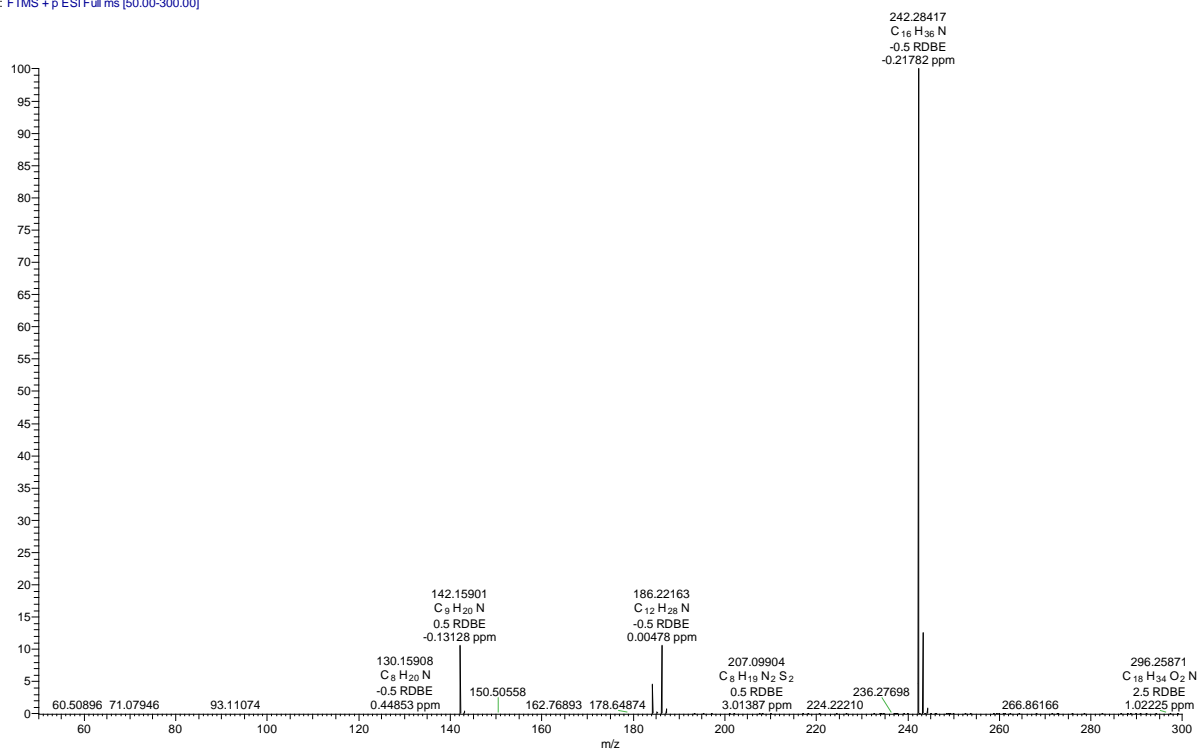
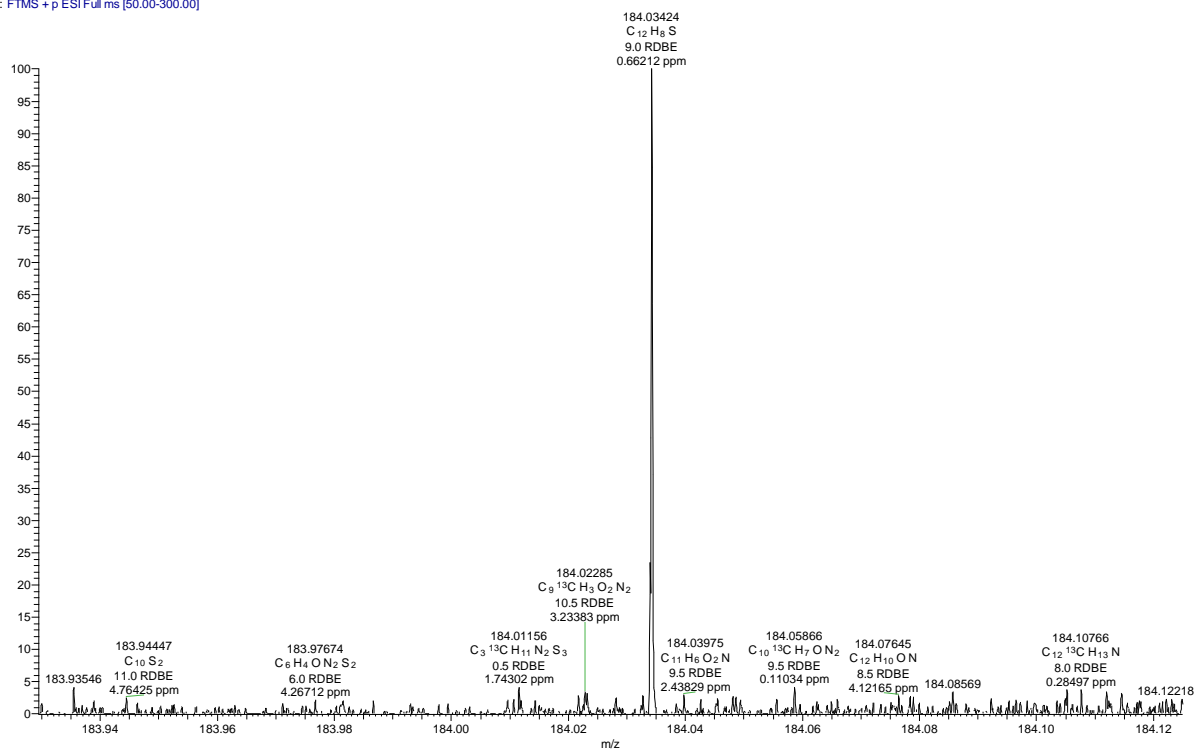


Figure A4.13: The mass spectra obtained from the ESI capillary set-up where the silica capillary locates 1.5 mm outside of the outer metallic capillary on ESI(+) 7 T FT-ICR MS. There are almost no desired peaks observed.

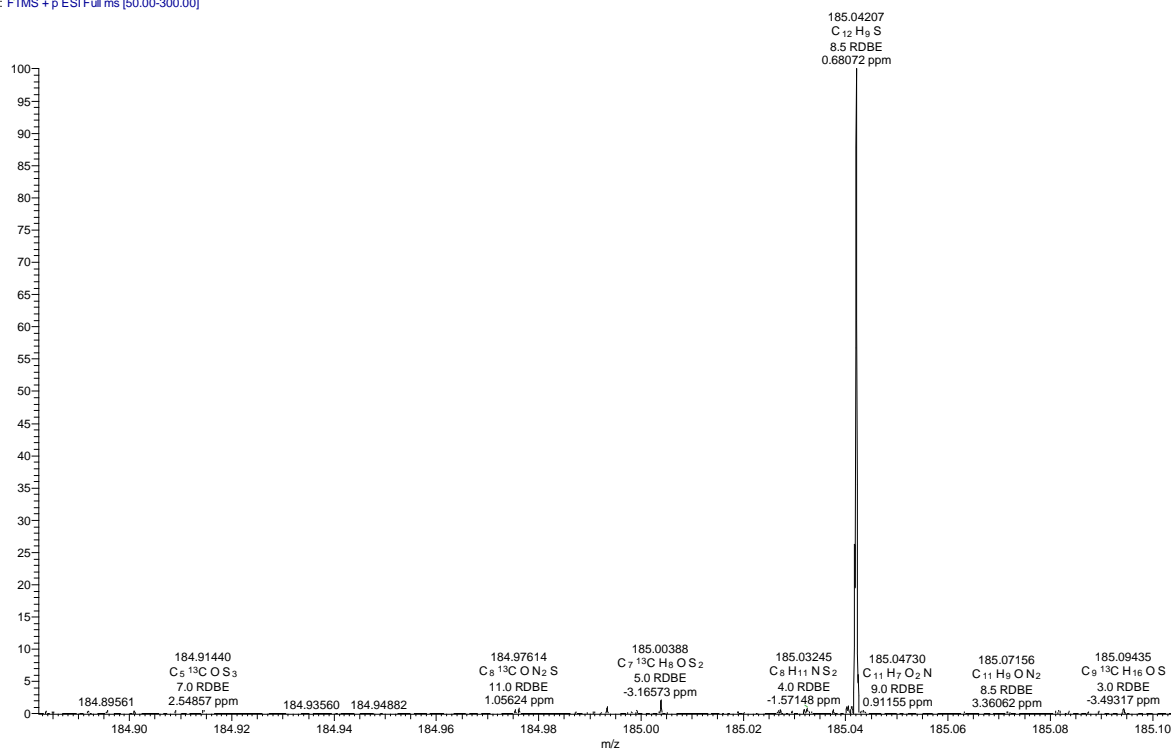
WNX-WB-105_2 (3 kV) #1-115 RT: 0.01-6.59 AV: 115 NL: 6.57E5
T: FTMS + p ESI Full ms [50.00-300.00]



WNX-WB-105_2 (3 kV) #1-115 RT: 0.01-6.59 AV: 115 NL: 8.67E1
T: FTMS + p ESI Full ms [50.00-300.00]



WNX-WB-105_2 (3 kV) #1-115 RT: 0.01-6.59 AV: 115 NL: 1.22E2
T: FTMS + p ESI Full ms [50.00-300.00]



WNX-WB-105_2 (3 kV) #1-115 RT: 0.01-6.59 AV: 115 NL: 6.02E1
T: FTMS + p ESI Full ms [50.00-300.00]

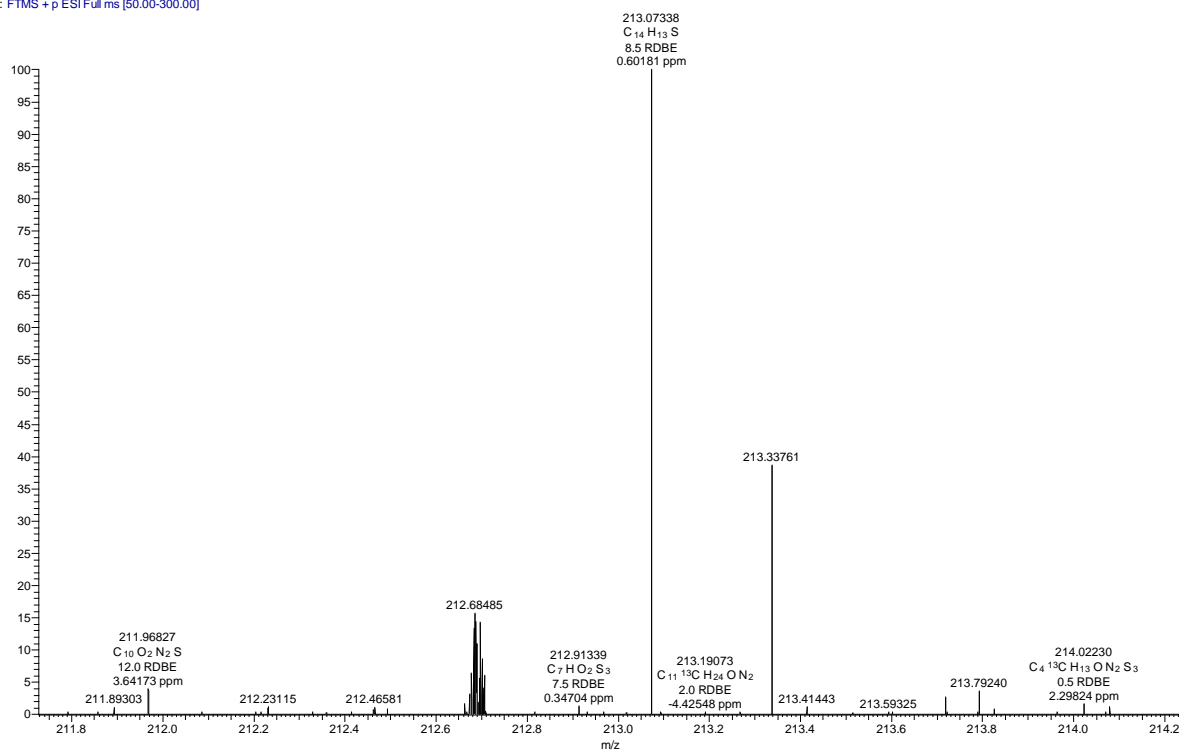
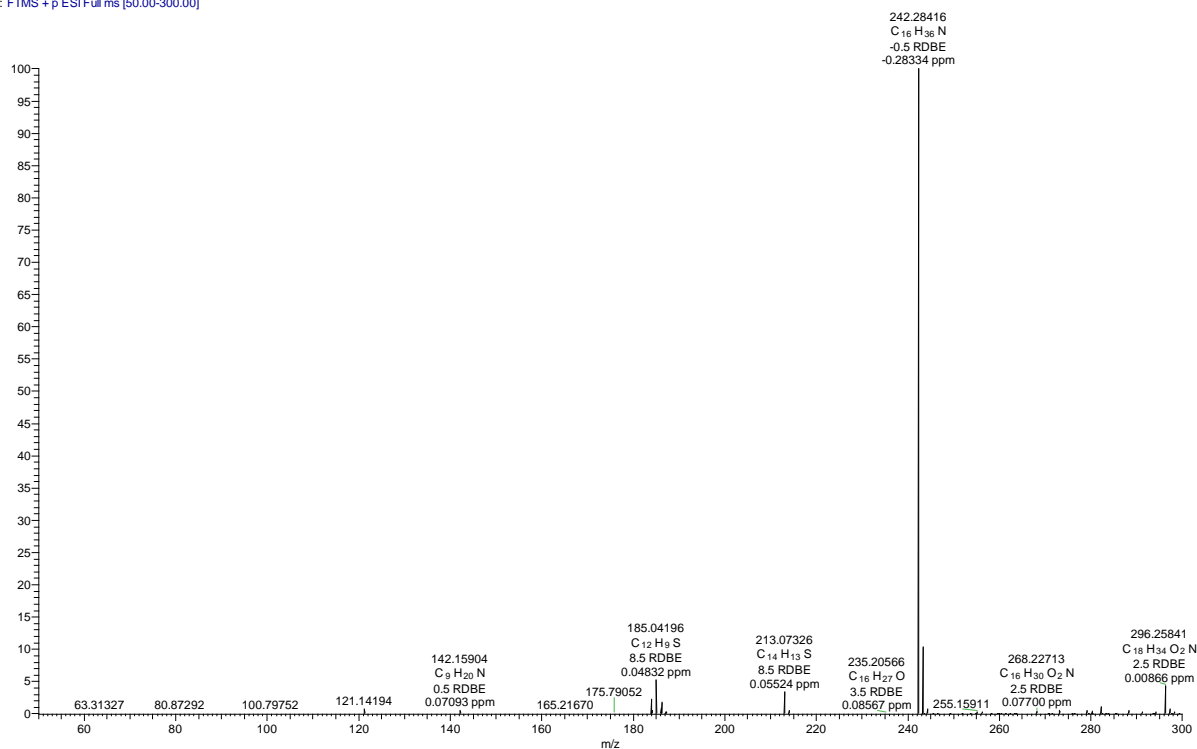


Figure A4.14: The mass spectra obtained from the ESI capillary set-up where the silica capillary locates 0.0 mm relative to the outer metallic capillary on ESI(+) 7 T FT-ICR MS. The desired peaks are observed.

WNX-WB-105_3-1 (3 kV) #1-86 RT: 0.01-5.00 AV: 86 NL: 1.26E5
T: FTMS + p ESI Full ms [50.00-300.00]



WNX-WB-105_3-1 (3 kV) #1-86 RT: 0.01-5.00 AV: 86 NL: 6.61E3
T: FTMS + p ESI Full ms [50.00-300.00]

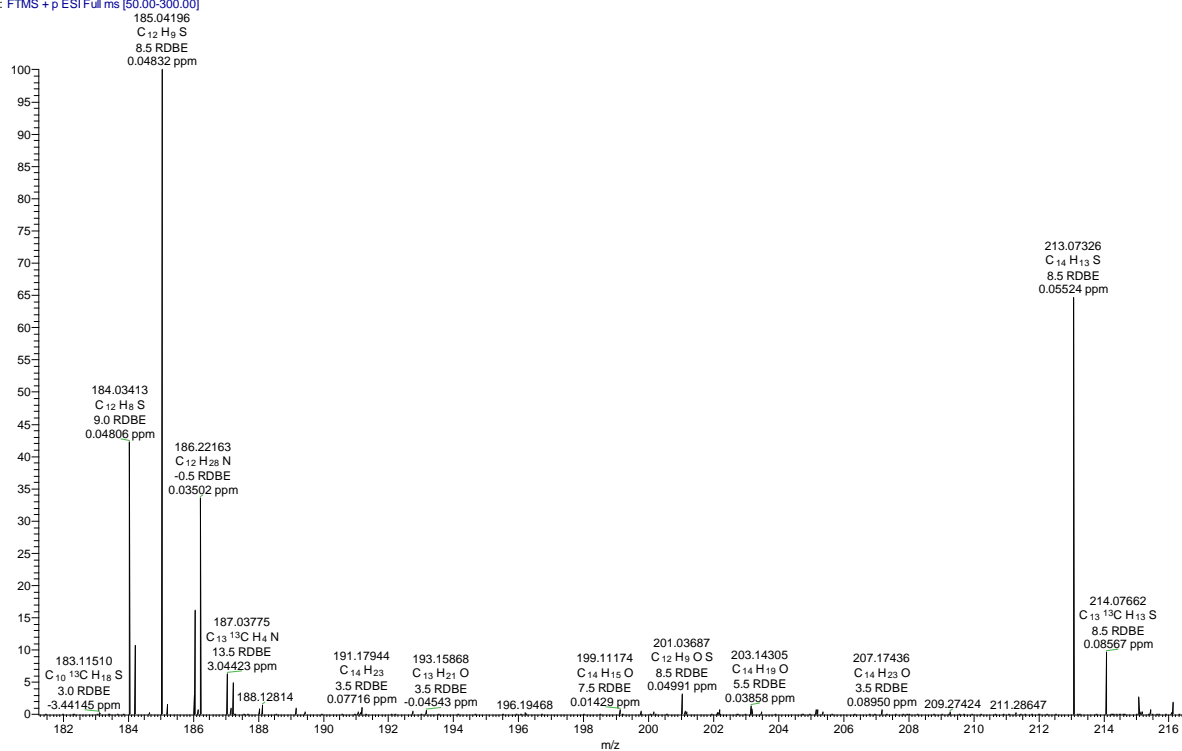
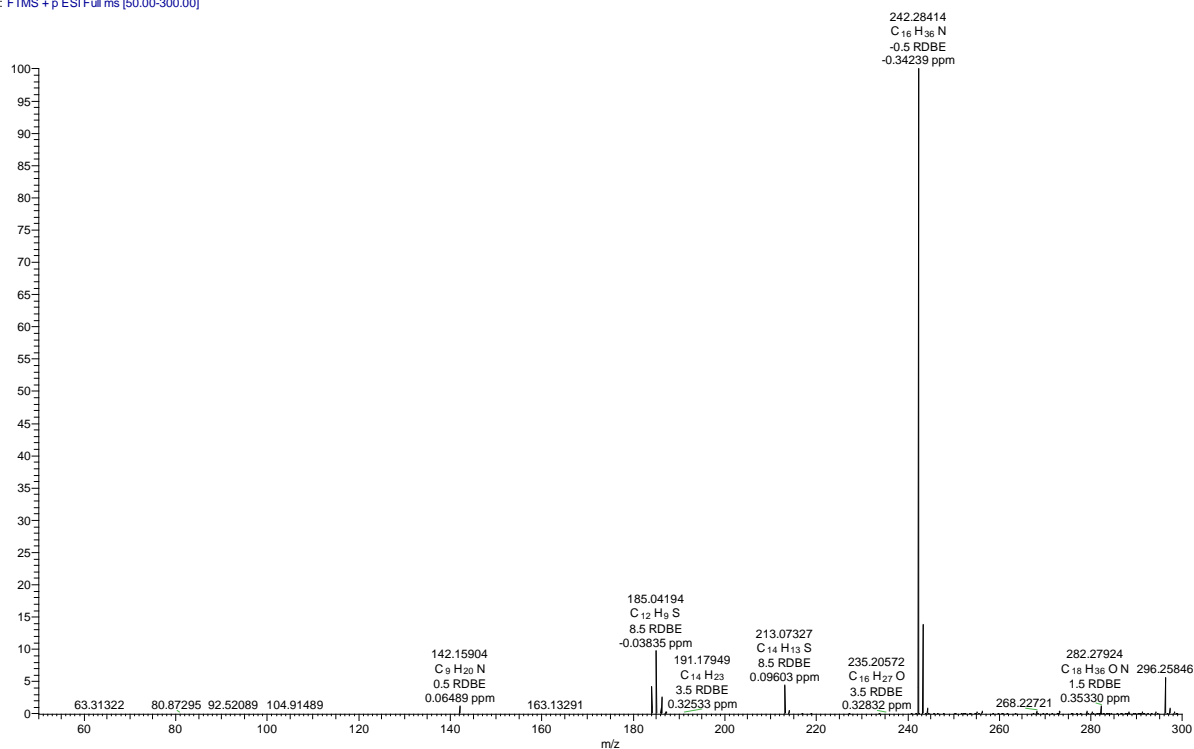


Figure A4.15: The mass spectra obtained from the ESI capillary set-up where the silica capillary locates -1.5 mm inside of the outer metallic capillary on ESI(+) 7 T FT-ICR MS. The relative abundance of the desired peaks increases comparing with **Figure A4.14**.

WNX-WB-105_4-1 (3 kV) #1-86 RT: 0.01-4.98 AV: 86 NL: 3.11E5
T: FTMS + p ESI Full ms [50.00-300.00]



WNX-WB-105_4-1 (3 kV) #1-86 RT: 0.01-4.98 AV: 86 NL: 3.05E4
T: FTMS + p ESI Full ms [50.00-300.00]

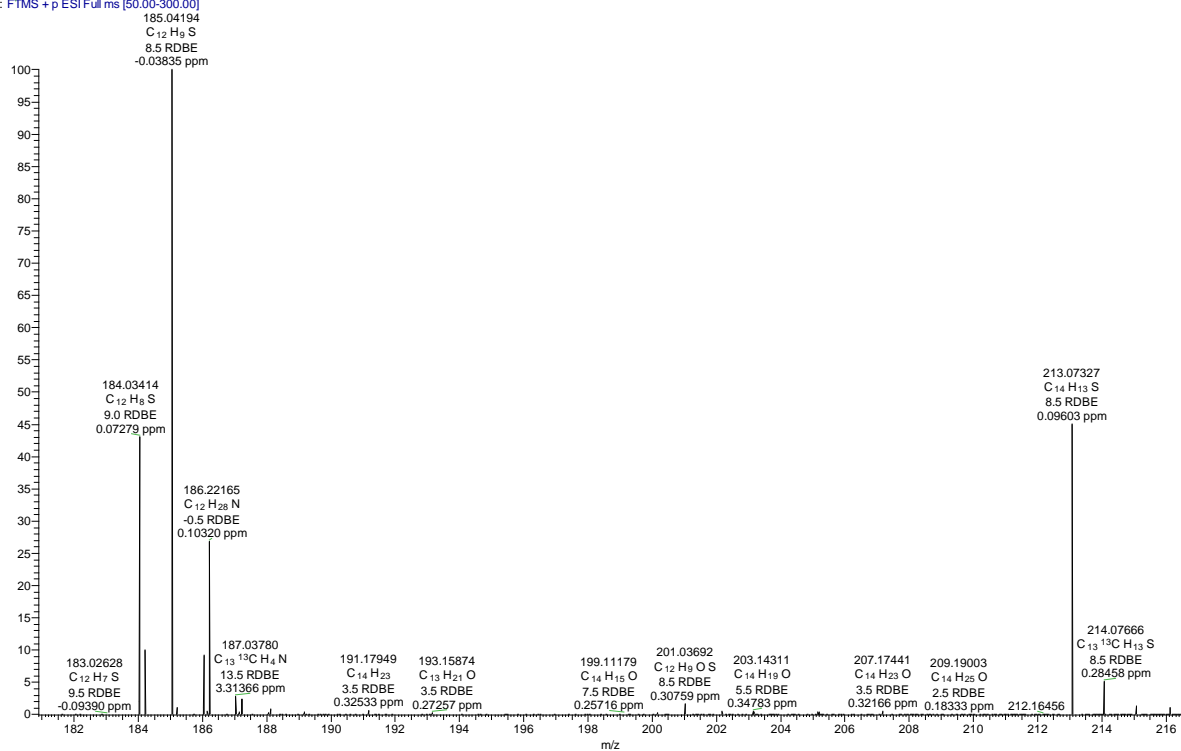
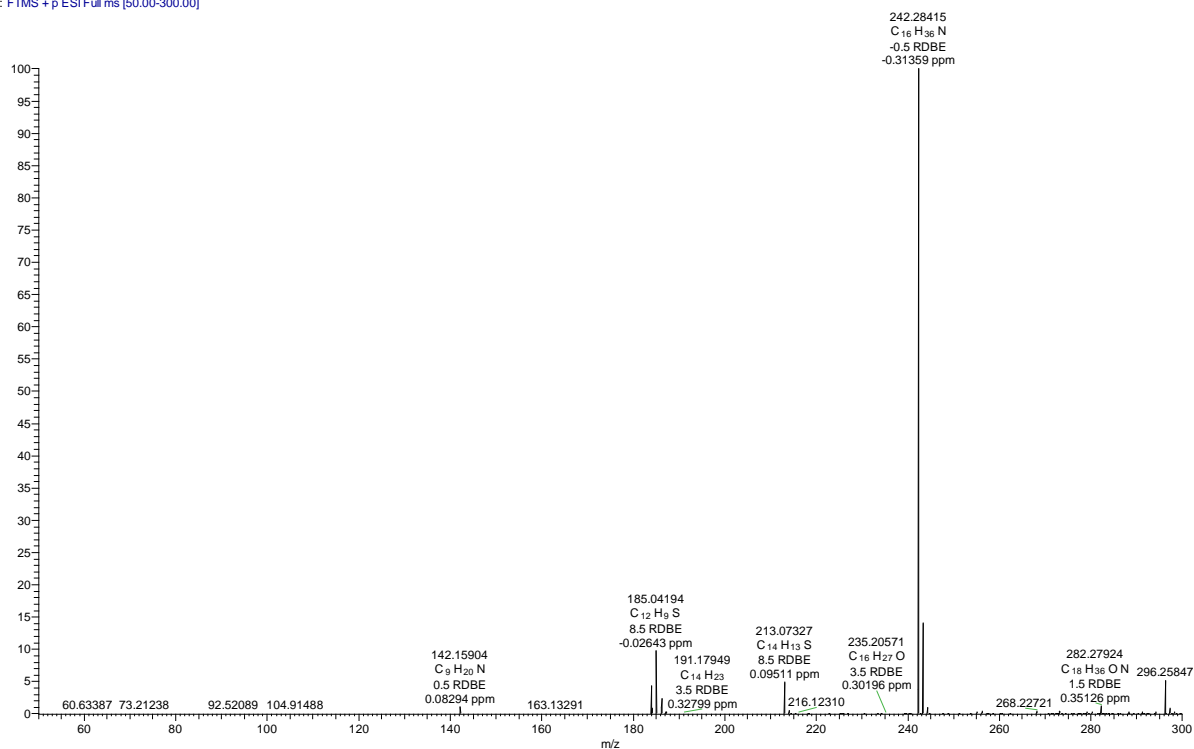


Figure A4.16: The mass spectra obtained from the ESI capillary set-up where the silica capillary locates -3.0 mm inside of the outer metallic capillary on ESI(+) 7 T FT-ICR MS. The relative abundance of the desired peaks sharply increases comparing with **Figure A4.15**.

WNX-WB-105_5-1 (3 kV) #1-78 RT: 0.01-4.52 AV: 78 NL: 3.34E5
T: FTMS + p ESI Full ms [50.00-300.00]



WNX-WB-105_5-1 (3 kV) #1-78 RT: 0.01-4.52 AV: 78 NL: 3.29E4
T: FTMS + p ESI Full ms [50.00-300.00]

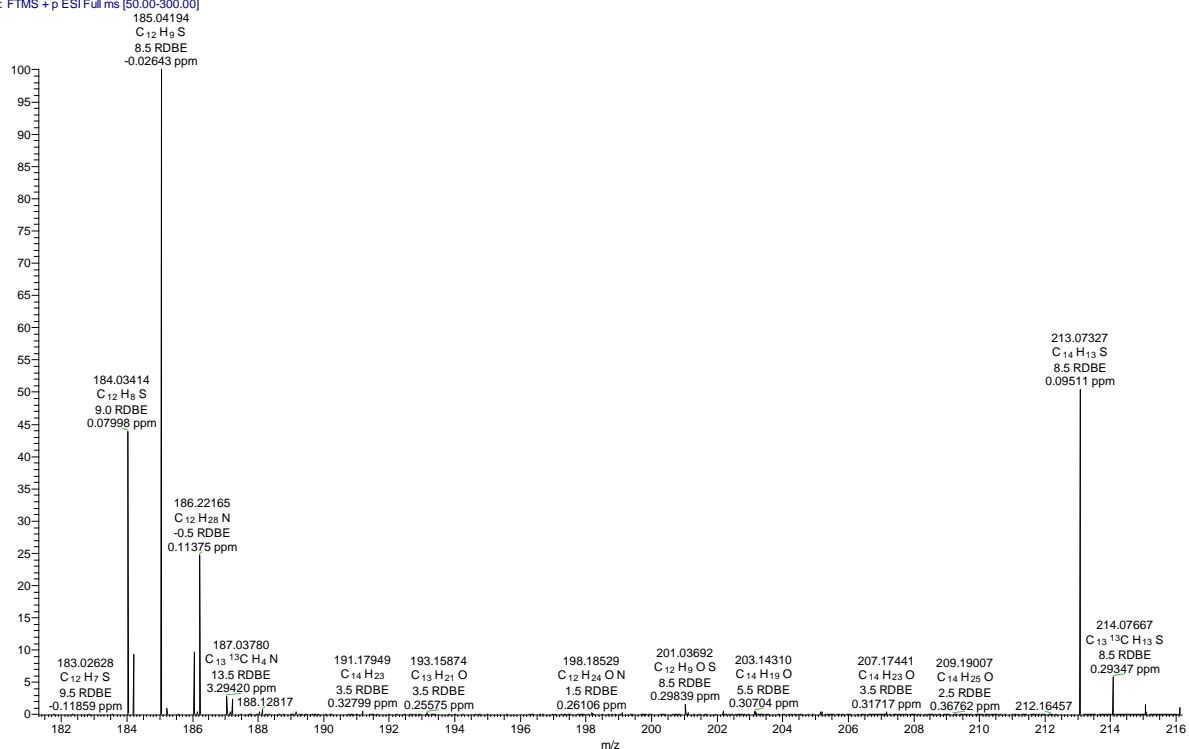


Figure A4.17: The mass spectra obtained from the ESI capillary set-up where the silica capillary locates -5.5 mm inside of the outer metallic capillary on ESI(+) 7 T FT-ICR MS. The relative abundance of the desired peaks increases comparing with **Figure A4.16**.

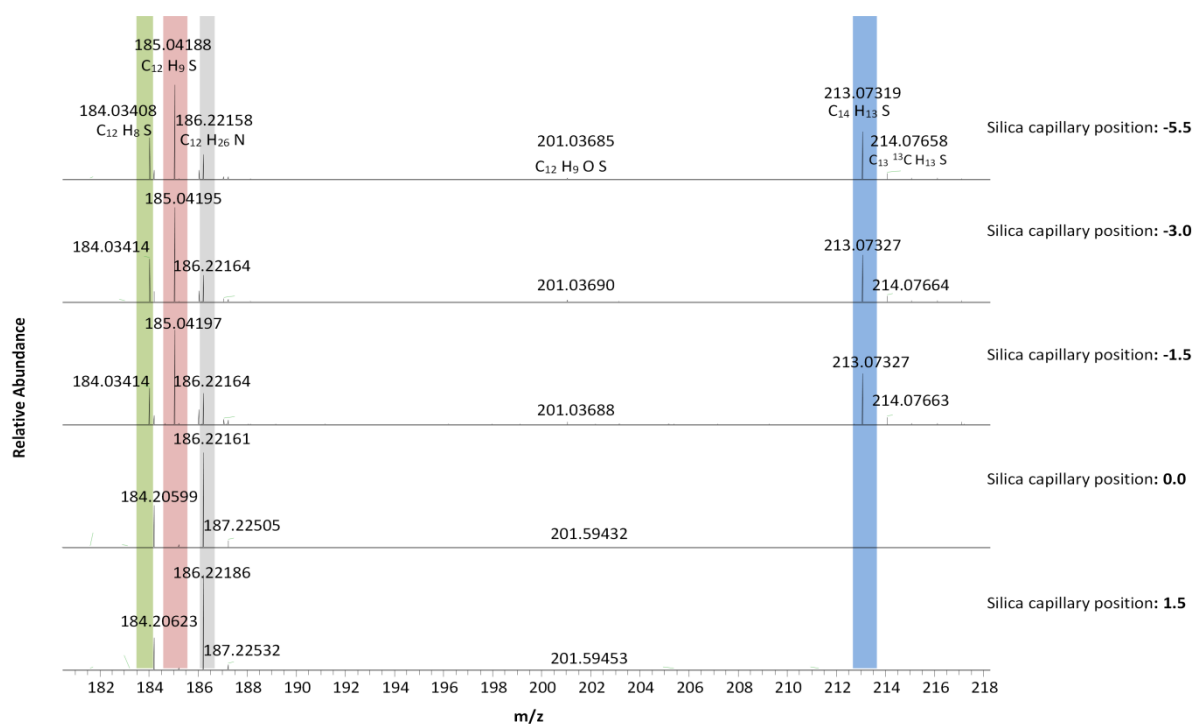


Figure A4.18: Comparison of mass spectra obtained from different relative distance between silica capillary and stainless steel capillary in Pos. ESI mode. The relative abundance of the desired peaks increases as the silica capillary moves inside of the metallic capillary.

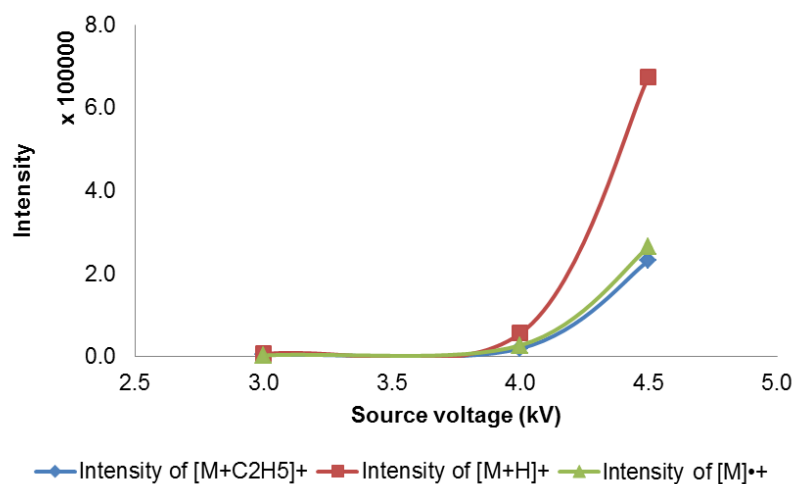
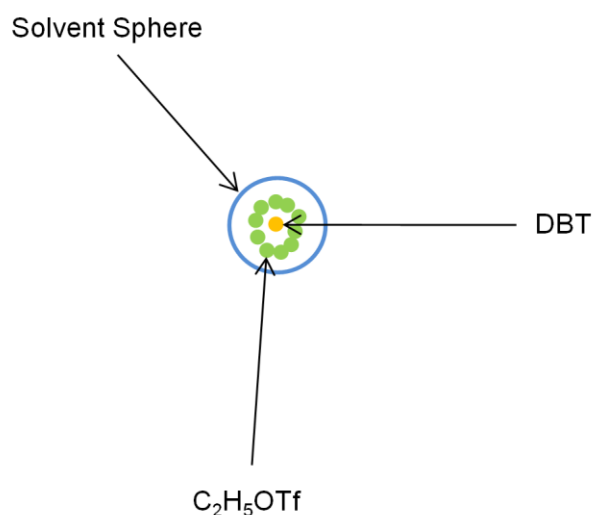


Figure A4.19: Effect of spray voltage on the intensity of characteristic peaks of [M+C₂H₅]⁺, [M+H]⁺ and [M]⁺⁺. This data is obtained by choosing the set-up where the silica position locates -1.5 mm outside of the stainless steel capillary. As the source voltage increasing, the intensity of the desired peaks increases.

Conclusion in this section of “Where does it happen?”

Based on the ^1H NMR data, computational data and ESI-MS data, the reaction occurs in the ESI only with electrochemistry involved, that is, it is an “**In-ESI**” reaction, not an “Off-ESI” reaction.

Solution model



Green represents $\text{C}_2\text{H}_5\text{OTf}$; Yellow represents DBT; Blue represents anhydrous 1,2-DCE.

Figure A4.20: Solution Model. $\text{C}_2\text{H}_5\text{OTf}$ has 10 times more chance to be transferred to the metal surface than DBT does.

How does it happen?

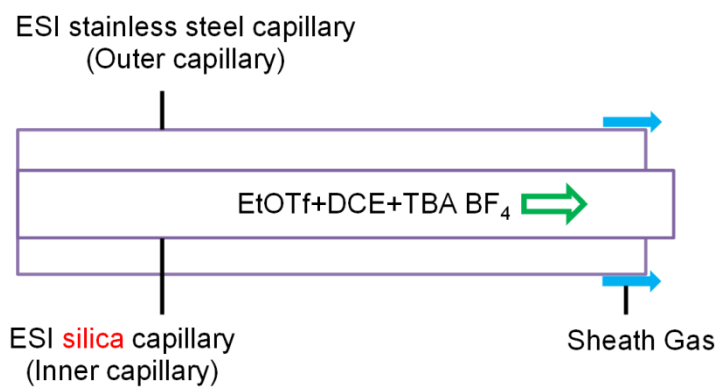
MS experiments for “in-ESI” reaction

In order to investigate the reaction mechanism, different experiments are devised by manipulating the silica capillary position, the solution constituent and the pathway the solution is injected. Green arrow represents that the solution is injected through the inner silica capillary. Yellow arrow represents the solution is injected through the outer stainless steel capillary. The inner solution is isolated from the outer solution by the silica capillary

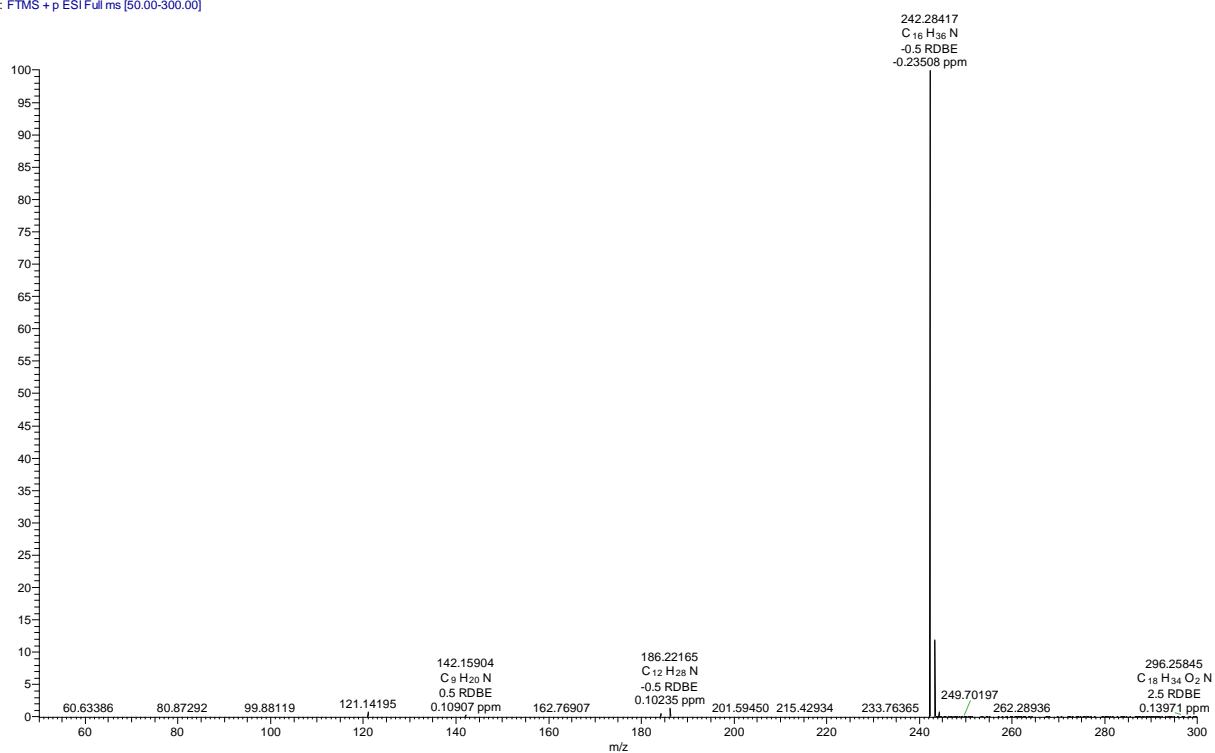
Table A4.4: Evaluation of the influence of Silica capillary position, solution constituent and the solution flow pathway on the peaks derived from DBT

	Silica capillary position (mm)	Solution flows	[M] ⁺ , a	[M+H] ⁺ , a	[M+C ₂ H ₅] ⁺ , a
Figure A4.21	1.5	Inner silica capillary EtOTf +DCE	×	×	×
Figure A4.22	1.5	Outer metallic capillary EtOTf+DCE	×	×	×
Figure A4.23	1.5	Inner silica capillary DBT +DCE	×	×	×
Figure A4.24	1.5	Outer metallic capillary DBT+DCE	√	√ tiny	×
Figure A4.25	1.5	Inner silica capillary DBT +DCE & Outer metallic capillary DCE	×	×	×
Figure A4.26	1.5	Inner silica capillary DBT +DCE & Outer metallic capillary EtOTf+DCE	√	√	√
Figure A4.27	0.0	Inner silica capillary DBT +DCE & Outer metallic capillary EtOTf+DCE	√	√	√

^aM represents DBT.



WNX-WB-106_1-1 (4 kV) #1-51 RT: 0.05-2.98 AV: 51 NL: 1.12E5
T: FTMS + p ESI Full ms [50.00-300.00]



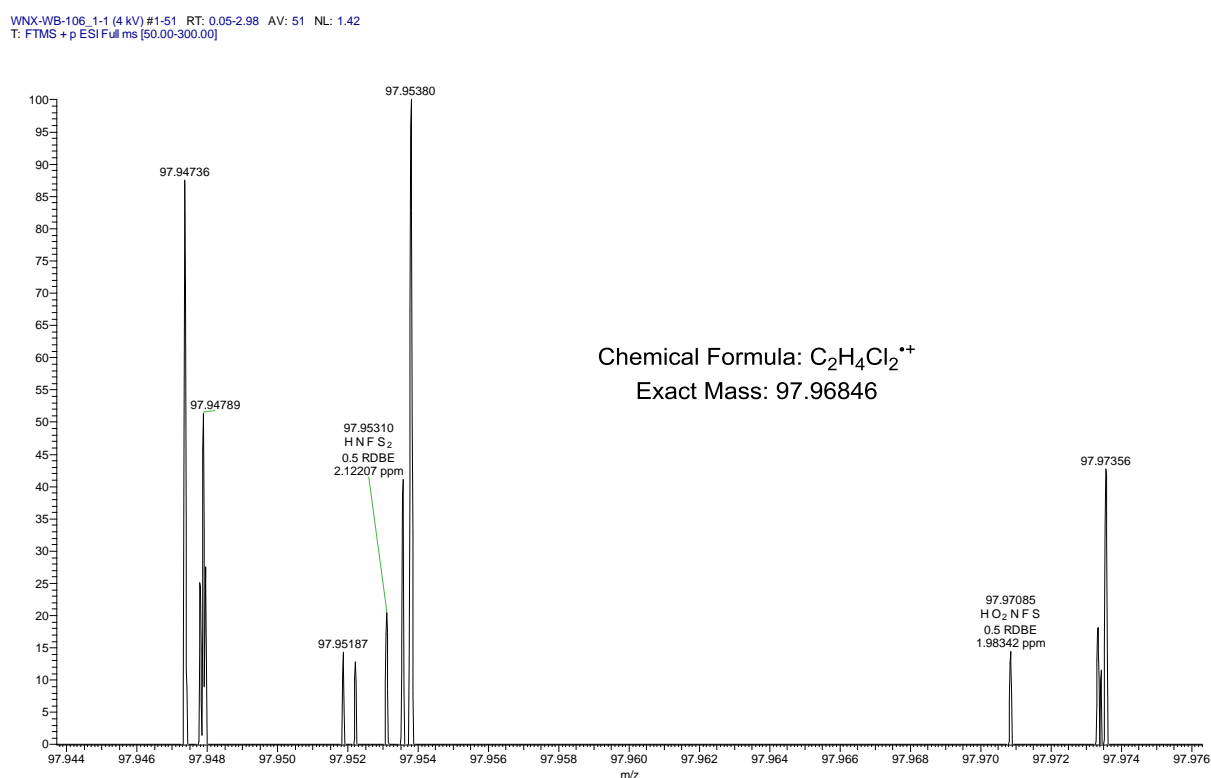
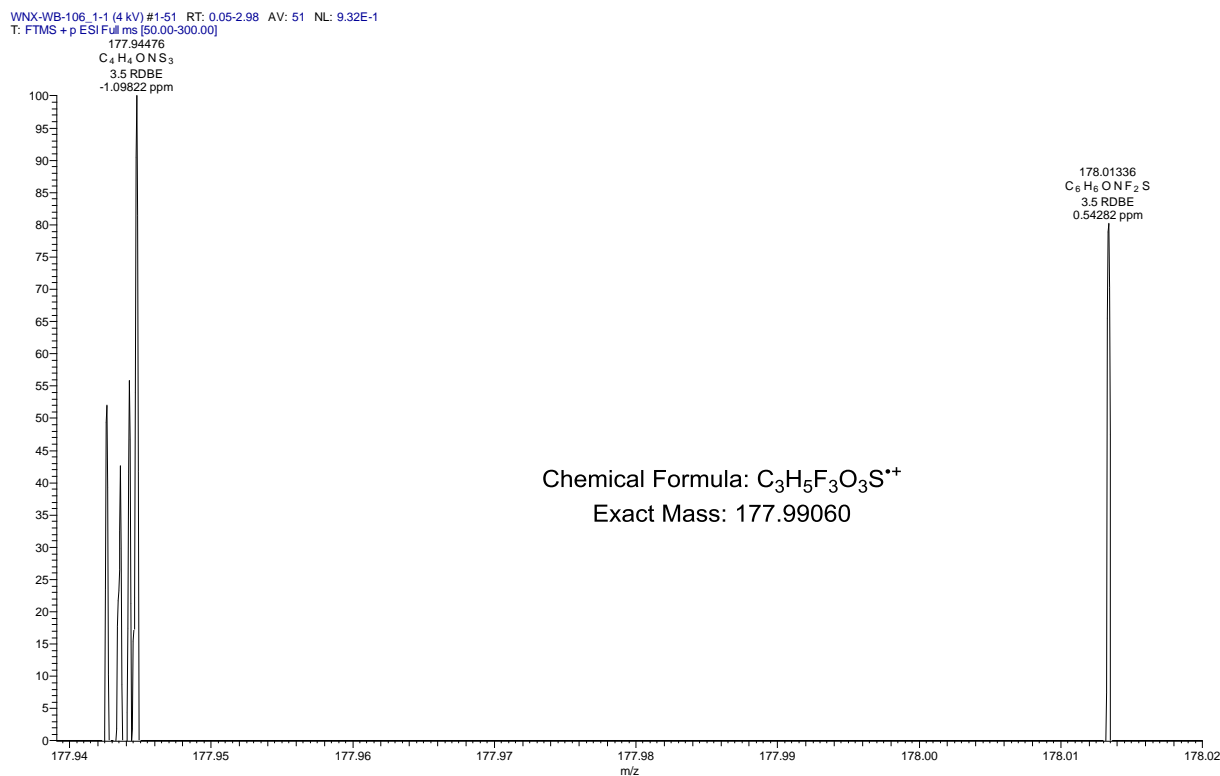
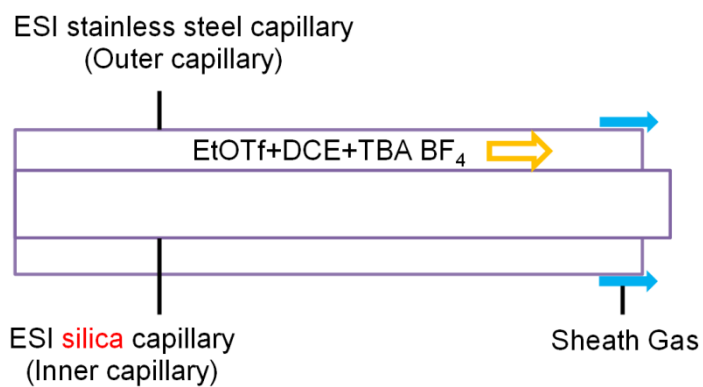
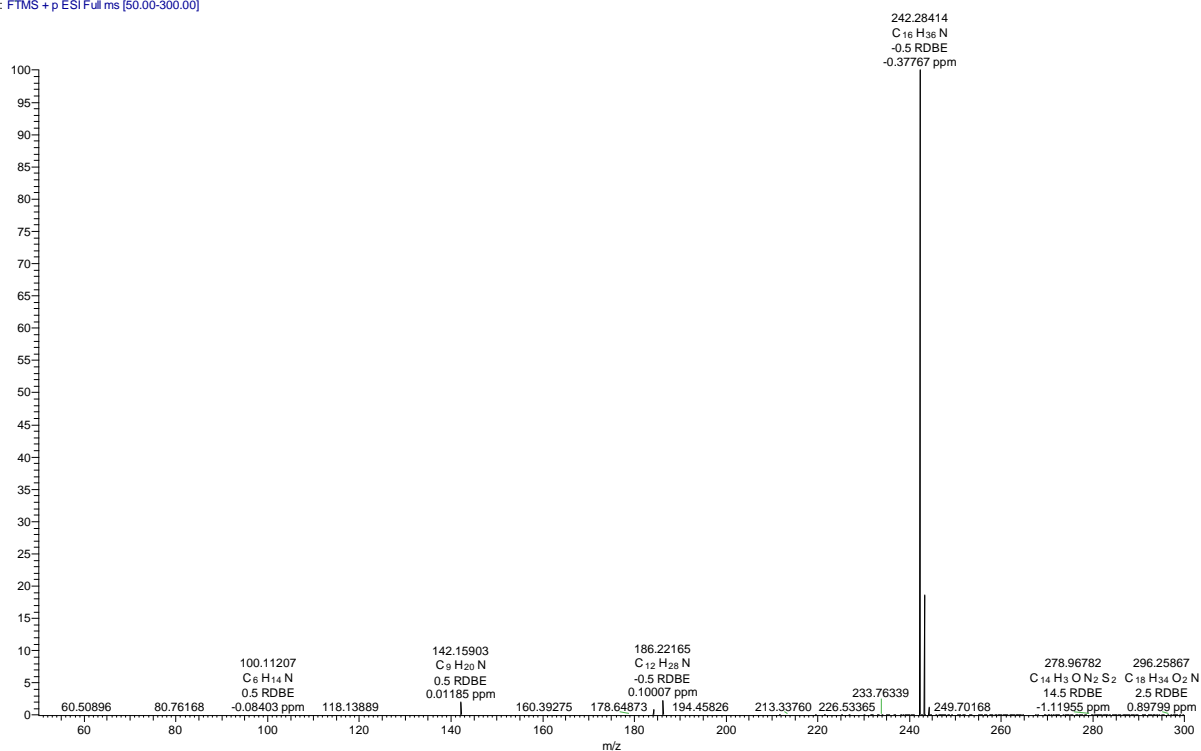


Figure A4.21: The mass spectra obtained from the ESI capillary set-up where the silica capillary locates 1.5 mm outside of the outer metallic capillary on ESI(+) 7 T FT-ICR MS. As expected, the reference peak from TBA BF_4 is observed suggesting that our ESI setup works well. No characteristic peaks from C_2H_5OTf or DCE are observed without contact with the metal needle.



WNX-WB-106_2-2 (4 kV) #1-66 RT: 0.01-3.51 AV: 66 NL: 2.61E7
T: FTMS + p ESI Full ms [50.00-300.00]



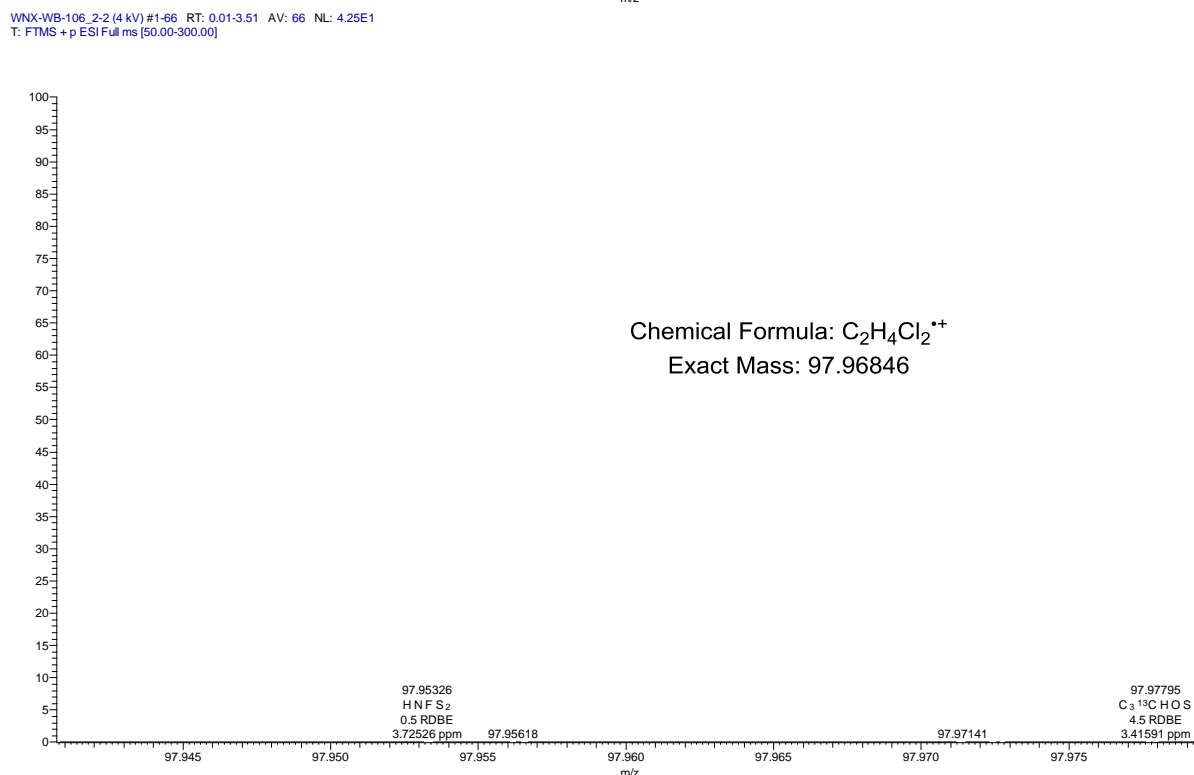
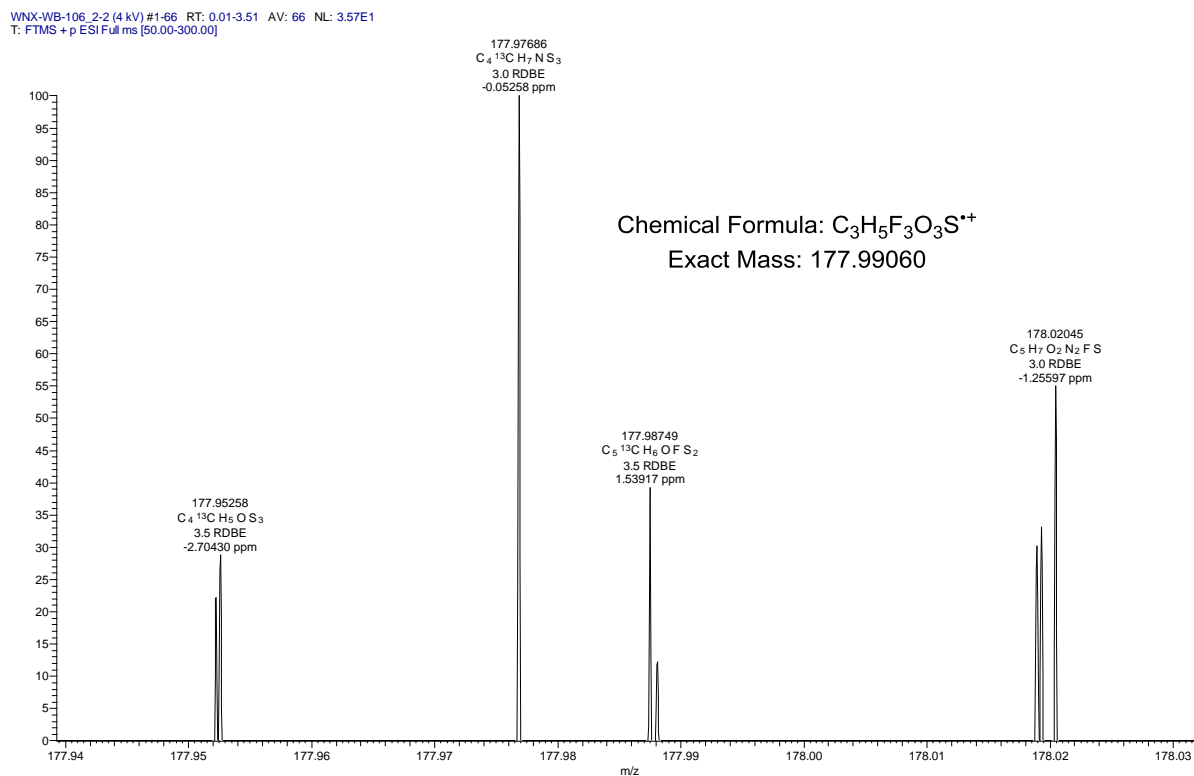
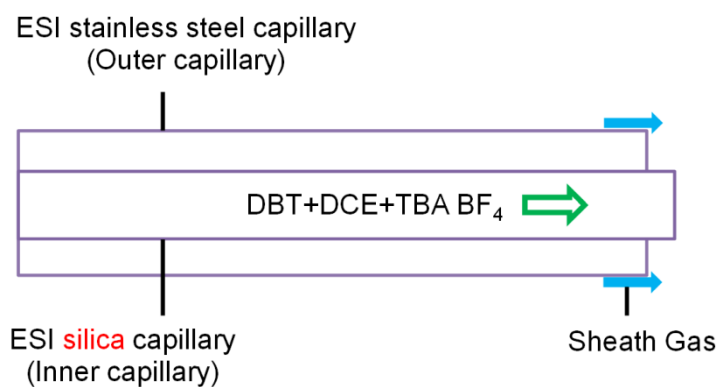
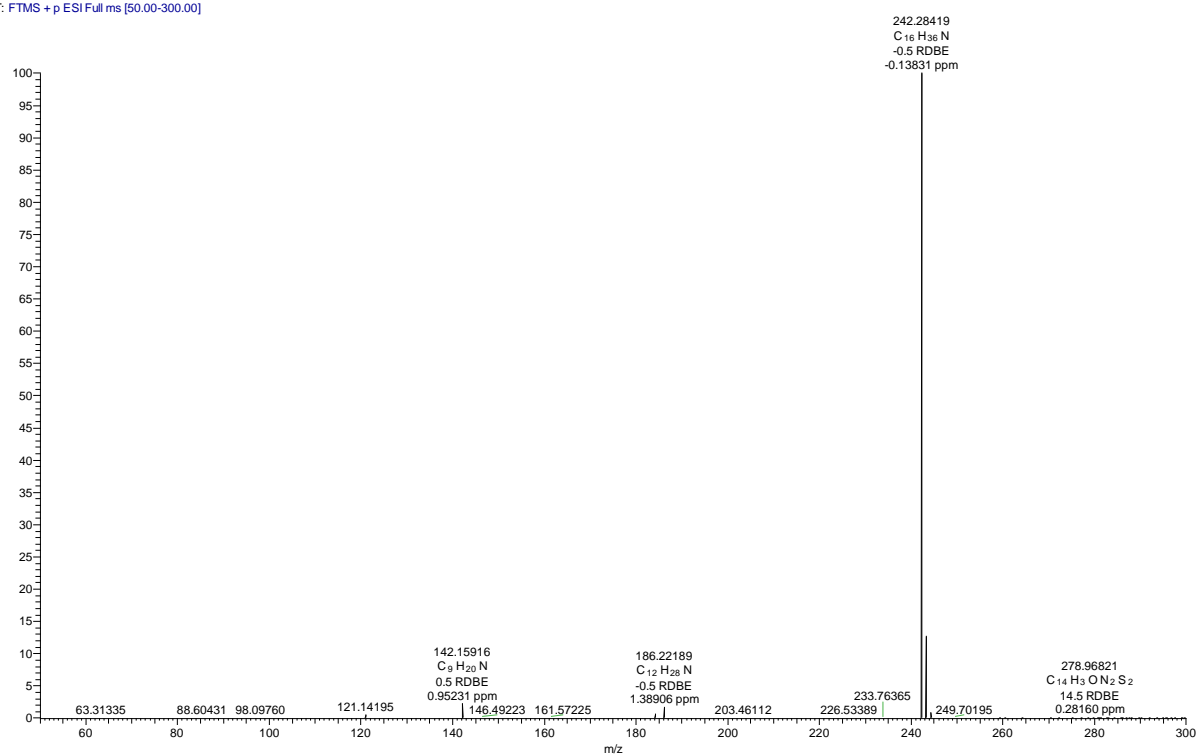


Figure A4.22: The mass spectra obtained from the ESI capillary set-up where the silica capillary locates 1.5 mm outside of the outer metallic capillary on ESI(+) 7 T FT-ICR MS. As expected, the reference peak from TBA BF_4 is observed suggesting that our ESI setup works well. No characteristic peaks from C_2H_5OTf or DCE are observed, and the explanation for which can be given as follows: radical cation of C_2H_5OTf or DCE is short-lived species and

cannot be detected on the time scale of FT-ICR MS; or the active open-shell species have reacted with other nucleophilic species and vanished before detection.



WNX-WB-106_3-1 (4 kV) #1-77 RT: 0.03-4.49 AV: 77 NL: 4.90E4
T: FTMS + p ESI Full ms [50.00-300.00]



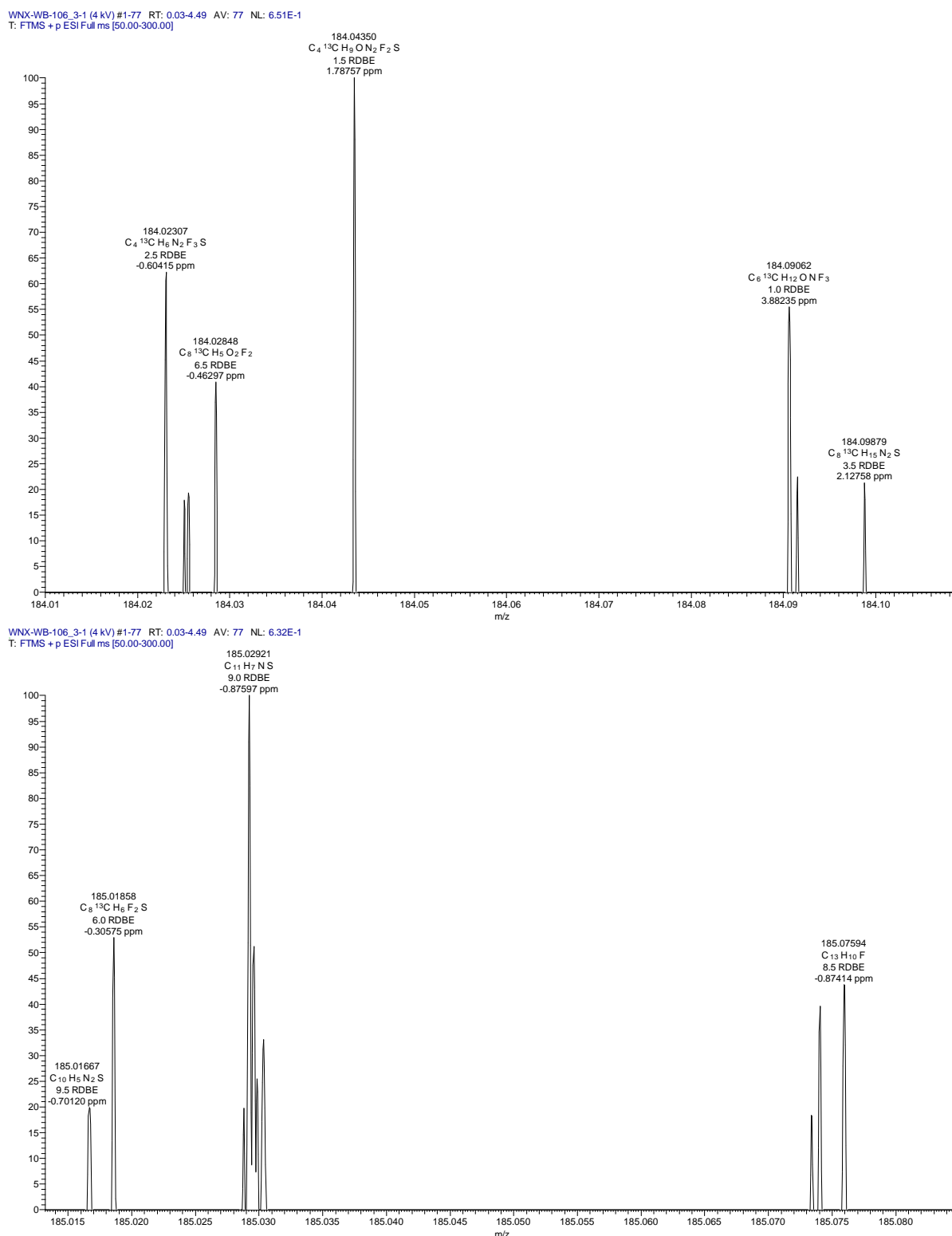
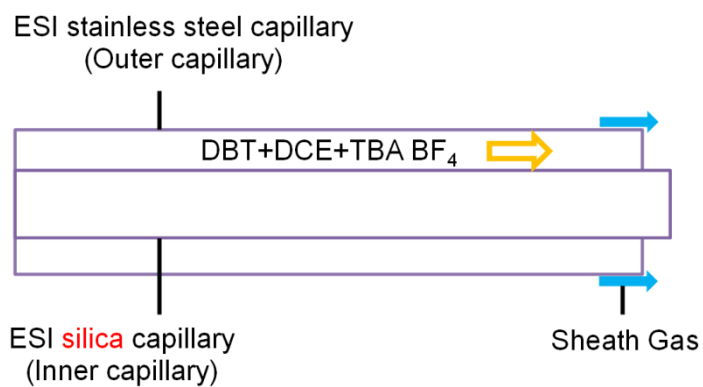
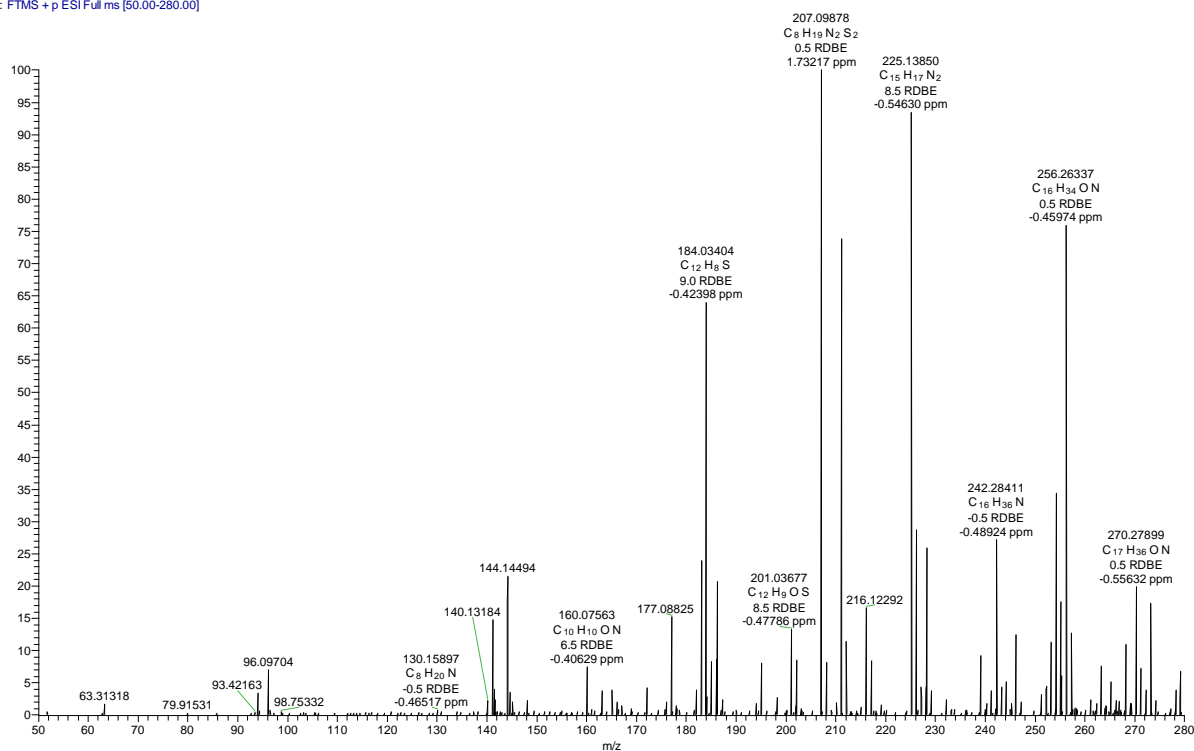


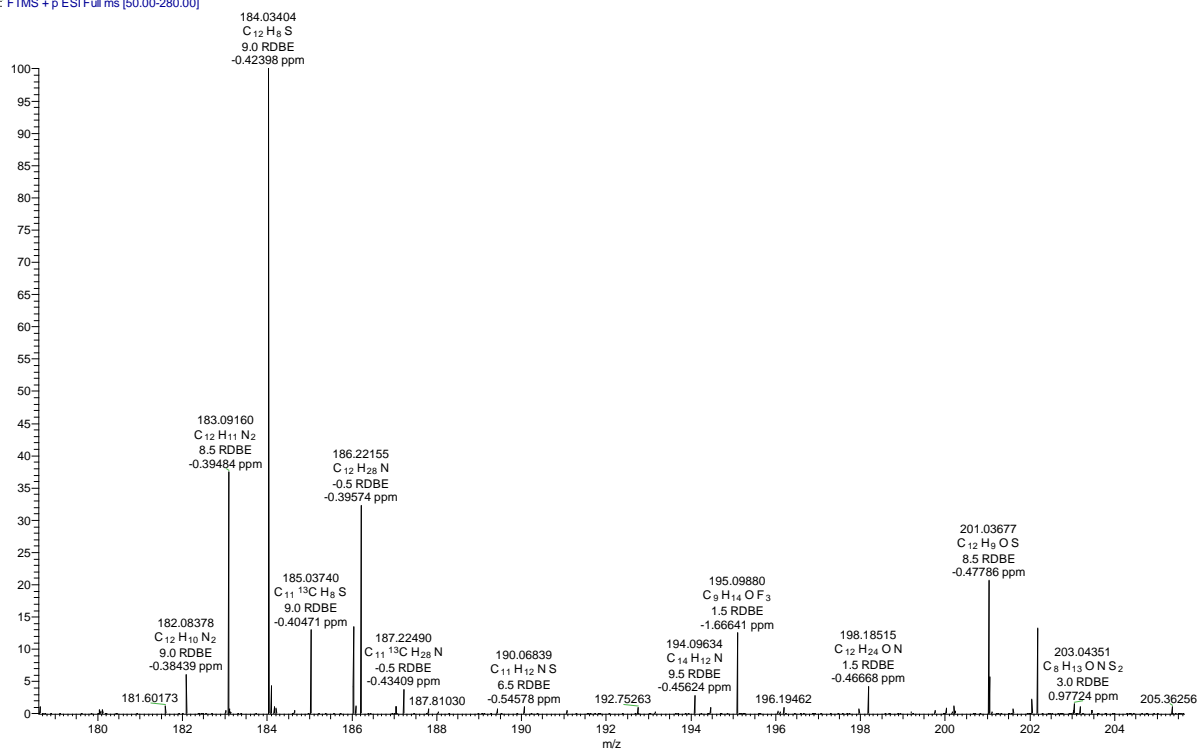
Figure A4.23: The mass spectra obtained from the ESI capillary set-up where the silica capillary locates 1.5 mm outside of the outer metallic capillary on ESI(+) 7 T FT-ICR MS. As expected, the reference peak from TBA BF₄ is observed suggesting that our ESI setup works well. No characteristic peaks from DBT or DCE are observed without contact with the metal needle.



WNX-WB-106_4 (4.0 kV) #1-124 RT: 0.00-4.01 AV: 124 NL: 5.72E3
T: FTMS + p ESI Full ms [50.00-280.00]



WNX-WB-106_4 (4.0 kV) #1-124 RT: 0.00-4.01 AV: 124 NL: 3.66E3
T: FTMS + p ESI Full ms [50.00-280.00]



WNX-WB-106_4 (4.0 kV) #1-124 RT: 0.00-4.01 AV: 124 NL: 4.76E2
T: FTMS + p ESI Full ms [50.00-280.00]

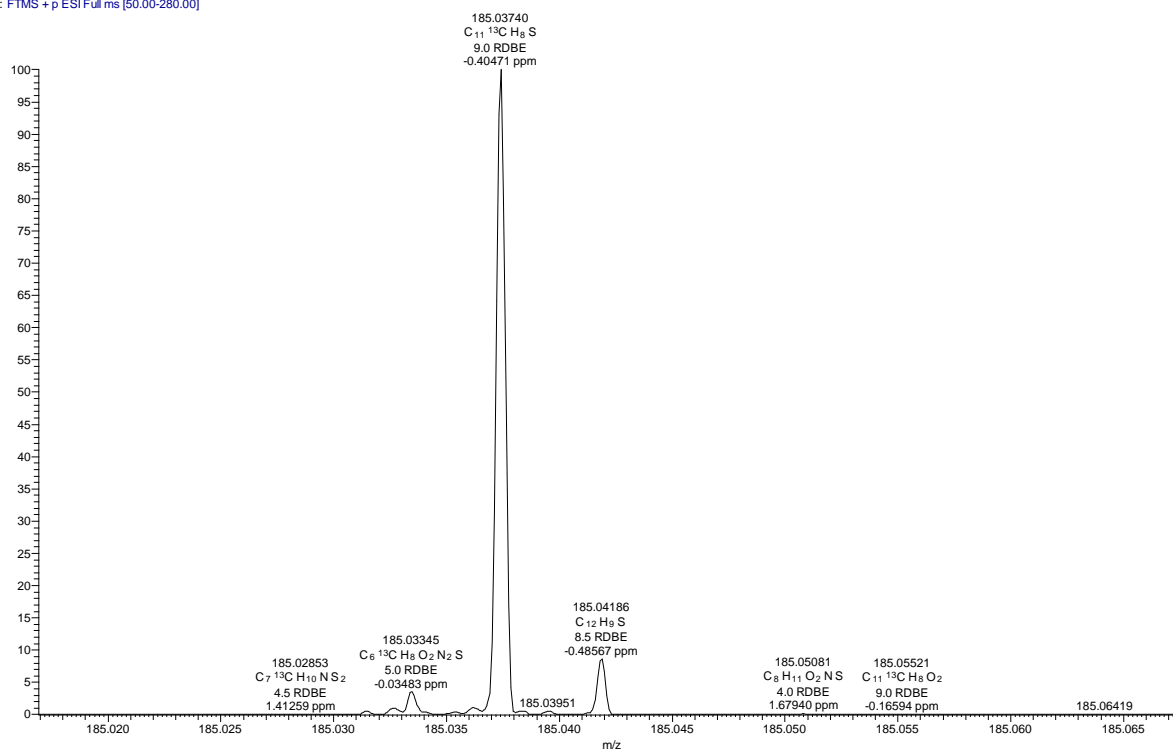
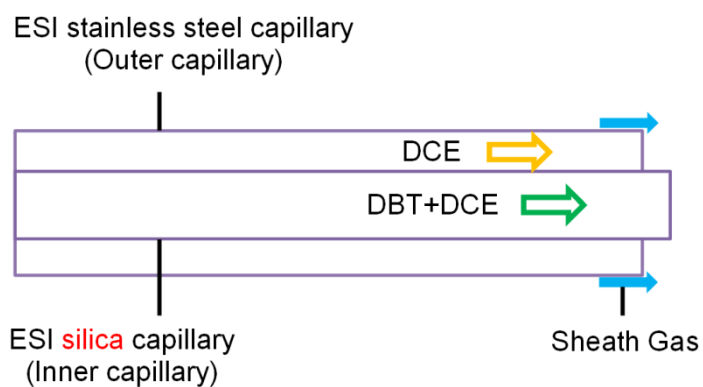
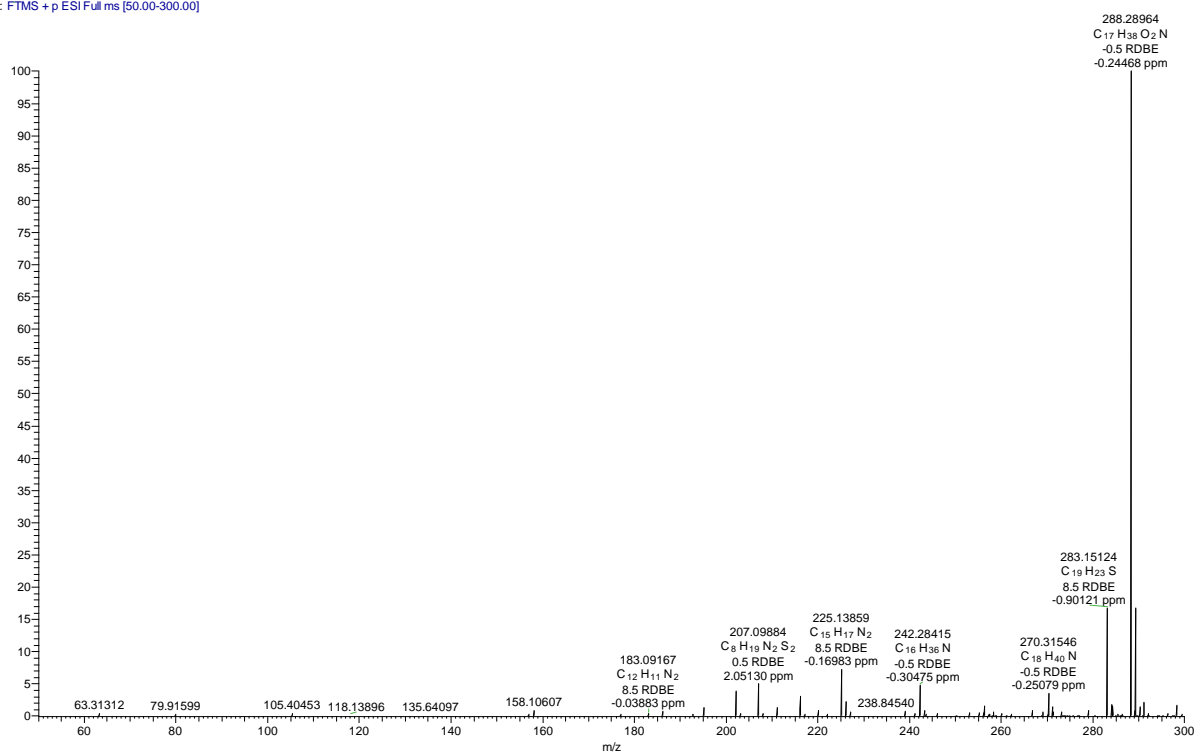


Figure A4.24: The mass spectra obtained from the ESI capillary set-up where the silica capillary locates 1.5 mm outside of the outer metallic capillary on ESI(+) 7 T FT-ICR MS. As expected, the reference peak from TBA BF₄ is observed suggesting that our ESI setup works well. Radical cation from DBT is observed at m/z 184.03412 when contacting with the metal

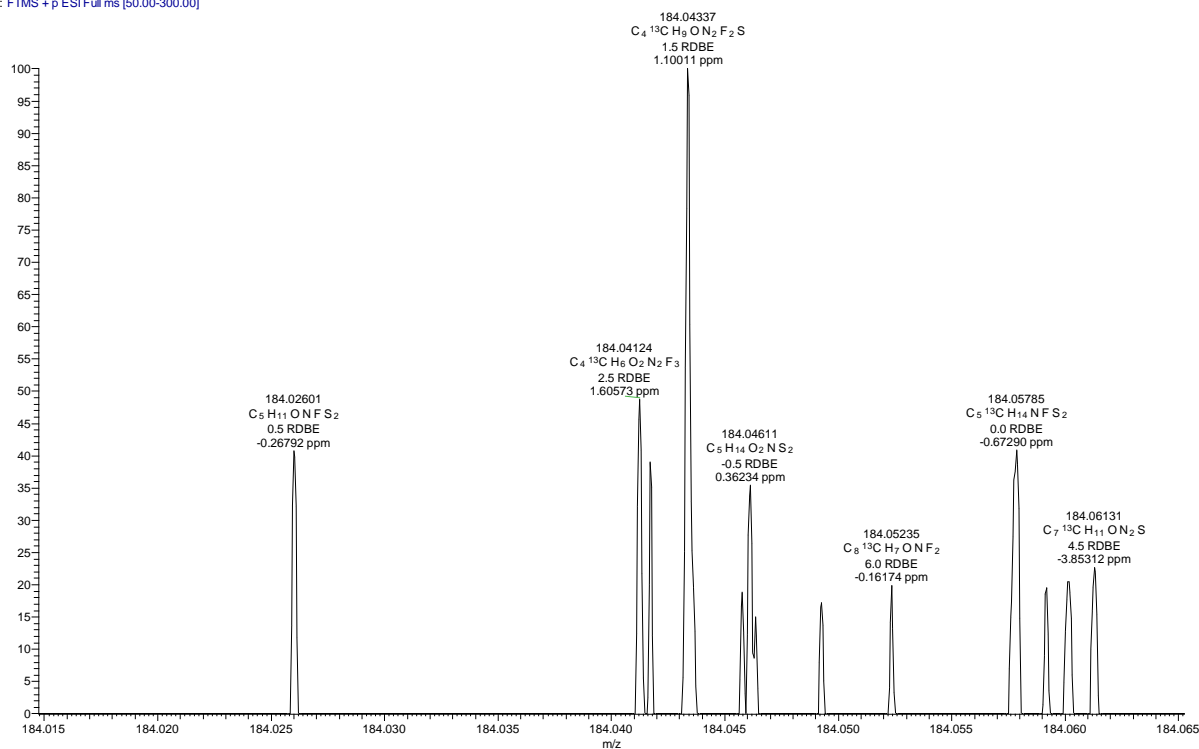
surface that connecting to a high voltage supply. A tiny protonated peak is also observed at m/z 185.04195.



WNX-WB-106 8 (4 #1-79 RT: 0.00-4.58 AV: 79 NL: 2.24E4
T: FTMS + p ESI Full ms [50.00-300.00])



WNX-WB-106_8 (4 #1-79 RT: 0.00-4.58 AV: 79 NL: 1.03
T: FTMS + p ESI Full ms [50.00-300.00])



WNX-WB-106_8 (4 #1-79 RT: 0.00-4.58 AV: 79 NL: 1.18
T: FTMS + p ESI Full ms [50.00-300.00])

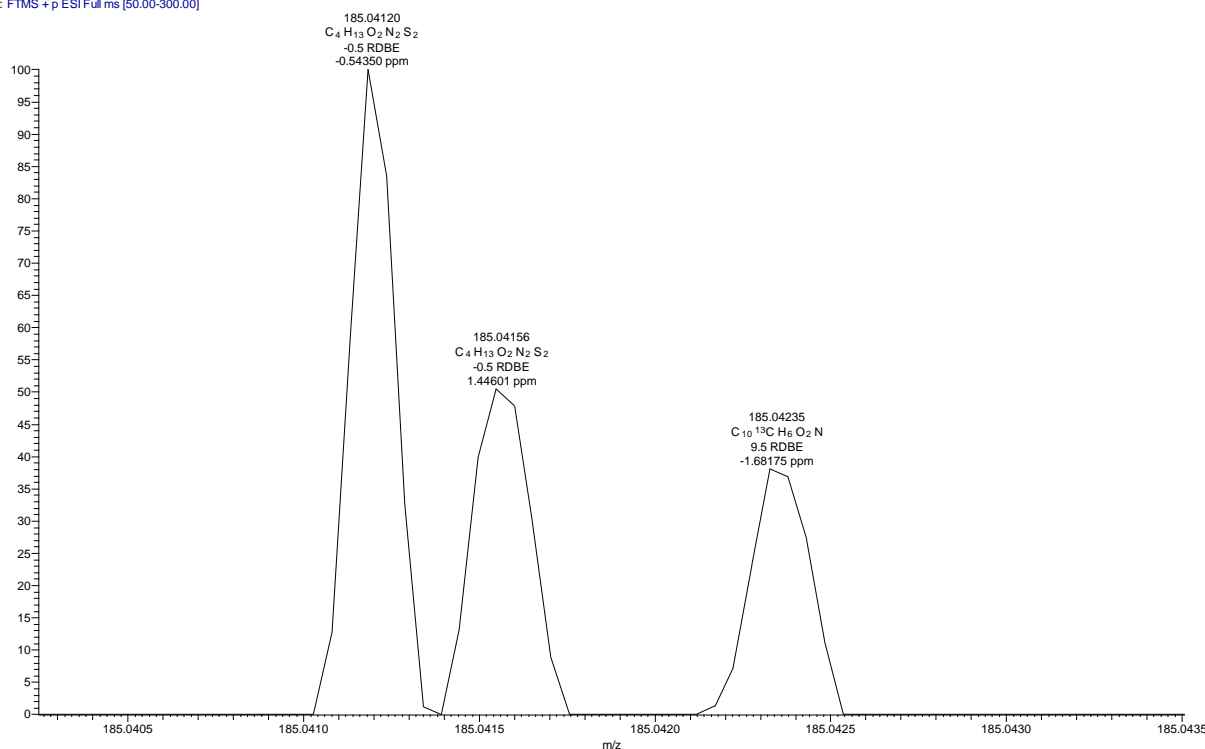
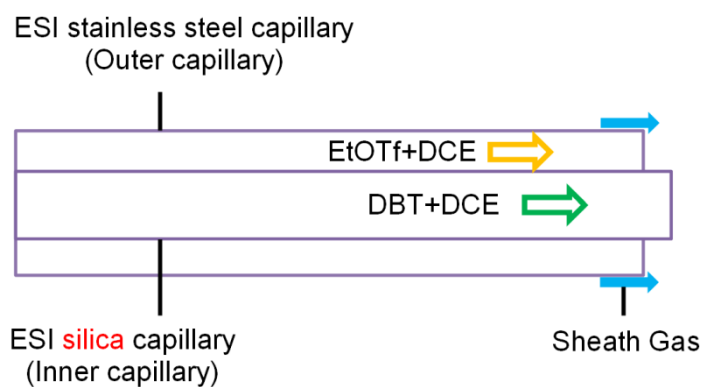
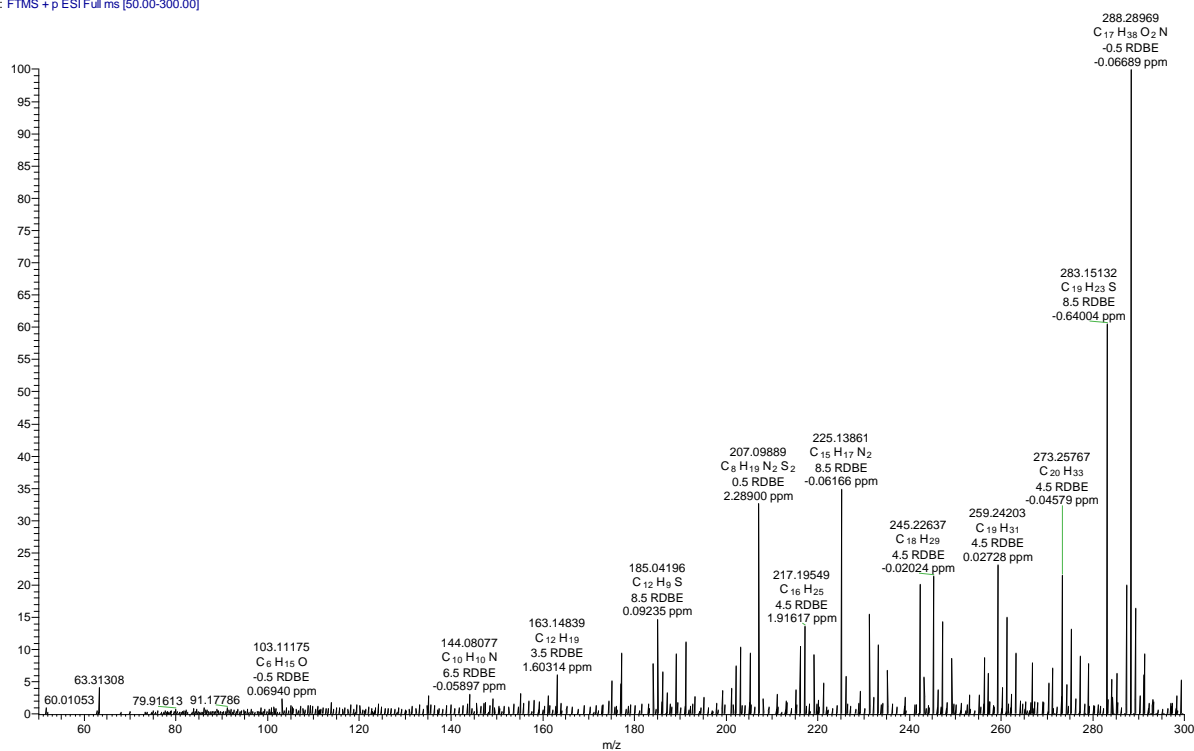


Figure A4.25: The mass spectra obtained from the ESI capillary set-up where the silica capillary locates 1.5 mm outside of the outer metallic capillary on ESI(+) 7 T FT-ICR MS. From the above experiments (**Figure A4.22 – A4.25**), we know that our ESI set-up works

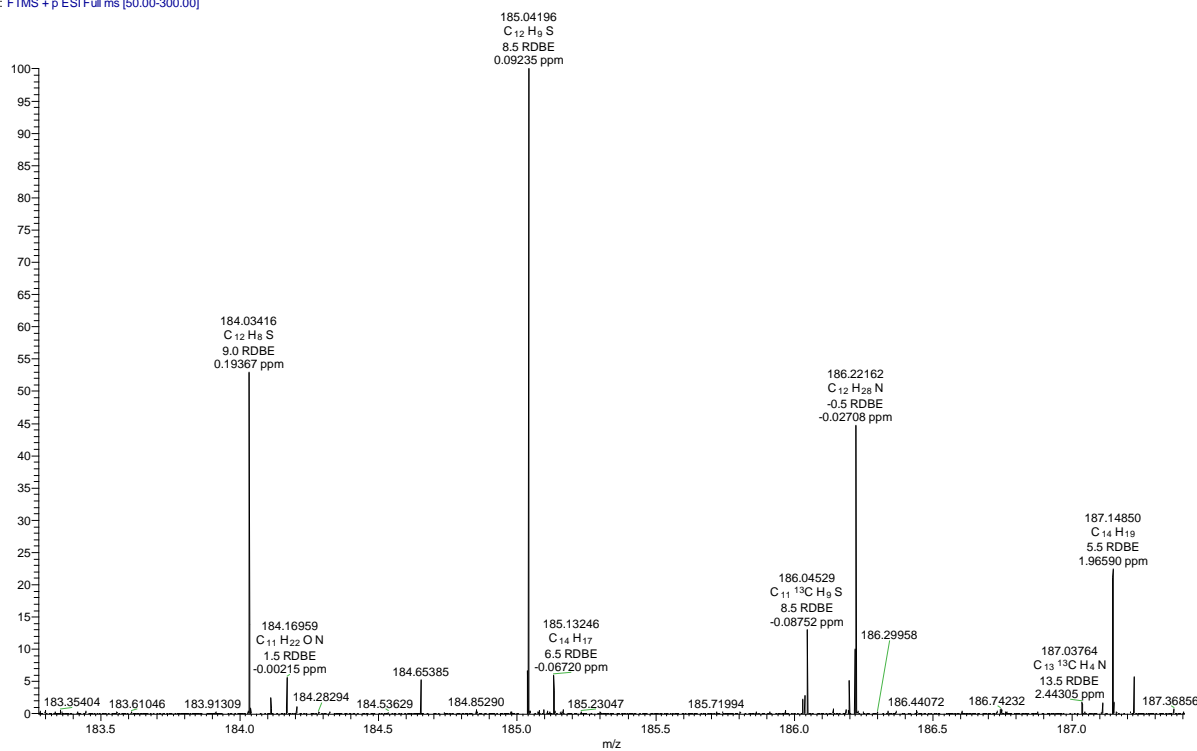
well. In order to reduce the suppression from TBA BF_4 , Only solvent DCE is used from now on. No characteristic peaks from DBT are observed in this case.



WNX-WB-106_9 (4 #1-104 RT: 0.00-6.03 AV: 104 NL: 3.20E3
T: FTMS + p ESI Full ms [50.00-300.00])



WNX-WB-106_9 (4 #1-104 RT: 0.00-6.03 AV: 104 NL: 4.70E2
T: FTMS + p ESI Full ms [50.00-300.00])



WNX-WB-106_9 (4 #1-104 RT: 0.00-6.03 AV: 104 NL: 6.45E1
T: FTMS + p ESI Full ms [50.00-300.00])

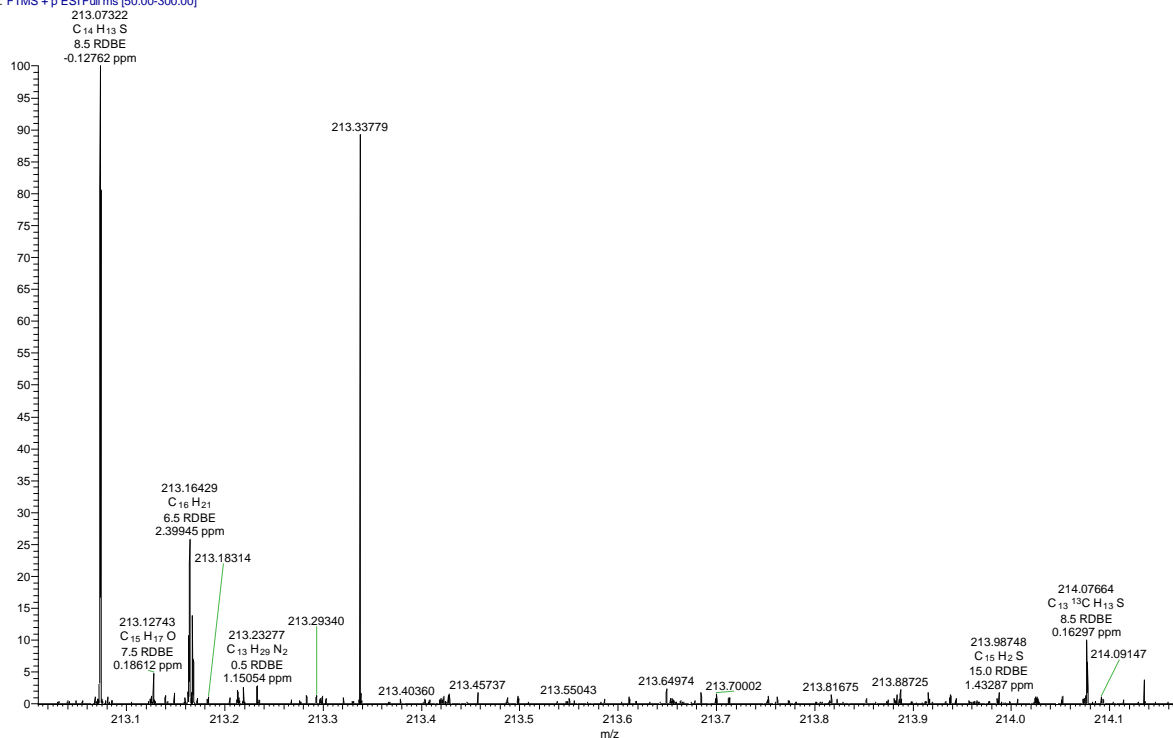
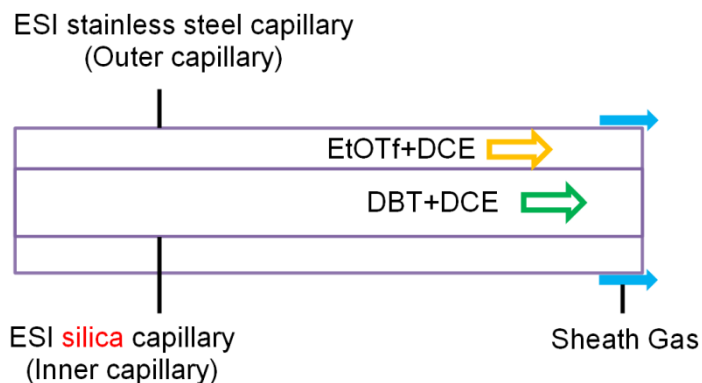
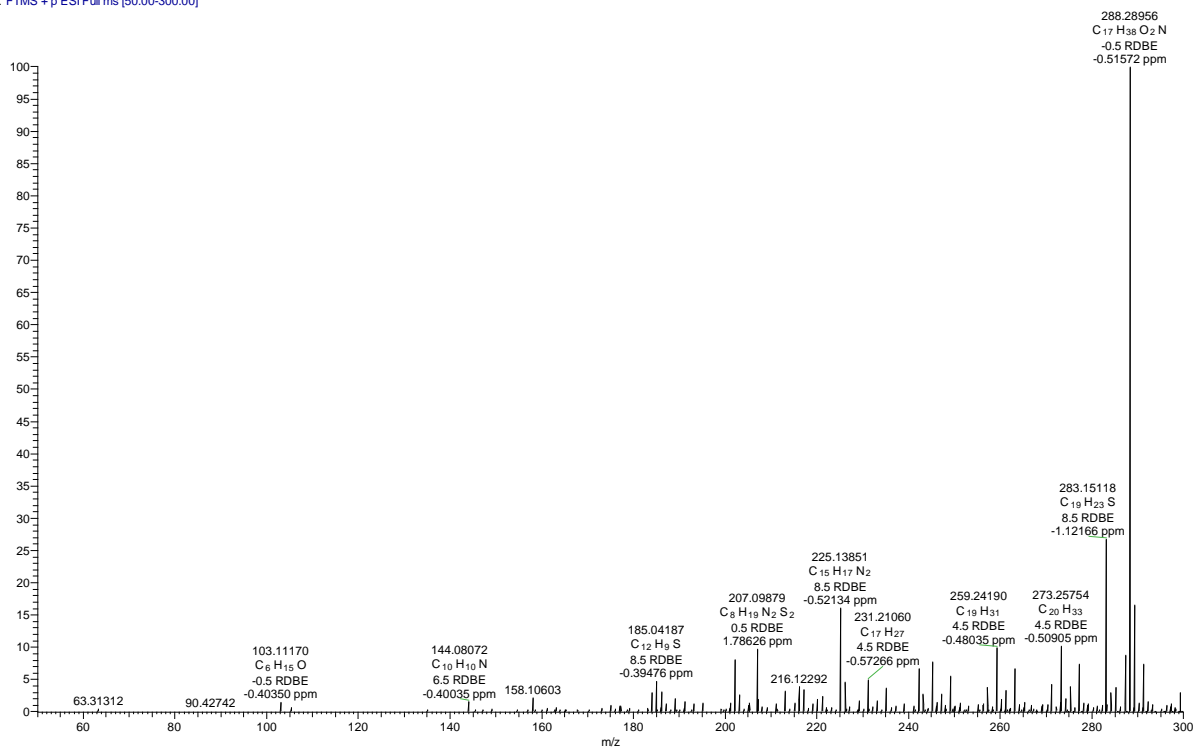


Figure A4.26: The mass spectra obtained from the ESI capillary set-up where the silica capillary locates 1.5 mm outside of the outer metallic capillary on ESI(+) 7 T FT-ICR MS. Characteristic peaks from DBT are observed at m/z 213.07325, 185.04195 and 184.03412

without DBT directly contact with the metal surface, explanation can be given as: first C_2H_5OTf is oxidized by losing one electron to produce a lower lying LUMO active species, and then DBT reacts with $[C_2H_5OTf]^{*+}$ to produce the corresponding $[M+C_2H_5]^+$ via nucleophilic substitution and $[M]^{*+}$ via charge transfer reaction in the gas-phase. For the production of $[M+H]^+$, H_2O in the air is assumed to participate in the production together with $[C_2H_5OTf]^{*+}$ in the gas phase.



WNX-WB-106_10 (4#1-139 RT: 0.00-7.97 AV: 139 NL: 2.10E4
T: FTMS + p ESI Full ms [50.00-300.00])



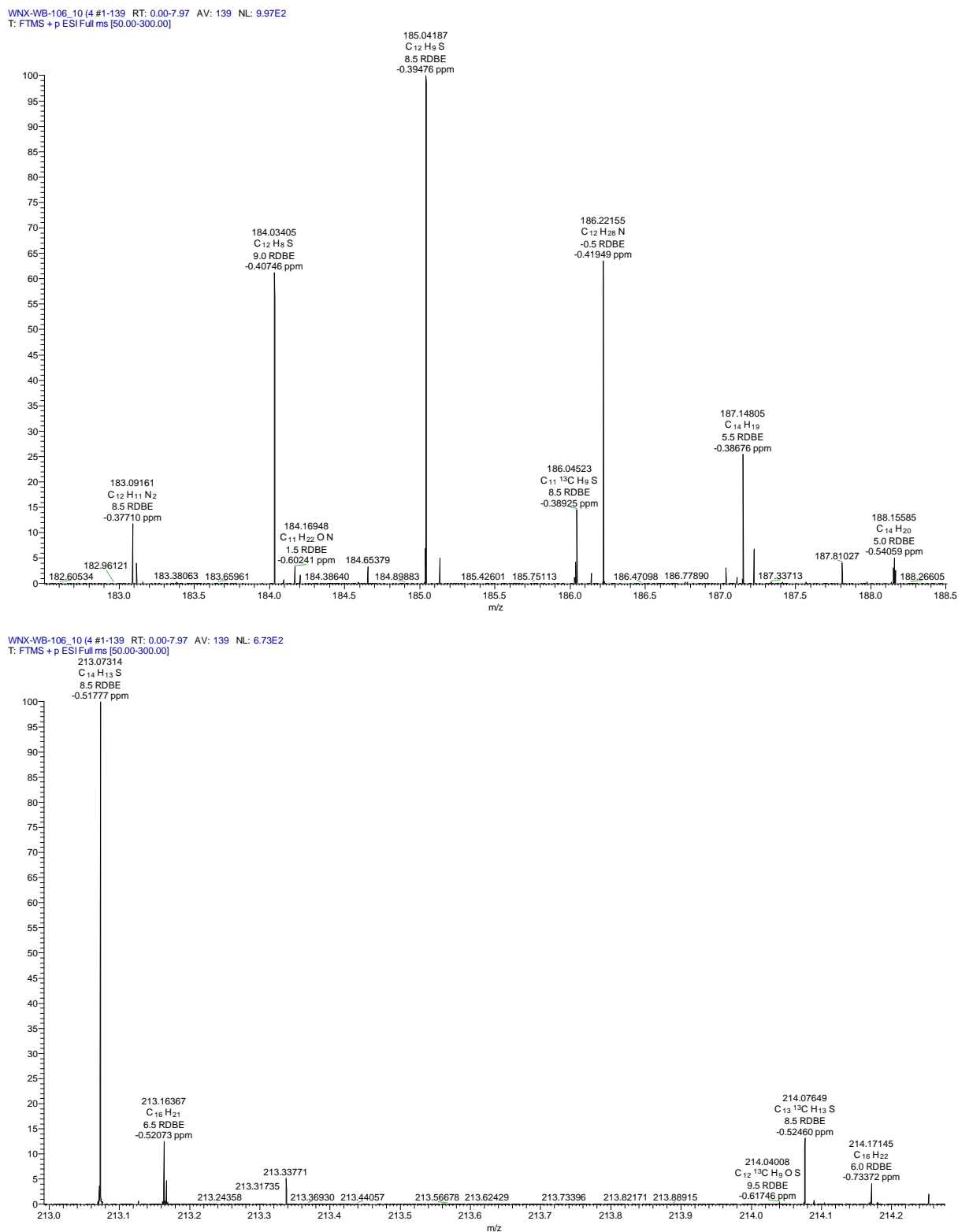


Figure A4.27: The mass spectra obtained from the ESI capillary set-up where the silica capillary locates 0.0 mm outside of the outer metallic capillary on ESI(+) 7 T FT-ICR MS. Characteristic peaks from DBT are observed at m/z 184.03412, 185.04195 and 213.07325 without DBT directly contacting with the metal surface, explanation can be given as same as in **Figure A4.26**. Moreover, the intensity of the characteristic peaks increases as contacting time interval of these two solutions increases.

.The influence of the silica capillary position on reaction

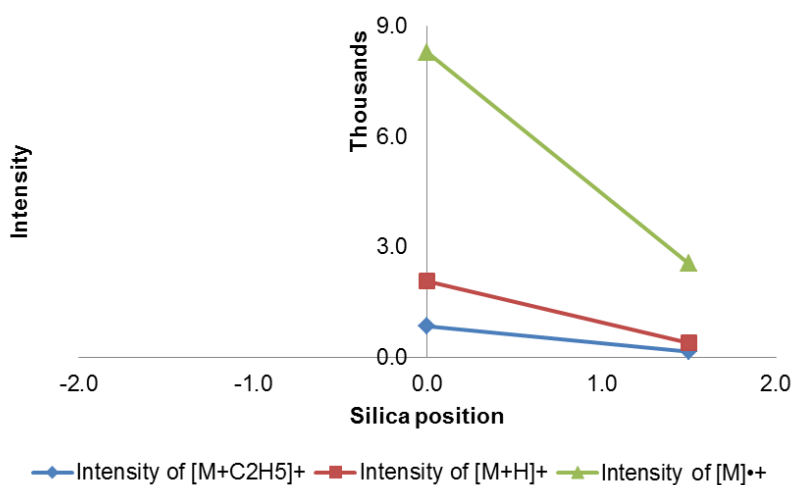


Figure A4.28: Evaluation of the influence of electrochemistry on the intensity of characteristic peaks of $[M+C_2H_5]^+$, $[M+H]^+$ and $[M]^{++}$ through silica position in 1-D space for mechanism study. The data are obtained from **Figure A4.26 - A4.27**.

Conclusion in MS experimental section of “How does it happen?”

- Reference peak from TBA BF_4 indicates that our ESI set up works normally.
- C_2H_5OTf radical cation is experimentally not observed under ESI(+) FT-ICR MS, which need to be further confirmed by calculation based on quantum mechanism.
- DBT radical cation is experimentally observed under ESI FT ICR MS.
- As the silica capillary goes further inside into the stainless steel capillary, the intensity of our desired peaks, $[M+C_2H_5]^+$, $[M+H]^+$ and $[M]^{++}$, increases.

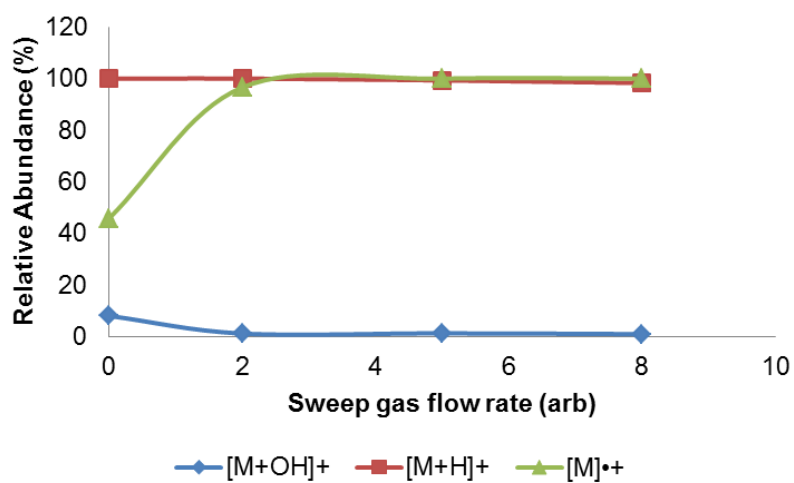
Experimental explanation of protonated peaks to DBT, $[M+H]^+$ 

Figure A4.29: Comparison of mass spectra obtained from sweep gas flow rates. As the sweep gas flow rate increases, the relative abundance of the $[M]^{\bullet+}$ increases, but the relative abundance of the $[M+OH]^+$, $[M+H]^+$ decreases.

Theoretical calculation for “in-ESI” reaction

The second reaction, which involves dibenzothiophene (DBT) and ethyl trifluoromethane- sulfonate (EtOTf) in DCE, was employed as a prototype for the reactions in ESI-MS. The reaction mechanisms and energy profile for the others were not calculated, but these were expected to be similar to present one.

Based on the proposed mechanism, the solvated reactants, DBT and EtOTf, are ionized on the anode first due to the high voltage. The 1st ionization energies for both reactants in DCE were calculated at the PBE0-GD3/6-311+G(d,p) level of theory and given in **Figure A4.30**.

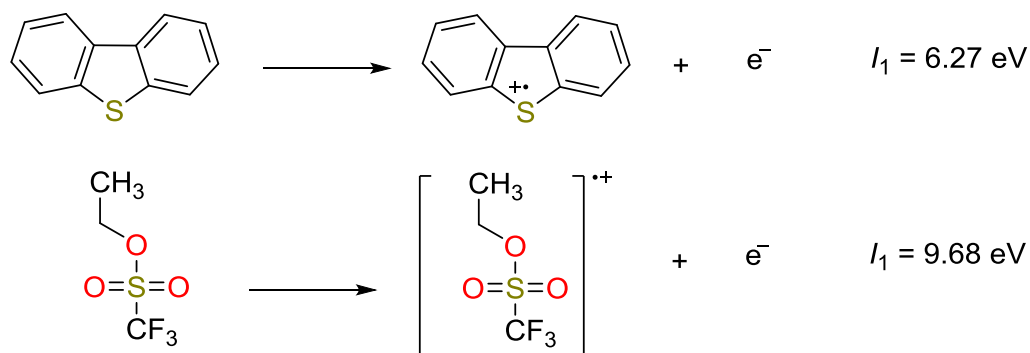


Figure A4.30: The calculated 1st ionization energies (I_1) for dibenzothiophene and ethyl trifluoromethanesulfonate in the 1, 2-dichloroethane solution.

After the ionization process, there would be several channels where collisions may occur among the molecular cations and neutral species. The collisions between radical cations were not considered herein due to the overwhelming electrostatic repulsions.

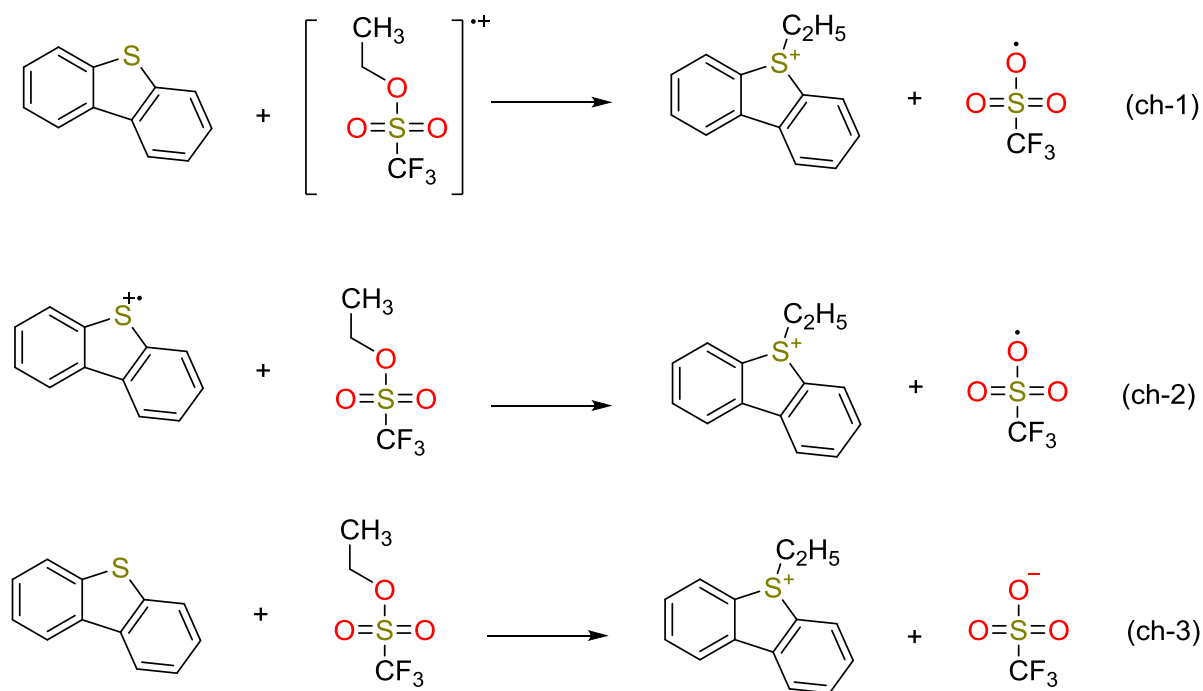


Figure A4.31: The possible collision channels for ethyl dibenzothiophene cation in the ESI-MS experiments.

The ethyl dibenzothiophene cation (EtDBT⁺) may be produced through three possible channels (as listed in **Figure A4.31**). The collisions amongst molecular species of similar charges may be excluded easily due to the overwhelming electrostatic repulsions. According to the calculated $\Delta_r G^\circ$ only the first channel seems to be plausible for EtDBT⁺ (see **Table A4.5**).

Two additional molecular cations were also observed in the ESI-MS experiments, i.e. dibenzothiophene radical cation (DBT^{•+}) and the protonated dibenzothiophene (DBTH⁺). DBT^{•+} may be generated either by ionization on the anode (see above) or via a simple charge-transfer reaction (See **Figure A4.32**), which can be highly exergonic.

Table A4.5: The changes of the standard Gibbs free energy ($\Delta_r G^\circ$, in kcal/mol) for the possible collision channels that produces the molecular cations detected in the ESI-MS experiments

channel	ch-1	ch-2	ch-3
$\Delta_r G^\circ$	-38.32	29.34	18.76

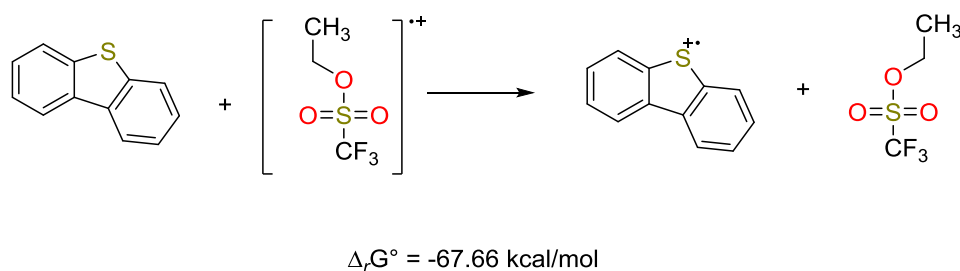


Figure A4.32: The charge-transfer reaction that produces $\text{DBT}^{\bullet+}$ in the ESI-MS experiments.

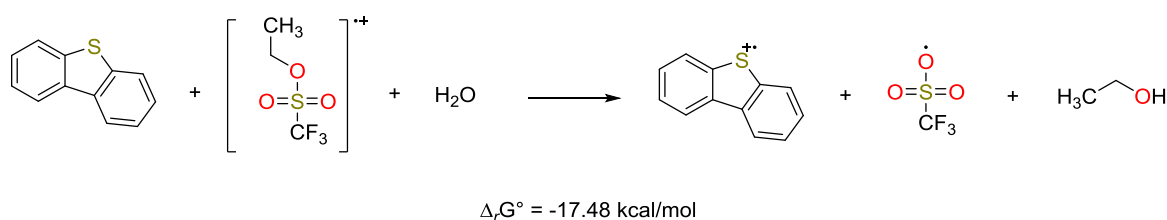


Figure A4.33: The gas-phase reaction that produces DBTH^+ in the ESI-MS experiments.

Due to the complicated hydrogen bondings it can be very difficult to determine the true conformation of water molecule(s)[137, 138]. We proposed the reaction involving a single water molecule, e.g. H_2O , as a prototype and the change of the standard Gibbs free energy was predicted to be -17.48 kcal/mol. Therefore the detected DBTH^+ in the ESI-MS experiment might be produced via this channel.

```
# EtDBT radical cation
28
Ch 1 Mul 1 (E,H,G)  -938.63271862  -938.389388  -938.441804
C      -2.052684    -1.727550    0.404500
C      -1.001463    -0.882855    0.063735
C      -1.313834     0.417757   -0.347256
C      -2.603406     0.906820   -0.442749
C      -3.635682     0.043578   -0.088327
C      -3.358137    -1.256034    0.329727
```

S	0.161097	1.342627	-0.721714	
C	1.195972	-0.064369	-0.379459	
C	0.431993	-1.159343	0.043083	
C	1.099279	-2.340933	0.347297	
C	2.482582	-2.395765	0.221483	
C	3.212962	-1.294800	-0.219434	
C	2.569569	-0.103261	-0.540085	
C	0.339857	2.366018	0.804822	
C	1.675364	3.073282	0.845758	
H	0.545283	-3.214835	0.670955	
H	3.001311	-3.317947	0.457727	
H	4.288824	-1.365875	-0.328173	
H	3.127074	0.748654	-0.911361	
H	-2.811955	1.913542	-0.786892	
H	-4.662009	0.385949	-0.149745	
H	-4.176963	-1.915415	0.594354	
H	-1.856946	-2.745686	0.721442	
H	-0.500331	3.062610	0.741920	
H	0.182571	1.680434	1.639615	
H	1.827214	3.719179	-0.021997	
H	1.699147	3.704107	1.737845	
H	2.505004	2.367983	0.923160	
# OTf radical				
8				
Ch 0 Mul 2 (E,H,G)	-960.81951860	-960.785319	-960.828640	
O	-1.287556	-0.748010	-1.173495	
S	-0.863767	0.048308	-0.001809	
C	0.993703	-0.007363	0.000106	
F	1.436808	0.614651	1.075878	
O	-1.288269	-0.725927	1.186501	
O	-1.241367	1.442210	-0.011385	
F	1.390972	-1.264222	0.010807	
F	1.438397	0.596801	-1.084982	
# DBT				
21				
Ch 0 Mul 1 (E,H,G)	-859.74150431	-859.569431	-859.613481	
C	0.000000	2.622744	0.959607	
C	0.000000	1.250227	0.728659	
C	0.000000	0.723338	-0.575152	
C	0.000000	1.603998	-1.659696	
C	0.000000	2.969425	-1.435706	
C	0.000000	3.475508	-0.132282	
C	0.000000	-0.723338	-0.575152	
C	0.000000	-1.250227	0.728659	
S	0.000000	0.000000	1.954808	
C	0.000000	-2.622744	0.959607	
C	0.000000	-3.475508	-0.132282	
C	0.000000	-2.969425	-1.435706	
C	0.000000	-1.603998	-1.659696	
H	0.000000	1.215684	-2.672940	
H	0.000000	3.654014	-2.276904	
H	0.000000	4.548276	0.028649	
H	0.000000	3.015984	1.970146	
H	0.000000	-3.015984	1.970146	
H	0.000000	-4.548276	0.028649	
H	0.000000	-3.654014	-2.276904	
H	0.000000	-1.215684	-2.672940	
# EtOTf radical cation				
15				
Ch 1 Mul 2 (E,H,G)	-1039.64568531	-1039.542829	-1039.595892	
C	-2.330628	-0.261332	-0.450719	
C	-3.611523	-0.621590	0.282562	
O	-1.221582	-0.377900	0.317438	
S	0.221689	0.855277	0.006251	
C	1.517636	-0.575667	0.007036	
F	2.650908	-0.036240	-0.320892	
O	0.215142	1.599497	1.219314	
O	-0.024561	1.339148	-1.314053	
F	1.526613	-1.073625	1.203734	
F	1.102980	-1.433409	-0.884570	
H	-2.175955	-1.107805	-1.201299	
H	-2.335457	0.645391	-1.075251	
H	-3.513567	-1.552755	0.841942	
H	-3.831651	0.195074	0.979802	
H	-4.419815	-0.709306	-0.444525	
# DBT radical cation				
21				
Ch 1 Mul 2 (E,H,G)	-859.45740921	-859.286098	-859.331253	
C	0.000000	2.621552	0.984036	
C	0.000000	1.247982	0.711726	
C	0.000000	0.728767	-0.602959	
C	0.000000	1.618467	-1.659375	
C	0.000000	2.997669	-1.397588	
C	0.000000	3.493073	-0.094839	

```
C      0.000000      -0.728767      -0.602959
C      0.000000      -1.247982       0.711726
S      0.000000       0.000000       1.898516
C      0.000000      -2.621552       0.984036
C      0.000000      -3.493073      -0.094839
C      0.000000      -2.997669      -1.397588
C      0.000000      -1.618467      -1.659375
H      0.000000       1.263928      -2.684092
H      0.000000       3.691745      -2.230658
H      0.000000       4.562665       0.077291
H      0.000000       2.990917       2.003326
H      0.000000      -2.990917       2.003326
H      0.000000      -4.562665       0.077291
H      0.000000      -3.691745      -2.230658
H      0.000000      -1.263928      -2.684092
# EtOTf
15
Ch 0 Mul 1 (E,H,G) -1040.04466784   -1039.936785   -1039.985947
C      2.102588      -0.445351       0.428231
C      3.417438      -0.574568      -0.290804
O      1.176681       0.175582      -0.513129
S      -0.161161       0.854783       0.025745
C      -1.298321      -0.615365      -0.030636
F      -2.490736      -0.253972       0.404420
O      -0.602271       1.765525      -0.988183
O      -0.023753       1.216653       1.413108
F      -1.391183      -1.068238      -1.266277
F      -0.815484      -1.574303       0.753142
H      1.690941      -1.416015       0.714148
H      2.172987       0.188397       1.313899
H      3.312512      -1.187076      -1.188444
H      3.797344       0.407413      -0.578751
H      4.145921      -1.051007       0.370554
# OTf anion
8
Ch -1 Mul 1 (E,H,G) -961.00159353   -960.965820   -961.006270
O      -1.235393       1.160091      -0.838230
S      -0.921076       0.000025       0.000143
C      0.937131      -0.000104      -0.000357
F      1.435802      -1.009160       0.730064
O      -1.235430      -1.306070      -0.585250
O      -1.235069       0.146075       1.423836
F      1.435126      -0.127828      -1.239143
F      1.435913       1.136927       0.508746
```

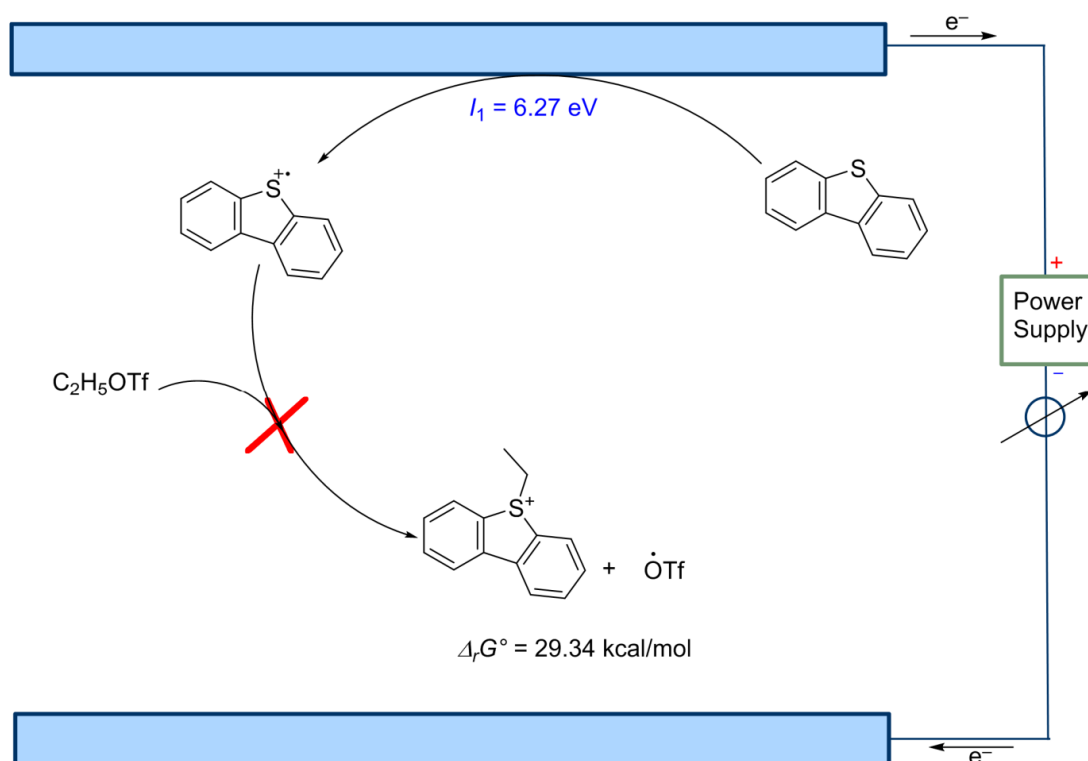


Figure A4.34: The pathway with DBT activated first under ESI(+) FT-ICR MS.

With the changes in free Gibbs energy positive values for the reactions above indicates the pathway from DBT activated first is supposed to be discarded.

Conclusion in this section of “How does it happen?”

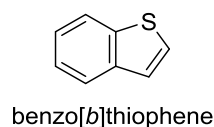
Based on the ESI-MS data and computational data, the “**In-ESI**” reaction can be described into 2 steps: firstly, $\text{C}_2\text{H}_5\text{OTf}$ in solution gets oxidized and forms a low lying LUMO specie; secondly, DBT react with the formed open-shell active species to produce the corresponding characteristic peaks, $[\text{M}+\text{C}_2\text{H}_5]^+$, $[\text{M}+\text{H}]^+$ and $[\text{M}]^{++}$, via ethylation and charge transfer. H_2O in the air together with $[\text{C}_2\text{H}_5\text{OTf}]^{*+}$ and DBT is assumed to produce the protonated peak, $[\text{M}+\text{H}]^+$.

Mass spectra obtained respectively from four sulfur-containing standards with C₂H₅OTf under ESI(+) FT-ICR MS

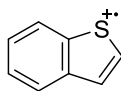
The standard ESI setup with stainless steel as capillary was used for the mass spectra collection of four different sulfur-containing compounds with C₂H₅OTf in DCE.

Sample preparation: dibenzo[*b,d*]thiophene (DBT) and C₂H₅OTf were respectively dissolved in anhydrous DCE at a concentration of 2.43 mM (DBT) and 22.36 mM (C₂H₅OTf) for the ESI experiments. Same concentration of 2.43 mM has been prepared for benzo[*b*]thiophene (BT), benzo[*b*]naphtho[2,1-*d*]thiophene (BNT) and 4,6-dimethyldibenzo[*b,d*]thiophene (4, 6-DM DBT).

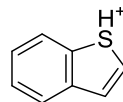
Benzo[*b*]thiophene (BT)



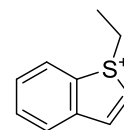
Chemical Formula: C₈H₆S⁺⁺
Exact Mass: 134.01847



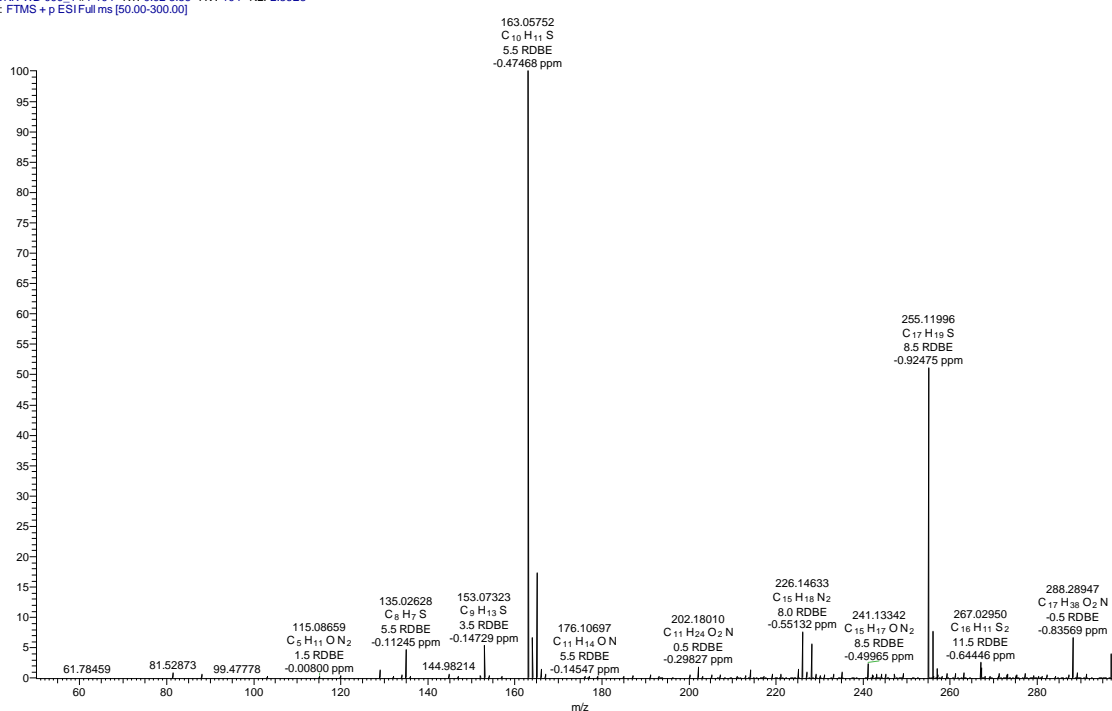
Chemical Formula: C₈H₇S⁺
Exact Mass: 135.02630



Chemical Formula: C₁₀H₁₁S⁺
Exact Mass: 163.05760



WNX-WB-099_1 #1-104 RT: 0.02-5.86 AV: 104 NL: 2.36E5
T: FTMS + p ESI Full ms [50.00-300.00]



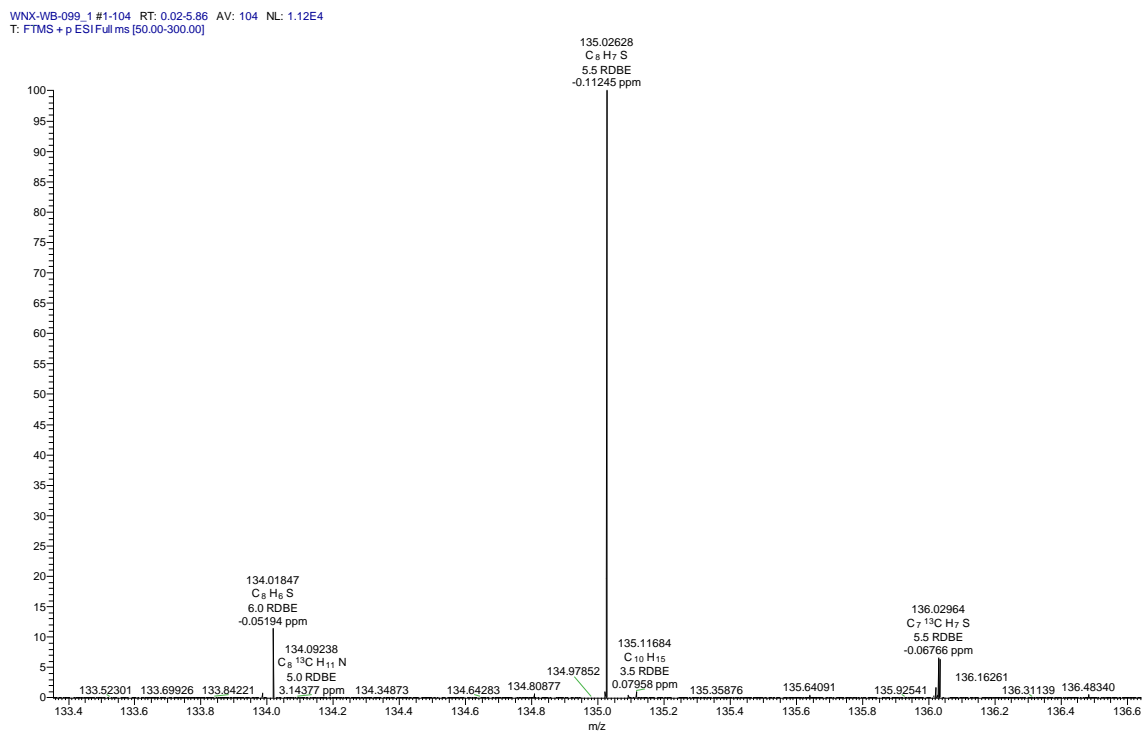
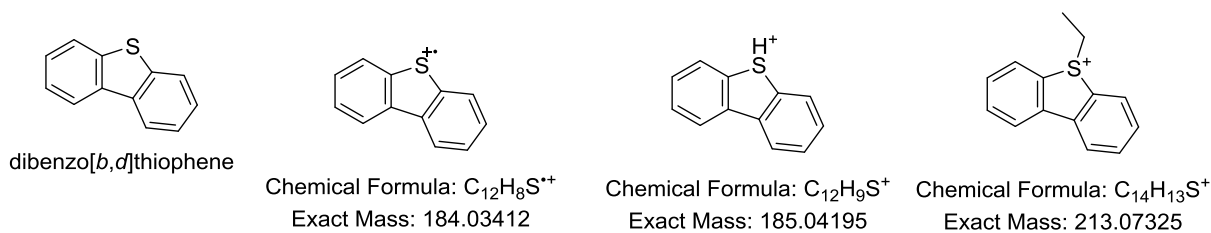


Figure A4.35: Mass spectra obtained from benzo[*b*]thiophene (BT) with C₂H₅OTf under ESI(+) FT-ICR MS.

Dibenzo[*b,d*]thiophene (DBT)



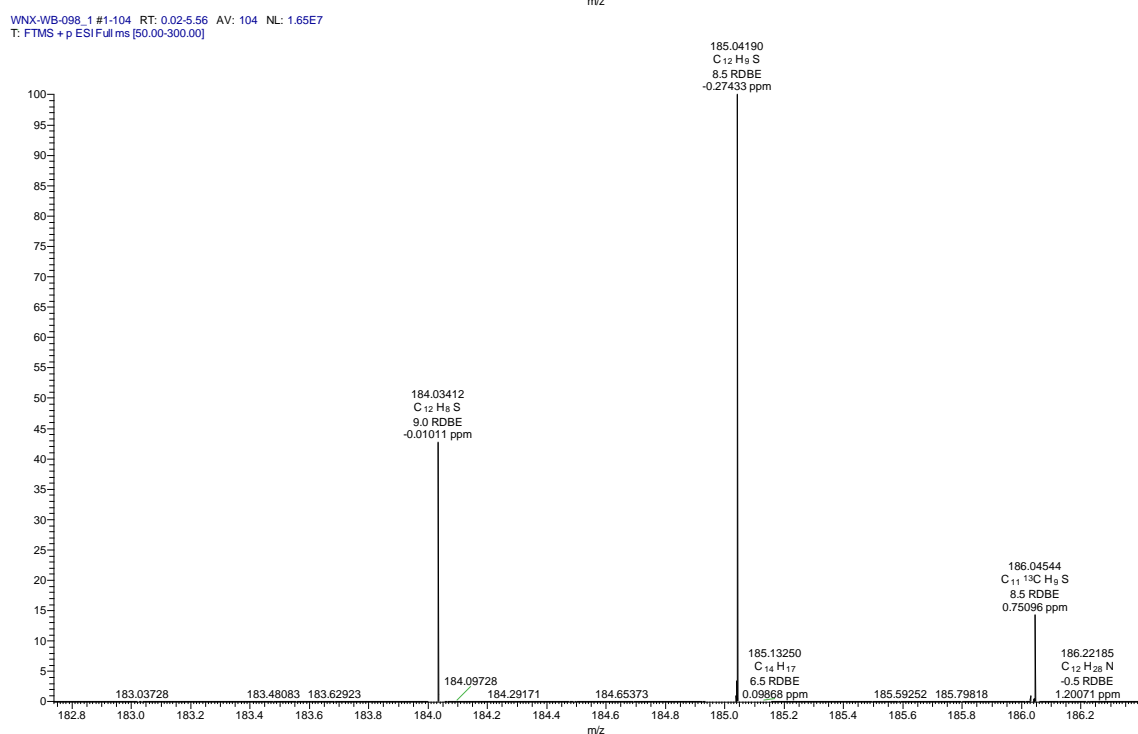
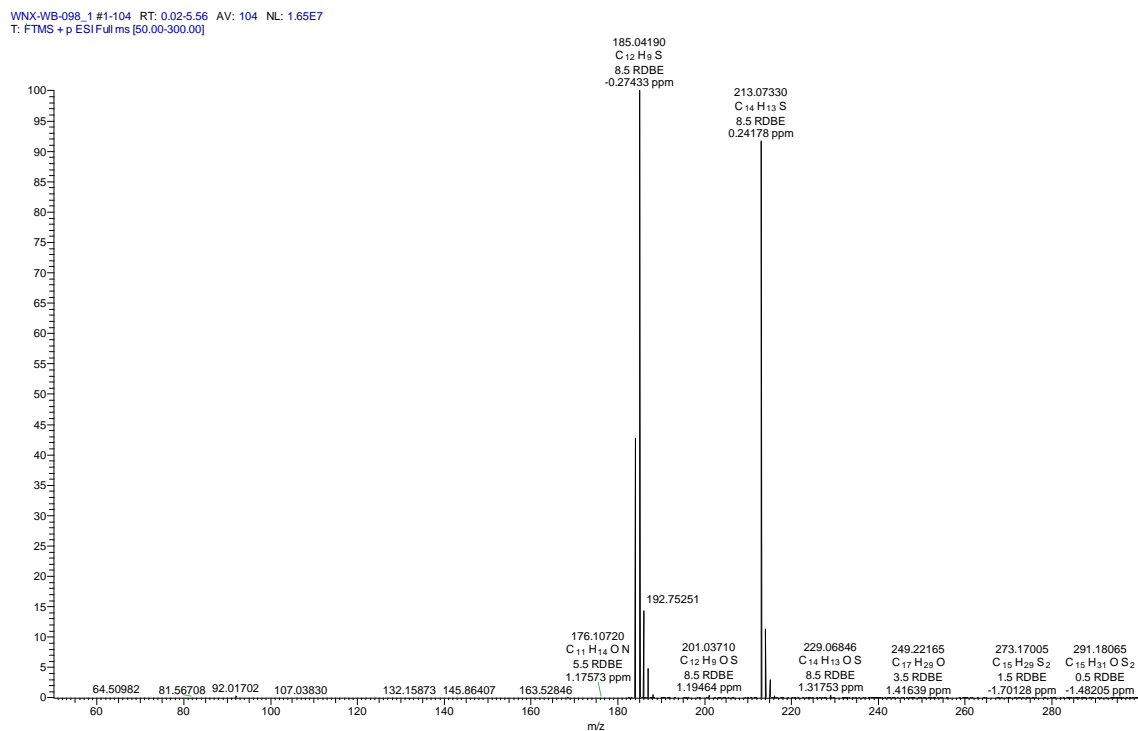
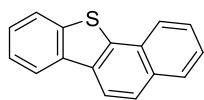
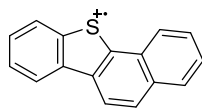
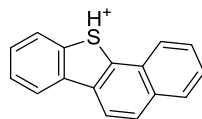
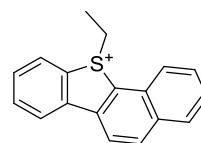
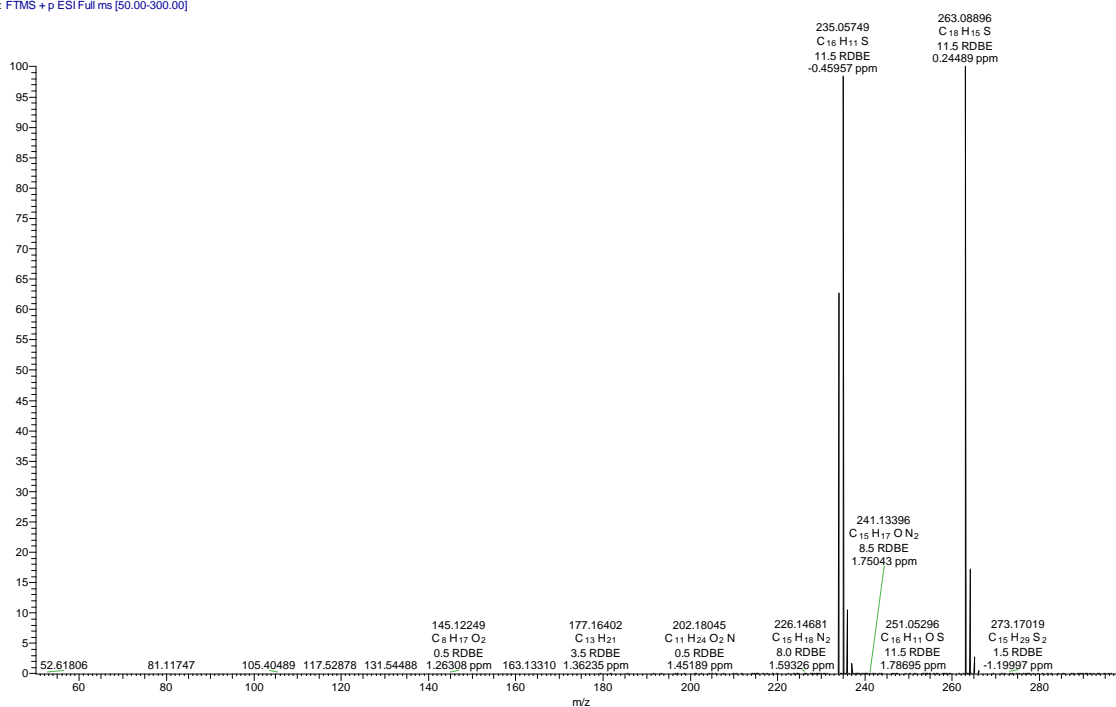


Figure A4.36: Mass spectra obtained from dibenzo[*b,d*]thiophene (DBT) with C₂H₅OTf under ESI(+) FT-ICR MS.

Benzo[b]naphtho[2,1-*d*]thiophene (BNT)benzo[b]naphtho[2,1-*d*]thiopheneChemical Formula: C₁₆H₁₀S⁺
Exact Mass: 234.04977Chemical Formula: C₁₆H₁₁S⁺
Exact Mass: 235.05760Chemical Formula: C₁₈H₁₅S⁺
Exact Mass: 263.08890

WNX-WB-100_2 #1-92 RT: 0.05-5.08 AV: 92 NL: 1.52E6
T: FTMS + p ESI Full ms [50.00-300.00]



WNX-WB-100_2 #1-92 RT: 0.05-5.08 AV: 92 NL: 1.49E6
T: FTMS + p ESI Full ms [50.00-300.00]

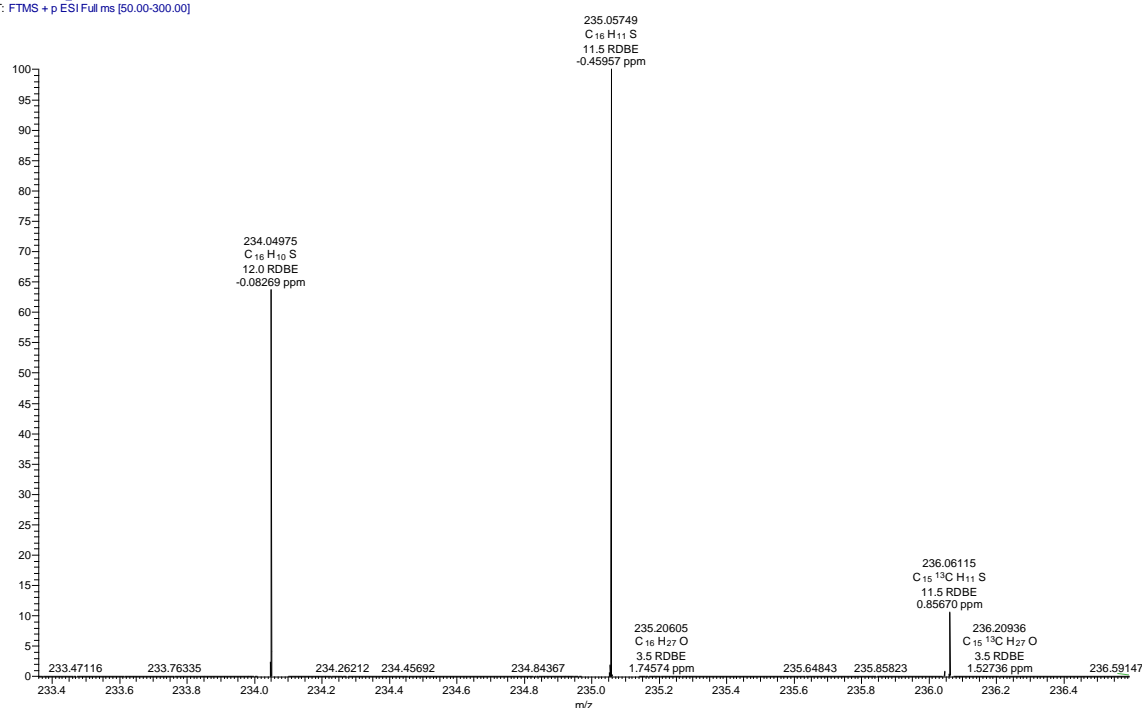
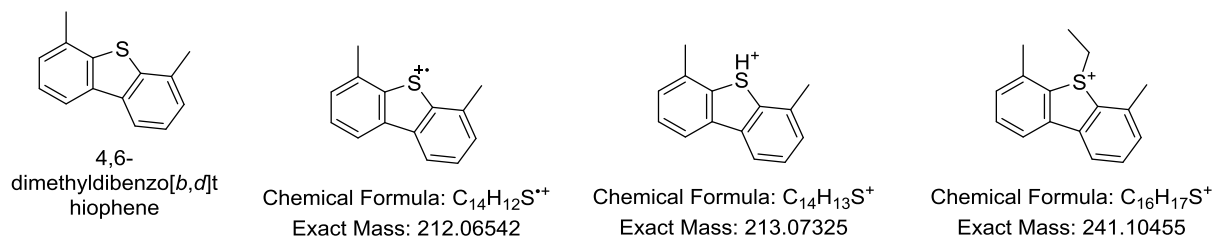
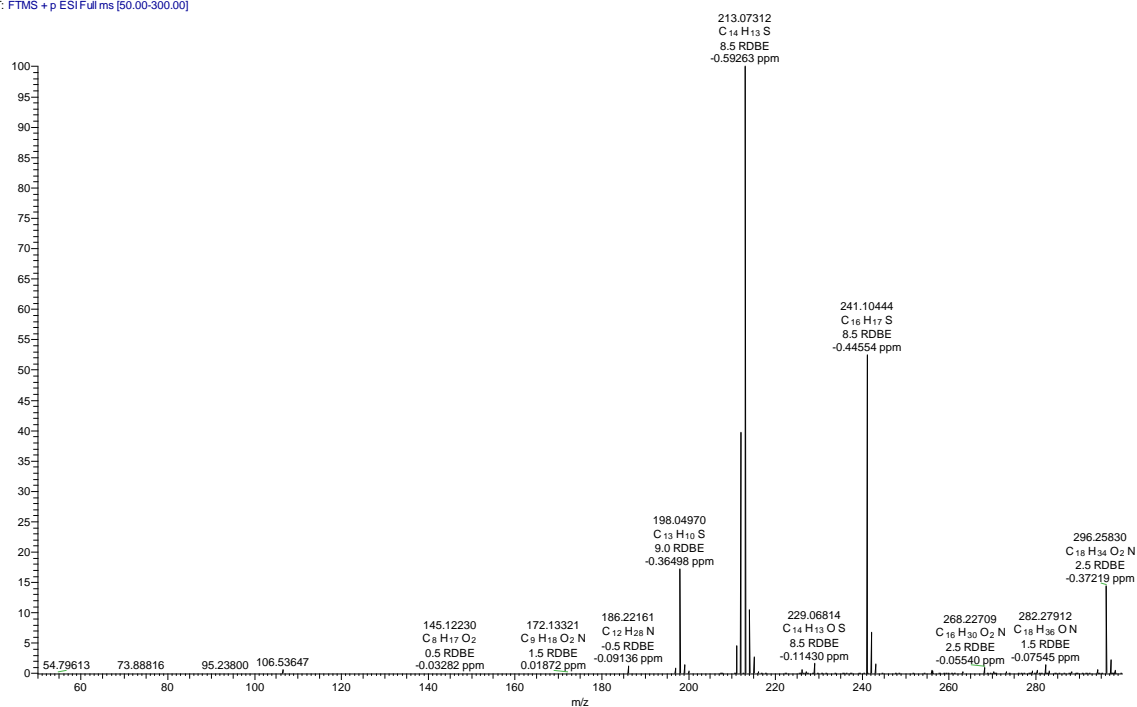


Figure A4.37: Mass spectra obtained from benzo[*b*]naphtho[2,1-*d*]thiophene (BNT) with C₂H₅OTf under ESI(+) FT-ICR MS.

4,6-dimethyldibenzo[*b,d*]thiophene (4,6-DM DBT)



WNX-WB-102_2 #1-107 RT: 0.05-6.08 AV: 107 NL: 3.46E5
T: FIMS + p ESI Full ms [50.00-300.00]



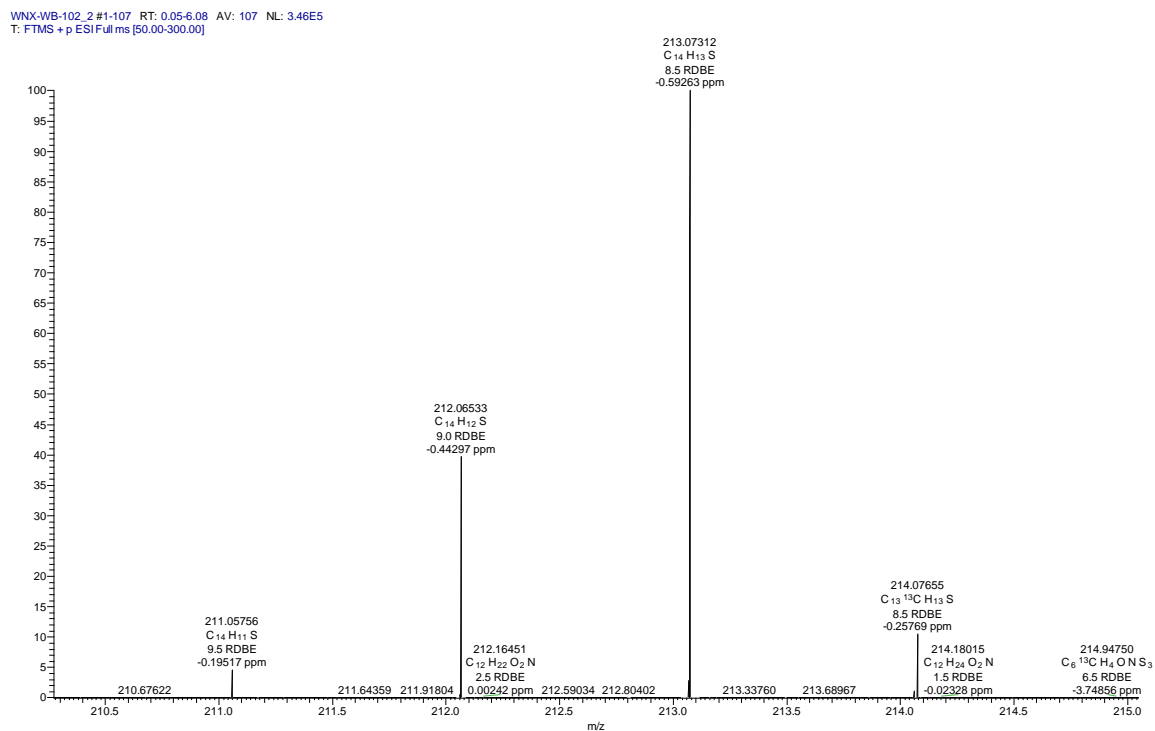


Figure A4.38: Mass spectra obtained from 4,6-dimethyldibenzo[*b,d*]thiophene (4, 6-DM DBT) with C₂H₅OTf under ESI(+) FT-ICR MS.

Chapter 5 Electrochemically-induced Selective Analysis of Sulfur-Containing in Heavy Crude Oils on the Millisecond Time Scale by Electrospray Ionization Mass Spectrometry*

**Redrafted from “Wang, X.; Wu, X.; Thiel, W.; Schrader, W., Electrochemically-induced Selective Analysis of Sulfur-Containing Species in Heavy Crude Oils on the Millisecond Time Scale by Electrospray Ionization Mass Spectrometry, will be submitted to Anal. Chem.”*

5.1 Abstracts

A rapid derivatization method on millisecond time scale is first developed for the selective analysis of sulfur-containing species in super complex mixture of crude oil. An electrospray (ESI) ion source can be generally recognized as a special type of electrolytic cell. This work is designed to take advantage of the electrolysis process, and converse neutral alkylating reagents, ethyl iodide and ethyl triflate (C_2H_5I and C_2H_5OTf), to the corresponding open-shell molecular radical cations by an electrochemical oxidation process inherent to positive-ion mode ESI, followed by the secondary reactions (mainly nucleophilic substitution) between active-alkylating radical cations and hetero-containing species in crude oils. The selective analysis towards sulfur-containing species is achieved by the inherent nucleophilic properties of heteroatom-containing species, the electrophilic property of active-alkylating species, the amount of alkylating reagents and the content of S- and N- containing compounds in crude oil. Theoretical calculation based on quantum mechanism in combined with 1H NMR as well as ESI mass spectrometry experiments are carried out in this work to quantitatively explain the selectivity. High selectivity towards S-containing species is obtained in the case with C_2H_5OTf involved. As a comparison, not only sulfur- but also nitrogen-containing compounds are accessed in the case of C_2H_5I . Electrochemically derivatization in ESI avoids tedious and time-consuming separation and results in rapid selectively analysis of non-polar S-containing species in petroleum.

5.2 Introduction

Crude oil is a heterogeneous supercomplex[8] mixture which complexity has challenged the analytical and petrochemical community for many decades. The characterization of the individual constituent in crude oil at a molecular level is the beginning for the understanding of the functionality and the various chemical and physical properties, which governs most of problems encountered in petroleum industry.[35][18] Ultrahigh-resolution Fourier transform ion cyclotron resonance mass spectrometry (FT-ICR MS) enables the direct characterization of complex mixtures and assignment of elemental compositions in crude oil that contain tens of thousands of individual components based on their ultrahigh mass resolution and high mass accuracy.[33, 35]

Although FT-ICR MS is a powerful method to characterize crude oil, the inherent charge competition and space charge effects in the ICR-cell lower the mass accuracy and the analytical efficiency when such complex mixtures as petroleum crude oil are being analyzed.[35] Chromatographic separation[2, 37, 143, 144] and extraction[36] to reduce the complexity in crude oil are physical ways to solve this problem. To improve the mass accuracy and data depth, spectral stitching method[35] is another good way to expand and enhance the sensitivity of crude oil analysis in petroleum field. Derivatization techniques are a chemical method employed to solve the above problem. It transforms chemical compounds based on specific functional groups in mixtures into other compounds that bare new chemical properties for the chemical analysis and add a degree of selectivity.

ESI is known for the selective analysis of polar compounds in mixtures via protonation or deprotonation.[60] Compounds that are not ionic in solution or insufficiently acidic or basic have bad response to ESI-MS. Muller et al. has developed a methylation method to form the preformed sulfonium ions that are polar enough for the selective analysis of non-polar polycyclic aromatic sulfur

heterocycles (PASHs) under ESI(+) mode. This methylation method uses ~100-250 times concentrated of silver tetrafluoroborate (AgBF_4) and iodomethane (CH_3I) than the sulfur content of PASHs, the reaction time lasts for 48 h, and the selectivity towards sulfur-containing compounds is based on the SARA fractionation and chromatographic separation.[40] In our previous work,[38, 145] an ethylation method is developed to for the selective analysis of sulfur-containing compounds in a whole heavy crude oil. This ethylation method employs only 2 times concentrated of AgBF_4 and iodomethane $\text{C}_2\text{H}_5\text{I}$ than the sulfur content, the reaction time lasts for 4 h, and the selective analysis is based on varying the organic chemistry and coordination chemistry.

Electrospray ion source is also a current-controlled electrolytic cell, and by using the inherent electrochemical red/ox reactions in ESI ion source, more unusual ESI-active species can be produced and are accessible to ESI. This significantly expand the range of ESI analysis.[84, 85][43] Herein, taking a step further, we develop a novel method for the same aim. This method takes the advantage of electrochemistry of electrospray ion source, discards the expensive AgBF_4 , only employs the alkylating reagent (ethyl trifluoromethanesulfonate, $\text{C}_2\text{H}_5\text{OTf}$) and realizes the selective analysis of sulfur-containing compounds in a whole heavy crude oil on a millisecond time scale. The mechanism study of the reaction between thiophenic sulfur compounds and ethyl trifluoromethanesulfonate ($\text{C}_2\text{H}_5\text{OTf}$) in ESI-MS can be viewed in our previous work.[146] Besides $\text{C}_2\text{H}_5\text{OTf}$, another alkylating reagent $\text{C}_2\text{H}_5\text{I}$ is also chosen to react with crude oil, to see how it goes.

5.3 Experimental section

10 mg of a heavy crude oil was mixed with 1 mmol of $\text{C}_2\text{H}_5\text{OTf}$ in 1 mL of anhydrous dichloroethane (DCE), and it was further dissolved to a final concentration of 500 $\mu\text{g}/\text{mL}$ in anhydrous dichloromethane (DCM) for positive

ESI FT-ICR MS measurement, the obtained sample is named as Sample **A**₁. The same procedure was applied to prepare the Sample **B**₁ by replacing C₂H₅OTf with C₂H₅I. All the crude oil measurement were performed on a 7 T LTQ FT-ICR MS equipped with ESI ion source (Thermo Fisher, Bremen, Germany). More experimental details are described in the Supporting Information.

5.4 Results and Discussion

5.4.1 Positive-ion ESI FT-ICR MS Spectra

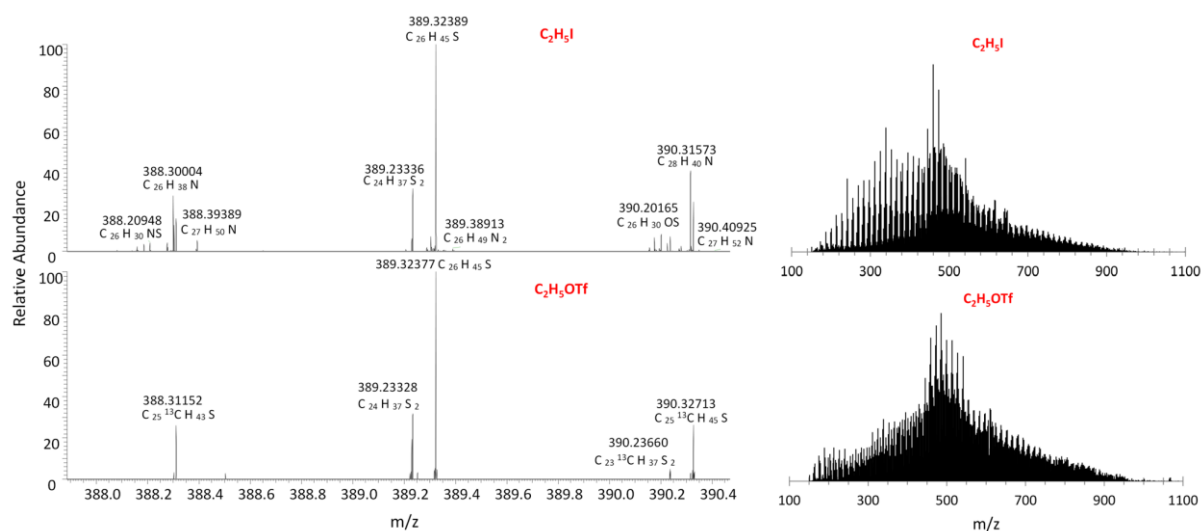


Figure 5.1: 7T FT-ICR mass spectra obtained from samples **A**₁ and sample **B**₁ in (+) ESI ionization mode for the mass range 100-1100 Da (right column) and the corresponding enlarged section of those in a range between m/z 387.8-390.4 (left column) with the assigned molecular formulas.

Figure 5.1 illustrates a first overview of discrimination from the two samples (right column). There were two obvious crests existing in the broadband FT-ICR mass spectra from the sample with C₂H₅I involved, **B**₁, while, only one crest was observed in the broadband mass spectra from the sample **A**₁ with C₂H₅OTf involved. Further details were exhibited in Figure 5.1 (left column) where the changes of the elemental compositions can be observed. In case of sample **A**₁,

sulfur-containing species were the dominant species, while in sample **B**₁, not only sulfur- but also nitrogen-containing compounds are accessible in positive ESI FT-ICR MS.

5.4.2 Heteroatom classes

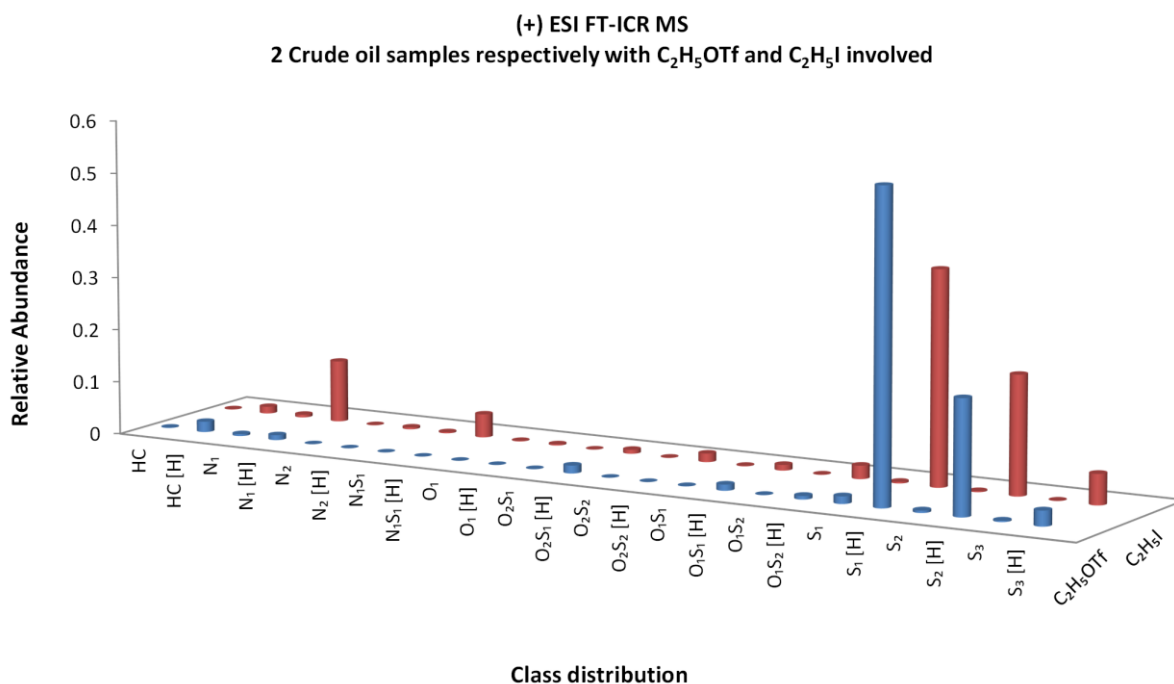


Figure 5.2: Comparison of heteroatom class distributions obtained from the sample **A**₁ (C₂H₅OTf) and sample **B**₁ (C₂H₅I). Note that relative and not absolute abundances are shown; the summary of all abundances from one method is 100%.

The heteroatom class distribution of sample **A**₁ (C₂H₅OTf) colored in blue in Figure 5.2 is showing mainly sulfur-containing compounds (S₁, S₂, S₃, O₁S₂, O₁S₁, O₂S₂, O₂S₁), and S₁ is present as the dominant species, while N₁ and CH species are present with a lower abundance. The heteroatom class distribution of sample **B**₁ (C₂H₅I) colored in red in Figure 5.2, depicts that not only sulfur- but also nitrogen-containing species (N₁, N₁S₁ and N₂) of ions are observed with high relative abundance, and when comparing to sample A₁, the relative abundance of N₁-species is increased by a factor of nine, and meanwhile the

relative abundance of S_1 -species decreases, What's more additional classes of N_1S_1 , N_2 and O_1 were only observed in this case of C_2H_5I . High selectivity towards sulfur-containing compounds was achieved in the system of C_2H_5OTf ; while, in the C_2H_5I reaction, a wider range of heteroatom classes is accessed. Herein, the class notation only represents the heteroatom-containing species present in original crude oil, e.g., S_1 represents the compounds bearing one sulfur atom in crude oil. The difference between cation and radical cation notation will be further discussed in the mechanism section. When doubling the amount of C_2H_5OTf and C_2H_5I (2 mmol), sample **A₂** (C_2H_5OTf) and sample **B₂** (C_2H_5I) are obtained. In both cases, there is only very slight change in relative abundance for each class distribution. No excess classes are accessed comparing to the case where 1 mmol is used. (See Supporting Information Figure A5.6 and A5.7).

5.4.3 Double bond equivalents (DBE)

Figure 5.3 shows DBE vs carbon number distribution for ions of S_1 , S_2 , S_3 , N_1 , and N_1S_1 heteroatom classes, derived from each of the sample **A₁** (C_2H_5OTf) colored in blue and sample **B₁** (C_2H_5I) colored in red based on positive ion ESI-MS. Note, here cation species denoted using [H] of each heteroatom class are represented. As described below, the class distribution varies between the above two systems.

5.4.3.1 S_1 class

The S_1 heteroatom class dominates in both sample **A₁** (C_2H_5OTf) and sample **B₁** (C_2H_5I), however, the ion abundance differences between C_2H_5OTf and C_2H_5I are pronounced. C_2H_5OTf clearly generates more S_1 ions over a wider range of DBE (~1-25) and carbon number (~9-76) with DBE 6 and 9 as most intense series than C_2H_5I (~1-16) and carbon number (~9-70) with DBE 3 as

most intense series, as shown in Figure 5.3. S_1 class species likely include condensed thiophene-type nonpolar compounds in crude oil.

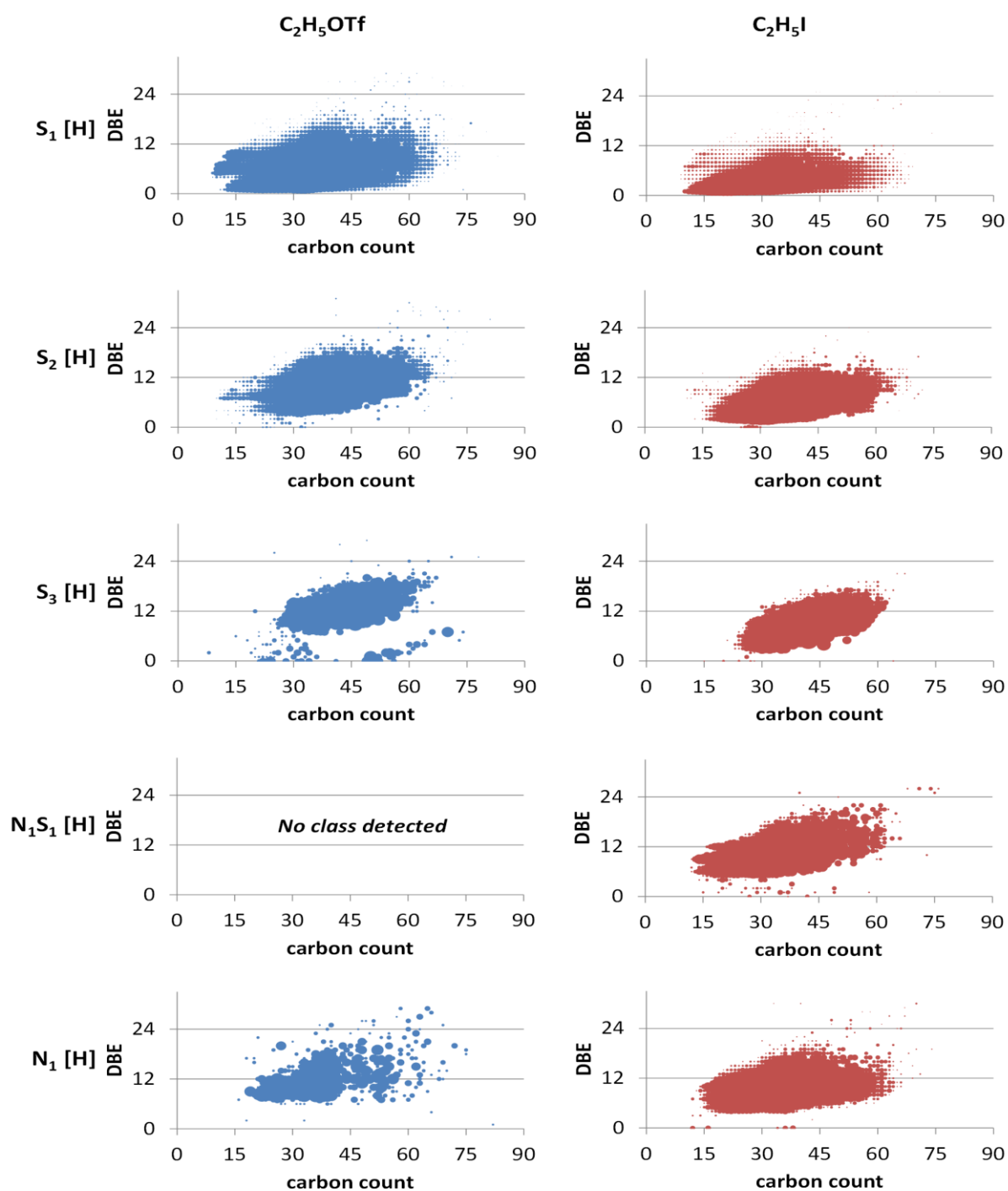


Figure 5.3: Comparison of DBE versus carbon number plots for S₁, S₂, S₃, N₁S₁, N₁ classes from sample A1 (C₂H₅OTf) and sample B1 (C₂H₅I), obtained by (+) ESI FT-ICR MS.

5.4.3.2 S_2 and S_3 classes

An obvious difference of DBE vs carbon number plots for the S_2 and S_3 classes from the two samples can be observed by the vertical upward shift of DBE value when comparing C_2H_5OTf to C_2H_5I . S_2 class in C_2H_5OTf spans from DBE 0 to 25 with the relative intense series starting from 4 to 19, and carbon number 10-75; whereas in C_2H_5I , the S_2 class exhibits a narrow range of DBE (0-16) with the relative intense series starting from 3 to 15, and carbon number 11-71. For S_3 class, the upward shift of DBE value is even more significant in C_2H_5OTf case, with DBE 15 as most intense series; whereas, DBE 9 is the dominant members for S_3 class in C_2H_5I case.

5.4.3.3 N_1 and N_1S_1 classes

More significant difference of compositional characterization between C_2H_5I and C_2H_5OTf case is for detection of compounds that contain nitrogen atoms, such as N_1 and N_1S_1 heteroatom classes. With C_2H_5I case, N_1 ion class exhibits a wide range in both DBE (4-30) and carbon number (12-71), with DBE 8 as the most intense series, as shown in the right bottom corner of Figure 5.3 colored in red; however, C_2H_5OTf accesses a narrower range in both DBE and carbon number as shown in the left bottom corner of Figure 5.3 colored in blue. N_1 class likely includes condensed pyridine-type compounds in crude oil. The biggest difference between sample A_1 and sample B_1 in Figure 5.3 is the detection for ions from N_1S_1 heteroatom class. N_1S_1 heteroatom class are totally absent in the reaction with C_2H_5OTf ; whereas, in the reaction with C_2H_5I , N_1S_1 heteroatom class spans a decent region in the Kendrick plots, it has DBE of 1-26 and carbon number (12-75), with DBE 9 as most intense series. Supporting Information Figures A5.8 – A5.15 show the color-coded image plots of DBE vs carbon number for members of a particular heteroatom class from sample A_1 and sample B_1 .

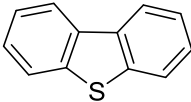
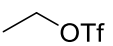
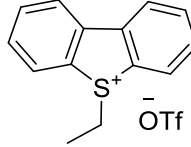
5.4.4 Mechanism of selectivity for ESI(+) with C₂H₅OTf

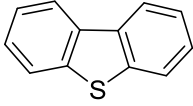
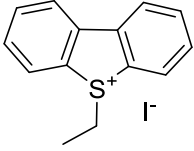
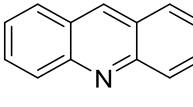
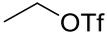
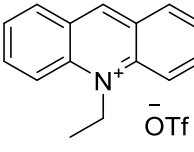
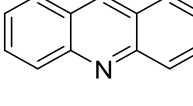
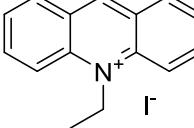
Derivatization coupled with analysis by ESI-MS offers an effective method for selective detection of neutral, nonpolar analytes. It can produce preformed ions in solution through what we denote as „off-ESI” reactions,[7, 31, 34, 38, 40, 92, 147] and these preformed ions are amenable to electrospray ionization. Derivatization that use the electrolysis character of ESI provides another profound way through what we denote as „in-ESI” reaction, to active analytes and create ESI-active species[75, 76] for rapid selective identification of neutral nonpolar components of complex mixture as crude oil.

5.4.4.1 Reactivity

An ESI ion source can be generally considered as a controlled-current electrolytic (CCE) flow cell, in which electrolysis ensures the charge balance between the ESI metal capillary (serving as working electrode) and a counter electrode. The neutral organic molecules can be oxidized by a loss of an electron to form odd-electron molecular radical cations under positive-ion mode ESI, and this is well known as electrochemical electron-transfer chemistry.

Table 5.1: Evaluation of sulfur- and nitrogen-containing standards in the S_N2 reaction^a

entry	A	B	time	C	C Yield, % ^b	$\Delta_a G^\circ$, kcal/mol ^c	$\Delta_r G^\circ$, kcal/mol ^c
1			1 min 24 h		0 0	29.35	9.19

2			1 min 24 h		0 0	29.36	15.01
3			1 min 24 h		0 0	25.76	-13.85
4			1 min 24 h		0 0	24.99	-8.47

^aA (10 mg) and B (1 mmol) in DCE (1 mL) at 25°C. ^bDetermined by ¹H NMR analysis of the crude reaction mixture. ^cCalculated based on the level of quantum mechanism.

Previous work [146] demonstrates that C₂H₅OTf loses one electron to the anode and forms the transient active C₂H₅OTf radical cation, and then the formed [C₂H₅OTf]⁺ reacts with the heteroatom-containing species and produces the heteroatom-containing cation species (cation is denoted using [H]) and heteroatom-containing radical cation (radical cation is denoted without [H]). The heteroatom-containing species can also lose one electron to the anode and form radical cation directly, if they can be efficiently transferred from solution to the metal surface. An overview of the reactivity can also be seen through the S_N2 reaction of S- and N-containing standards as shown in Table 5.1. From the reaction yields determined by ¹H NMR (supporting Information Figure A5.1 – A5.5), we know that no reactions occur in glass flask (“**off-ESI**” reaction), and this is further confirmed by the calculation data as shown in Table 5.1. The S_N2 reaction of DBT with alkylating reagents used in glass flask at room temperature is thermodynamically and kinetically unfavorable, and it will not occur in a spontaneous manner; The S_N2 reaction of ACR with alkylating reagents used in glass flask at room temperature is exothermic reaction, nevertheless, the activation barriers are rather high (e.g., C₂H₅OTf, Δ_aG° = 25.76 kcal/mol at 25°C), so it can be expected that none of them may occur in glass flask without any energetic or catalytic involved at room temperature. Thus, the reaction is

activated by the electrolytic cell, that is represented by the ESI sprayer (“In-ESI” reaction).

5.4.4.2 Selectivity

The previous work [146] shows that the reaction will start from the activation of alkylating reagents, and then a series of reactions, e.g., ethylation, charge transfer reaction and protonation, occur between the active $[\text{C}_2\text{H}_5\text{OTf}]^{*+}$ and thiophenic sulfur compounds. Here, only ethylation between the $[\text{C}_2\text{H}_5\text{OTf}]^{*+}$ and the sulfur-containing compounds is chosen and calculated for the selectivity analysis. The obtained active radical cations of alkylating reagents ($[\text{C}_2\text{H}_5\text{OTf}]^{*+}$ and $[\text{C}_2\text{H}_5\text{I}]^{*+}$) are much more electrophilic, and they are readily attacked by DBT and ACR to produce the ethylated ions in spontaneous fashion as shown in Table 5.2. When a reaction is thermodynamically and kinetically feasible, the reaction yield is determined by the amount of reactants, just like in this case. Although nitrogen-containing species like pyridine-type are much more nucleophilic than sulfur-containing species like thiophene-type compounds, however, the sulfur content is roughly 40 times more than the nitrogen content in the crude oil employed,[148] which roughly means sulfur-containing species have 40 times of chances more to collide with the active alkylating reagents radical cation than nitrogen-containing species do as shown in Table 5.2, and this is the reason why sulfur-containing species are dominant in both $\text{C}_2\text{H}_5\text{OTf}$ and $\text{C}_2\text{H}_5\text{I}$ reactions. This phenomena is more pronounced with the more electrophilic species, like $[\text{C}_2\text{H}_5\text{OTf}]^{*+}$, so the high selectivity towards sulfur-containing species is obtained in Sample **A**₁ with $\text{C}_2\text{H}_5\text{OTf}$ involved under ESI(+) as shown in Table 5.2 (entry 1 and 3).

As for the $\text{C}_2\text{H}_5\text{I}$ case of Sample **B**₁, the sulfur-containing species are also dominant species when comparing to other classes, but nitrogen species are observed with a significant increase (e.g. N_1 increase at a factor of 9; N_1S_1 and

N_2 present as new species) comparing to the reaction of $\text{C}_2\text{H}_5\text{OTf}$. The reason is because $[\text{C}_2\text{H}_5\text{I}]^{*+}$ is less electrophilic than $[\text{C}_2\text{H}_5\text{OTf}]^{*+}$, and the thermodynamic advantage of the reaction between nitrogen-containing species with the active open-shell $[\text{C}_2\text{H}_5\text{I}]^{*+}$ as shown in Table 5.2 (entry 2 and 4) plays some role comparing to the S-containing compounds (also O-containing species), and that is why not only sulfur-, but also nitrogen-containing species are detected in positive-ion ESI, even though the amount of nitrogen content is 40 times less than that of sulfur content in the employed crude oil.

Table 5.2: The changes of the standard Gibbs free energy ($\Delta_r G^\circ$, in kcal/mol) for the ethylation that produces the molecular cations detected in the ESI-MS experiments^a

entry	A	B'	C'	$\Delta_r G^\circ$, kcal/mol ^b
1				-38.32
2				-34.76
3				-65.57
4				-62.00

^aA and B' in the gas phase at 25°C. ^bCalculated at the level of quantum mechanism.

Hydrocarbon (HC) species (Supporting Information Figure A5.16) are also accessed in both C_2H_5I and C_2H_5OTf case in positive ESI despite with a low relative abundance, which can be explained by the electrophilic substitution reaction with the active radical cation of alkylating reagents. It is worth noting that HC even with low DBE (e.g. 2, see Supporting Information Figure A5.17) can also be detected.

5.4.4.3 Cation and radical cation

Van Berkel et al first reported the discovery of radical cations in ESI(+), [85] and in our study, not only radical cation, but also cation of heteroatom-containing species are produced and detected. [146] It is worth noting that cation is denoted using [H], which represents not only protonated species, but also ethylated species, and those without [H] represent the radical species. Interestingly, for every heteroatom class from both the reactions of C_2H_5OTf and C_2H_5I based on ESI(+), cation molecular species are present advantageously comparing to its corresponding radical cation molecular species, as shown in Figure 5.2, e.g. S_1 [H] species is 42 times more than S_1 species in sample **A**₁ under positive ESI; N_1 [H] species is 22 times more than N_1 species in sample **B**₁ under ESI(+). The difference can further be illustrated by the DBE vs carbon number plots (Supporting information Figure A5.18). The reason why cation of each class is dominantly detected comparing to its radical cation might be due to two reasons: (1) two channels (ethylation and protonation) produce the cation [H] species; (2) the open-shell radical cation is not stable enough when comparing to its cation species, either it is consumed to produce other species before detection, or it is too short-lived before detection.

5.5 Conclusion

We have previously studied the mechanism of the reaction between the sulfur-containing standards (thiophene-type compounds and ethyl trifluoromethanesulfonate (C_2H_5OTf) in ESI(+), and figured out that this is a two-step reaction: firstly, (C_2H_5OTf) is electrochemically oxidized in solution phase in the ESI spray capillary, and the active $[C_2H_5OTf]^{*+}$ is produced; secondly, the thiophene-type compounds react with the produced actively open-shell species, and produce the ethylated, protonated, and oxidized species in gas phase.[146] The method is further introduced to this study with real crude oil, and we found that the sulfur-containing compounds are absolutely dominant species when C_2H_5OTf is involved to the crude oil with a wide range of double bond equivalent (DBE) and carbon number value in ESI FT-ICR MS. Whereas, in the reaction of C_2H_5I , it accesses a wide range of heteroatom classes including sulfur-, nitrogen- and oxygen-containing compounds.

1 mmol of alkylating reagents is enough for all the analysis in our study. Derivatization through electrochemical electron-transfer chemistry in positive ESI provides a very efficient and promising strategy for rapid analysis of the petroleum heavy crude oil without any chromatographic separation and fractionation, and meanwhile, it abandons the use of expensive silver salts, avoids long reaction time, and finally achieves the selective analysis towards sulfur-containing species in a whole heavy crude oil mixture on the millisecond time scale at low cost. ESI ion source here serves as special electrolytic cell, an efficient reactor. It triggers some energetically unfavorable reactions and extends the range of ESI analysis. Theoretical calculations facilitate the mechanism study quantitatively.

Acknowledgements

The authors thank Dr. David Stranz (Sierra Analytics, Modesto, CA) for assistance during data interpretation.

Appendix 5

This section contains additional information about the experimental section and Appendix Figures that mentioned in the main text, for details see below.

NOTE: For better explanation and understanding in this study, “**Off-ESI**” reaction represents the reaction in glassware. “**In-ESI**” reaction represents the reaction in ESI ion source.

Experimental section

Sample and chemicals. The heavy crude oil sample used in this work was provided by Shell (C, 81.68%; H, 9.98%; N, 0.14%; S, 5.60%; and O, 2.08%).^[148] Iodoethane (C₂H₅I) and ethyl trifluoromethanesulfonate (CF₃SO₂O C₂H₅) were purchased from Sigma-Aldrich (high purity, Steinheim, Germany). Dibenzothiophene (DBT), Acridine (ACR), anhydrous dichloroethane (DCE) and dichloromethane (DCM) were purchased from Sigma-Aldrich (high purity, St. Louis, MO). DCM was further dried before use.

Sample preparation. 10 mg of a heavy crude oil from Shell was mixed with 1 mmol of C₂H₅OTf in 1 mL of anhydrous dichloroethane (DCE), and it was further dissolved to a final concentration of 500 µg/mL in anhydrous dichloromethane (DCM) for positive ESI FT-ICR MS measurement, the obtained sample is named as Sample **A**₁. The same procedure was applied to prepare the Sample **B**₁ by replacing C₂H₅OTf with C₂H₅I. Doubling the amount of alkylating reagents (C₂H₅OTf and C₂H₅I) respectively, we get the samples named Sample **A**₂ and Sample **B**₂ for comparison.

All the crude oil measurement were performed on a 7 T LTQ FT-ICR MS equipped with ESI ion source (Thermo Fisher, Bremen, Germany).

Nuclear Magnetic Resonance Spectroscopy preparation. ^1H NMR was performed on Bruker Advance 300 NMR spectrometer. Chemical shifts of ^1H NMR spectra and the coupling constants were obtained through analysis of the spectra using MestReNova NMR-Software version 10.0.2-15465. The chemical shifts is reported as in units of parts per million (ppm). The spectrum is referenced through the solvent lock (^2H) signal according to IUPAC (International Union of Pure and Applied Chemistry) recommended secondary referencing method and the manufacturer's protocols and is relative to the residual CHCl_3 signal ($\delta = 7.26$, singlet) in chloroform solvent CDCl_3 . Multiplicities were given as: s (singlet); br s (broad singlet); d (doublet); t (triplet); q (quartet); m (multiplet), etc. The number of proton (n) for a given resonance is indicated by nH.

10 mg of standard (DBT or ACR) was mixed with 1 mmol of alkylating reagents ($\text{C}_2\text{H}_5\text{OTf}$ or $\text{C}_2\text{H}_5\text{I}$) in 1 mL anhydrous dichloroethane (DCE) for 1 min and 24 h at 25°C . The crude reaction mixtures with standards involved were evaporated to dryness under reduced pressure to remove DCE and the excess $\text{C}_2\text{H}_5\text{OTf}$ and $\text{C}_2\text{H}_5\text{I}$ respectively. The NMR sample was prepared by dissolving it in 0.5 mL of CDCl_3 for ^1H NMR analysis.

ESI FT-ICR MS analysis. Mass spectra were obtained using a 7 T linear quadrupole ion-trap (LTQ) FT-ICR MS (Thermo Fisher, Bremen, Germany) equipped with a commercially available ESI source (Thermo Fisher, Bremen, Germany) under positive mode. Target total charge value (AGC value) was set between $1\text{E}5$ and $1\text{E}6$. The measurements were carried out with a transfer capillary temperature of 275°C , a skimmer voltage of 30 V, and a tube lens voltage of 110 V. ESI conditions were as follows: flow rate $5\ \mu\text{L}/\text{min}$; spray voltage, 4.3 kV; a sheath gas flow of 5 (arbitrary unit); an auxiliary gas flow of 2 (arbitrary unit). The Instrument was calibrated with the Thermo Scientific Pierce LTQ Velos ESI positive ion calibration solution. The mass spectra were also

externally calibrated using a mixture of the Agilent electrospray calibration with the masses 300.04812, 622.02896, 922.00980, and the whole mass range was covered in the samples.

Data acquisition and analysis. Data was collected and processed with the LTQ FT Ultra 2.5.5 (Thermo Fisher, Bremen, Germany) data acquisition system with acquisition mass range of $150 < m/z < 1200$; and then was imported into the composer software (Sierra Analytics, Modesto, CA). The following chemical constraints were applied: number of H unlimited, $0 < C < 200$, $0 < S < 3$, $0 < O < 2$, $0 < N < 2$, and $0 < \text{double bond equivalent (DBE)} < 40$, with a mass accuracy better than 1 ppm. The calculated molecular formulas were sorted into their heteroatom class ($N_nO_oS_s$) according to their Kendrick mass defects,[30, 82]double bond equivalence (DBE = number of rings plus double bonds involving carbon) distribution, and carbon number distribution.[18, 40] The assignments of the most abundant ions were confirmed by corresponding ^{13}C peak. The obtained mass lists were transferred into Excel for data evaluation and preparation of the figures shown.

Computational details**Data acquisition and analysis.** All calculations were carried out by using the hybrid PBE0 functional[131] plus the Grimme-type D3 correction for dispersion interaction[132] and Pople's triple- ζ basis set with polarization and diffuse functions, i.e. PBE0-GD3/6-311+G(d,p). This computational protocol had been benchmarked and recommended for general chemical application.[133] The reactions in the 1, 2-dichloroethane solution (DCE) were studied by means of the self-consistent reaction field method of the integral equation formalism model.[134] All optimized structures of the energy minimum and transition state were confirmed by subsequent frequency analyses. Intrinsic reaction coordinate calculations, moreover, were also performed for the transition states, so that they can be validated further along the reaction coordinate and the starting geometries for searching the reactant and product

complexes could be determined as well. The Gaussian 09 program was used for all calculations.[135]

The optimized molecular structures for the solution reactions.

```
# dibenzothiophene
21
Ch 0 Mul 1 (E,H,G) -859.74656744 -859.574475 -859.618520
C 0.000000 2.624423 0.960966
C 0.000000 1.251311 0.728990
C 0.000000 0.723848 -0.575502
C 0.000000 1.604262 -1.661526
C 0.000000 2.970415 -1.436553
C 0.000000 3.477039 -0.132149
C 0.000000 -0.723848 -0.575502
C 0.000000 -1.251311 0.728990
S 0.000000 0.000000 1.955912
C 0.000000 -2.624423 0.960966
C 0.000000 -3.477039 -0.132149
C 0.000000 -2.970415 -1.436553
C 0.000000 -1.604262 -1.661526
H 0.000000 1.216604 -2.674984
H 0.000000 3.654896 -2.277782
H 0.000000 4.549726 0.028788
H 0.000000 3.018044 1.971324
H 0.000000 -3.018044 1.971324
H 0.000000 -4.549726 0.028788
H 0.000000 -3.654896 -2.277782
H 0.000000 -1.216604 -2.674984
# acridine
23
Ch 0 Mul 1 (E,H,G) -555.05081786 -554.857412 -554.901677
C 0.000000 3.571991 0.764034
C 0.000000 2.375648 1.420440
C 0.000000 1.149336 0.694780
C 0.000000 1.205811 -0.741810
C 0.000000 2.473654 -1.389316
C 0.000000 3.624477 -0.656900
C 0.000000 0.000000 -1.437729
C 0.000000 -1.205811 -0.741810
C 0.000000 -1.149336 0.694780
C 0.000000 -2.375648 1.420440
H 0.000000 -2.317963 2.503358
C 0.000000 -3.571991 0.764034
C 0.000000 -3.624477 -0.656900
C 0.000000 -2.473654 -1.389316
H 0.000000 4.498838 1.328100
H 0.000000 2.317963 2.503358
H 0.000000 2.504228 -2.474568
H 0.000000 4.588387 -1.154106
H 0.000000 0.000000 -2.524564
H 0.000000 -4.498838 1.328100
H 0.000000 -4.588387 -1.154106
H 0.000000 -2.504228 -2.474568
N 0.000000 0.000000 1.378662
# ethyl triflate
15
Ch 0 Mul 1 (E,H,G) -1040.05127505 -1039.943800 -1039.993396
C 2.112199 -0.439225 0.436996
C 3.418410 -0.578466 -0.291485
O 1.180865 0.200435 -0.504052
S -0.162628 0.850346 0.023006
C -1.293628 -0.626974 -0.028105
F -2.498731 -0.252979 0.359597
O -0.612758 1.755355 -0.999109
O -0.050429 1.241278 1.406702
F -1.345739 -1.103999 -1.256731
F -0.832759 -1.559651 0.792246
H 1.687677 -1.404521 0.717225
H 2.192070 0.196519 1.319218
H 3.303309 -1.191623 -1.187294
H 3.810424 0.399887 -0.575328
H 4.140325 -1.064705 0.369316
# ethyl iodide
8
Ch 0 Mul 1 (E,H,G) -6998.25459147 -6998.183792 -6998.217204
C 0.578806 -2.388191 0.000000
C -0.605708 -1.453253 0.000000
H 0.209318 -3.419846 0.000000
```

```

H      1.201018      -2.250751      0.886519
H      1.201018      -2.250751     -0.886519
H     -1.224970      -1.554373      0.889279
H     -1.224970      -1.554373     -0.889279
I      0.000000      0.642995      0.000000
# transition state of the reaction for dibenzothiophene and ethyl triflate
36
Ch 0 Mul 1 (E,H,G) -1899.76745014  -1899.488488  -1899.565149
C     -3.135366      2.375309      0.789438
C     -2.840107      1.184915      0.124498
C     -1.880406      1.207148     -0.899364
C     -1.204619      2.363402     -1.263024
C     -1.512610      3.534549     -0.583117
C     -2.471656      3.539186      0.431740
S     -1.614155     -0.394731     -1.588012
C     -2.826156     -1.098891     -0.523001
C     -3.387367     -0.143970      0.340301
C     -4.353501     -0.558182      1.256987
C     -4.731818     -1.892274      1.295575
C     -4.162644     -2.824187      0.425841
C     -3.202337     -2.435482     -0.499753
C      0.351423     -0.783258     -0.173668
C      0.455757     -2.257487     -0.291466
H     -4.805207      0.158608      1.934067
H     -5.482113     -2.215169      2.008609
H     -4.474108     -3.861841      0.466297
H     -2.768112     -3.153392     -1.185948
H     -0.458835      2.356690     -2.049358
H     -0.999060      4.452520     -0.845491
H     -2.697479      4.464666      0.949561
H     -3.874522      2.387793      1.582939
H      0.854752     -0.118114     -0.861326
H     -0.238073     -0.330079      0.611181
H      0.730619     -2.563189     -1.300988
H      1.238627     -2.594571      0.392700
H     -0.470867     -2.746171      0.016077
S      2.977739      0.505930      0.710045
O      1.915156     -0.469465      1.126388
O      3.712503      1.054083      1.837681
O      2.530212      1.430183     -0.327687
C      4.178139     -0.602840     -0.161959
F      4.644913     -1.529975      0.666026
F      3.568137     -1.212192     -1.179823
F      5.198469      0.099613     -0.639099
# transition state of the reaction for dibenzothiophene and ethyl iodide
29
Ch 0 Mul 1 (E,H,G) -7857.97080118  -7857.727197  -7857.788941
C      2.377759      2.283541     -1.105528
C      2.142911      1.165623     -0.305364
C      1.388084      1.325445      0.866632
C      0.861935      2.549064      1.255030
C      1.105732      3.646664      0.439708
C      1.858027      3.513182     -0.728936
S      1.172903     -0.200069      1.724599
C      2.142214     -1.056891      0.529820
C      2.577542     -0.207605     -0.500131
C      3.343593     -0.747967     -1.532291
C      3.653430     -2.100210     -1.517433
C      3.214729     -2.924995     -0.480140
C      2.454007     -2.409629      0.561739
C     -0.986518     -0.646687      0.849932
C     -1.086602     -2.096837      1.187011
I     -3.456023     -0.134098     -0.484225
H      3.694613     -0.114572     -2.339564
H      4.248114     -2.521443     -2.320236
H      3.471953     -3.978134     -0.481246
H      2.122193     -3.044290      1.375175
H      0.279831      2.648135      2.163887
H      0.706538      4.615535      0.717582
H      2.037752      4.382895     -1.350955
H      2.960098      2.190278     -2.015632
H     -1.396314      0.105266      1.508986
H     -0.627745     -0.318135     -0.115082
H     -0.973112     -2.256435     -2.261465
H     -2.066119     -2.481243      0.900729
H     -0.336106     -2.675756      0.644955
# transition state of the reaction for acridine and ethyl triflate
38
Ch 0 Mul 1 (E,H,G) -1595.07961228  -1594.778360  -1594.854027
C     -2.100230     -2.387695     -0.161959
C     -2.422902     -1.003524     -0.102028
C     -3.805279     -0.627290     -0.186294
C     -4.803301     -1.634927     -0.296217
C     -4.454369     -2.952291     -0.337810

```

C	-3.086615	-3.325234	-0.279407
C	-3.102039	1.680492	-0.098034
C	-1.741505	1.222020	-0.026171
N	-1.446305	-0.089420	0.020347
C	-0.705489	2.199821	-0.025611
C	-1.013413	3.530878	-0.054794
C	-2.358013	3.981591	-0.084864
C	-3.376452	3.076308	-0.113017
C	0.513510	-0.698801	0.852643
C	0.082949	-1.504967	2.025292
O	2.449668	-0.936872	1.199045
S	3.353562	0.144860	0.668594
C	3.668692	-0.434575	-1.062478
F	4.440531	0.432784	-1.703974
O	4.652021	0.149238	1.317844
O	2.668984	1.422951	0.495252
F	4.263288	-1.620228	-1.057847
F	2.511346	-0.540602	-1.717353
H	-5.842973	-1.329252	-0.354513
H	-5.214864	-3.719784	-0.425765
H	-2.820635	-4.375259	-0.336173
H	-1.061167	-2.689530	-0.138426
H	0.334207	1.895334	-0.041098
H	-0.209869	4.259495	-0.065525
H	-2.566689	5.045269	-0.100695
H	-4.411607	3.398781	-0.157766
H	0.662509	-1.122779	-0.125851
H	0.643179	0.361543	0.967737
H	-0.989300	-1.394119	2.193690
H	0.307465	-2.562787	1.890201
H	0.597498	-1.137256	2.913498
C	-4.113959	0.728466	-0.157241
H	-5.151986	1.046752	-0.195882
# transition state of the reaction for acridine and ethyl iodide			
31			
Ch 0	Mul 1 (E,H,G)	-7553.28293904	-7553.017305 -7553.079050
C	0.556662	-3.628573	0.000000
C	0.293152	-2.990398	1.207722
C	-0.220879	-1.650574	1.165324
N	-0.428898	-1.016148	0.000000
C	-0.220879	-1.650574	-1.165324
C	0.293152	-2.990398	-1.207722
C	0.512331	-3.617923	2.465368
C	0.223779	-2.962065	3.625312
C	-0.307827	-1.647306	3.583327
C	-0.524585	-1.006308	2.396551
C	-0.524585	-1.006308	-2.396551
C	-0.307827	-1.647306	-3.583327
C	0.223779	-2.962065	-3.625312
C	0.512331	-3.617923	-2.465368
C	-0.449008	1.126777	0.000000
C	-1.925417	1.379345	0.000000
I	0.383918	3.717156	0.000000
H	0.906475	-4.628899	2.477610
H	0.388516	-3.441839	4.583300
H	-0.553448	-1.145187	4.512838
H	-0.957131	-0.013696	2.385259
H	-0.957131	-0.013696	-2.385259
H	-0.553448	-1.145187	-4.512838
H	0.388516	-3.441839	-4.583300
H	0.906475	-4.628899	-2.477610
H	0.115652	1.058782	0.914664
H	0.115652	1.058782	-0.914664
H	-2.223802	1.941566	0.885182
H	-2.223802	1.941566	-0.885182
H	-2.463696	0.428826	0.000000
H	0.960733	-4.636953	0.000000
# product complex of the reaction for dibenzothiophene and ethyl triflate			
36			
Ch 0	Mul 1 (E,H,G)	-1899.80177261	-1899.520546 -1899.597273
C	-3.408054	2.452863	0.257281
C	-2.811287	1.219707	0.013708
C	-1.428425	1.184381	-0.200780
C	-0.625573	2.309027	-0.189745
C	-1.245217	3.529321	0.063362
C	-2.619078	3.596764	0.284508
S	-0.854893	-0.482357	-0.480524
C	-2.516307	-1.113394	-0.345516
C	-3.436382	-0.095304	-0.072747
C	-4.780241	-0.433899	0.052163
C	-5.163969	-1.761131	-0.098836
C	-4.229536	-2.753361	-0.387758
C	-2.881636	-2.435662	-0.526805
C	-0.159710	-0.903194	1.174816

```

C      0.121121      -2.383333      1.289002
H     -5.520993      0.330180      0.258724
H     -6.210679      -2.026397     -0.001465
H     -4.550927      -3.780258     -0.516717
H     -2.152499      -3.197236     -0.774958
H      0.435902      2.229836     -0.381790
H     -0.647736      4.433336      0.081299
H     -3.082896      4.558002      0.475599
H     -4.477435      2.520003      0.422318
H      0.751119      -0.303040      1.219556
H     -0.889537      -0.543027      1.901313
H      0.799545      -2.727116      0.506570
H      0.610716      -2.553757      2.251004
H     -0.792690      -2.979895      1.270610
S      2.982242      0.741485     -0.073903
O      2.629102      0.893607      1.343891
O      3.924662      1.724454     -0.603065
O      1.823143      0.456475     -0.941010
C      3.922709      -0.853748     -0.117479
F      5.015093      -0.778967      0.638860
F      3.165617      -1.853929      0.343224
F      4.290931      -1.151238     -1.361064
# product complex of the reaction for dibenzothiophene and ethyl iodide
29
Ch 0 Mul 1 (E,H,G) -7857.99675515   -7857.750661   -7857.811803
C      2.471649      2.683742     -0.180598
C      2.030656      1.374945     -0.011047
C      0.651216      1.143323      0.029731
C     -0.297574      2.141267     -0.088703
C      0.169578      3.440624     -0.265018
C      1.537124      3.704642     -0.309028
S      0.286561     -0.589401      0.243836
C      2.025365     -0.985231      0.301578
C      2.818373      0.157663      0.148849
C      4.201694      0.011550      0.186051
C      4.747301     -1.252847      0.373750
C      3.933804     -2.371656      0.540639
C      2.547581     -2.247944      0.518695
C     -0.154802     -1.072273     -1.481373
C     -0.379795     -2.561219     -1.585160
I     -3.417223     -0.233957      0.281226
H      4.846430      0.876005      0.075324
H      5.824932     -1.368181      0.402009
H      4.378686     -3.346777      0.700592
H      1.909764     -3.109421      0.675391
H     -1.357316      1.910021     -0.042866
H     -0.542537      4.251895     -0.362186
H      1.879832      4.724673     -0.442332
H      3.532724      2.903982     -0.211307
H     -1.074757     -0.509156     -1.653171
H      0.654732     -0.700294     -2.111262
H     -1.178674     -2.886635     -0.915425
H     -0.687030     -2.782976     -2.610175
H      0.528011     -3.132492     -1.381140
# product complex of the reaction for acridine and ethyl triflate
38
Ch 0 Mul 1 (E,H,G) -1595.14539486   -1594.840576   -1594.917139
C     -2.905838     -2.264081     -0.045417
C     -2.722928     -0.862473     -0.057765
C     -3.851039     -0.032534     -0.338814
C     -5.109844     -0.625647     -0.624399
C     -5.254716     -1.981247     -0.617831
C     -4.139992     -2.795371     -0.317952
C     -2.464545      1.921811     -0.010430
C     -1.350879      1.069780      0.267999
N     -1.508716     -0.287519      0.193740
C     -0.115787      1.658768      0.620201
C     -0.008340      3.025389      0.663757
C     -1.096304      3.877382      0.367201
C     -2.302101      3.332665      0.039916
C     -0.334446     -1.157192      0.421255
C     -0.178434     -1.551068      1.876243
O      2.726200     -2.037340      0.264843
S      3.393519     -0.761655      0.547640
C      3.456285      0.054123     -1.114863
F      4.038923      1.249615     -1.037016
O      4.797343     -0.858776      0.946754
O      2.589251      0.188085      1.332928
F      4.133506     -0.686341     -1.989775
F      2.217986      0.231144     -1.593751
H     -5.947173      0.028338     -0.841240
H     -6.213784     -2.436945     -0.832514
H     -4.259354     -3.872855     -0.296915
H     -2.091707     -2.931648      0.194584

```

H	0.752863	1.062596	0.874472
H	0.946628	3.459217	0.939797
H	-0.967944	4.952395	0.408951
H	-3.161126	3.955868	-0.183008
H	-0.435470	-2.021936	-0.230883
H	0.544830	-0.630149	-0.069763
H	-0.047337	-0.667445	2.504218
H	-1.040543	-2.116378	2.238480
H	0.719880	-2.163010	1.964218
C	-3.689823	1.347740	-0.321821
H	-4.538770	1.987277	-0.543358
# product complex of the reaction for acridine and ethyl iodide			
31			
Ch 0 Mul 1 (E,H,G)	-7553.34108837	-7553.071217	-7553.132384
C	3.230551	-1.482114	0.194863
C	1.930848	-1.943836	0.036733
C	0.868730	-0.994580	-0.084861
N	1.151993	0.343280	-0.028103
C	2.434835	0.807771	0.068660
C	3.511506	-0.121183	0.204004
C	1.642244	-3.334500	-0.006466
C	0.361544	-3.769586	-0.175199
C	-0.679630	-2.823562	-0.307032
C	-0.447717	-1.472740	-0.264689
C	2.739923	2.187388	0.032856
C	4.040718	2.604513	0.152379
C	5.106741	1.692345	0.313570
C	4.843368	0.354883	0.334606
C	0.040977	1.314550	-0.117178
C	-0.253941	1.709694	-1.551562
I	-3.856011	0.518571	0.223638
H	2.466208	-4.032038	0.094856
H	0.136854	-4.828843	-0.210803
H	-1.698730	-3.167705	-0.446224
H	-1.292740	-0.801996	-0.367847
H	1.967102	2.928705	-0.105781
H	4.251599	3.667518	0.116964
H	6.121424	2.059080	0.410469
H	5.638680	-0.373805	0.445514
H	-0.837753	0.876787	0.354214
H	0.305825	2.171483	0.498390
H	-0.549648	0.839724	-2.142397
H	-1.083367	2.419026	-1.560621
H	0.612431	2.175706	-2.027246
H	4.042571	-2.195111	0.300319

The optimized molecular structures for the reactions in ESI-MS

# dibenzothiophene			
21			
Ch 0 Mul 1 (E,H,G)	-859.74150431	-859.569431	-859.613481
C	0.000000	2.622744	0.959607
C	0.000000	1.250227	0.728659
C	0.000000	0.723338	-0.575152
C	0.000000	1.603998	-1.659696
C	0.000000	2.969425	-1.435706
C	0.000000	3.475508	-0.132282
C	0.000000	-0.723338	-0.575152
C	0.000000	-1.250227	0.728659
S	0.000000	0.000000	1.954808
C	0.000000	-2.622744	0.959607
C	0.000000	-3.475508	-0.132282
C	0.000000	-2.969425	-1.435706
C	0.000000	-1.603998	-1.659696
H	0.000000	1.215684	-2.672940
H	0.000000	3.654014	-2.276904
H	0.000000	4.548276	0.028649
H	0.000000	3.015984	1.970146
H	0.000000	-3.015984	1.970146
H	0.000000	-4.548276	0.028649
H	0.000000	-3.654014	-2.276904
H	0.000000	-1.215684	-2.672940
# acridine			
23			
Ch 0 Mul 1 (E,H,G)	-555.04459233	-554.851244	-554.895482
C	0.000000	3.568694	0.766839
C	0.000000	2.371812	1.419990
C	0.000000	1.147218	0.691988
C	0.000000	1.205634	-0.744412
C	0.000000	2.474713	-1.388061
C	0.000000	3.623302	-0.653599
C	0.000000	0.000000	-1.439382
C	0.000000	-1.205634	-0.744412

```
C      0.000000      -1.147218      0.691988
C      0.000000      -2.371812      1.419990
H      0.000000      -2.304959      2.501964
C      0.000000      -3.568694      0.766839
C      0.000000      -3.623302     -0.653599
C      0.000000      -2.474713     -1.388061
H      0.000000      4.494722      1.332518
H      0.000000      2.304959      2.501964
H      0.000000      2.508785     -2.473555
H      0.000000      4.588066     -1.149657
H      0.000000      0.000000     -2.526688
H      0.000000     -4.494722      1.332518
H      0.000000     -4.588066     -1.149657
H      0.000000     -2.508785     -2.473555
N      0.000000      0.000000      1.375357
# ethyl triflate cation
15
Ch 1 Mul 2 (E,H,G) -1039.64568531 -1039.542829 -1039.595892
C      -2.330628     -0.261332     -0.450719
C      -3.611523     -0.621590     0.282562
O      -1.221582     -0.377900     0.317438
S      0.221689      0.855277     0.006251
C      1.517636     -0.575667     0.007036
F      2.650908     -0.036240     -0.320892
O      0.215142      1.599497     1.219314
O      -0.024561      1.339148     -1.314053
F      1.526613     -1.073625     1.203734
F      1.102980     -1.433409     -0.884570
H      -2.175955     -1.107805     -1.201299
H      -2.335457      0.645391     -1.075251
H      -3.513567     -1.552755      0.841942
H      -3.831651      0.195074      0.979802
H      -4.419815     -0.709306     -0.444525
# ethyl iodide cation
8
Ch 1 Mul 2 (E,H,G) -6997.90121134 -6997.831780 -6997.866312
C      0.573111     -2.423948      0.000000
C      -0.585296     -1.476311      0.000000
H      0.137809     -3.431697      0.000000
H      1.193722     -2.333495     -0.892188
H      1.193722     -2.333495     -0.892188
H      -1.226070     -1.508009      0.888536
H      -1.226070     -1.508009     -0.888536
I      0.000000      0.651250      0.000000
# ethyl dibenzothiophene cation
28
Ch 1 Mul 1 (E,H,G) -938.63271862 -938.389388 -938.441804
C      -2.052684     -1.727550      0.404500
C      -1.001463     -0.882855      0.063735
C      -1.313834      0.417757     -0.347256
C      -2.603406      0.906820     -0.442749
C      -3.635682      0.043578     -0.088327
C      -3.358137     -1.256034      0.329727
S      0.161097      1.342627     -0.721714
C      1.195972     -0.064369     -0.379459
C      0.431993     -1.159343      0.043083
C      1.099279     -2.340933     -0.347297
C      2.482582     -2.395765      0.221483
C      3.212962     -1.294800     -0.219434
C      2.569569     -0.103261     -0.540085
C      0.339857      2.366018      0.804822
C      1.675364      3.073282      0.845758
H      0.545283     -3.214835      0.670955
H      3.001311     -3.317947     -0.457727
H      4.288824     -1.365875     -0.328173
H      3.127074      0.748654     -0.911361
H      -2.811955      1.913542     -0.786892
H      -4.662009      0.385949     -0.149745
H      -4.176963     -1.915415      0.594354
H      -1.856946     -2.745686      0.721442
H      -0.500331      3.062610      0.741920
H      0.182571      1.680434      1.639615
H      1.827214      3.719179     -0.021997
H      1.699147      3.704107      1.737845
H      2.505004      2.367983      0.923160
# ethyl acridine cation
30
Ch 1 Mul 1 (E,H,G) -633.98316919 -633.715998 -633.767221
C      0.000249     -1.880168      0.078775
C      1.211224     -1.201683      0.018628
C      1.198936      0.218658     -0.140183
N      -0.000022      0.871118     -0.262070
C      -1.198813      0.218383     -0.140244
C      -1.210855     -1.201938      0.018537
```

C	2.449655	-1.890492	0.116656	
C	3.628619	-1.207243	0.077735	
C	3.607938	0.197982	-0.053753	
C	2.434270	0.901322	-0.161433	
C	-2.434213	0.900910	-0.161355	
C	-3.607774	0.197391	-0.053718	
C	-3.628256	-1.207864	0.077589	
C	-2.449199	-1.890945	0.116477	
C	-0.000340	2.328113	-0.506042	
C	-0.000973	3.131385	0.782140	
H	2.430424	-2.969240	0.227999	
H	4.574870	-1.728971	0.154827	
H	4.545296	0.743449	-0.065140	
H	2.480476	1.977906	-0.237912	
H	-2.480516	1.977507	-0.237643	
H	-4.545214	0.742722	-0.064949	
H	-4.574444	-1.729721	0.154594	
H	-2.429814	-2.969692	0.227786	
H	0.864595	2.554437	-1.126983	
H	-0.865185	2.553871	-1.127302	
H	0.882911	2.915714	1.386646	
H	-0.001889	4.197938	0.547688	
H	-0.884510	2.914207	1.386623	
H	0.000359	-2.960813	0.189402	
# triflate radical				
8				
Ch 0	Mul 2 (E,H,G)	-960.81951860	-960.785319	-960.828640
O		-1.287556	-0.748010	-1.173495
S		-0.863767	0.048308	-0.001809
C		0.993703	-0.007363	0.000106
F		1.436808	0.614651	1.075878
O		-1.288269	-0.725927	1.186501
O		-1.241367	1.442210	-0.011385
F		1.390972	-1.264222	0.010807
F		1.438397	0.596801	-1.084982
# iodine				
1				
Ch 0	Mul 2 (E,H,G)	-6919.07587248	-6919.073512	-6919.093375
I		0.000000	0.000000	0.000000

Figures

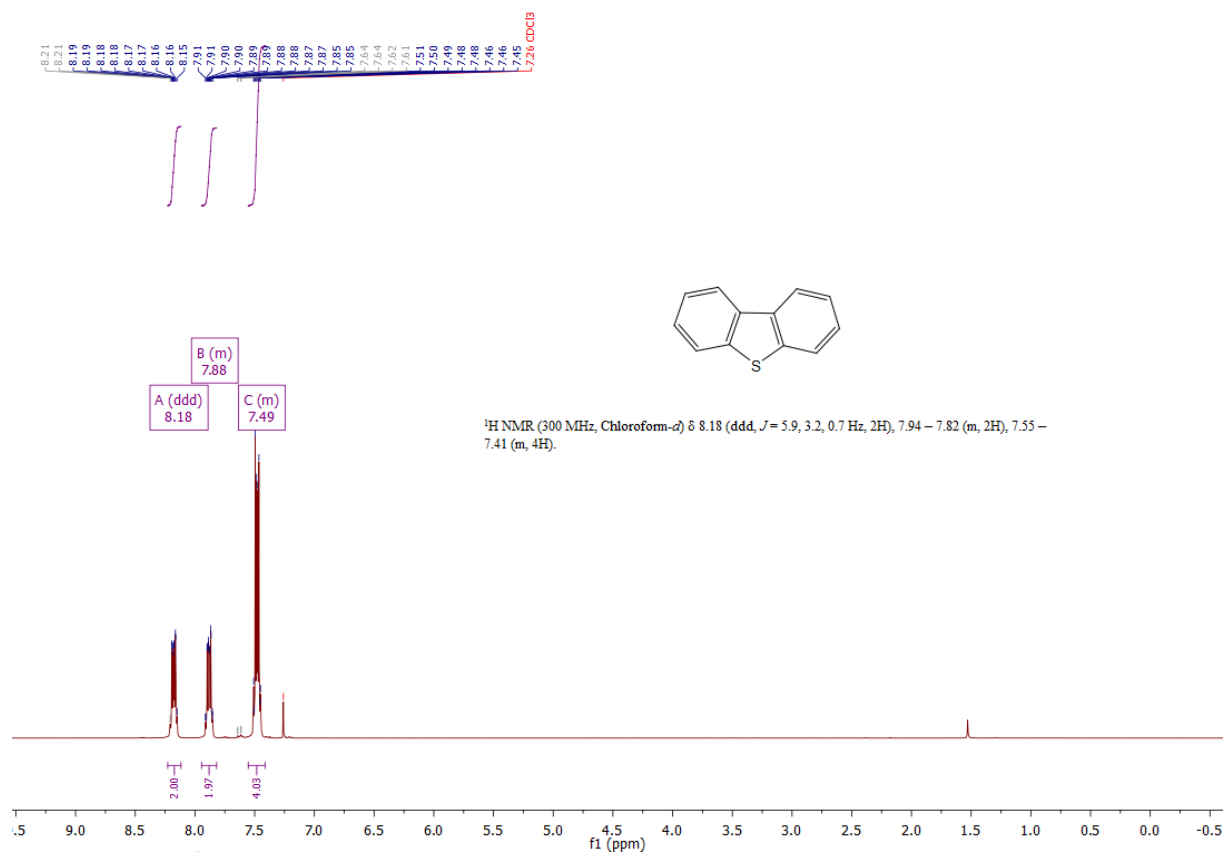


Figure A5.1: ¹H NMR spectra of dibenzo[b,d]thiophene (DBT) in CDCl₃.

^1H NMR (300 MHz, Chloroform- d) δ 8.18 (ddd, $J = 5.9, 3.2, 0.7$ Hz, 2H), 7.94 – 7.82 (m, 2H), 7.55 – 7.41 (m, 4H).[140]

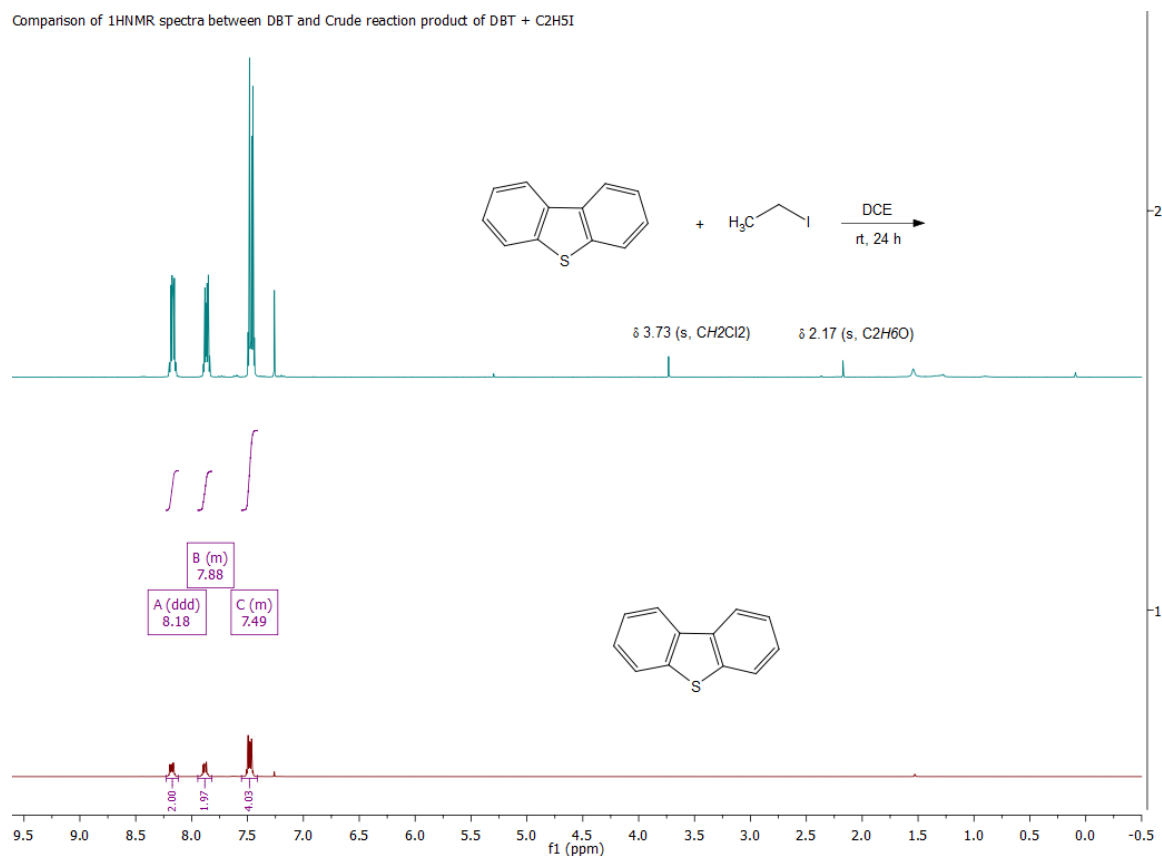


Figure A5.2: Comparison of ^1H NMR spectra obtained from DBT standard and the crude reaction mixture of DBT with $\text{C}_2\text{H}_5\text{I}$ in 1 mL DCE at 25 °C for 24 h.

From the comparison of ^1H NMR spectra above, we know that there is no reaction occurring between DBT and $\text{C}_2\text{H}_5\text{I}$ in DCE at 25 °C in glass flask, which is further confirmed by theoretical calculation.[146]

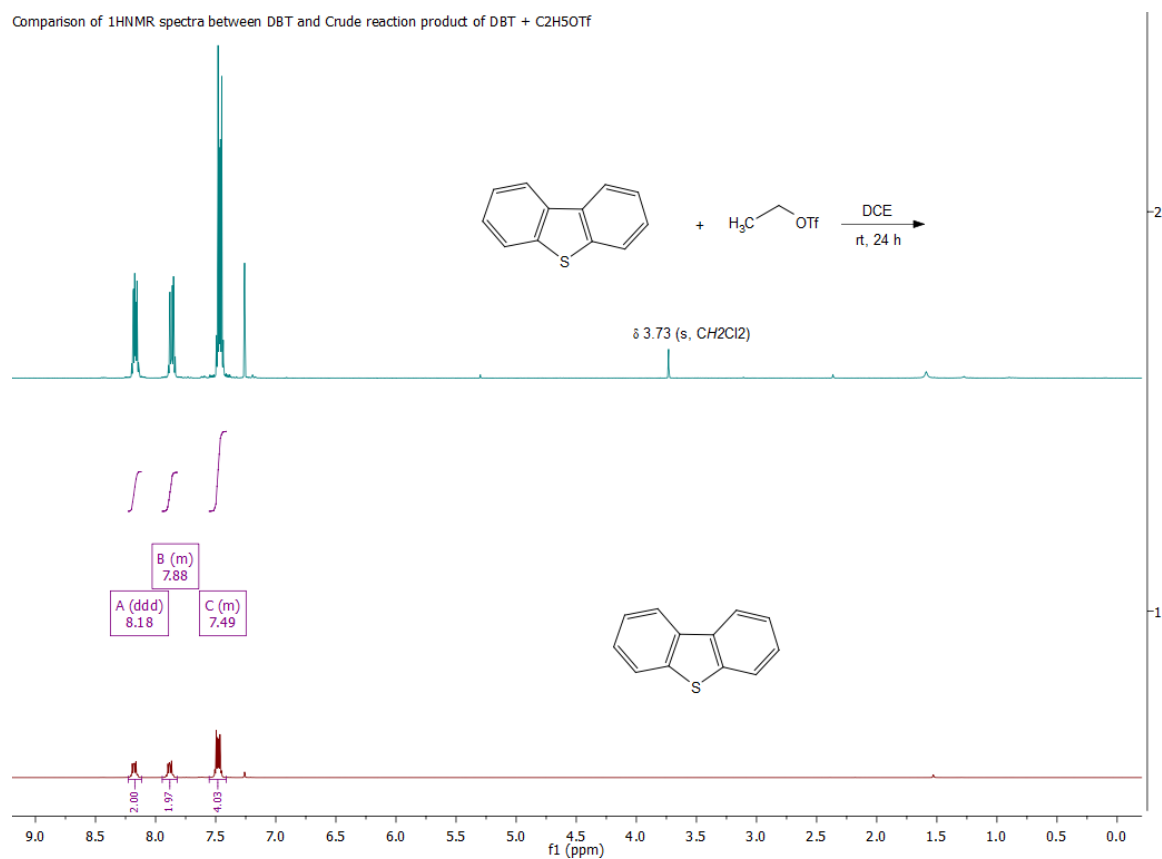


Figure A5.3: Comparison of ^1H NMR spectra obtained from DBT standard and the crude reaction mixture of DBT with $\text{C}_2\text{H}_5\text{OTf}$ in 1 mL DCE at 25 °C for 24 h.

From the comparison of ^1H NMR spectra above, we know that there is no reaction occurring between DBT and $\text{C}_2\text{H}_5\text{OTf}$ in DCE at 25 °C in glass flask, which is further confirmed by theoretical calculation.[146]

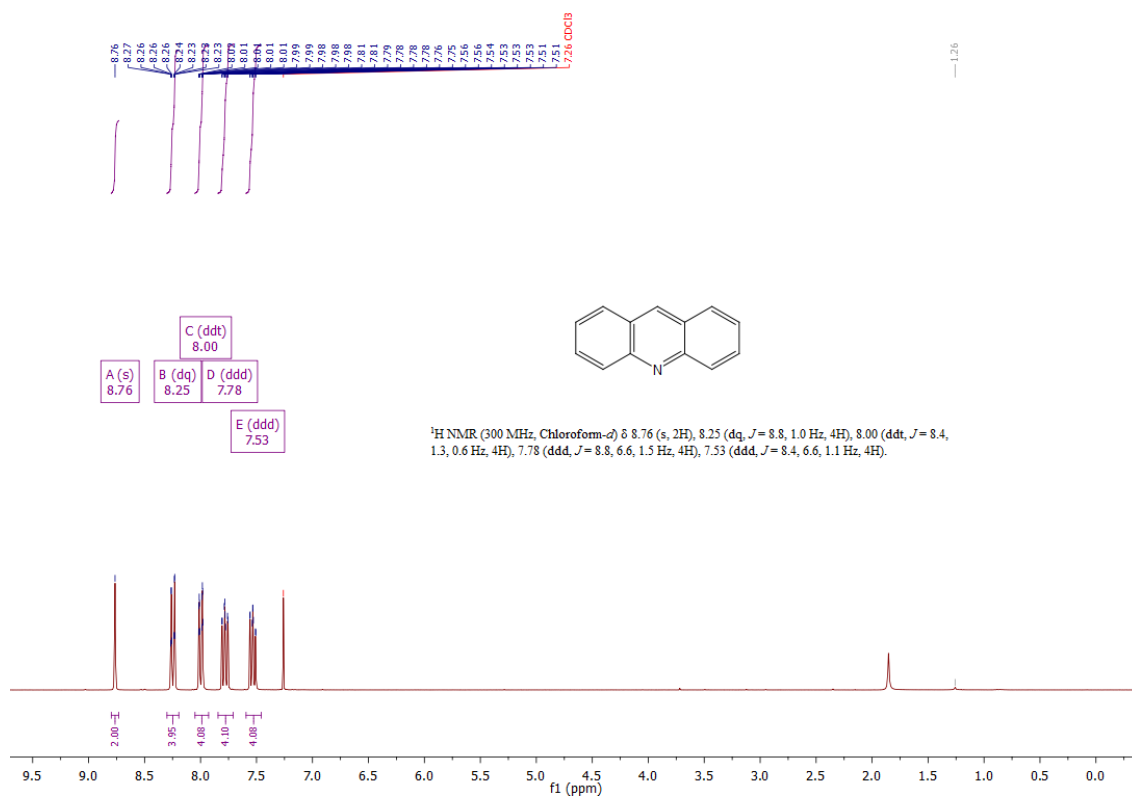


Figure A5.4: ¹H NMR spectra of ACR in CDCl₃

¹H NMR (300 MHz, Chloroform-*d*) δ 8.76 (s, 2H), 8.25 (dq, *J* = 8.8, 1.0 Hz, 4H), 8.00 (ddt, *J* = 8.4, 1.3, 0.6 Hz, 4H), 7.78 (ddd, *J* = 8.8, 6.6, 1.5 Hz, 4H), 7.53 (ddd, *J* = 8.4, 6.6, 1.1 Hz, 4H).[149]

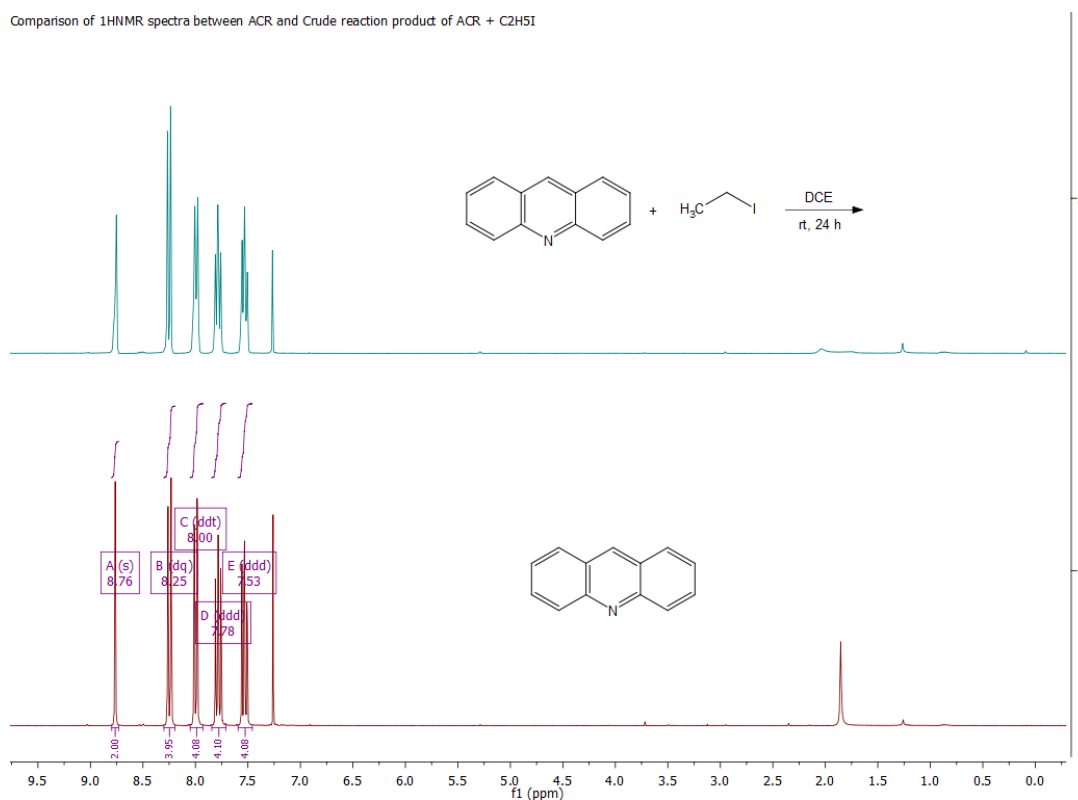


Figure A5.5: Comparison of ^1H NMR spectra obtained from ACR standard and the crude reaction mixture of ACR with $\text{C}_2\text{H}_5\text{I}$ in 1 mL DCE at 25 °C for 24 h.

From the comparison of ^1H NMR spectra above, we know that there is no reaction occurring between ACR and $\text{C}_2\text{H}_5\text{I}$ in DCE at 25 °C in glass flask, which is further confirmed by theoretical calculation.

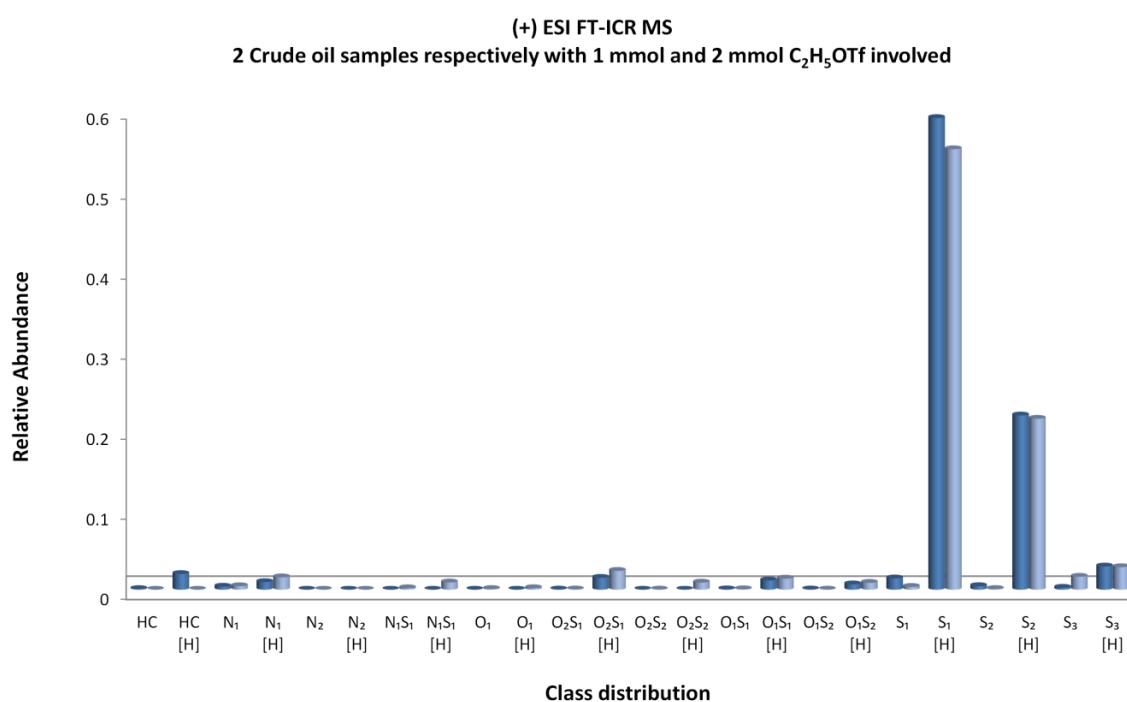


Figure A5.6: Comparison of class distribution based on 1 mmol and 2 mmol of $\text{C}_2\text{H}_5\text{OTf}$ in crude oil for sample A_1 and sample A_2 .

There is a very slight difference for the case of $\text{C}_2\text{H}_5\text{OTf}$ when comparing sample A_1 and sample A_2 in relative abundance, which means 1 mmol of $\text{C}_2\text{H}_5\text{OTf}$ is enough for the reaction and detection of each of classes.

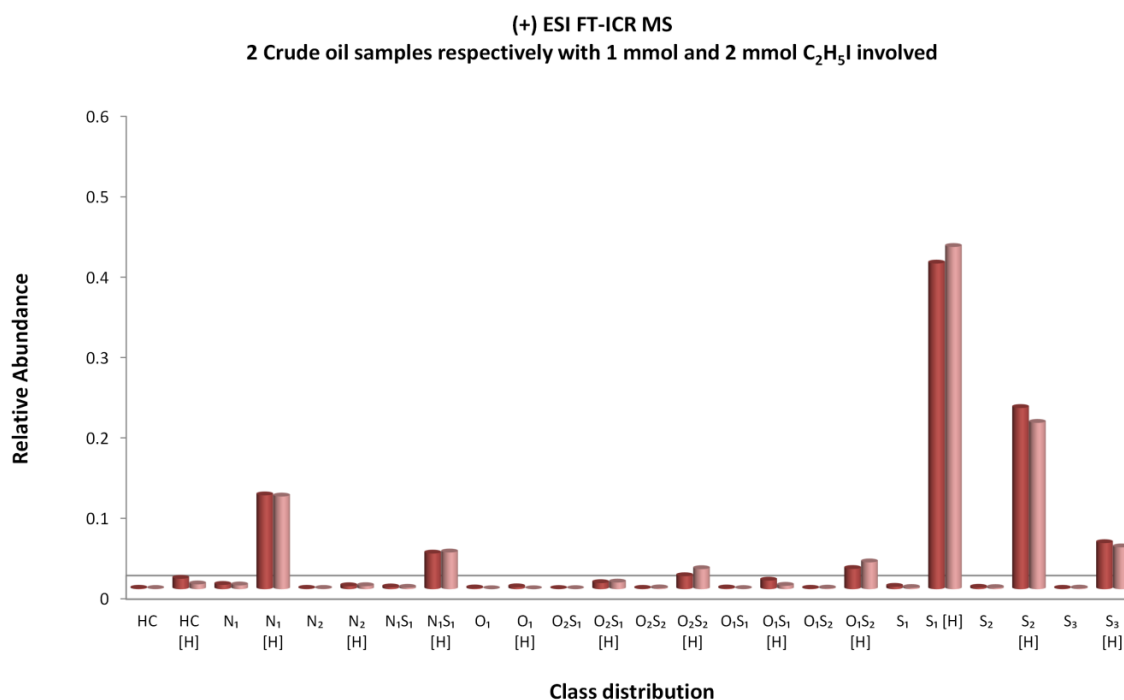


Figure A5.7: Comparison of class distribution based on 1 mmol and 2 mmol of C₂H₅I in crude oil for sample B₁ and sample B₂.

There is a very slight difference for the case of C₂H₅I when comparing sample B₁ and sample B₂ in relative abundance, which means 1 mmol of C₂H₅I is enough for the reaction and detection of each of classes.

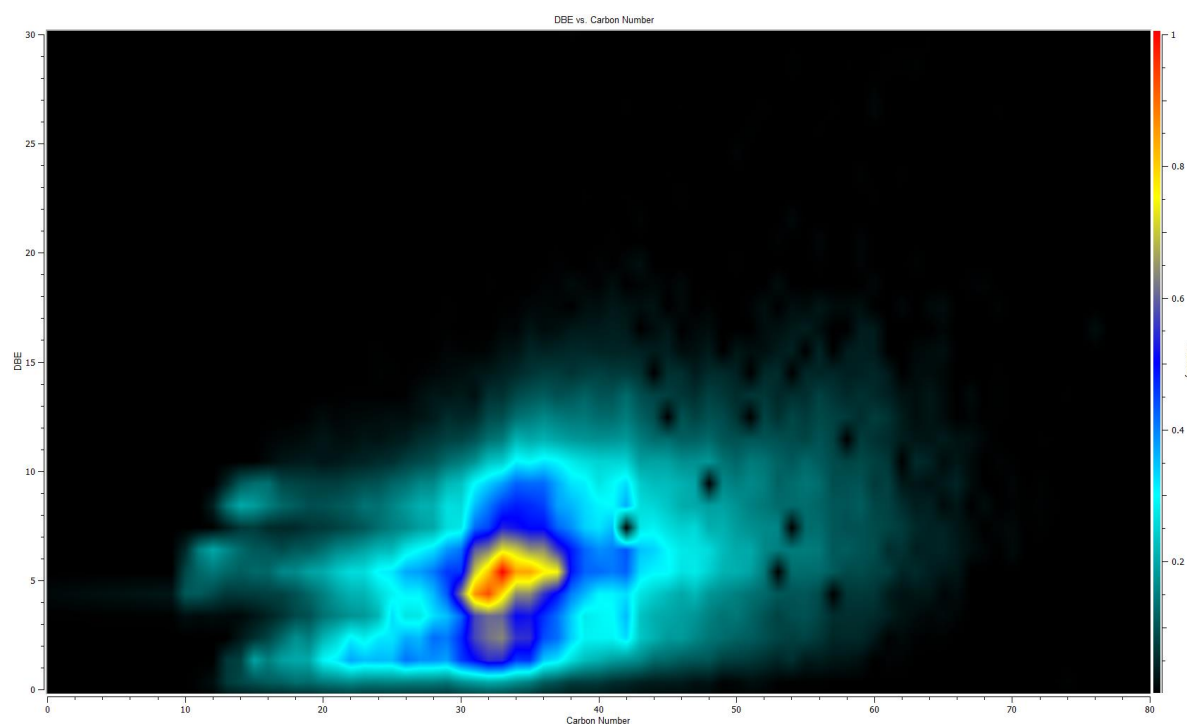


Figure A5.8: Color-coded image plots of DBE vs carbon number for members of S₁ class from sample A₁ (C₂H₅OTf).

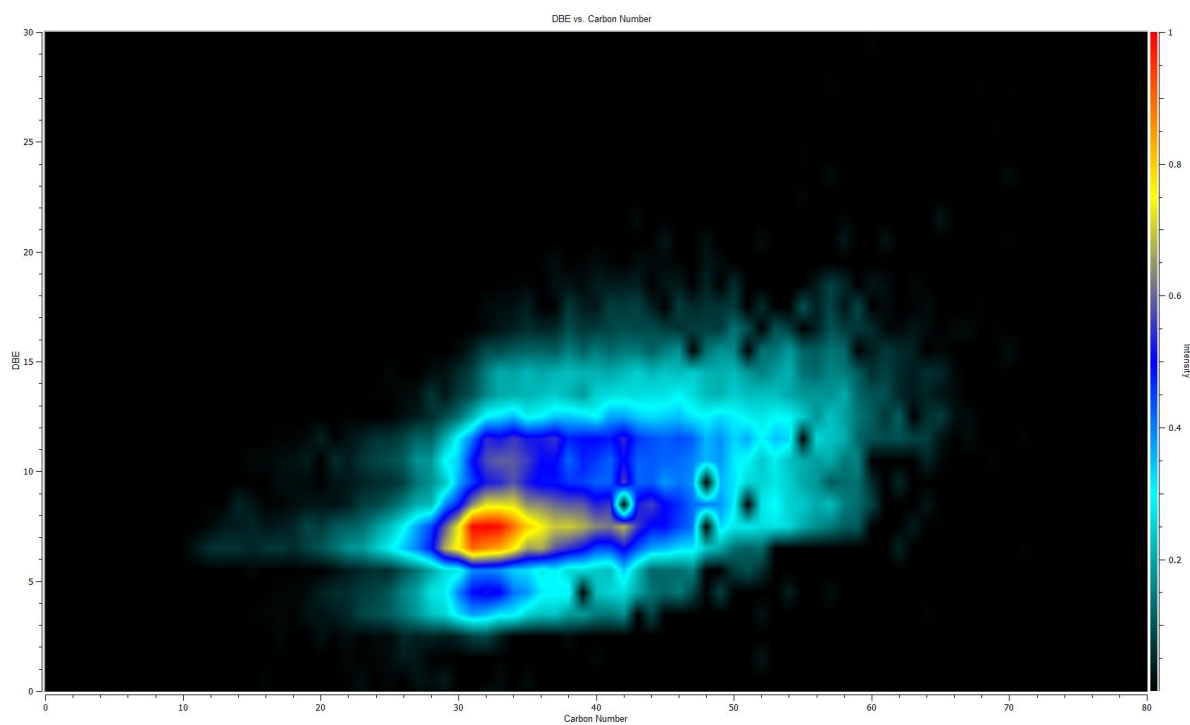


Figure A5.9: Color-coded image plots of DBE vs carbon number for members of S₂ class from sample A₁ (C₂H₅OTf).

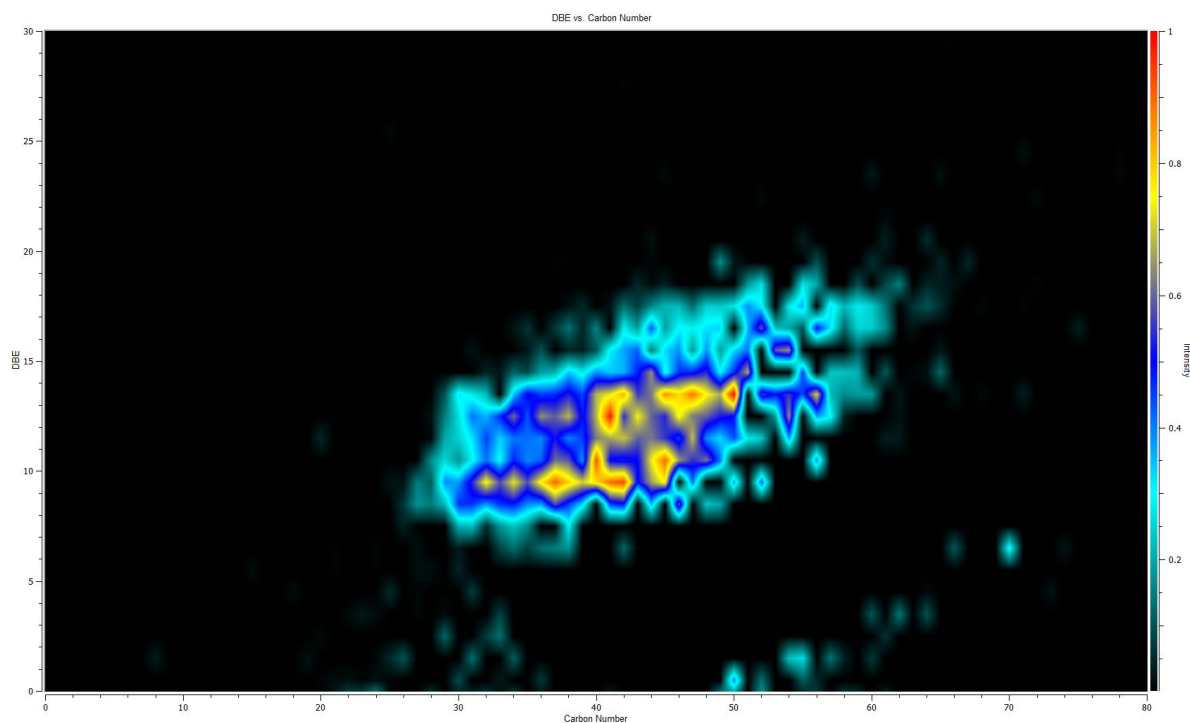


Figure A5.10: Color-coded image plots of DBE vs carbon number for members of S₃ class from sample A₁ (C₂H₅OTf).

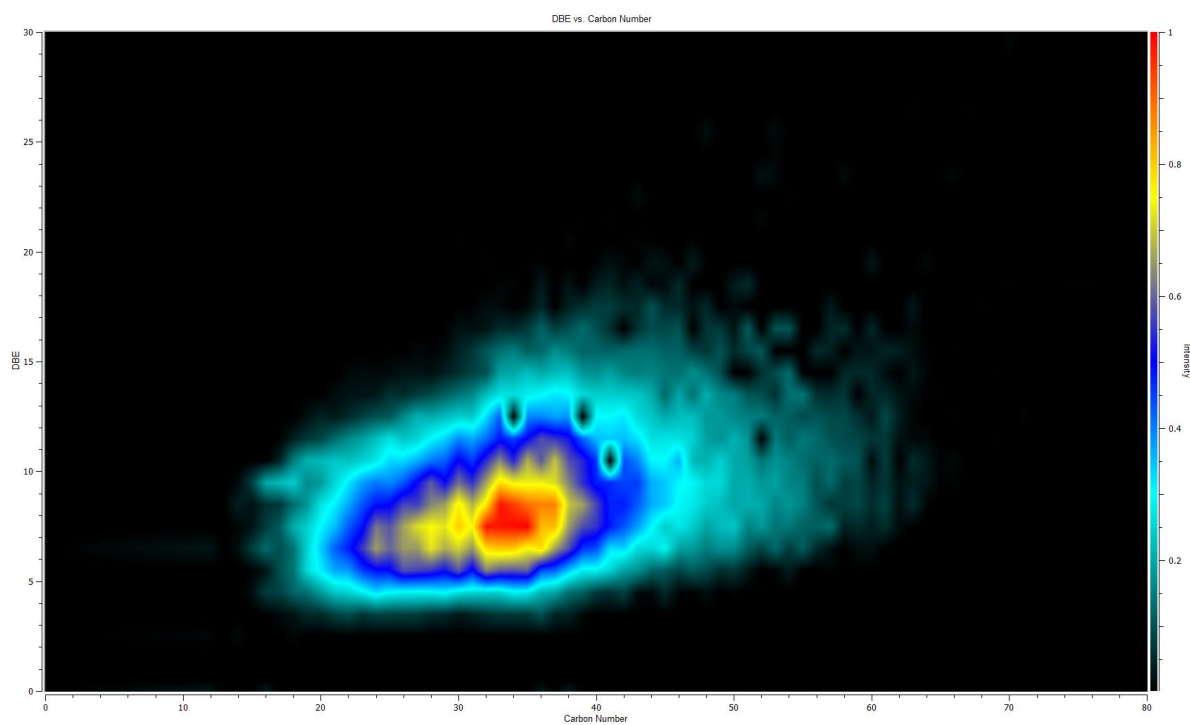


Figure A5.11: Color-coded image plots of DBE vs carbon number for members of N_1 class from sample B_1 (C_2H_5I).

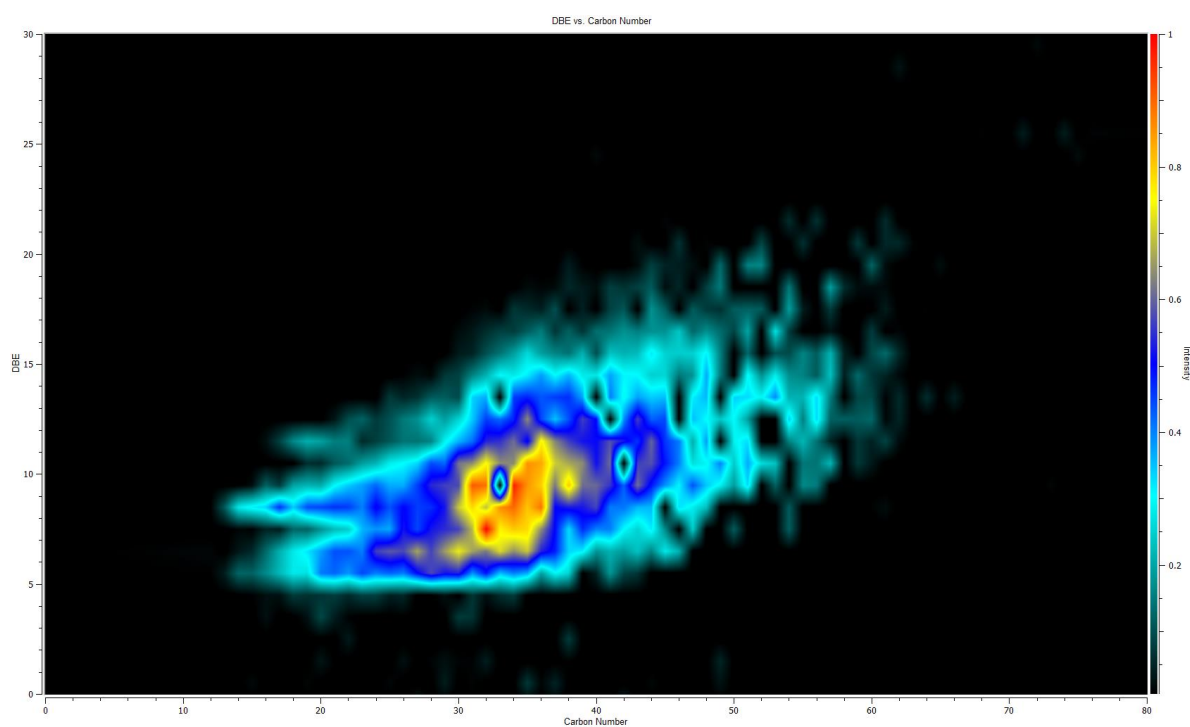


Figure A5.12: Color-coded image plots of DBE vs carbon number for members of N_1S_1 class from sample B_1 (C_2H_5I).

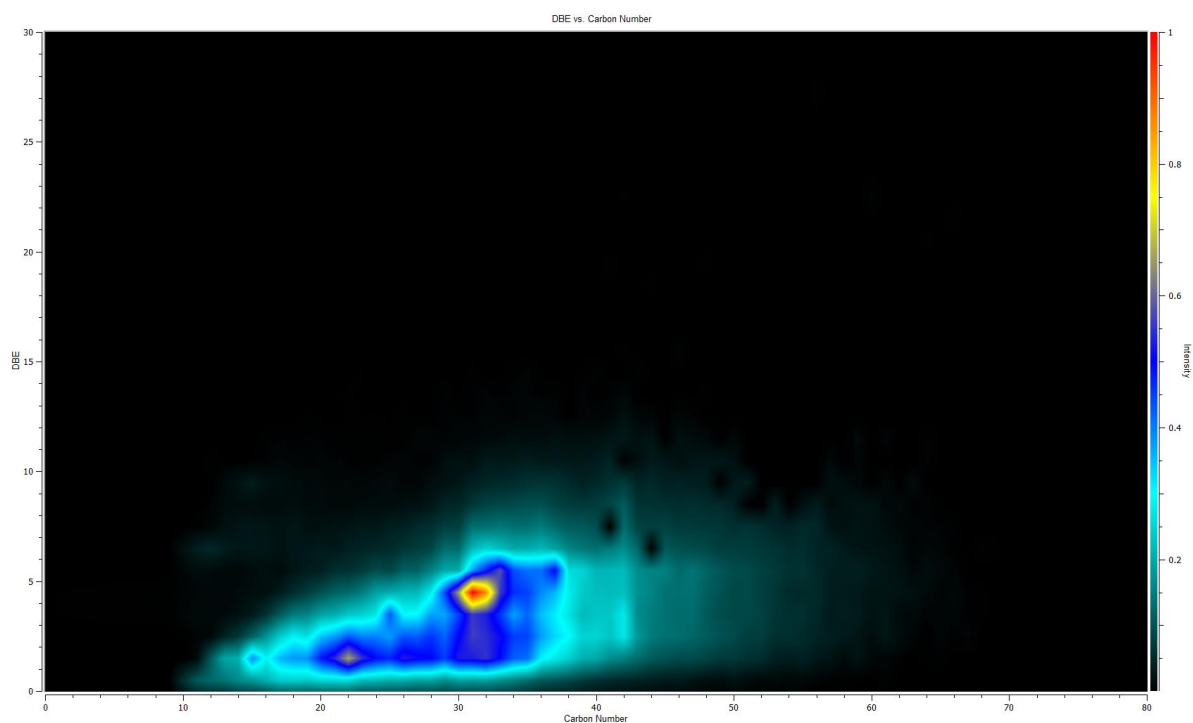


Figure A5.13: Color-coded image plots of DBE vs carbon number for members of S₁ class from sample B₁ (C₂H₅I).

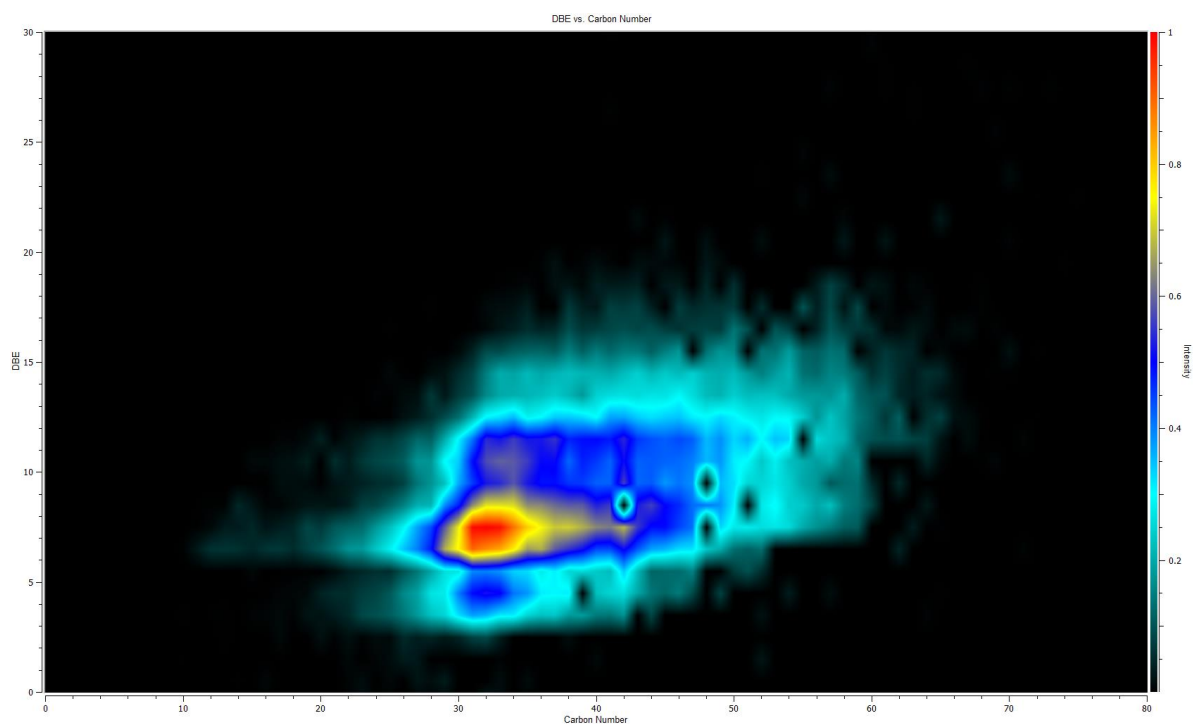


Figure A5.14: Color-coded image plots of DBE vs carbon number for members of S₂ class from sample B₁ (C₂H₅I).

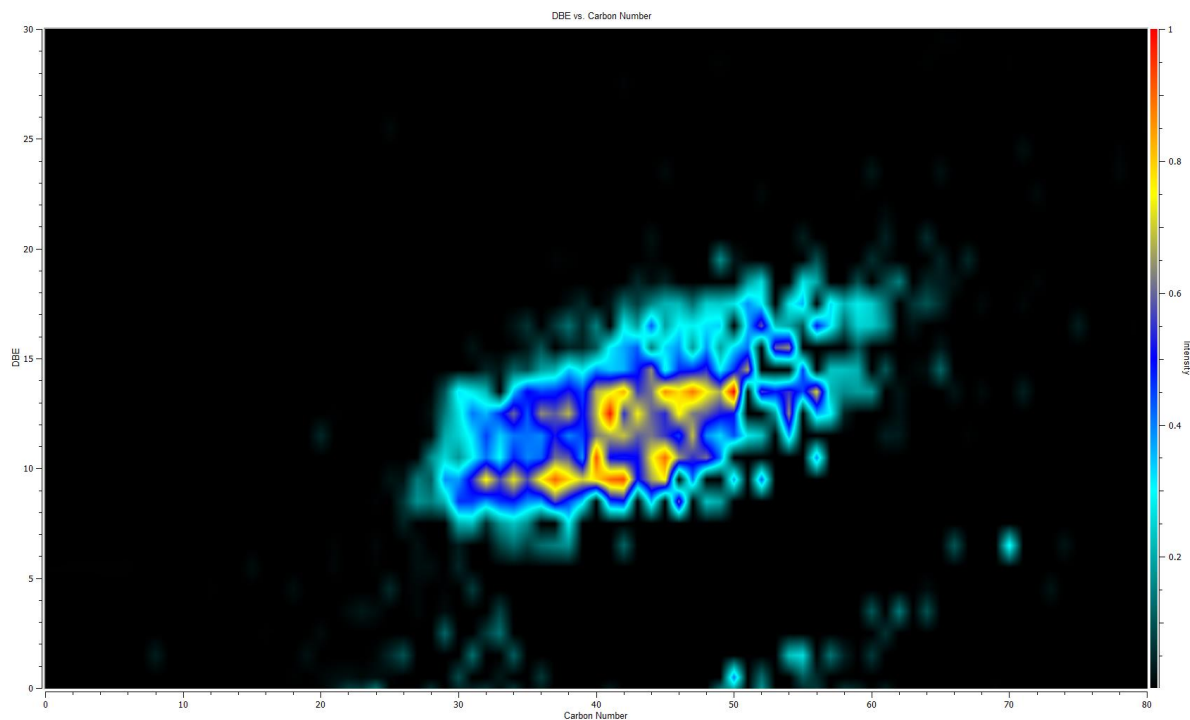


Figure A5.15: Color-coded image plots of DBE vs carbon number for members of S_3 class from sample B_1 (C_2H_5I).

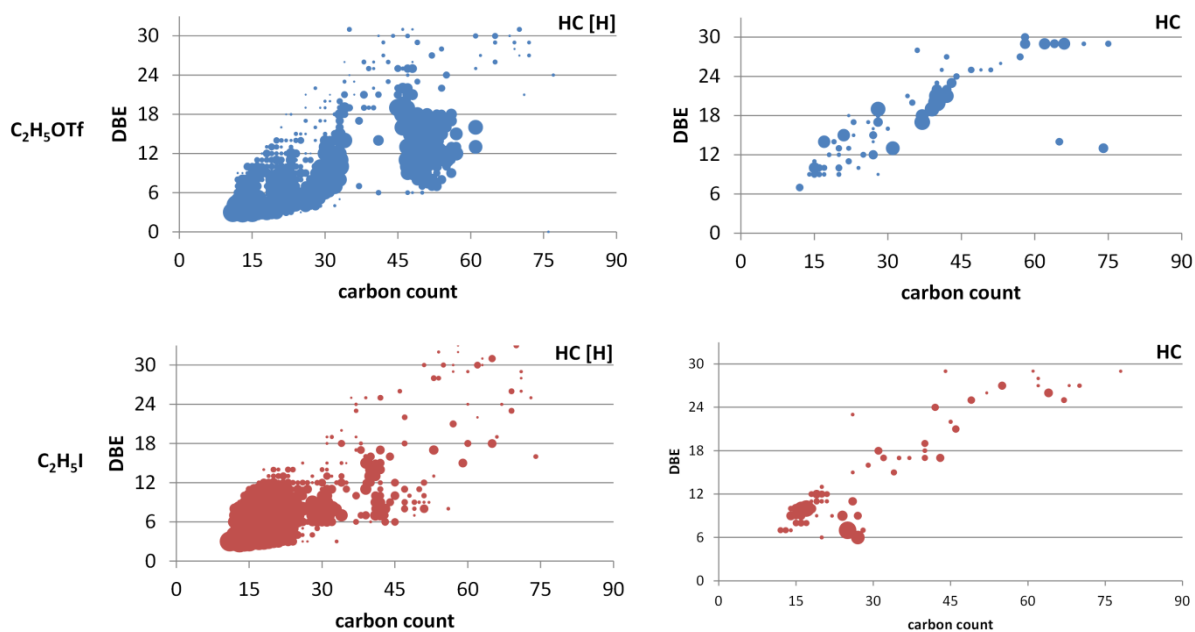


Figure A5.16: DBE vs carbon number for members of HC classes from sample A1 (C_2H_5OTf) and sample B1 (C_2H_5I).

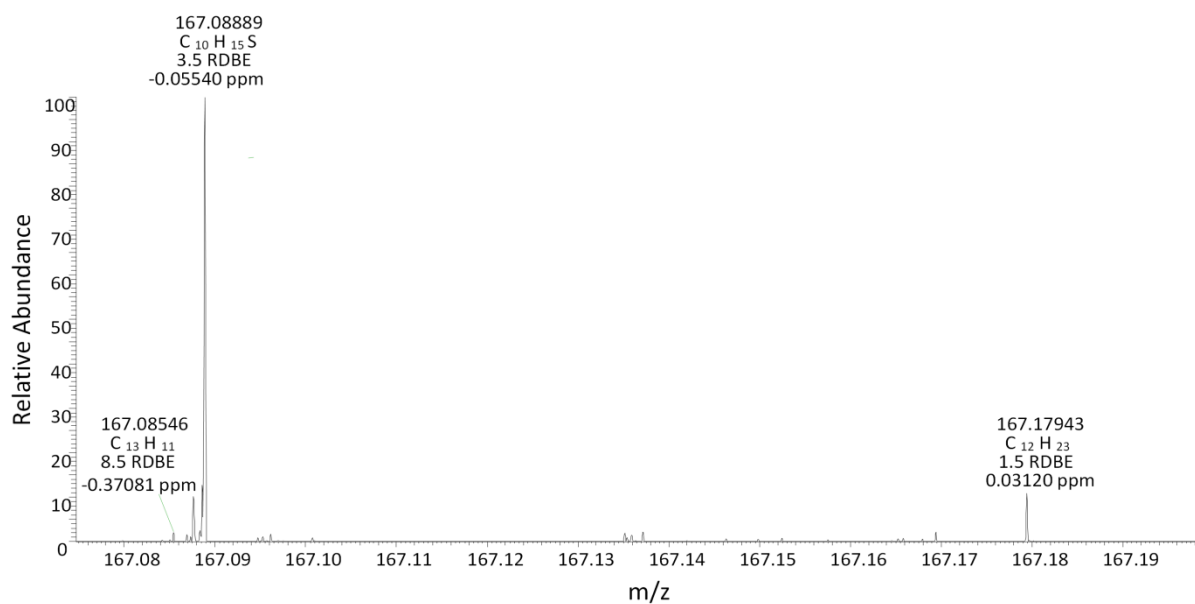


Figure A5.17: Enlarged section of mass spectra that contain a low DBE (2) of HC species from sample A_1 .

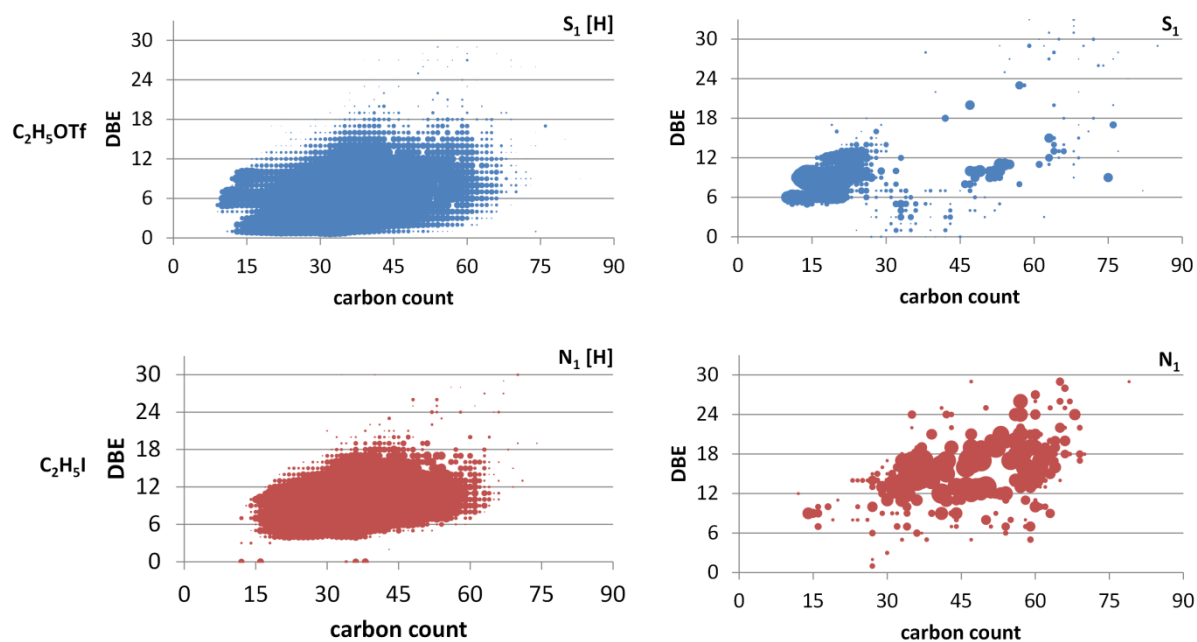


Figure A5.18: Comparison of DBE vs carbon number for members of cation and radical cation classes from Sample A_1 and Sample B_1 .

Chapter 6 Electrospray Fourier Transform Ion Cyclotron Resonance Mass Spectrometry (ESI FT-ICR MS): Reactivity of Poly Aromatic Hydrocarbon and Poly Aromatic Heterocycles in Heavy Crude Oils towards Benzyl Halides*

**Redrafted from “Wang, X.; Schrader, W., Electrospray Fourier Transform Ion Cyclotron Resonance Mass Spectrometry (ESI FT-ICR MS): Reactivity of Poly Aromatic Hydrocarbon and Poly Aromatic Heterocycles in Heavy Crude Oils towards Benzyl Halides, will be submitted to Energy & Fuels”*

6.1 Abstracts

Crude oil is a highly heterogeneous mixture consisted of not only hydrocarbons but also diverse heteroatoms (N, S and O) and metal-containing (Fe, V and Ni) species; it thus is termed as a *supercomplex* mixture in nature. With sufficiently ultrahigh mass resolving power and mass accuracy, Fourier Transform Ion Cyclotron Resonance Mass Spectrometry (FT-ICR MS) enables assignment of elemental compositions in such complex mixtures. However, the space charge effects limit the mass accuracy measurements in FT-ICR MS due to the high number of ions present during each transient. Selective analysis towards crude oil is one approach to overcome the problems. Electrospray (ESI) is useful for the speciation of polar molecules. Herein a heavy crude oil is benzylated, respectively by three benzyl halides with the presence of AgBF_4 and three samples were obtained. Another three crude oil samples are prepared with only benzyl halides involved. Highly selective analysis towards nitrogen and sulfur-containing species were obtained respectively through these contrast reactions by positive ESI FT-ICR MS. A marriage of chemical methods and ultrahigh resolution FT-ICR MS utilizing electrospray ionization is a powerful method aiding selective analysis of crude oil; vice versa, crude oil, *an ultracomplex substrate system*, challenges the organic chemists besides the analysts.

6.2 Introduction

Nowadays, the petroleum refining trends are shifting toward production of sour, heavier crude oils due to the decline of the sweet, light crudes.[150] A big disadvantage of heavier crude oils as energy sources is that they contain higher amounts of unwanted hetero-aromatic components comparing to the lighter crudes. Although only less than 10% of $\text{N}_n\text{O}_o\text{S}_s$ -containing molecules are present in a crude oil, they are typically the most problematic with respect to

fouling, inactivating catalysts, creating deposits, having an influence on corrosion and in regard to pollution of environment,[33] which leads to the necessity of improved upgrading processes. Therefore, a better understanding of crude oil on the molecular level is quite essential for the solution of the problems. Crude oil, however, is termed of a *supercomplex* mixture containing tens of thousands of chemically distinct species and has challenged the current analytical and petrochemical community over decades to uncover its complexity.[8, 10, 18] An established complementary and unrivalled tool for crude oil analysis is ultrahigh resolution Fourier Transform Ion Cyclotron Resonance Mass Spectrometry (FT-ICR MS).[33] The high mass accuracy of this method allows the determination of elemental composition of individual molecular species,[8, 151-153] revealing heteroatom class, type (DBE = number of rings plus double bonds to carbon), and carbon number.[33, 40]

There are many ionization methods available for ultrahigh resolution MS but electrospray ionization (ESI)[60] is most widely known method, efficient for ionization of polar molecules by generation of protonated (basic neutrals) or deprotonated (acidic neutrals) ions[31, 90]. Ultrahigh resolution FT-ICR MS equipped with ESI has emerged as a powerful technique for assignment of unique elemental compositions ($C_cH_hN_nO_oS_s$) of heteroatomic species in crude oil mixtures [18, 43, 154, 155]. However, besides the complexity of crude oil itself, recent reports have shown that suppression and discrimination effects can occur throughout a comprehensive characterization of highly complex systems[35, 42, 108, 156], and selective analysis is one of approaches to obtain a deeper knowledge by selectively looking into certain chemical species at a time.

Positive ESI (protonation) is particularly efficient for the speciation of the most basic petroleum components, and the conventional reagents for ESI (+) protonation are formic (pK_a 3.77) or acetic acid (pK_a 4.76). Nonpolar sulfur and hydrocarbon (HC) which are not basic enough to be readily ionized are not

typically accessed by ESI (+). Therefore, a derivatization method needs to be added to make the compounds accessible for electrospray ionization. Muller et al. [40] introduced methylation of thiophenic sulfur to enhance the detection of nonpolar polycyclic aromatic sulfur heterocycles (PASHs) by positive ESI-MS, but in this case prior chromatographic separation was needed for the selective analysis.

Herein, for the first time we introduce benzyl halides as reactants to crude oil analysis towards sulfur-containing species based on two different mechanism: with the presence of AgBF_4 , traditional two-electron transfer reaction is utilized to produce preformed polar sulfonium ions that are visible under ESI(+) conditions; with the absence of AgBF_4 , one-electron transfer reaction is employed to enable sulfur-containing species ionizable by using the inherent electrochemistry of ESI ion source [76, 79]. Selectivity towards sulfur-containing compounds depends on the reactivity of benzyl halides, the reactivity of heteroatom-containing species and the amount of heteroatom-containing species in whole heavy crude oil.

6.3 Experimental section

6.3.1 Chemicals and crude oil sample

Benzyl bromide ($\text{C}_7\text{H}_7\text{Br}$) and Benzyl chloride ($\text{C}_7\text{H}_7\text{Cl}$) were purchased from Sigma-Aldrich (high purity, Steinheim, Germany). Silver tetrafluoroborate (AgBF_4), dichloroethane (DCE) and dichloromethane (DCM) purchased from Sigma-Aldrich (high purity, St. Louis, Mo). Benzyl iodide ($\text{C}_7\text{H}_7\text{I}$) was prepared according to the literature procedures and all the spectra data was consistent with the literature report [157]. A heavy crude oil was provided by Shell Global Solutions, Amsterdam, The Netherlands, and bulk properties were: carbon 81.68%, hydrogen 9.98%, nitrogen 0.14%, sulfur 5.60%, and oxygen 2.08%.

6.3.2 Modification of heavy crude oil

AgBF₄-involved benzylation of heavy crude oil. 10 mg of heavy crude oil were dissolved in 1 mL of anhydrous dichloroethane (DCE). During mixing, a solution of 1 mmol of AgBF₄ in 1 mL DCE was added. According to the Table 6.1 above, after 2 min, 1 mmol of benzyl halide was then added and the corresponding silver halide precipitated. After 4 h, the solid was removed by centrifugation and washed with 1 mL DCE, and the three benzylated samples obtained were named with a sequence number as M1, M2 and M3. The three samples were prepared at a concentration of 500 µg/mL by DCM diluting for the ESI measurement. For a reference, heavy crude oil coded M0 was dissolved in 1 mL of DCE and diluted by DCM to a final concentration of 500 µg/mL for the ESI measurement.

Modification of heavy crude oil without AgBF₄. 10 mg of heavy crude oil were dissolved in 1 mL of anhydrous dichloroethane (DCE). During mixing, as summarized in Table 6.1, 1 mmol of benzyl halide was then added. After 4 h, another 3 samples obtained were named with a sequence number as M4, M5 and M6. The samples were prepared at a concentration of 500 µg/mL by DCM diluting for the ESI measurement.

6.3.3 ESI FT-ICR MS analysis

Mass analysis was performed on a 7 T LTQ FR-ICR mass spectrometer (Thermo Fisher, Bremen, Germany) equipped with commercially available ESI sources (Thermo Fisher, Bremen, Germany). The data were collected and processed with the LTQ FT Ultra 2.5.5 (Thermo Fisher, Bremen, Germany) data acquisition system. The spectra were collected in positive mode using ESI. The ions were generated from an electrospray source equipped with a stainless steel-ESI needle; typical ESI conditions were as follows: flow rate 5 µg/min; spray voltage, 4.0 kV; a sheath gas flow of 5 (arbitrary unit); an auxiliary gas flow of 2

(arbitrary unit). The measurements were carried out with a transfer capillary temperature of 275 °C, a capillary voltage of 30 V, and a tube lens voltage of 110 V. Acquisition mass range, $150 < m/z < 1200$; target total charge value (AGC value) between 1E5 and 1E6. The Instrument was calibrated with the Thermo Scientific Pierce LTQ Velos ESI positive ion calibration solution. In addition, external calibration was performed using a mixture of the Agilent electrospray calibration with the masses 322.04812, 622.02896, 922.00980, thus the whole mass range was covered in the samples.

6.3.4 Data analysis

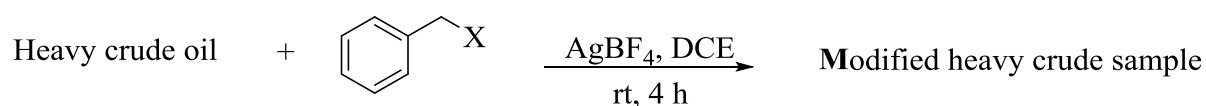
The acquired data was then imported into the composer software (Sierra Analytics, Modesto, CA) and the resulting assignments of elemental compositions were checked by Xcalibur software (Thermo-Fisher, Bremen, Germany). The following chemical constraints were applied: number of H unlimited, $0 < C < 200$, $0 < S < 3$; $0 < O < 3$, $0 < N < 3$, and $0 < \text{double bond equivalent (DBE)} < 40$, with a mass accuracy of less than 1 ppm. The calculated molecular formulas were processed by sorting them into heteroatom classes based on Kendrick mass defects and their double bond equivalent (DBE) distribution [82]. The assignments of the most abundant ions were confirmed by corresponding ^{13}C peak. The obtained mass lists were imported into Excel (Microsoft) packages for data evaluation and preparation of the figures shown.

6.4 Results and Discussion

A number of different conditions have been investigated for the modification reaction of heavy crude oil. In Table 6.1 the reaction conditions are summarized. M0 is chosen as a reference. The series of M1, M2 and M3 reactions show the results of the reaction of the many different components present in a heavy crude oil with chlorinated, bromated and iodated benzylhalides in the presence

of a silver salt, while the series of M4, M5 and M6 shows the same reaction without the presence of the silver salt. The results show that depending on the reaction conditions different components within the crude oil react with the benzyl halides and therefore, different components can be detected by ESI(+)-MS.

Table 6.1: Heteroatom class distribution from the modified heavy crude oil samples in anhydrous DCE



Serial No.	X	PhCH ₂ X	AgBF ₄	Heteroatom class distribution with relative abundance above 5%
M0	--	0 mmol	0 mmol	N, NS, S
M1	Cl	1 mmol	1 mmol	S, S2, CH
M2	Br	1 mmol	1 mmol	S, S2, CH
M3	I	1 mmol	1 mmol	S, S2, NS2, N
M4	Cl	1 mmol	0 mol	N, NOS, NS, NOS2
M5	Br	1 mmol	0 mmol	N, S, NS, S2, NOS
M6	I	1 mmol	0 mmol	S, S2, S3

Here we choose 5% of relative abundance as a relative value to evaluate the degree of selectivity for certain heteroatom-containing compounds. The less the presence of the heteroatomic species with the relative abundance above 5% are, the higher the degree of selectivity are achieved by a reaction, such as the highly selective analysis towards the three sulfur containing-compounds in M6 case.

ESI is a widely used ionization method that covers a broad range of components, often with a higher polarity. The results prior to a chemical modification for sample M0 are shown in Figure 6.1. Here the class distribution

shows that the ionization method favors the polar components with N[H] and NS[H] classes being the most widely appearing classes. This demonstrates that the natural diversity that is covered by ESI makes it possible to see basic nitrogen species exhibiting excellent positive ESI response at an overwhelming relative abundance, even if the nitrogen content in heavy crude oil is only 0.14%. S₁ class is accessed at a relative abundance of less than 5%, even though the sulfur content (5.60%) in original heavy crude oil is almost 15 times higher than the nitrogen's.

6.4.1 Reactivity of polyaromatic heterocycles in heavy crude oils towards benzyl halides with AgBF₄

The results change when the crude oil is being reacted with benzylhalides. Here three different benzylhalides have been investigated, and the results from these reactions are coded in M1 (benzyl chloride), M2 (benzyl bromide) and M3 (benzyl iodide) as shown in Figure 6.1. The first change can be seen from the mass spectra, especially in M1 and M2 cases, the mass patterns with obvious periodicities of 90 nominal mass units indicate that a self-polymerization of benzyl cation (electrophilic aromatic substitution) occurs (big signals in the mass spectra of M1 and M2), so the self-polymerization of the benzyl cation contributes most to the hydrocarbon CH[H] class distribution in M1 and M2 cases, and this can be further confirmed by the Kendrick plots of CH class (M1 and M2) in Figure 6.2.

Figure 6.1b (right column) exhibits the heteroatom class distribution of M0, M1, M2 and M3 samples. The flip happened after the benzylation as illustrated in M1, M2 and M3, the sulfur-containing species such as S₁ and S₂ classes prevailed over nitrogen-containing species to be accessed with a high degree of selectivity, especially in M1 (C₇H₇Cl) and M2 (C₇H₇Br) cases.

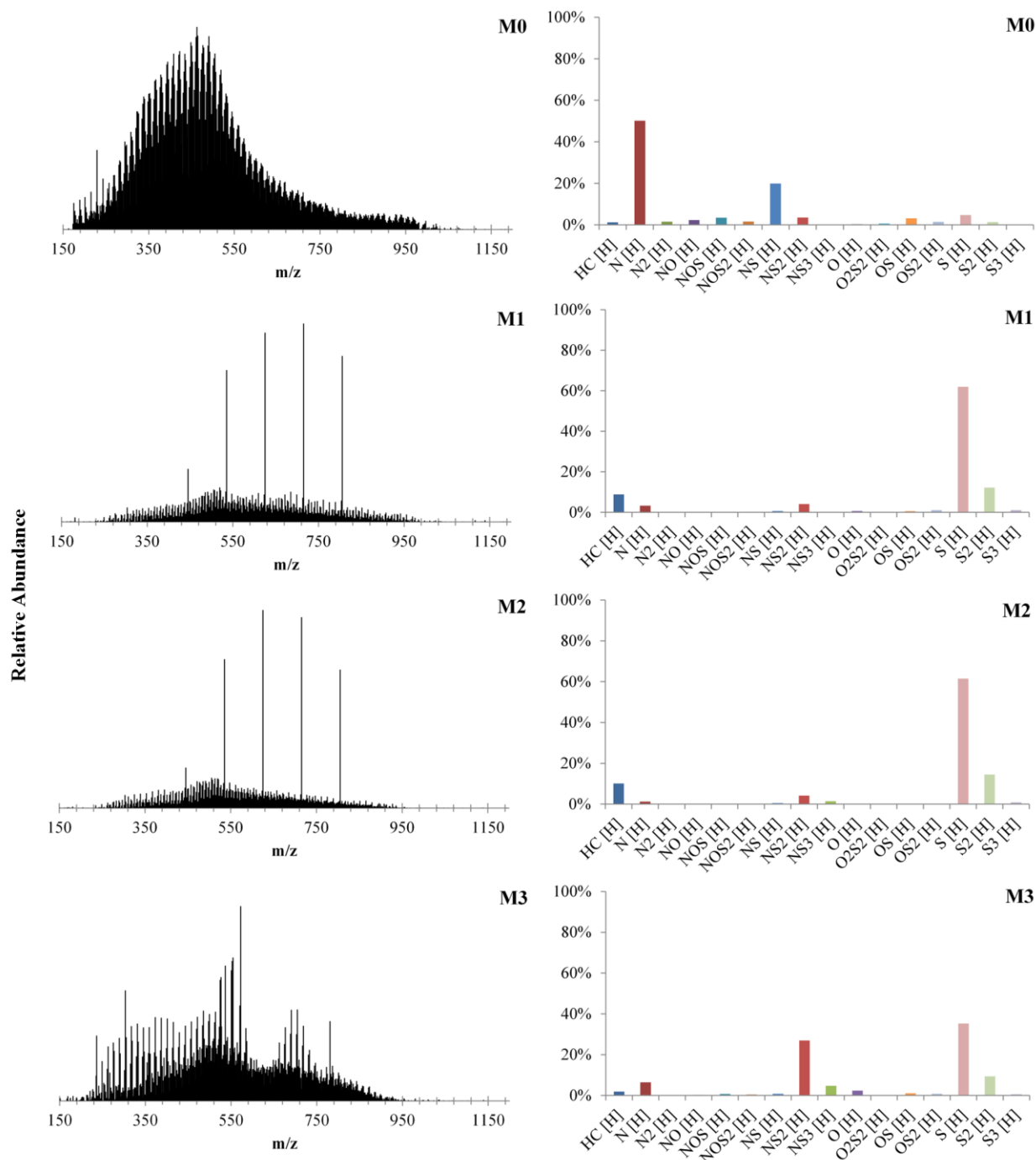


Figure 6.1: Comparison of broadband positive-ion ESI 7 T FT-ICR mass spectra and the corresponding heteroatom class distribution obtained for benzylated heavy crude oil samples (M1, M2 and M3). Herein, M0 is taken as a reference for the comparison.

Herein, it is worth stressing that, the hydrocarbon class in M1 and M2 cases is derived from the self-polymerization of benzyl cation, not from the hydrocarbon compounds in crude oils, so apart from this consideration, we can

assume that the benzylation of crude oil exclusively worked on sulfur-species. Some changes appear in M3 case (C_7H_7I) in comparison with M1 (C_7H_7Cl) and M2 (C_7H_7Br) cases: the relative abundance of $NS_2[H]$ species increases by a factor of more than seven in M3 case, but the relative abundance of S_1 class decreases. NS_3 as a new class was observed in M2 and M3 cases.

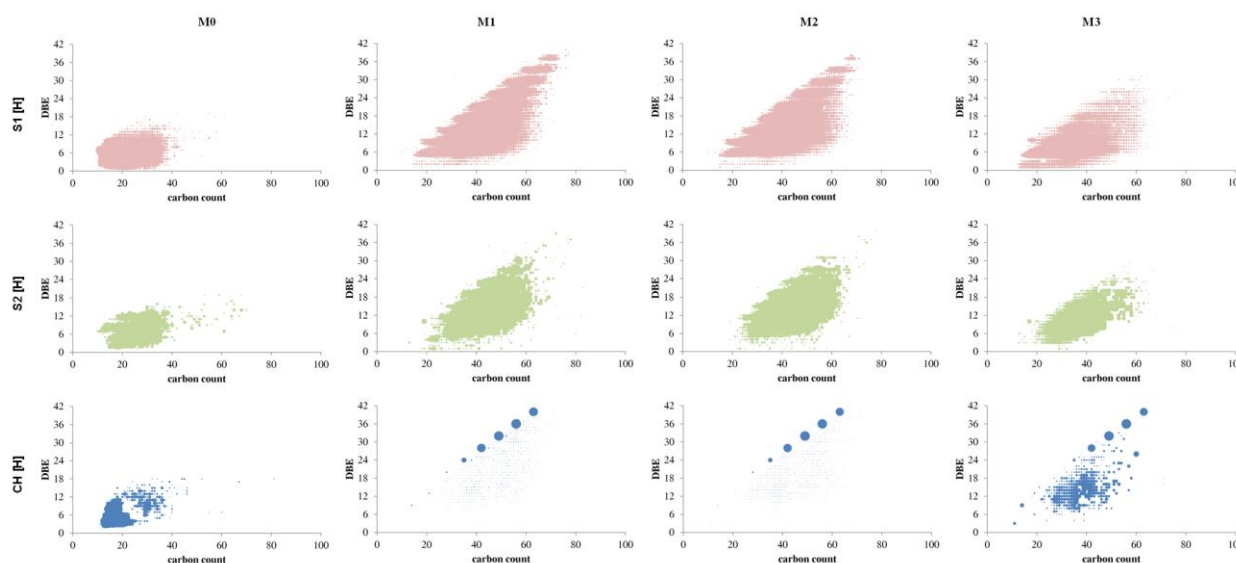


Figure 6.2: Comparison of Kendrick plots (DBE vs. Carbon number plots) for ions of the $S_1[H]$, $S_2[H]$ and $CH[H]$ classes for M1, M2 and M3 samples based on Table 6.1, obtained by (+) ESI FT-ICR MS. Herein, M0 is taken as a reference.

The compound distribution based on elemental composition of a complex mixture is best represented by DBE vs. carbon number distribution for each given class. After benzylation $S_1[H]$, $S_2[H]$ and $CH[H]$ in M1, M2 and M3 cases are accessed with a higher DBE value and a larger carbon number comparing those in M0 case as shown in Figure 6.2. It is reported that the maximum possible DBE value for $C_cH_hS_1$ and other heteroatom class is approximately equal to 25[33]. Herein, taking the $S_1[H]$ for example, the $S_1[H]$ class for M1, M2 and M3 spans a wider DBE (up to 42) and carbon number range. If we look in detail, there is an obvious periodicity of 4 DBE units addition for $S_1[H]$ in vertical axis, and same phenomenon can be found for DBE vs. carbon number

distribution of $S_2[H]$ specie in M1, M2 and M3 cases in Figure 6.2, and this indicates multi-benylation occurred for sulfur-containing species, but nucleophilic substitution occurred first, followed by another electrophilic aromatic substitution. For CH[H] class, this phenomenon are more obvious. Self-polymerization of benzyl cations occurs faster than the electrophilic aromatic substitution on hydrocarbons present in crude oil, so the most contribution for CH[H] class is from the self-polymerization, not from the hydrocarbons in crude oil. The large dots in CH[H] for M1, M2 and M3 belong to the products of self-polymerization of benzyl cations.

The Mechanism behind selectivity towards sulfur-containing species in M1, M2 and M3 cases are explained as follows. Ag^+ is a soft Lewis acid, and a sulfur atom is a softer Lewis base, and it is more nucleophilic comparing with other heteroatom (N and O)[158] in polar aprotic solvent (dichloroethane). The sulfur content in heavy crude oil is 5.60% (nitrogen 0.14% and oxygen 2.08%), therefore Ag^+ is thermodynamically and kinetically preferable to coordinate with sulfur atom, and then the S-C bond (sulfonium cation) is formed by the strong driving force from the precipitation of silver halide (AgX). The above reaction is irreversible and occurs in the product direction (sulfonium cation) mostly to completion. It is worth noting that besides the nucleophilic substitution on the sulfur atoms, electrophilic aromatic substitution on aromatic rings occurs because of the sufficient presence of benzyl cations which has been confirmed by the obvious periodicities at 90 nominal mass units in Figure 6.1 and at 4 DBE units in Figure 6.2 for $S_1[H]$, $S_2[H]$ and CH[H] classes. The explanation for the increase of $NS_2[H]$ in M3 case (benzyl iodide) comparing to M2 (benzyl chloride) and M3 (benzyl bromide) cases as shown in Figure 6.1 might lie in the reactivity of the benzyl halides, or the strengths of the carbon-halogen bonds (C-Cl is strongest and C-I is weakest). Benzyl iodide is the most chemical reactive towards $AgBF_4$ in DCE among the three benzyl halides, and the reaction rate is fastest, when comparing to benzyl chloride and benzyl bromide, which means

any nucleophilic sulfur atoms are surrounded by sufficient benzyl cations, even though NS_2 compounds in crude oil might be present in low abundance comparing to other sulfur-containing species like S_1 and S_2 , they can still be tagged. In contrast, the reaction rate of benzyl chloride and AgBF_4 is slower than the rate of benzyl iodide and AgBF_4 , so it produces benzyl cations in a longer time, which means not sufficient in short time, so the products will be determined by the amount of reactants, because the relative abundance of S_1 and S_2 in crude oil are higher than NS_2 , so S_1 and S_2 will be first selectively tagged. This is reactivity-selectivity principle (RSP): more reactivity, less selectivity.[159]

6.4.2 Reactivity of polyaromatic heterocycles in heavy crude oils towards benzyl halides

Benzyl halide is a reagent with multi-active sites. When AgBF_4 is added to benzylate crude oil, nucleophilic substitution occurs on sulfur atom or /and EAS occurs on carbon atom depending on reaction condition but if we only add benzyl halide to crude oil the outcome can be different. Figure 6.3 shows the mass spectra and the heteroatom class distribution from the crude oil samples with benzyl halide and without AgBF_4

The mass spectra distribution in M4 reaction is obviously different from the M0 reaction. The extra bump in M4 reaction indicates another new heteroatom class detected compared to M0 reaction.. This is confirmed by the corresponding heteroatom class distribution as depicted in M4 case in Figure 6.3.

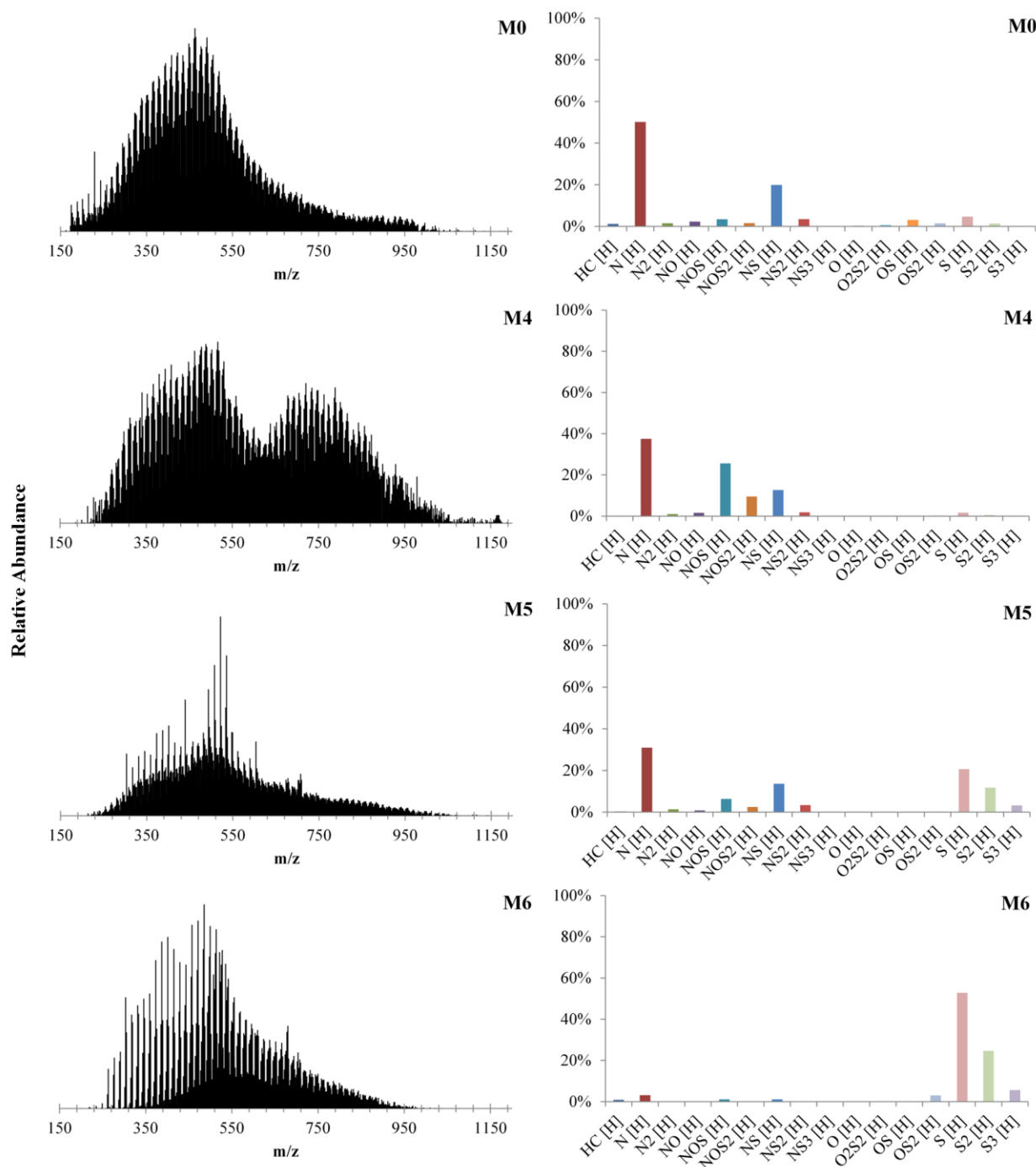


Figure 6.3: Comparison of broadband positive-ion ESI 7 T FT-ICR mass spectra and the corresponding heteroatom class distribution obtained from samples of M4, M5 and M6 based on Table 6.1. Herein, M0 is taken as a reference for the comparison.

The N₁[H] and N₁S₁[H] classes are the most abundant in untreated heavy crude oil sample M0, and some obvious change occurs when benzyl chloride is

added to modify the crude oil. Here, more nitrogen-containing species such as $N_1O_1S_1[H]$ and $N_1O_1S_2[H]$ are present in the higher proportion, especially the relative abundance of $N_1O_1S_1[H]$ class has increased by a factor of at least 7.5 as shown in Figure 6.3. It is worth noting that nitrogen-containing compounds are exclusively accessed in M4 case in comparing to M0 case. In contrast, the M6 is dominated totally by sulfur-containing species including the $S_1[H]$, $S_2[H]$ and $S_3[H]$ classes, suggesting that benzyl iodide aids accessing the sulfur selective analysis in whole crude oil as shown in the lower right corner in Figure 6.3. Whereas when benzyl bromide is introduced to modify the crude oil, both nitrogen and sulfur-containing species ($N_1[H]$, $N_1S_1[H]$, $N_1S_2[H]$, $N_1O_1S_1[H]$, $S_1[H]$, S_2 and $S_3[H]$ classes) in M5 give good ESI response. As a summary, benzyl chloride aids only nitrogen-containing species detectable, while benzyl iodide facilitates the selective detection of sulfur-containing species, and benzyl bromide plays no favorites towards between nitrogen and sulfur-containing species.

Figure 6.4 displays DBE versus carbon number plots for the $N_1[H]$, $N_1S_1O_1[H]$, $S_1[H]$, $S_2[H]$ and $S_3[H]$ classes from the four heavy crude oil samples of M0, M4, M5 and M6. An obvious trend can be observed in the pattern that is related to an increase both in DBE and carbon number value for sulfur-containing species, such as $S_1[H]$, $S_2[H]$ and $S_3[H]$ classes. For example the $S_3[H]$ class is totally absent in M0 and M4 case, but in M5, the $S_3[H]$ class gives a positive ESI response of above 5% at relative abundance. The $S_1[H]$ class in M6 case spans a DBE range of 3-25 and carbon number of 15-69, while the S_1 class ranges from DBE ~ 3-14 and carbon number of 20-50 with low relative abundance in M4 case. Another obvious difference lies in a decrease of DBE vs. carbon number plots for $N_1S_1O_1[H]$ class in M6 case compared with the other three cases (M0, M4 and M5). The $N_1[H]$ -species dominates the M0 case at a highest relative abundance compared to M4, M5 and M6 which can be seen from the depth of the color of DBE vs. carbon number plots as depicted in

the top left corner of Figure 6.4, DBE from 4 to 25 and carbon number from 13 to 75. M6 shows least preference towards the N_1 -species.

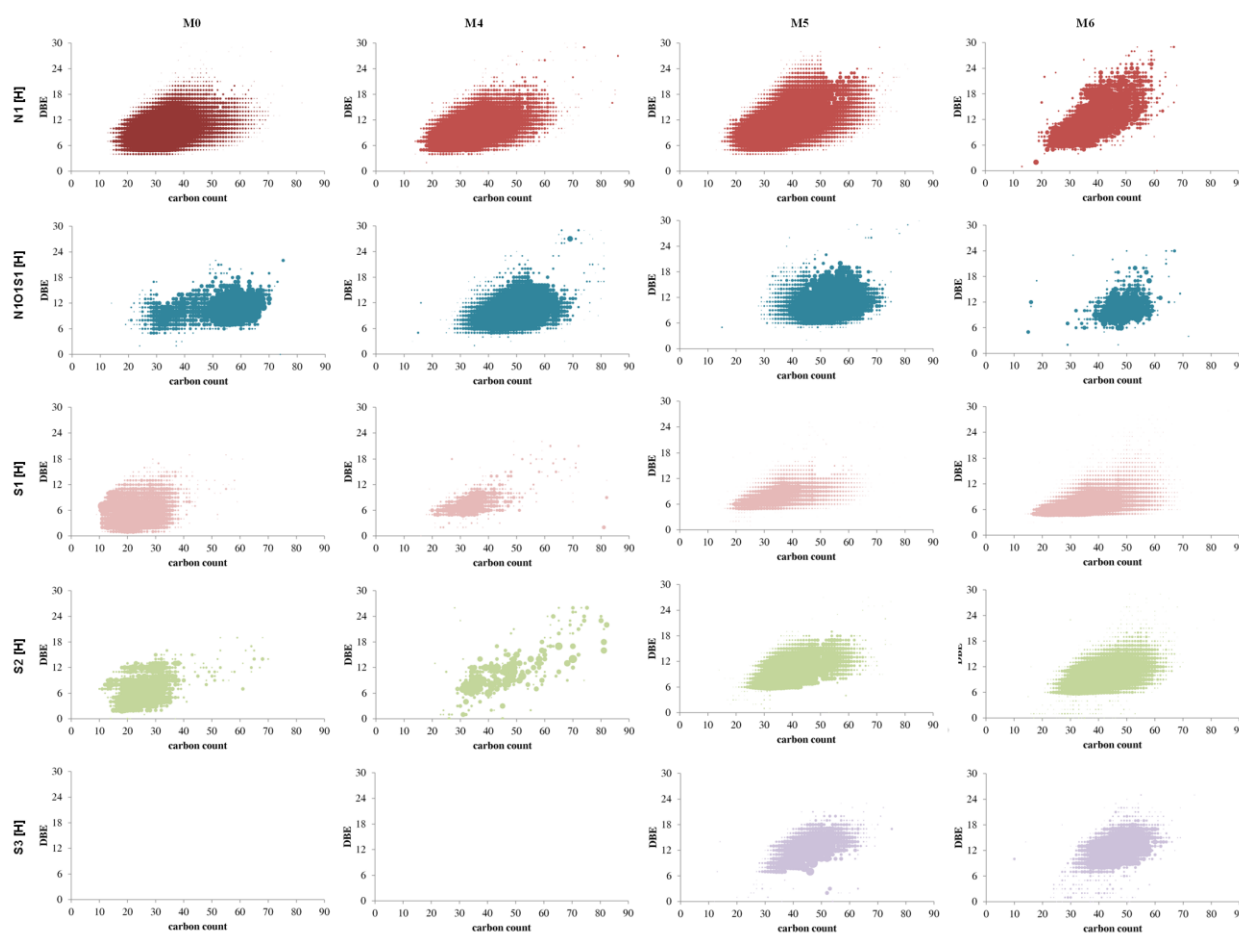


Figure 6.4: Comparison of Kendrick plots (DBE vs. Carbon number plots) for ions of the $N_1[H]$, $N_1O_1S_1[H]$, $S_1[H]$ and $S_2[H]$ classes for M4, M5 and M6 samples based on Table 6.1, obtained by (+) ESI FT-ICR MS. Herein, M0 is taken as a reference.

Mechanism behind selectivity towards nitrogen and sulfur containing species. As for M4-M6 cases without $AgBF_4$ involved, the proposing mechanism is considered from another point of view that is the inherent electrochemistry of ESI ion source. ESI ion source is acting as electrolytic cell[79], and oxidation occurred in positive ESI mode. Oxidation of benzyl

halide involves a removal of an electron from the halogen non-bonding orbital and produces a corresponding benzyl halide radical-cation[160]. Chloride is located in 3rd period, bromide 4th period and iodide 5th period in the period table, and the valence electrons of Cl, Br and I are respectively located in the 3rd, 4th and 5th energy level, so order of the energy required to remove an electron from halogen atom is $\text{Cl} > \text{Br} > \text{I}$, thus, the activity order of oxidation among the three benzyl halide is $\text{C}_7\text{H}_7\text{I} > \text{C}_7\text{H}_7\text{Br} > \text{C}_7\text{H}_7\text{Cl}$, and correspondingly, the produced benzyl iodide radical cation is the most electrophilic, and benzyl chloride radical cation is the least electrophilic, and benzyl bromide radical cation ranks in between. When the benzyl halide radical cation was produced, we have different kind of nucleophiles in crude oils, such as, nitrogen and sulfur-containing compounds. Benzyl iodide radical cation is the most reactive, and both nitrogen atoms and sulfur-atoms are expected to be able to react with it (reactions for nitrogen and sulfur atoms are both thermodynamic and kinetic favorable), but because of advantage of the sulfur content (5.6%) vs nitrogen content (0.14%), sulfur-containing products will dominates the product class distribution, that is, the sulfur-containing compounds will first selectively react with benzyl iodide radical cation, so the sulfur-containing species will be selectively accessed with the benzyl iodide involved case (M6) in Figure 6.3. While benzyl chloride radical cation is the least reactive, it is expected nucleophilic substitution between nitrogen-containing compounds and benzyl chloride radical cation are thermodynamically favorable than reaction of sulfur-containing species, because nitrogen is more basic and nucleophilic for benzyl chloride radical cation, and so nitrogen-containing species will be first selectively tagged as shown in M4 case in Figure 6.3. The electrophilicity of benzyl bromide radical cation lies in between benzyl iodide and benzyl chloride radical cation, so it results in a detection of mixture of both nitrogen and sulfur-containing compounds as shown in M5 case in Figure 6.3, or we can say that M5 exhibits a broader class

distribution including when comparing to M4 (benzyl chloride) and M6 (benzyl iodide).

6.5 Conclusion

The present results clearly demonstrate that the modification of crude oil by benzyl halide is effective and promising in selective analysis of crude oil by positive ion ESI FT-ICR MS. At the presence of AgBF_4 , three benzyl halides ($\text{C}_7\text{H}_7\text{Cl}$, $\text{C}_7\text{H}_7\text{Br}$ and $\text{C}_7\text{H}_7\text{I}$) all aids visualization of sulfur-containing species. At the absence of AgBF_4 , $\text{C}_7\text{H}_7\text{I}$ selectively leads sulfur-containing compounds detectable; $\text{C}_7\text{H}_7\text{Cl}$ exclusively facilitates accessing the nitrogen-containing species, while benzyl bromide plays a peacemaker in analysis of crude oil, in which case, both nitrogen and sulfur-containing compounds are present at a roughly equally relative abundance. All the results above are based on the ultrahigh mass resolution ESI FT-ICR MS, which allows identifying of unique elemental formulations and assigning of masses to distinct classes ($\text{N}_n\text{S}_s\text{O}_o$ composition), type (DBE), and carbon number distributions. This consolidated methodology and technology above achieve the detection of nonpolar sulfur-containing molecules at lower concentration besides the polar basic species, and meanwhile it avoids the prior chromatographic separation and fractionation. Organic chemistry together with analytical techniques might be a very promising approach to solve the complex mixture problems, such as crude oil.

On the other hand, crude oil, as an ultra-complex substrate system, has a wealth of functional and structural information; different polyaromatic heterocycles can be induced to react with benzyl halide under certain condition. However, the complexity of crude oil extremely challenges the organic chemistry. This present research is a bold attempt to carry out a bulk selective reaction by extending the traditional simple substrate system (usually 2 or 3 known reactants) to an extraordinarily chemically complex unknown substrate system (more than 50, 000)[161]. However, the crude oil analysis has long

inspired the development of analytical techniques; especially the complexity of crude oil has significantly promoted the prosperity of mass spectrometry, such as the ultrahigh resolution mass spectrometry [10]. Similarly, the problem offered by crude oil will drive the development of organic chemistry on some level and aspects.

Acknowledgements

The authors acknowledge the generous funding and gift of samples from Shell Global Solutions, Amsterdam and Houston, TX. The authors also thank Dr. David Stranz (Sierra Analytics, Modesto, CA) for assistance in MS-data evaluation.

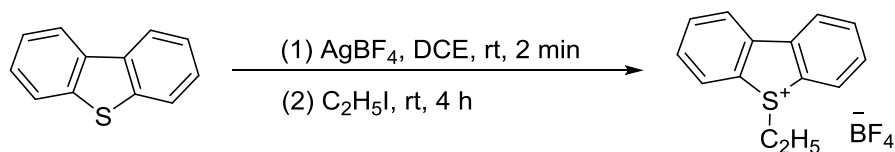
Chapter 7 Summary

Energy is becoming more and more indispensable in the development of human society to change or adapt to nature. It has been estimated that modern industrialized society has consumed approximately 10 times more energy than agricultural society. As energy resources, crude oil has been one of the most heavily used. However, as the decrease of the light crude oil resources, heavy and unconventional crude oil is becoming more important before sustainable energy sources can supply the demand at an affordable price. Nevertheless, unconventional crude oils contain higher amount of unwanted heteroatoms, which causes problems during petroleum upgrading processing, and pollute the environment during combustion by releasing SO_x and NO_x . Thus, understanding of the complete and detailed compositions and the underlying chemistry of petroleum are essential to improve upgrading process of petroleum and reduce the pollution and corrosion to environment.

Facing the challenge of complexity of crude oil, the ultrahigh resolution mass spectrometry, FT-ICR MS and the high-field Orbitrap FTMS has emerged as the most powerful tool to obtain the compositions of complex mixtures with high mass accuracy. However, due to the discrimination of ionization methods, suppression effects of samples, and the space charge effects in mass analyzer, it is not possible to fully characterize a crude oil sample only by one-shot. Therefore, unification of different techniques of analytical community and interdisciplinary studies is meaningful and essential, which provides the compositional and chemical information from different perspectives

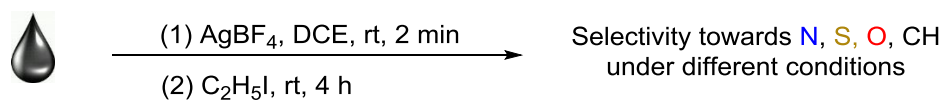
Derivatization coupled with ESI-MS opens a window to see the crude oil from chemical perspective based on the functionality.

In Chapter 2, a method has been established for the selective analysis towards sulfur-containing compound. Alkylation (methylation, ethylation) is first done for a sulfur-containing standard (dibenzothiophene, DBT) to obtain the optimum condition. And then this condition was applied into a simple simulation system consisting of standard aromatic CH-, N-, O- and S-containing compounds, and finally to a heavy crude oil. In both simulation system and a real crude oil, only sulfur-containing species were selectively alkylated. The deuterium labeled alkylating reagents (CD_3I and $\text{C}_2\text{D}_5\text{I}$) were employed to differentiate the tagged sulfur species from the original crude oil. As a result, the preformed sulfonium ions were produced and ready to analysis by ESI-MS. A high-field Orbitrap FTMS is employed for the crude oil analysis with a mass accuracy better than 1 ppm.



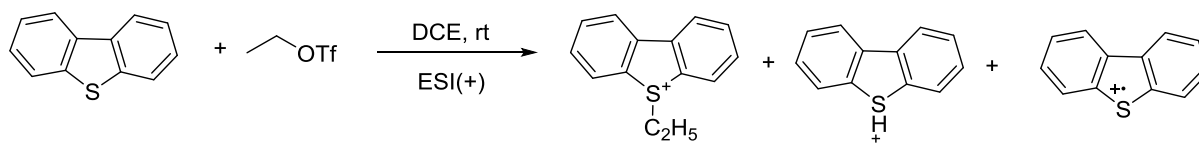
Scheme 7.1: Ethylation of dibenzothiophene (DBT).

Chapter 3 has addressed the role of chemical control on the selective analysis of a whole heavy crude oil. By use of different mole ratio of crude oil: silver tetrafluoroborate (AgBF_4): ethyl iodide ($\text{C}_2\text{H}_5\text{I}$), not only polar basic nitrogen-containing compound, but also but also less basic sulfur-containing species, neutral hydrocarbons and even acidic oxygen-containing species are sequentially selectively analyzed by positive ESI FT-ICR MS. Mechanism were different for different classes of compounds: Protonation basic nitrogen-containing compounds; S_2N for the selective analysis of sulfur-containing species; and electrophilic aromatic substitution (EAS) and then protonation (HBF_4) for O- and CH- containing species in crude oil.



Scheme 7.2: Ethylation of crude oil under different conditions.

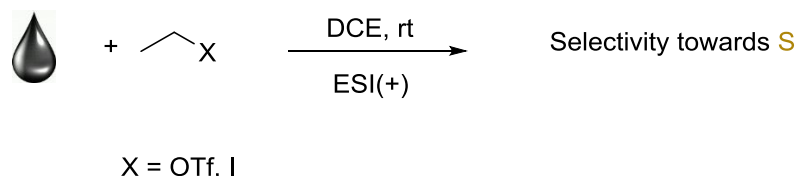
Chapter 4 has investigated the mechanism study of electrochemically induced electron transfer reaction of thiophene-type compounds with ethyl triflate by using the inherent electrochemistry of ESI. Electrospray capillary serves as a special electrolytic cell (a reactor), and the ethyl triflate is oxidized in metal solution interface to form active intermediates, and then the secondary reactions occurs in the gas phase to form the ultimate ions that are detected by MS. Theoretical calculation based on quantum mechanism (QM) is involved to facilitate the mechanism study.



Scheme 7.3: Reaction of dibenzothiophene (DBT) under positive ESI mode.

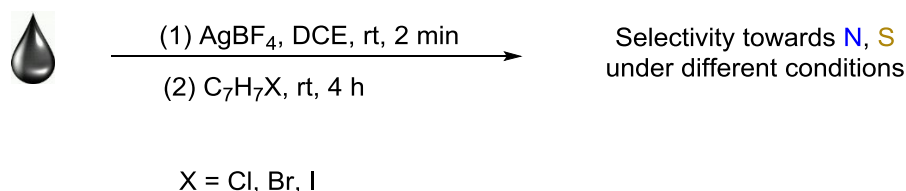
Chapter 5 has described a rapid derivatization method on millisecond time scale for the selective analysis of whole heavy crude oils. This is an application of method developed in Chapter 4 by taking the advantage of the electrolysis process of an ESI ion source. Both ethyl iodide and ethyl triflate ($\text{C}_2\text{H}_5\text{I}$ and $\text{C}_2\text{H}_5\text{OTf}$) are employed. The selective analysis towards sulfur-containing species is achieved by the inherent nucleophilic properties of heteroatom-containing species, the electrophilic property of active-alkylating species, the amount of alkylating reagents and the content of S- and N- containing compounds in crude oil. As a result, high selectivity towards S-containing species is achieved in the case with $\text{C}_2\text{H}_5\text{OTf}$ involved; not only sulfur- but also nitrogen-containing compounds are accessed in the case of $\text{C}_2\text{H}_5\text{I}$. Theoretical

calculation has been done to quantitatively explain the selectivity towards sulfur-containing species. This work uses the electrochemical electron transfer chemistry for crude oil analysis.



Scheme 7.4: Reaction of crude oil under positive ESI mode.

Chapter 6 has evaluated the reactivity of polycyclic aromatic hydrocarbons (PAHs) and polycyclic aromatic heterocycles (PAXHs) in heavy crude oils towards benzyl halides. A series of nitrogen-containing species have the reactivity towards benzyl chloride; a series of sulfur-containing species have the reactivity towards benzyl iodide; and both nitrogen- and sulfur-containing species are active under benzyl bromide condition. AgBF_4 as another parameter is added together with three benzyl halides to modify heavy crude oils to see how different poly aromatic species respond. As a result, a series of sulfur-containing species as well as hydrocarbons show the reactivity towards benzyl halide and benzyl bromide with the AgBF_4 present; both sulfur- and nitrogen-containing compounds are active under the system of benzyl iodide and AgBF_4 , but hydrocarbons decreases to a little.



Scheme 7.5: Benzylation of crude oil under different conditions.

In a word, advances in ultrahigh resolution MS instrumentation deepen our knowledge of petroleum compounds, but it is far not enough. This work reveals that selective analysis of crude oil complex mixtures can be achieved by adding a chemical dimension. Facing the complexity of crude oil, the combination of different analytical techniques, e.g. MS, ^1H NMR, liquid chromatography (LC), gas chromatography (GC), etc. with organic chemistry, theoretical chemistry, electrochemistry, etc. offers promising ways to gain better understanding of crude oil, and may ultimately unlock the black box of the crude oil from different perspectives and different levels in future.

In this thesis, the different chemical reactions have been investigated in details for selective analysis of a heavy crude oil.

References

1. Rodgers, R.P., et al., *Advanced characterization of petroleum crude and products by high field Fourier transform ion cyclotron resonance mass spectrometry*. Abstracts of Papers of the American Chemical Society, 2002. **224**: p. U570-U570.
2. Lababidi, S. and W. Schrader, *Online normal-phase high-performance liquid chromatography/Fourier transform ion cyclotron resonance mass spectrometry: Effects of different ionization methods on the characterization of highly complex crude oil mixtures*. Rapid Communications in Mass Spectrometry, 2014. **28**(12): p. 1345-1352.
3. *Petroleum*. February 2016.; Available from: <https://en.wikipedia.org/wiki/Petroleum>.
4. *The Black Gold Rush: Where's All the Oil?* ; Available from: <http://www.serifwebresources.com/control.php?uid=8fd43a09015bb97325ac3d4756b69885b3be09b2&post=898895>.
5. Speight, J.G., *Petroleum Chemistry And Refining*. Applied Energy Technology Series. September 1, 1997, Boca Raton, Florida: CRC Press.
6. al., A.e., "*Highlighting Heavy Oil*" (PDF). Oilfield Review., Summer 2006.
7. Lobodin, V.V., et al., *Tetramethylammonium Hydroxide as a Reagent for Complex Mixture Analysis by Negative Ion Electrospray Ionization Mass Spectrometry*. Analytical Chemistry, 2013. **85**(16): p. 7803-7808.
8. Panda, S.K., J.T. Andersson, and W. Schrader, *Characterization of Supercomplex Crude Oil Mixtures: What Is Really in There?* Angewandte Chemie-International Edition, 2009. **48**(10): p. 1788-1791.
9. Rudzinski, W.E., et al., *Isolation and characterization of the saturate and aromatic fractions of a Maya crude oil*. Energy & Fuels, 2000. **14**(4): p. 839-844.
10. Panda, S.K., J.T. Andersson, and W. Schrader, *Mass-spectrometric analysis of complex volatile and nonvolatile crude oil components: a challenge*. Analytical and Bioanalytical Chemistry, 2007. **389**(5): p. 1329-1339.
11. Silva, S.L., et al., *Chromatographic and spectroscopic analysis of heavy crude oil mixtures with emphasis in nuclear magnetic resonance spectroscopy: A review*. Analytica Chimica Acta, 2011. **707**(1): p. 18-37.
12. Ramaswamy, V., S.L.S. Sarowha, and I.D. Singh, *Structural Characterization of Bombay High Crude-Oil Fractions by Nuclear-Magnetic-Resonance Spectroscopy*. Fuel, 1986. **65**(9): p. 1281-1283.
13. Vukovic, J.P., et al., *NMR and Chemometric Characterization of Vacuum Residues and Vacuum Gas Oils from Crude Oils of Different Origin*. Croatica Chemica Acta, 2015. **88**(1): p. 89-U94.
14. Ali, F.A., N. Ghaloum, and A. Hauser, *Structure representation of asphaltene GPC fractions derived from Kuwaiti residual oils*. Energy & Fuels, 2006. **20**(1): p. 231-238.
15. Xian, F., C.L. Hendrickson, and A.G. Marshall, *High Resolution Mass Spectrometry*. Analytical Chemistry, 2012. **84**(2): p. 708-719.
16. Marshall, A.G., C.L. Hendrickson, and G.S. Jackson, *Fourier transform ion cyclotron resonance mass spectrometry: A primer*. Mass Spectrometry Reviews, 1998. **17**(1): p. 1-35.
17. Panda, S.K., W. Schrader, and J.T. Andersson, *Fourier transform ion cyclotron resonance mass spectrometry in the speciation of high molecular weight sulfur heterocycles in vacuum gas oils of different boiling ranges*. Analytical and Bioanalytical Chemistry, 2008. **392**(5): p. 839-848.
18. Marshall, A.G. and R.P. Rodgers, *Petroleomics: The next grand challenge for chemical analysis*. Accounts of Chemical Research, 2004. **37**(1): p. 53-59.
19. Laboratory, P.N.N. *FTICR Theory: A Brief Review*. July 2015; Available from: http://panomics.pnnl.gov/training/tutorials/ft_icr_tutorial.stm.
20. *Lorentz force*. 4 June 2016; Available from: https://en.wikipedia.org/wiki/Lorentz_force.
21. *Accelerators Create Matter from Energy*. Available from: <https://cnx.org/contents/Ax2o07UI@7.61:aypTUEkP@4/Accelerators-Create-Matter-fro>.

22. Barrow, M.P., W.I. Burkitt, and P.J. Derrick, *Principles of Fourier transform ion cyclotron resonance mass spectrometry and its application in structural biology*. *Analyst*, 2005. **130**(1): p. 18-28.
23. Marshall, A.G. and C.L. Hendrickson, *Fourier transform ion cyclotron resonance detection: principles and experimental configurations*. *International Journal of Mass Spectrometry*, 2002. **215**(1-3): p. 59-75.
24. Marshall, A.G. *Fourier Transform Ion Cyclotron Resonance (FT-ICR)*. 28 January 2015; Available from: <https://nationalmaglab.org/education/magnet-academy/watch-play/interactive/fourier-transform-ion-cyclotron-resonance-ft-icr>.
25. Comisarow, M.B. and A.G. Marshall, *Fourier-Transform Ion-Cyclotron Resonance Spectroscopy*. *Chemical Physics Letters*, 1974. **25**(2): p. 282-283.
26. Marshall, A.G. and M.B. Comisarow, *Fourier-Transform Methods in Spectroscopy*. *Journal of Chemical Education*, 1975. **52**(10): p. 638-641.
27. Scigelova, M., et al., *Fourier Transform Mass Spectrometry*. *Molecular & Cellular Proteomics*, 2011. **10**(7).
28. Balogh, M.P., *Debating resolution and mass accuracy in mass spectrometry*. *Spectroscopy*, 2004. **19**(10): p. 34-+.
29. Page, J.S., et al., *Automatic gain control in mass spectrometry using a jet disrupter electrode in an electrodynamic ion funnel*. *Journal of the American Society for Mass Spectrometry*, 2005. **16**(2): p. 244-253.
30. Hughey, C.A., et al., *Elemental composition analysis of processed and unprocessed diesel fuel by electrospray ionization fourier transform ion cyclotron resonance mass spectrometry*. *Energy & Fuels*, 2001. **15**(5): p. 1186-1193.
31. Qian, K., et al., *Reading chemical fine print: Resolution and identification of 3000 nitrogen-containing aromatic compounds from a single electrospray ionization Fourier transform ion cyclotron resonance mass spectrum of heavy petroleum crude oil*. *Energy & Fuels*, 2001. **15**(2): p. 492-498.
32. Rodgers, R.P., et al., *Environmental applications of ESI FT-ICR mass spectrometry: The identification of polar N, S and O containing PAH species in crude oil and coal extracts*. *Abstracts of Papers of the American Chemical Society*, 2003. **226**: p. U563-U564.
33. Marshall, A.G. and R.P. Rodgers, *Petroleomics: Chemistry of the underworld*. *Proceedings of the National Academy of Sciences of the United States of America*, 2008. **105**(47): p. 18090-18095.
34. Lobodin, V.V., et al., *Silver Cationization for Rapid Speciation of Sulfur-Containing Species in Crude Oils by Positive Electrospray Ionization Fourier Transform Ion Cyclotron Resonance Mass Spectrometry*. *Energy & Fuels*, 2014. **28**(1): p. 447-452.
35. Gaspar, A. and W. Schrader, *Expanding the data depth for the analysis of complex crude oil samples by Fourier transform ion cyclotron resonance mass spectrometry using the spectral stitching method*. *Rapid Communications in Mass Spectrometry*, 2012. **26**(9): p. 1047-1052.
36. Lababidi, S., et al., *Deep Well Deposits: Effects of Extraction on Mass Spectrometric Results*. *Energy & Fuels*, 2013. **27**(3): p. 1236-1245.
37. Lababidi, S., et al., *Direct Coupling of Normal-Phase High-Performance Liquid Chromatography to Atmospheric Pressure Laser Ionization Fourier Transform Ion Cyclotron Resonance Mass Spectrometry for the Characterization of Crude Oil*. *Analytical Chemistry*, 2013. **85**(20): p. 9478-9485.
38. Wang, X. and W. Schrader, *Selective Analysis of Sulfur-Containing Species in a Heavy Crude Oil by Deuterium Labeling Reactions and Ultrahigh Resolution Mass Spectrometry*. *Int J Mol Sci*, 2015. **16**(12): p. 30133-43.
39. Schrader, W. and H.W. Klein, *Liquid chromatography Fourier transform ion cyclotron resonance mass spectrometry (LC-FTICR MS): an early overview*. *Analytical and Bioanalytical Chemistry*, 2004. **379**(7-8): p. 1013-1024.
40. Muller, H., J.T. Andersson, and W. Schrader, *Characterization of high-molecular-weight sulfur-containing aromatics in vacuum residues using Fourier transform ion cyclotron resonance mass spectrometry*. *Analytical Chemistry*, 2005. **77**(8): p. 2536-2543.
41. Panda, S.K., et al., *Atmospheric pressure laser ionization (APLI) coupled with Fourier transform ion cyclotron resonance mass spectrometry applied to petroleum samples analysis*:

- comparison with electrospray ionization and atmospheric pressure photoionization methods.* Rapid Communications in Mass Spectrometry, 2011. **25**(16): p. 2317-2326.
42. Gaspar, A., et al., *Characterization of Saturates, Aromatics, Resins, and Asphaltenes Heavy Crude Oil Fractions by Atmospheric Pressure Laser Ionization Fourier Transform Ion Cyclotron Resonance Mass Spectrometry.* Energy & Fuels, 2012. **26**(6): p. 3481-3487.
 43. Guricza, L.M. and W. Schrader, *Electrospray ionization for determination of non-polar polyaromatic hydrocarbons and polyaromatic heterocycles in heavy crude oil asphaltenes.* Journal of Mass Spectrometry, 2015. **50**(3): p. 549-557.
 44. Kingdon, K.H., *A method for the neutralization of electron space charge by positive ionization at very low gas pressures.* Physical Review, 1923. **21**(4): p. 408-418.
 45. Hu, Q.Z., et al., *The Orbitrap: a new mass spectrometer.* Journal of Mass Spectrometry, 2005. **40**(4): p. 430-443.
 46. Knight, R.D., *Storage of Ions from Laser-Produced Plasmas.* Applied Physics Letters, 1981. **38**(4): p. 221-223.
 47. Oksman, P., *A Fourier-Transform Time-of-Flight Mass-Spectrometer - a Simion Calculation Approach.* International Journal of Mass Spectrometry and Ion Processes, 1995. **141**(1): p. 67-76.
 48. Makarov, A., *Electrostatic axially harmonic orbital trapping: A high-performance technique of mass analysis.* Analytical Chemistry, 2000. **72**(6): p. 1156-1162.
 49. Hardman, M. and A.A. Makarov, *Interfacing the orbitrap mass analyzer to an electrospray ion source.* Analytical Chemistry, 2003. **75**(7): p. 1699-1705.
 50. Makarov, A., et al., *Performance evaluation of a hybrid linear ion trap/orbitrap mass spectrometer.* Analytical Chemistry, 2006. **78**(7): p. 2113-2120.
 51. Makarov, A., et al., *Dynamic range of mass accuracy in LTQ Orbitrap hybrid mass spectrometer.* Journal of the American Society for Mass Spectrometry, 2006. **17**(7): p. 977-982.
 52. *Orbitrap.* 18 March 2016; Available from: <https://en.wikipedia.org/wiki/Orbitrap>.
 53. Denisov, E., et al., *Orbitrap mass spectrometry with resolving powers above 1,000,000.* International Journal of Mass Spectrometry, 2012. **325**: p. 80-85.
 54. Zhurov, K.O., A.N. Kozhinov, and Y.O. Tsybin, *Evaluation of High-Field Orbitrap Fourier Transform Mass Spectrometer for Petroleomics.* Energy & Fuels, 2013. **27**(6): p. 2974-2983.
 55. Kozhinov, A.N. and Y.O. Tsybin, *Filter Diagonalization Method-Based Mass Spectrometry for Molecular and Macromolecular Structure Analysis.* Analytical Chemistry, 2012. **84**(6): p. 2850-2856.
 56. Perry, R.H., R.G. Cooks, and R.J. Noll, *Orbitrap Mass Spectrometry: Instrumentation, Ion Motion and Applications.* Mass Spectrometry Reviews, 2008. **27**(6): p. 661-699.
 57. Schrader, W., Y. Xuan, and A. Gaspar, *Studying ultra-complex crude oil mixtures by using high-field asymmetric waveform ion mobility spectrometry (FAIMS) coupled to an electrospray ionisation-LTQ-Orbitrap mass spectrometer.* European Journal of Mass Spectrometry, 2014. **20**(1): p. 43-49.
 58. Constapel, M., et al., *Atmospheric-pressure laser ionization: a novel ionization method for liquid chromatography/mass spectrometry.* Rapid Communications in Mass Spectrometry, 2005. **19**(3): p. 326-336.
 59. Schiewek, R., et al., *Ultrasensitive determination of polycyclic aromatic compounds with atmospheric-pressure laser ionization as an interface for GC/MS.* Analytical Chemistry, 2007. **79**(11): p. 4135-4140.
 60. Fenn, J.B., et al., *Electrospray Ionization-Principles and Practice.* Mass Spectrometry Reviews, 1990. **9**(1): p. 37-70.
 61. Kebarle, P. and U.H. Verkerk, *Electrospray: From Ions in Solution to Ions in the Gas Phase, What We Know Now.* Mass Spectrometry Reviews, 2009. **28**(6): p. 898-917.
 62. Taflin, D.C., T.L. Ward, and E.J. Davis, *Electrified Droplet Fission and the Rayleigh Limit.* Langmuir, 1989. **5**(2): p. 376-384.
 63. Tang, L. and P. Kebarle, *Dependence of Ion Intensity in Electrospray Mass-Spectrometry on the Concentration of the Analytes in the Electrosprayed Solution.* Analytical Chemistry, 1993. **65**(24): p. 3654-3668.

64. Kebarle, P. and M. Peschke, *On the mechanisms by which the charged droplets produced by electrospray lead to gas phase ions*. *Analytica Chimica Acta*, 2000. **406**(1): p. 11-35.
65. Cech, N.B. and C.G. Enke, *Effect of affinity for droplet surfaces on the fraction of analyte molecules charged during electrospray droplet fission*. *Analytical Chemistry*, 2001. **73**(19): p. 4632-4639.
66. Enke, C.G., *A predictive model for matrix and analyte effects in electrospray ionization of singly-charged ionic analytes*. *Analytical Chemistry*, 1997. **69**(23): p. 4885-4893.
67. Asperger, A., et al., *On the signal response of various pesticides in electrospray and atmospheric pressure chemical ionization depending on the flow-rate of eluent applied in liquid chromatography-tandem mass spectrometry*. *Journal of Chromatography A*, 2001. **937**(1-2): p. 65-72.
68. Stephenson, J.L. and S.A. McLuckey, *Ion/ion proton transfer reactions for protein mixture analysis*. *Analytical Chemistry*, 1996. **68**(22): p. 4026-4032.
69. Thomson, B.A., Iribarne, J. V., *On the evaporation of small ions from charged droplets*. *J. Chem. Phys.*, 1976. **64**: p. 2287.
70. Thomson, B.A. and J.V. Iribarne, *Field-Induced Ion Evaporation from Liquid Surfaces at Atmospheric-Pressure*. *Journal of Chemical Physics*, 1979. **71**(11): p. 4451-4463.
71. Dole, M., L.L. Mack, and R.L. Hines, *Molecular Beams of Macroions*. *Journal of Chemical Physics*, 1968. **49**(5): p. 2240-&.
72. Wilm, M.S. and M. Mann, *Electrospray and Taylor-Cone Theory, Does Beam of Macromolecules at Last*. *International Journal of Mass Spectrometry*, 1994. **136**(2-3): p. 167-180.
73. Wilm, M., *Principles of Electrospray Ionization*. *Molecular & Cellular Proteomics*, 2011. **10**(7).
74. Fenn, J.B., et al., *Electrospray Ionization for Mass-Spectrometry of Large Biomolecules*. *Science*, 1989. **246**(4926): p. 64-71.
75. Vanberkel, G.J. and F.M. Zhou, *Electrospray as a Controlled Current Electrolytic Cell - Electrochemical Ionization of Neutral Analytes for Detection by Electrospray Mass-Spectrometry*. *Analytical Chemistry*, 1995. **67**(21): p. 3958-3964.
76. Blades, A.T., M.G. Ikonou, and P. Kebarle, *MECHANISM OF ELECTROSPRAY MASS-SPECTROMETRY - ELECTROSPRAY AS AN ELECTROLYSIS CELL*. *Analytical Chemistry*, 1991. **63**(19): p. 2109-2114.
77. Van Berkel, G.J., *Electrolytic corrosion of a stainless-steel electrospray emitter monitored using an electrospray-photodiode array system*. *Journal of Analytical Atomic Spectrometry*, 1998. **13**(7): p. 603-607.
78. Kertesz, V. and G.J. Van Berkel, *Control of analyte electrolysis in electrospray ionization mass spectrometry using repetitively pulsed high voltage*. *International Journal of Mass Spectrometry*, 2011. **303**(2-3): p. 206-211.
79. Van Berkel, G.J. and V. Kertesz, *Using the electrochemistry of the electrospray ion source*. *Anal Chem*, 2007. **79**(15): p. 5510-20.
80. Van Berkel, G.J., et al., *Computational simulation of redox reactions within a metal electrospray emitter*. *Analytical Chemistry*, 1999. **71**(23): p. 5288-5296.
81. Nielsen, S.B., M. Masella, and P. Kebarle, *Competitive gas-phase solvation of alkali metal ions by water and methanol*. *Journal of Physical Chemistry A*, 1999. **103**(48): p. 9891-9898.
82. Kendrick, E., *A Mass Scale Based on $Ch_2=14.0000$ for High Resolution Mass Spectrometry of Organic Compounds*. *Analytical Chemistry*, 1963. **35**(13): p. 2146-&.
83. Van Berkel, G.J., et al., *Derivatization for electrospray ionization mass spectrometry. 3. Electrochemically ionizable derivatives*. *Analytical Chemistry*, 1998. **70**(8): p. 1544-1554.
84. Van Berkel, G.J., J.M.E. Quirke, and C.L. Adams, *Derivatization for electrospray ionization-mass spectrometry. 4. Alkenes and alkynes*. *Rapid Communications in Mass Spectrometry*, 2000. **14**(10): p. 849-858.
85. Vanberkel, G.J., S.A. McLuckey, and G.L. Glish, *Electrochemical Origin of Radical Cations Observed in Electrospray Ionization Mass-Spectra*. *Analytical Chemistry*, 1992. **64**(14): p. 1586-1593.
86. Cho, Y., et al., *Developments in FT-ICR MS instrumentation, ionization techniques, and data interpretation methods for petroleomics* *Mass Spectrometry Reviews*, 2015. **34**(2): p. 248-263.

87. Panda, S.K., J.T. Andersson, and W. Schrader, *Mass-spectrometric analysis of complex volatile and nonvolatile crude oil components: a challenge*. *Anal Bioanal Chem*, 2007. **389**(5): p. 1329-39.
88. Makarov, A., E. Denisov, and O. Lange, *Performance Evaluation of a High-field Orbitrap Mass Analyzer*. *Journal of the American Society for Mass Spectrometry*, 2009. **20**(8): p. 1391-1396.
89. Vetere, A. and W. Schrader, *1-and 2-Photon Ionization for Online FAIMS-FTMS Coupling Allows New Insights into the Constitution of Crude Oils*. *Analytical Chemistry*, 2015. **87**(17): p. 8874-8879.
90. Qian, K.N., et al., *Resolution and identification of elemental compositions for more than 3000 crude acids in heavy petroleum by negative-ion microelectrospray high-field Fourier transform ion cyclotron resonance mass spectrometry*. *Energy & Fuels*, 2001. **15**(6): p. 1505-1511.
91. Purcell, J.M., et al., *Sulfur speciation in petroleum: Atmospheric pressure photoionization or chemical derivatization and electrospray ionization fourier transform ion cyclotron resonance mass spectrometry*. *Energy & Fuels*, 2007. **21**(5): p. 2869-2874.
92. Rudzinski, W.E., K. Zhou, and X.M. Luo, *Mass spectrometric characterization of organosulfur compounds using palladium(II) as a sensitivity-enhancing reagent*. *Energy & Fuels*, 2004. **18**(1): p. 16-21.
93. Roussis, S.G. and R. Proulx, *Molecular weight distributions of heavy aromatic petroleum fractions by Ag⁺ electrospray ionization mass spectrometry*. *Analytical Chemistry*, 2002. **74**(6): p. 1408-1414.
94. Panda, S.K., W. Schrader, and J.T. Andersson, *beta-cyclodextrin as a stationary phase for the group separation of polycyclic aromatic compounds in normal-phase liquid chromatography*. *Journal of Chromatography A*, 2006. **1122**(1-2): p. 88-96.
95. Fox, B.S., M.K. Beyer, and V.E. Bondybey, *Coordination chemistry of silver cations*. *Journal of the American Chemical Society*, 2002. **124**(45): p. 13613-13623.
96. Abul Haj, M., C.B. Aakeroy, and J. Desper, *Silver(I) coordination chemistry: from 1-D chains to molecular rectangles*. *New Journal of Chemistry*, 2013. **37**(1): p. 204-211.
97. Schrader, W., et al., *Characterization of non-polar aromatic hydrocarbons in crude oil using atmospheric pressure laser ionization and Fourier transform ion cyclotron resonance mass spectrometry (APLI FT-ICR MS)*. *Analyst*, 2008. **133**(7): p. 867-869.
98. Kharrat, A.M., et al., *Issues with comparing SARA methodologies*. *Energy & Fuels*, 2007. **21**(6): p. 3618-3621.
99. Swiegers, G.F. and T.J. Malefetse, *New self-assembled structural motifs in coordination chemistry*. *Chemical Reviews*, 2000. **100**(9): p. 3483-3537.
100. Hutchinson, D.J., et al., *Sensitivity of Silver(I) Complexes of a Pyrimidine-Hydrazone Ligand to Solvent, Counteranion, and Metal-to-Ligand Ratio Changes*. *Inorganic Chemistry*, 2012. **51**(9): p. 5070-5081.
101. Acheson, R.M. and D.R. Harrison, *Synthesis, Spectra, and Reactions of Some S-Alkylthiophenium Salts*. *Journal of the Chemical Society C-Organic*, 1970(13): p. 1764-&.
102. Ansell, G.B., *Crystal-Structure of a 1/1 Complex between Silver-Iodide and Morpholine*. *Journal of the Chemical Society-Perkin Transactions 2*, 1976(1): p. 104-106.
103. Wu, C.P., et al., *Ambient Analysis of Saturated Hydrocarbons Using Discharge-Induced Oxidation in Desorption Electrospray Ionization*. *Journal of the American Society for Mass Spectrometry*, 2010. **21**(2): p. 261-267.
104. Cho, Y., Y.H. Kim, and S. Kim, *Planar Limit-Assisted Structural Interpretation of Saturates/Aromatics/Resins/Asphaltenes Fractionated Crude Oil Compounds Observed by Fourier Transform Ion Cyclotron Resonance Mass Spectrometry*. *Analytical Chemistry*, 2011. **83**(15): p. 6068-6073.
105. Shea, R.C., et al., *Characterization of laser-induced acoustic desorption coupled with a Fourier transform ion cyclotron resonance mass spectrometer*. *Analytical Chemistry*, 2006. **78**(17): p. 6133-6139.
106. Palacio Lozano, D.C., et al., *Analysis of the molecular weight distribution of vacuum residues and their molecular distillation fractions by laser desorption ionization mass spectrometry*. *Fuel*, 2016. **171**: p. 247-252.

107. Headley, J.V., K.M. Peru, and M.P. Barrow, *Advances in mass spectrometric characterization of naphthenic acids fraction compounds in oil sands environmental samples and crude oil-A review*. Mass Spectrometry Reviews, 2016. **35**(2): p. 311-328.
108. Gaspar, A., et al., *Impact of Different Ionization Methods on the Molecular Assignments of Asphaltenes by FT-ICR Mass Spectrometry*. Analytical Chemistry, 2012. **84**(12): p. 5257-5267.
109. Pinkston, D.S., et al., *Analysis of Asphaltenes and Asphaltene Model Compounds by Laser-Induced Acoustic Desorption/Fourier Transform Ion Cyclotron Resonance Mass Spectrometry*. Energy & Fuels, 2009. **23**: p. 5564-5570.
110. Barrow, M.P., et al., *Athabasca Oil Sands Process Water: Characterization by Atmospheric Pressure Photoionization and Electrospray Ionization Fourier Transform Ion Cyclotron Resonance Mass Spectrometry*. Analytical Chemistry, 2010. **82**(9): p. 3727-3735.
111. Schmitt-Kopplin, P., et al., *Combining chip-ESI with APLI (cESILI) as a multimode source for analysis of complex mixtures with ultrahigh-resolution mass spectrometry*. Analytical and Bioanalytical Chemistry, 2008. **391**(8): p. 2803-2809.
112. Cho, Y., et al., *Application of Saturates, Aromatics, Resins, and Asphaltenes Crude Oil Fractionation for Detailed Chemical Characterization of Heavy Crude Oils by Fourier Transform Ion Cyclotron Resonance Mass Spectrometry Equipped with Atmospheric Pressure Photoionization*. Energy & Fuels, 2012. **26**(5): p. 2558-2565.
113. Hsu, C.S., K.N. Qian, and W.K. Robbins, *Nitrogen speciation of polar petroleum compounds by compound class separation and online liquid chromatography - mass - spectrometry (LC-MS)*. Hrc-Journal of High Resolution Chromatography, 1994. **17**(4): p. 271-276.
114. Guricza, L.M. and W. Schrader, *New Separation Approach for Asphaltene Investigation: Argentation Chromatography Coupled with Ultrahigh-Resolution Mass Spectrometry*. Energy & Fuels, 2015. **29**(10): p. 6224-6230.
115. Hughey, C.A., R.P. Rodgers, and A.G. Marshall, *Resolution of 11 000 compositionally distinct components in a single Electrospray ionization Fourier transform ion cyclotron resonance mass spectrum of crude oil*. Analytical Chemistry, 2002. **74**(16): p. 4145-4149.
116. Tomczyk, N.A., et al., *On the nature and origin of acidic species in petroleum. 1. Detailed acid type distribution in a California crude oil*. Energy & Fuels, 2001. **15**(6): p. 1498-1504.
117. Perst, H., *In Carbonium Ions*; 1976: Olah, G. A.; Schleyer, P. v. R., Eds.; Wiley: New York.
118. Cech, N.B. and C.G. Enke, *Practical implications of some recent studies in electrospray ionization fundamentals*. Mass Spectrometry Reviews, 2001. **20**(6): p. 362-387.
119. Schrader, W., S. Doring, and W. Joppek, *Mass spectrometric studies of DNA adducts from a reaction with terpenoids*. Angewandte Chemie-International Edition, 2004. **43**(48): p. 6657-6660.
120. Griep-Raming, J., et al., *Investigation of reactive intermediates of chemical reactions in solution by electrospray ionization mass spectrometry: radical chain reactions*. Angewandte Chemie-International Edition, 2002. **41**(15): p. 2738-+.
121. Chen, P., *Electrospray ionization tandem mass spectrometry in high-throughput screening of homogeneous catalysts*. Angewandte Chemie-International Edition, 2003. **42**(25): p. 2832-2847.
122. Meyer, S., R. Koch, and J.O. Metzger, *Investigation of reactive intermediates of chemical reactions in solution by electrospray ionization mass spectrometry: Radical cation chain reactions*. Angewandte Chemie-International Edition, 2003. **42**(38): p. 4700-4703.
123. Meyer, S. and J.O. Metzger, *Use of electrospray ionization mass spectrometry for the investigation of radical cation chain reactions in solution: detection of transient radical cations*. Analytical and Bioanalytical Chemistry, 2003. **377**(7-8): p. 1108-1114.
124. Santos, L.S., et al., *Probing the mechanism of the Baylis-Hillman reaction by electrospray ionization mass and tandem mass spectrometry*. Angewandte Chemie-International Edition, 2004. **43**(33): p. 4330-4333.
125. Furmeier, S., et al., *Chelation-controlled radical chain reactions studied by electrospray ionization mass spectrometry*. Chemistry-a European Journal, 2005. **11**(19): p. 5545-5554.
126. Santos, L.S., *Online mechanistic investigations of catalyzed reactions by electrospray ionization mass spectrometry: A tool to intercept transient species in solution*. European Journal of Organic Chemistry, 2008(2): p. 235-253.

127. Schrader, W., et al., *Characterization of Key Intermediates in a Complex Organocatalytic Cascade Reaction Using Mass Spectrometry*. *Angewandte Chemie-International Edition*, 2009. **48**(8): p. 1463-1466.
128. Alachraf, M.W., et al., *Electrospray mass spectrometry for detailed mechanistic studies of a complex organocatalyzed triple cascade reaction*. *Organic & Biomolecular Chemistry*, 2011. **9**(4): p. 1047-1053.
129. Wang, H.Y., et al., *ESI-MS Studies and Calculations on Second-Generation Grubbs and Hoveyda-Grubbs Ruthenium Olefin Metathesis Catalysts*. *Organometallics*, 2012. **31**(5): p. 1627-1634.
130. Gabelica, V., E. De Pauw, and M. Karas, *Influence of the capillary temperature and the source pressure on the internal energy distribution of electrosprayed ions*. *International Journal of Mass Spectrometry*, 2004. **231**(2-3): p. 189-195.
131. Adamo, C. and V. Barone, *Toward reliable density functional methods without adjustable parameters: The PBE0 model*. *Journal of Chemical Physics*, 1999. **110**(13): p. 6158-6170.
132. Grimme, S., et al., *A consistent and accurate ab initio parametrization of density functional dispersion correction (DFT-D) for the 94 elements H-Pu*. *Journal of Chemical Physics*, 2010. **132**(15).
133. Huenerbein, R., et al., *Effects of London dispersion on the isomerization reactions of large organic molecules: a density functional benchmark study*. *Physical Chemistry Chemical Physics*, 2010. **12**(26): p. 6940-6948.
134. Scalmani, G. and M.J. Frisch, *Continuous surface charge polarizable continuum models of solvation. I. General formalism*. *Journal of Chemical Physics*, 2010. **132**(11).
135. Frisch, M.J.T., G. W.; Schlegel, H. B.; Scuseria, G. E.; Robb, M. A.; Cheeseman, J. R.; Scalmani, G.; Barone, V.; Mennucci, B.; Petersson, G. A.; Nakatsuji, H.; Caricato, M.; Li, X.; Hratchian, H. P.; Izmaylov, A. F.; Bloino, J.; Zheng, G.; Sonnenberg, J. L.; Hada, M.; Ehara, M.; Toyota, K.; Fukuda, R.; Hasegawa, J.; Ishida, M.; Nakajima, T.; Honda, Y.; Kitao, O.; Nakai, H.; Vreven, T.; Montgomery, J. A., Jr.; Peralta, J. E.; Ogliaro, F.; Bearpark, M.; Heyd, J. J.; Brothers, E.; Kudin, K. N.; Staroverov, V. N.; Kobayashi, R.; Normand, J.; Raghavachari, K.; Rendell, A.; Burant, J. C.; Iyengar, S. S.; Tomasi, J.; Cossi, M.; Rega, N.; Millam, J. M.; Klene, M.; Knox, J. E.; Cross, J. B.; Bakken, V.; Adamo, C.; Jaramillo, J.; Gomperts, R.; Stratmann, R. E.; Yazyev, O.; Austin, A. J.; Cammi, R.; Pomelli, C.; Ochterski, J. W.; Martin, R. L.; Morokuma, K.; Zakrzewski, V. G.; Voth, G. A.; Salvador, P.; Dannenberg, J. J.; Dapprich, S.; Daniels, A. D.; Farkas, Ö.; Foresman, J. B.; Ortiz, J. V.; Cioslowski, J.; Fox, D. J. , *Gaussian~09 {R}evision {E}.01*. 2009, Gaussian Inc. Wallingford CT 2009.
136. Kowalski, M.H., et al., *Electrochemical and Photoelectronic Spectral Study of Compounds with High Ionization-Potentials - Anodic-Oxidation of Vinyl Triflates in Aprotic-Solvents*. *Journal of Physical Organic Chemistry*, 1990. **3**(10): p. 670-676.
137. Xantheas, S.S. and T.H. Dunning, *Ab-Initio Studies of Cyclic Water Clusters (H₂O)_N, N = 1-6 .I. Optimal Structures and Vibrational-Spectra*. *Journal of Chemical Physics*, 1993. **99**(11): p. 8774-8792.
138. Liu, K., J.D. Cruzan, and R.J. Saykally, *Water clusters*. *Science*, 1996. **271**(5251): p. 929-933.
139. Sun, L.L., et al., *CuI/TMEDA-Catalyzed Annulation of 2-Bromo Alkynylbenzenes with Na₂S: Synthesis of Benzo[b]thiophenes*. *Journal of Organic Chemistry*, 2011. **76**(18): p. 7546-7550.
140. Sanz, R., et al., *A route to regioselectively functionalized carbazoles, dibenzofurans, and dibenzothiophenes through anionic cyclization of benzyne-tethered aryllithiums*. *Journal of Organic Chemistry*, 2006. **71**(16): p. 6291-6294.
141. Sigma-Aldrich, *Spectral data were obtained from Advanced Chemistry Development, Inc.* 2016.
142. Xu, X.Y., et al., *Synthesis of 4,6-Dimethyldibenzothiophene and 1,2,3,4-Tetrahydro-4,6-dimethyldibenzothiophene via Tilak Annulation*. *Helvetica Chimica Acta*, 2011. **94**(10): p. 1754-1763.
143. Panda, S.K., et al., *Distribution of polycyclic aromatic sulfur heterocycles in three Saudi Arabian crude oils as determined by Fourier transform ion cyclotron resonance mass spectrometry*. *Energy & Fuels*, 2007. **21**(2): p. 1071-1077.

144. Muller, H., et al., *Evaluation of Quantitative Sulfur Speciation in Gas Oils by Fourier Transform Ion Cyclotron Resonance Mass Spectrometry: Validation by Comprehensive Two-Dimensional Gas Chromatography*. Journal of the American Society for Mass Spectrometry, 2012. **23**(5): p. 806-815.
145. Wang, X.S., W., *Adding a Chemical Dimension as Tool for Selective Analysis of a Heavy Crude Oil by Fourier Transform Ion Cyclotron Resonance Mass Spectrometry (FT-ICR MS)*. Will be submitted to Anal. Chem.
146. Wang, X., et al., *Electrochemically-induced Electron Transfer Reaction of Thiophene-Type Compounds with Ethyl Triflate in Electrospray Mass Spectrometry*. Will be submitted to Angew Chem Int Edit.
147. Roussis, S.G. and R. Prouix, *Probing the molecular weight distributions of non-boiling petroleum fractions by Ag⁺ electrospray ionization mass spectrometry*. Rapid Communications in Mass Spectrometry, 2004. **18**(15): p. 1761-1775.
148. Strausz, O.P., T.W. Mojelsky, and E.M. Lown, *The Chemistry of Alberta Oil Sand Bitumen*. International Symposium on Heavy Oil and Residue Upgrading and Utilization : Proceedings, 1992: p. 29-35.
149. Sharples, R.B. Bradley, and J.A. Ferretti, *Nuclear Magnetic-Resonance of Heterocyclic-Compounds Related to Anthracene*. Organic Magnetic Resonance, 1974. **6**(2): p. 115-120.
150. Hook, M., R. Hirsch, and K. Aleklett, *Giant oil field decline rates and their influence on world oil production*. Energy Policy, 2009. **37**(6): p. 2262-2272.
151. Klein, G.C., et al., *Mass spectral analysis of asphaltenes. I. Compositional differences between pressure-drop and solvent-drop asphaltenes determined by electrospray ionization Fourier transform ion cyclotron resonance mass spectrometry*. Energy & Fuels, 2006. **20**(5): p. 1965-1972.
152. Klein, G.C., et al., *Mass spectral analysis of asphaltenes. II. Detailed compositional comparison of asphaltenes deposit to its crude oil counterpart for two geographically different crude oils by ESI FT-ICR MS*. Energy & Fuels, 2006. **20**(5): p. 1973-1979.
153. Hsu, C.S., et al., *Petroleomics: advanced molecular probe for petroleum heavy ends*. Journal of Mass Spectrometry, 2011. **46**(4): p. 337-343.
154. Savory, J.J., et al., *Parts-Per-Billion Fourier Transform Ion Cyclotron Resonance Mass Measurement Accuracy with a "Walking" Calibration Equation*. Analytical Chemistry, 2011. **83**(5): p. 1732-1736.
155. Fu, J.M., et al., *Comprehensive compositional analysis of hydrotreated and untreated nitrogen-concentrated fractions from syncrude oil by electron ionization, field desorption ionization, and electrospray ionization ultrahigh-resolution FT-ICR mass spectrometry*. Energy & Fuels, 2006. **20**(3): p. 1235-1241.
156. Cho, Y.J., et al., *Application of Saturates, Aromatics, Resins, and Asphaltenes Crude Oil Fractionation for Detailed Chemical Characterization of Heavy Crude Oils by Fourier Transform Ion Cyclotron Resonance Mass Spectrometry Equipped with Atmospheric Pressure Photoionization*. Energy & Fuels, 2012. **26**(5): p. 2558-2565.
157. Hoang, C.T., et al., *Amino Acid Homologation by the Blaise Reaction: A New Entry into Nitrogen Heterocycles*. Journal of Organic Chemistry, 2009. **74**(11): p. 4177-4187.
158. Pearson, R.G., *Hard and Soft Acids and Bases*. Journal of the American Chemical Society, 1963. **85**(22): p. 3533-&.
159. Mayr, H. and A.R. Ofial, *The reactivity-selectivity principle: an imperishable myth in organic chemistry*. Angewandte Chemie-International Edition, 2006. **45**(12): p. 1844-1854.
160. Mohan, H. and K.D. Asmus, *Radical Cations from Alkyl Iodides in Aqueous-Solution*. Journal of the Chemical Society-Perkin Transactions 2, 1987(12): p. 1795-1800.
161. Rodgers, R.P., T.M. Schaub, and A.G. Marshall, *Petroleomics: MS returns to its roots*. Analytical Chemistry, 2005. **77**(1): p. 20a-27a.

Appendix

List of Figures

Figure 1.1: Heavy crude oil liquid.	12
Figure 1.2: Distribution of world oil reserves.	13
Figure 1.3: Schematic illustration of SARA analysis.	14
Figure 1.4: Trajectory of a particle with a positive ($q>0$) or negative ($q<0$) charge under the influence of a spatially uniform magnetic field \mathbf{B} , which is pointing perpendicularly out of the screen. Charged particles experience the Lorentz force ($\mathbf{F} = q \mathbf{v} \times \mathbf{B}$).	17
Figure 1.5: Sketch of ion cyclotron motion in a spatially uniform magnetic field \mathbf{B} with direction perpendicularly pointing inwards the screen. A positive ion has a spiral-shape ion cyclotron motion.	18
Figure 1.6: Cyclotron.	19
Figure 1.7: Schematic representation of a cylindrical FT-ICR analyzer cell. The magnetic field axis is coaxial with the trapping axis (z-axis), and the trapping electrodes not shown are located at each end of the cell. A charged particle is orbiting in the ICR cell.	20
Figure 1.8: An overview of FT-ICR MS raw data processing.	22
Figure 1.9: Influence of magnetic field strength on resolution. A comparison of the non-apodized resolution (full width at half maximum, FWHM) achievable for a range of masses for 1 s transient employing magnetic field strengths of 1 to 40 T is presented. Both axes are logarithmic.	23
Figure 1.10: Influence of transient duration on resolution. A comparison of the non-apodized resolution (full width at half maximum, FWHM) achievable for a range of masses with magnetic field strengths of 7 and 21 T and for durations of transients of 1 and 5 s is represented. Both axes are logarithmic.	25
Figure 1.11: Sketch of the cylindrical Kingdon trap. A direct current (DC) voltage is applied between a rectilinear wire and a surrounding cylinder. As a result, a charged particle represented in red is dynamically trapped in the free space between the inner and outer electrodes.	27
Figure 1.12: Sketch of the Knight-style Kingdon trap. The modified geometry of the outer electrode creates a quadrupolar potential superimposed upon the radial logarithmic potential of the trap. Ions are produced by pulsed laser ablation of solid targets.	30
Figure 1.13: Sketch of the Orbitrap mass analyzer from side view. Ions are injected into the Orbitrap at the point displaced from its equator with a velocity (red arrow) perpendicular to the z-axis, and then they begin coherent axial oscillations without any further excitation.	31
Figure 1.14: Cross-section of the C-trap and Orbitrap analyzer (ion optics and differential pumping not shown) is represented. Ion packet enters the analyzer during the voltage ramp and forms rings that induce current detected by the amplifier.	34
Figure 1.15: Cut-outs of a standard (top) and a high-field (bottom) Orbitrap analyzer.	38
Figure 1.16: Experimental values of resolving power at 400 m/z for a deuterated heavy crude oil sample. Resolving power obtained using 1.5 s detection time and external mass calibration under full scan mode.	38
Figure 1.17: Experimental mass accuracy vs m/z with external mass calibration under full scan mode for a deuterated heavy crude oil sample.	40
Figure 1.18: API ionization methods and applicable compounds.	41

- Figure 1.19:** Schematic diagram of major processes in the atmospheric pressure region of an ESI ion source in the positive ion mode. The penetration of the imposed electric field into the liquid leads to an enrichment near the meniscus of positive ions in solution, which causes a destabilization of the meniscus and formation of a cone and a jet charged by an excess of positive ions. Solvent evaporation of the droplets brings the charges closer together. The increasing Coulombic repulsion destabilizes the droplets, which results in emitting jets of charged offspring droplets. The evaporation of offspring droplets leads to emission of the second generation of offspring droplets, and so forth, until the free gas-phase ions form at some point. Charge balance is achieved in the ESI device by electrochemical oxidation at the positive electrode and reduction at the negative electrode. TDC represents the total droplets current..... 43
- Figure 1.20:** The ion evaporation model (IEM). An individual ion leaves the charged droplet in a solvated state, because the reaction free enthalpy that needs to be overcome when the ion escapes from the droplet, ΔG , is lowest not for the naked ion, but for the solvated ions. 45
- Figure 1.21:** The charged residue model (CRM). It assumes that the ESI droplets are generated by containing one ion that is released after solvent evaporation. A calculation shows that for a concentration of 1 pmol/ μ l, a droplet with a diameter of 200 nm contains on average less than one analyte molecule..... 46
- Figure 1.22:** Compositional sorting process based on their elemental compositions. Above the mass spectra (bottom) is heteroatom class distribution, and above the class plots is the DBE distribution for N_1 class. Carbon number (a degree of alkylation) is placed on the top for N_1 species with DBE = 8. . 53
- Figure 1.23:** DBE vs. carbon number plots for the N_1 [H] class from a protonated heavy crude oil, obtained by (+) ESI high-field Orbitrap FTMS..... 54
- Figure 2.1:** ^1H NMR spectra (top) and HRMS (ESI FT-ICR MS) spectra (bottom) of 5-ethylidibenzo[*b,d*]thiophenium tetrafluoroborate..... 65
- Figure 2.2:** ESI FT-ICR MS spectrum of a mixture of the ethylated standards (ANTH, DBT, ACR and DBF)..... 68
- Figure 2.3:** ESI(+) Orbitrap FTMS mass spectrum of heavy crude oil (left) and deuterium labelling methylated heavy crude oil (right). 69
- Figure 2.4:** Class distribution for heavy crude oil from direct analysis (left) and after deuterium labelling methylated heavy crude oil (right). 70
- Figure 2.5:** DBE versus carbon number plots for the N_1 [H] and N_1S_1 [H] classes from the protonated heavy crude oil (left) and for the D_3S_1 [H] and D_3S_2 [H] classes from the deuterated methylated heavy crude oil (right). Note that the [H] indicates a protonated molecule. 71
- Figure 2.6:** Heteroatom class distribution for deuterium labelling ethylated heavy crude oil. 72
- Figure 2.7:** DBE versus carbon number plots for the D_5S_1 and D_5S_2 classes from the deuterated ethylated heavy crude oil..... 73
- Figure 3.1:** 7 T FT-ICR mass spectra obtained from eight samples based on Table 3.1 in (+) ESI ionization mode for the mass range 150-1200 Da (left column) and the corresponding enlarged section of the first four samples in a range between m/z 445.0-446.5 (right column) with the assigned molecular formulas..... 82
- Figure 3.2:** Comparison of heteroatom class distributions obtained from the above eight samples based on Table 3.1. Note that relative and not absolute abundances are shown; the summary of all abundances from one method is 100%..... 83
- Figure 3.3:** Comparison of Kendrick plots of the N_1 , S_1 , O_1 and CH classes obtained from B1 (top), B2 (middle) and B4 (bottom) samples using ESI(+) 7 T FT-ICR MS..... 85
- Figure 3.4:** Plots of DBE vs. carbon number distribution for O_2 , O_3 and O_4 from B4 sample..... 86

- Figure A3.1:** Comparison of color change of untreated reaction solutions from B2, B4, B5 and B6 samples. Original crude oil solution in anhydrous DCE is yellow brown, but after reaction the color is changed because the molecular structures are changed..... 93
- Figure A3.2:** Comparison of Kendrick plots of the N1S1, S2, O2 and O3 classes obtained from B1 (top), B2 (middle) and B4 (bottom) samples using ESI (+)FT-ICR MS..... 94
- Figure A3.3:** Comparison of ^1H NMR spectra from methylation and ethylation of dibenzothiophene (DBT) under the same reaction condition (the mole ratio of DBT: AgBF_4 : $\text{C}_2\text{H}_5\text{I}$ (or CH_3I) as 1: 2: 2). 95
- Figure A3.4:** A comparison of ^1H NMR spectra of Acridine under different reaction conditions. The significant complex effect between Ag^+ and basic nitrogen can be illustrated by the ^1H NMR spectra of Acridine under different reaction conditions. In the presence of Ag^+ , larger insoluble complex in DCE are generated and exit from the reaction solution. 96
- Figure A3.5:** ^1H NMR data of 5-ethyldibenzo[*b,d*]thiophenium tetrafluoroborate. **5-ethyldibenzo[*b,d*]thiophenium tetrafluoroborate (colourless needles, 99%).** ^1H NMR (300 MHz, CDCl_3): δ 8.39 (ddd, $J = 8.0, 1.1, 0.6$ Hz, 2H, $2 \times Ph$), 8.10 (ddd, $J = 7.8, 1.3, 0.6$ Hz, 2H, $2 \times Ph$), 7.85 (td, $J = 7.7, 1.1$ Hz, 2H, $2 \times Ph$), 7.79 – 7.68 (m, 2H, $2 \times Ph$), 4.19 (q, $J = 7.1$ Hz, 2H, $2 \times \text{CH}_2\text{CH}_3$), 0.88 (t, $J = 7.1$ Hz, 3H, $3 \times \text{CH}_2\text{CH}_3$). 96
- Figure A3.6:** HRMS (ESI FT-ICR MS) data of 5-ethyldibenzo[*b,d*]thiophenium tetrafluoroborate. Found: m/z 213.07322. Calcd for $\text{C}_{14}\text{H}_{13}\text{S}^+$: m/z 213.07325. 97
- Figure A3.7:** The pH test of B4 sample. B4 is diluted by 2 mL of anhydrous 1,2-DCE after reaction before pH test. HBF_4 ($\text{HF} + \text{BF}_3$) system is actually a superacid system, which was observed in the pH test. Also a white fume in moist air was observed when opening the reaction bottle cap. 97
- Figure 4.1:** Electrospray(+) mass spectrum of the reaction mixture of DBT and $\text{C}_2\text{H}_5\text{OTf}$ in anhydrous 1,2-DCE on 7 T FT-ICR MS using standard ESI spray capillary set-up as shown in Figure 4.3b. M represents DBT..... 102
- Figure 4.2:** Sketch of electrospray ionization system at the positive ion mode. ESI metal capillary is connected to a High Voltage (HV) supply. The electrons are produced via the oxidation inside the ESI metal capillary. A circuit that consists of the ESI spray capillary, the HV supply and the counter electrode is established when electrons move to the counter electrode through the metal wire continuously. TC represents the total current in the circuit..... 103
- Figure 4.3:** (a) Fused silica electrospray capillary setup. In a 1-D space, the origin is defined at the edge of the outer capillary with the positive direction pointing to the right. The fused silica capillary position relative to the outer capillary can be understood as a location in the 1-D space. Green arrow represents that the solution flow is injected through the inner fused silica capillary. Yellow arrow represents that the solution flow is injected through the outer metallic capillary. The inner solution flow is isolated by the fused silica capillary from the outer solution flow. (b) Standard electrospray capillary setup. The solution is usually injected only through the inner metallic capillary. 104
- Figure 4.4:** Evaluation of the influence of electrochemistry on the intensity of characteristic peaks of $[\text{M}+\text{C}_2\text{H}_5]^+$, $[\text{M}+\text{H}]^+$ and $[\text{M}]^{++}$ through silica position in 1-D space. 106
- Figure 4.5:** Proposed mechanism. 108
- Figure 4.6:** Comparison of mass spectra obtained from the ESI-MS experiments with different sweep gas flow rates. Sg represents sweep gas. As the sweep gas flow rate increases, the relative abundance of $[\text{M}]^{++}$ to DBT increases, but the relative abundance of $[\text{M}+\text{OH}]^+$ and $[\text{M}+\text{H}]^+$ decreases..... 109
- Figure A4.1:** ^1H NMR spectra of BT in CDCl_3 . [139] 116
- Figure A4.2:** Comparison of ^1H NMR spectra obtained from BT standard and the crude reaction mixture of BT with $\text{C}_2\text{H}_5\text{OTf}$ in 1 mL DCE at room temperature. From the comparison of ^1H NMR spectra above, we know that no reaction occurs between BT and $\text{C}_2\text{H}_5\text{OTf}$ in DCE at 25 °C in glass flask. 116
- Figure A4.3:** ^1H NMR spectra of DBT in CDCl_3 . [140] 117

- Figure A4.4:** Comparison of ^1H NMR spectra obtained from DBT standard and the crude reaction mixture of DBT with $\text{C}_2\text{H}_5\text{OTf}$ in 1 mL DCE at room temperature. From the comparison of ^1H NMR spectra above, we know that no reaction occurs between DBT and $\text{C}_2\text{H}_5\text{OTf}$ in DCE at 25 °C in glass flask. 117
- Figure A4.5:** ^1H NMR spectra of BNT in CDCl_3 . [141] 118
- Figure A4.6:** Comparison of ^1H NMR spectra obtained from BNT standard and the crude reaction mixture of BNT with $\text{C}_2\text{H}_5\text{OTf}$ in 1 mL DCE at room temperature. From the comparison of ^1H NMR spectra above, we know that no reaction occurs between BNT and $\text{C}_2\text{H}_5\text{OTf}$ in DCE at 25 °C in glass flask. 118
- Figure A4.7:** ^1H NMR spectra of 4, 6-dimethyl DBT in CDCl_3 . [142]..... 119
- Figure A4.8:** Comparison of ^1H NMR spectra obtained from 4, 6-dimethyl DBT standard and the crude reaction mixture of 4, 6-dimethyl DBT with $\text{C}_2\text{H}_5\text{OTf}$ in 1 mL DCE at room temperature. From the comparison of ^1H NMR spectra above, we know that no reaction occurs between 4, 6-dimethyl DBT and $\text{C}_2\text{H}_5\text{OTf}$ in DCE at 25 °C in glass flask. 119
- Figure A4.9:** The reactions in 1,2-dichloroethane at 298.15 K. 120
- Figure A4.10:** The Gibbs free energy surface for the reaction of dibenzothiophene and ethyl trifluoromethanesulfonate in the 1, 2-dichloroethane solution. The key atomic distances (in Å) for the transition state are indicated by dash lines. 121
- Figure A4.11:** Silica electrospray capillary setup on 7 T FT-ICR MS..... 128
- Figure A4.12:** Characteristic peaks from DBT and reference peaks from TAB BF_4 obtained on ESI(+) 7 T FT-ICR MS. 129
- Figure A4.13:** The mass spectra obtained from the ESI capillary set-up where the silica capillary locates 1.5 mm outside of the outer metallic capillary on ESI(+) 7 T FT-ICR MS. There are almost no desired peaks observed. 131
- Figure A4.14:** The mass spectra obtained from the ESI capillary set-up where the silica capillary locates 0.0 mm relative to the outer metallic capillary on ESI(+) 7 T FT-ICR MS. The desired peaks are observed..... 133
- Figure A4.15:** The mass spectra obtained from the ESI capillary set-up where the silica capillary locates -1.5 mm inside of the outer metallic capillary on ESI(+) 7 T FT-ICR MS. The relative abundance of the desired peaks increases comparing with **Figure A4.14**. 134
- Figure A4.16:** The mass spectra obtained from the ESI capillary set-up where the silica capillary locates -3.0 mm inside of the outer metallic capillary on ESI(+) 7 T FT-ICR MS. The relative abundance of the desired peaks sharply increases comparing with **Figure A4.15**. 135
- Figure A4.17:** The mass spectra obtained from the ESI capillary set-up where the silica capillary locates -5.5 mm inside of the outer metallic capillary on ESI(+) 7 T FT-ICR MS. The relative abundance of the desired peaks increases comparing with **Figure A4.16**. 136
- Figure A4.18:** Comparison of mass spectra obtained from different relative distance between silica capillary and stainless steel capillary in Pos. ESI mode. The relative abundance of the desired peaks increases as the silica capillary moves inside of the metallic capillary. 137
- Figure A4.19:** Effect of spray voltage on the intensity of characteristic peaks of $[\text{M}+\text{C}_2\text{H}_5]^+$, $[\text{M}+\text{H}]^+$ and $[\text{M}]^{++}$. This data is obtained by choosing the set-up where the silica position locates -1.5 mm outside of the stainless steel capillary. As the source voltage increasing, the intensity of the desired peaks increases. 137
- Figure A4.20:** Solution Model. $\text{C}_2\text{H}_5\text{OTf}$ has 10 times more chance to be transferred to the metal surface than DBT does. 138
- Figure A4.21:** The mass spectra obtained from the ESI capillary set-up where the silica capillary locates 1.5 mm outside of the outer metallic capillary on ESI(+) 7 T FT-ICR MS. As expected, the

reference peak from TBA BF₄ is observed suggesting that our ESI setup works well. No characteristic peaks from C₂H₅OTf or DCE are observed without contact with the metal needle. 141

Figure A4.22: The mass spectra obtained from the ESI capillary set-up where the silica capillary locates 1.5 mm outside of the outer metallic capillary on ESI(+) 7 T FT-ICR MS. As expected, the reference peak from TBA BF₄ is observed suggesting that our ESI setup works well. No characteristic peaks from C₂H₅OTf or DCE are observed, and the explanation for which can be given as follows: radical cation of C₂H₅OTf or DCE is short-lived species and cannot be detected on the time scale of FT-ICR MS; or the active open-shell species have reacted with other nucleophilic species and vanished before detection. 143

Figure A4.23: The mass spectra obtained from the ESI capillary set-up where the silica capillary locates 1.5 mm outside of the outer metallic capillary on ESI(+) 7 T FT-ICR MS. As expected, the reference peak from TBA BF₄ is observed suggesting that our ESI setup works well. No characteristic peaks from DBT or DCE are observed without contact with the metal needle. 145

Figure A4.24: The mass spectra obtained from the ESI capillary set-up where the silica capillary locates 1.5 mm outside of the outer metallic capillary on ESI(+) 7 T FT-ICR MS. As expected, the reference peak from TBA BF₄ is observed suggesting that our ESI setup works well. Radical cation from DBT is observed at *m/z* 184.03412 when contacting with the metal surface that connecting to a high voltage supply. A tiny protonated peak is also observed at *m/z* 185.04195. 147

Figure A4.25: The mass spectra obtained from the ESI capillary set-up where the silica capillary locates 1.5 mm outside of the outer metallic capillary on ESI(+) 7 T FT-ICR MS. From the above experiments (**Figure A4.22 – A4.25**), we know that our ESI set-up works well. In order to reduce the suppression from TBA BF₄, Only solvent DCE is used from now on. No characteristic peaks from DBT are observed in this case. 149

Figure A4.26: The mass spectra obtained from the ESI capillary set-up where the silica capillary locates 1.5 mm outside of the outer metallic capillary on ESI(+) 7 T FT-ICR MS. Characteristic peaks from DBT are observed at *m/z* 213.07325, 185.04195 and 184.03412 without DBT directly contact with the metal surface, explanation can be given as: first C₂H₅OTf is oxidized by losing one electron to produce a lower lying LUMO active species, and then DBT reacts with [C₂H₅OTf]^{•+} to produce the corresponding [M+C₂H₅]⁺ via nucleophilic substitution and [M]^{•+} via charge transfer reaction in the gas-phase. For the production of [M+H]⁺, H₂O in the air is assumed to participate in the production together with [C₂H₅OTf]^{•+} in the gas phase. 151

Figure A4.27: The mass spectra obtained from the ESI capillary set-up where the silica capillary locates 0.0 mm outside of the outer metallic capillary on ESI(+) 7 T FT-ICR MS. Characteristic peaks from DBT are observed at *m/z* 184.03412, 185.04195 and 213.07325 without DBT directly contacting with the metal surface, explanation can be given as same as in **Figure A4.26**. Moreover, the intensity of the characteristic peaks increases as contacting time interval of these two solutions increases. 153

Figure A4.28: Evaluation of the influence of electrochemistry on the intensity of characteristic peaks of [M+C₂H₅]⁺, [M+H]⁺ and [M]^{•+} through silica position in 1-D space for mechanism study. The data are obtained from **Figure A4.26 - A4.27**. 154

Figure A4.29: Comparison of mass spectra obtained from sweep gas flow rates. As the sweep gas flow rate increases, the relative abundance of the [M]^{•+} increases, but the relative abundance of the [M+OH]⁺, [M+H]⁺ decreases. 155

Figure A4.30: The calculated 1st ionization energies (*I*₁) for dibenzothiophene and ethyl trifluoromethanesulfonate in the 1, 2-dichloroethane solution. 156

Figure A4.31: The possible collision channels for ethyl dibenzothiophene cation in the ESI-MS experiments. 157

Figure A4.32: The charge-transfer reaction that produces DBT^{•+} in the ESI-MS experiments. 158

Figure A4.33: The gas-phase reaction that produces DBTH⁺ in the ESI-MS experiments. 158

Figure A4.34: The pathway with DBT activated first under ESI(+) FT-ICR MS. 161

- Figure A4.35:** Mass spectra obtained from benzo[*b*]thiophene (BT) with C₂H₅OTf under ESI(+) FT-ICR MS. 163
- Figure A4.36:** Mass spectra obtained from dibenzo[*b,d*]thiophene (DBT) with C₂H₅OTf under ESI(+) FT-ICR MS. 164
- Figure A4.37:** Mass spectra obtained from benzo[*b*]naphtho[2,1-*d*]thiophene (BNT) with C₂H₅OTf under ESI(+) FT-ICR MS..... 166
- Figure A4.38:** Mass spectra obtained from 4,6-dimethyldibenzo[*b,d*]thiophene (4, 6-DM DBT) with C₂H₅OTf under ESI(+) FT-ICR MS..... 167
- Figure 5.1:** 7T FT-ICR mass spectra obtained from samples **A₁** and sample **B₁** in (+) ESI ionization mode for the mass range 100-1100 Da (right column) and the corresponding enlarged section of those in a range between *m/z* 387.8-390.4 (left column) with the assigned molecular formulas. 172
- Figure 5.2:** Comparison of heteroatom class distributions obtained from the sample **A₁** (C₂H₅OTf) and sample **B₁** (C₂H₅I). Note that relative and not absolute abundances are shown; the summary of all abundances from one method is 100%. 173
- Figure 5.3:** Comparison of DBE versus carbon number plots for S₁, S₂, S₃, N₁S₁, N₁ classes from sample A₁ (C₂H₅OTf) and sample B₁ (C₂H₅I), obtained by (+) ESI FT-ICR MS..... 175
- Figure A5.1:** ¹HNMR spectra of dibenzo[*b,d*]thiophene (DBT) in CDCl₃. 192
- Figure A5.2:** Comparison of ¹HNMR spectra obtained from DBT standard and the crude reaction mixture of DBT with C₂H₅I in 1 mL DCE at 25 °C for 24 h. 193
- Figure A5.3:** Comparison of ¹HNMR spectra obtained from DBT standard and the crude reaction mixture of DBT with C₂H₅OTf in 1 mL DCE at 25 °C for 24 h. 194
- Figure A5.4:** ¹HNMR spectra of ACR in CDCl₃..... 195
- Figure A5.5:** Comparison of ¹HNMR spectra obtained from ACR standard and the crude reaction mixture of ACR with C₂H₅I in 1 mL DCE at 25 °C for 24 h. 196
- Figure A5.6:** Comparison of class distribution based on 1 mmol and 2 mmol of C₂H₅OTf in crude oil for sample A₁ and sample A₂..... 196
- Figure A5.7:** Comparison of class distribution based on 1 mmol and 2 mmol of C₂H₅I in crude oil for sample B₁ and sample B₂. 197
- Figure A5.8:** Color-coded image plots of DBE vs carbon number for members of S₁ class from sample A₁ (C₂H₅OTf). 197
- Figure A5.9:** Color-coded image plots of DBE vs carbon number for members of S₂ class from sample A₁ (C₂H₅OTf). 198
- Figure A5.10:** Color-coded image plots of DBE vs carbon number for members of S₃ class from sample A₁ (C₂H₅OTf). 198
- Figure A5.11:** Color-coded image plots of DBE vs carbon number for members of N₁ class from sample B₁ (C₂H₅I)..... 199
- Figure A5.12:** Color-coded image plots of DBE vs carbon number for members of N₁S₁ class from sample B₁ (C₂H₅I)..... 199
- Figure A5.13:** Color-coded image plots of DBE vs carbon number for members of S₁ class from sample B₁ (C₂H₅I)..... 200
- Figure A5.14:** Color-coded image plots of DBE vs carbon number for members of S₂ class from sample B₁ (C₂H₅I)..... 200
- Figure A5.15:** Color-coded image plots of DBE vs carbon number for members of S₃ class from sample B₁ (C₂H₅I)..... 201
- Figure A5.16:** DBE vs carbon number for members of HC classes from sample A₁ (C₂H₅OTf) and sample B₁ (C₂H₅I). 201

- Figure A5.17:** Enlarged section of mass spectra that contain a low DBE (2) of HC species from sample A₁. 202
- Figure A5.18:** Comparison of DBE vs carbon number for members of cation and radical cation classes from Sample A₁ and Sample B₁. 202
- Figure 6.1:** Comparison of broadband positive-ion ESI 7 T FT-ICR mass spectra and the corresponding heteroatom class distribution obtained for benzylated heavy crude oil samples (M1, M2 and M3). Herein, M0 is taken as a reference for the comparison..... 211
- Figure 6.2:** Comparison of Kendrick plots (DBE vs. Carbon number plots) for ions of the S₁[H], S₂[H] and CH[H] classes for M1, M2 and M3 samples based on Table 6.1, obtained by (+) ESI FT-ICR MS. Herein, M0 is taken as a reference. 212
- Figure 6.3:** Comparison of broadband positive-ion ESI 7 T FT-ICR mass spectra and the corresponding heteroatom class distribution obtained from samples of M4, M5 and M6 based on Table 6.1. Herein, M0 is taken as a reference for the comparison. 215
- Figure 6.4:** Comparison of Kendrick plots (DBE vs. Carbon number plots) for ions of the N₁[H], N₁O₁S₁[H], S₁[H] and S₂[H] classes for M4, M5 and M6 samples based on Table 6.1, obtained by (+) ESI FT-ICR MS. Herein, M0 is taken as a reference. 217

List of Schemes

- Scheme 2.1:** Ethylation of DBT..... 67
- Scheme 3.1:** Ethylation of crude oil under different reaction conditions. 79
- Scheme 3.2:** Ethylation of a sulfur-containing compound..... 88
- Scheme 3.3:** Electrophilic Aromatic Substitution (EAS). 91
- Scheme 4.1:** Reaction of dibenzo[*b,d*]thiophene (DBT) and ethyl trifluoromethanesulfonate (C₂H₅OTf) in anhydrous 1,2-dichloroethane (1,2-DCE) at room temperature..... 101
- Scheme 7.1:** Ethylation of dibenzothiophene (DBT)..... 222
- Scheme 7.2:** Ethylation of crude oil under different conditions. 223
- Scheme 7.3:** Reaction of dibenzothiophene (DBT) under positive ESI mode..... 223
- Scheme 7.4:** Reaction of crude oil under positive ESI mode. 224
- Scheme 7.5:** Benzylation of crude oil under different conditions. 224

List of Tables

Table 1.1: Hydrocarbon composition of crude oil.....	11
Table 1.2: Elemental composition of crude oil.....	12
Table 3.1: The heteroatom class distribution of the 4 most abundant classes with different mole ratios of AgBF ₄ : C ₂ H ₅ I: heavy crude oil	81
Table A4.1: Evaluation of sulfur-containing standards in the S _N 2 reaction ^a	115
Table A4.2: The changes of the standard Gibbs free energy (in kcal/mol) for the solution reactions ($\Delta_r G^\circ$) and activation ($\Delta_a G^\circ$) with respect to the separated reactants	121
Table A4.3: Evaluation of the influence of silica capillary position on characteristic peaks derived from DBT	129
Table A4.4: Evaluation of the influence of Silica capillary position, solution constituent and the solution flow pathway on the peaks derived from DBT.....	139
Table A4.5: The changes of the standard Gibbs free energy ($\Delta_r G^\circ$, in kcal/mol) for the possible collision channels that produces the molecular cations detected in the ESI-MS experiments.....	158
Table 5.1: Evaluation of sulfur- and nitrogen-containing standards in the S _N 2 reaction ^a	177
Table 5.2: The changes of the standard Gibbs free energy ($\Delta_r G^\circ$, in kcal/mol) for the ethylation that produces the molecular cations detected in the ESI-MS experiments ^a	180
Table 6.1: Heteroatom class distribution from the modified heavy crude oil samples in anhydrous DCE.....	209

List of Abbreviations

Å	angstrom
AcOH	acetic acid
ACR	acridine
AGC	automatic gain control
ANTH	anthracene
APCI	atmospheric pressure chemical ionization
APLI	atmospheric pressure laser ionization
APPI	atmospheric pressure photoionization
BT	benzothiophene
BNT	benzonaphthothiophene
CCE	controlled-current electrolytic cell
CRM	charge residue model
δ	chemical shift (ppm)
DB	double bonds
DBE	double bond equivalent
DBF	dibenzofuran
DBT	dibenzothiophene
DC	direct current
DCE	1,2-dichloroethane
DCM	dichloromethane
4,6-DMDBT	4,6-dimethyldibenzothiophene
EAS	electrophilic aromatic substitution
eFT	enhanced Fourier transform
e.g.	example
EI	electron ionization
eq.	equivalent
Eq.	equation
ESI-MS	electrospray mass spectrometry
Et	ethyl
etc.	and so forth
FID	free induction decay
FT-ICR	Fourier transforms ion cyclotron resonance Mass Spectrometry
FWHM	full width at half maximum
GC	gas chromatography
h	hours
HC	hydrocarbon
HF Orbitrap	high-field Orbitrap
^1H NMR	proton nuclear magnetic resonance
HRMS	high resolution mass spectrometry
HV	high voltage

I_1	first ionization energy
IEM	ion evaporation model
IT	ion trap
J	coupling constant
KMD	Kendrick mass defect
KNM	Kendrick nominal mass
LC	liquid chromatography
LUMO	lowest unoccupied molecular orbital
LTQ	linear ion trap
μ	micro
m/z	mass to charge ratio
PA	proton affinity
PAHs	polycyclic aromatic hydrocarbons
PANHs	polycyclic aromatic nitrogen heterocycles
PASHs	polycyclic aromatic sulfur heterocycles
PAXHs	polycyclic aromatic heterocycles
pH	proton log units
ppm	parts per million
QM	Quantum mechanics
R	rings
REMPI	resonance-enhanced multiphoton ionization
RF	radio frequency
RMS	root-mean-square
RSP	reactivity-selectivity principle
RT	room temperature
SARA	saturate aromatic resin and asphaltene
TOF	time-of-flight
TC	total current
XRD	X-ray diffraction

List of Publications

List of Publications

- Xuxiao Wang and Wolfgang Schrader. Selective Analysis of Sulfur-Containing Species in a Heavy Crude Oil by Deuterium Labeling Reactions and Ultrahigh Resolution Mass Spectrometry coupled with Positive Electrospray Ionization. *Int J Mol Sci* 2015, 16 (12), 30133-43.
- Xuxiao Wang and Wolfgang Schrader. Adding a Chemical Dimension as Tool for Selective Analysis of a Heavy Crude Oil by Fourier Transform Ion Cyclotron Resonance Mass Spectrometry (FT-ICR MS). (Will be submitted to *Anal. Chem.*)
- Xuxiao Wang, Xin Wu, Walter Thiel and Wolfgang Schrader. Experimental Evaluation of Electrochemically-induced Electron Transfer Reaction in Electrospray mass spectrometry. (Will be submitted to *Angew. Chem. Int. Ed.*)
- Xuxiao Wang, Xin Wu, Walter Thiel and Wolfgang Schrader. Electrochemically-induced Selective Analysis of Sulfur-Containing in Heavy Crude Oils on the Millisecond Time Scale by Electrospray Ionization Mass Spectrometry. (Will be submitted to *Anal. Chem.*)
- Xuxiao Wang and Wolfgang Schrader. Electrospray Fourier Transform ion cyclotron resonance mass spectrometry (ESI FT-ICR MS): Reactivity of poly aromatic hydrocarbon and poly aromatic heterocycles in heavy crude oils towards benzyl halides. (Will be submitted to *Energy & Fuel*)

List of Oral Presentations

- ANAKON 2013-GDCh (die wichtigste Konferenz in Deutschland, Österreich und der Schweiz für den Wissensaustausch in der Analytischen Chemie und verwandten Gebieten), 04.-07.03.2013 in Essen, Germany (**Poster presentation**).
- The 61st ASMS international conference (American Society for Mass Spectrometry), 09.-13.06.2013 in Minneapolis, Minnesota, USA (**Poster presentation**).
- The 46th DGMS conference (Deutschen Gesellschaft für Massenspektrometrie), 10.-13.03.2013 in Berlin, Germany (**Poster presentation**).
- FTMS Fachgruppentagung der DGMS, 26.-27.09.2013 in Heidelberg, Germany (**Oral presentation**).
- The 47th DGMS conference (Deutschen Gesellschaft für Massenspektrometrie), 02.-05.03.2014 in Frankfurt/Main, Germany (**Poster presentation**).
- The 20th IMSC (International Mass Spectrometry Conference), 24.-29.08.2017 in Geneva, Switzerland (**Poster presentation**).
- The 48th DGMS conference (Deutschen Gesellschaft für Massenspektrometrie), 01.-04.03.2015 in Wuppertal, Germany (**Organization und Oral presentation**).
- FTMS Fachgruppentagung der DGMS, 17.-18.09.2015 in Bonn, Germany (**Oral presentation**).

Curriculum Vitae

Der Lebenslauf ist in der Online-Version aus Gründen des Datenschutzes nicht enthalten.

Acknowledgements

First, I would like to sincerely express my gratitude to my supervisor, Prof. Dr. Wolfgang Schrader for his courage and insight to take me from far away China as a Ph.D. student in Max-Planck-Institut für Kohlenforschung, because I knew nothing about mass spectrometry and crude oil four and half years ago, and he was always patient for my questions and gradual progress. In four and half years, I have learned not only abundant professional knowledge of MS and crude oil, but also enriched my knowledge of modern chemistry and modern physics, and established a firm love and keen interest in natural science as well as math. In addition to science, he also helps me a lot with improving my English and Deutsch. His precious care and help for students as well as his humor impress me deeply. I am really grateful for his invaluable guidance, insightful advice, consistent encouragement, sufficient resources and the great freedom that he has given to me during my entire Ph.D. research.

I would also like to acknowledge my Co-Gutachter, Prof. Dr. Carsten Schmuck who has taken time to read my thesis and improve it with his insightful comments and suggestions.

I am grateful to Wasim Alachraf, Sami Lababidi, Alessandro Vetere and Xin Wu for their help and support in my research. Sami introduced me to the world of crude oil analysis; Wasim helped me a lot with the mass spectrometry when I first came to our research group; Alessandro gave me the great help in his methodical logic in solving instrumental problems which I learned a lot. Xin Wu introduced me to the world of calculation and helped me a lot with it.

I would like to thank the whole MS department: Werner Jopek, Beate Diettrich and Marion Blumenthal for their help and patience in teaching my Deutsch; Heinz-Klein and Manfred Scheppat for the great experience and knowledge in the field of mass spectrometry; Daniel Margold, Dino Richter, Dirk Kampen, Christopher Grundmann, Simone Marcus and Alesander Woyk for their technical help during my work in the MS lab. In addition, I would like to thank my previous and current colleagues for the enjoyable time in Prof. Dr. Schrader's group, include: Ivy Lim for her kind-hearted help in my life in Germany, my lovely officemate Lilla Mohnarne Guricza, Jennifer Reece, Amallesh Roy, Jandyson Machado Santos, Rouji Luo, Aikaterini Kondyli, Thierry Ghislain and Zahra Farmani, and especially my lovely friend Spanish Maria Angeles Fernandez with whom I had a precious time.

Also, I want to thank all of my Chinese friends in MPI, Mülheim an der Ruhr, with whom I spent a lovely time in Germany.

Last but not least, no words can sufficiently express my gratitude towards my beloved parents, Mr. Xueyi Wang and Mrs. Chunhua Jin, my brother Xuyang Wang and my sister Xuli Wang. The present achievement could not be attained without their endless love and encouragement.

And now these three remain: faith, hope and love, but the greatest of these is love.